Modélisation de l'évolution de la microstructure et de l'intégrité de surface en usinage à grande vitesse du Ti6Al4V

Xiang Xu

HESAM UNIVERSITÉ

西安交通大學 XI'AN JIAOTONG UNIVERSITY

Arts et Métiers Sciences et Technologies

ÉCOLE DOCTORALE SCIENCES DES MÉTIERS DE L'INGÉNIEUR

Laboratoire des Matériaux et Procédés of ENSAM, Campus of Cluny

GRADUATE SCHOOL OF XI'AN JIAOTONG UNIVERSITY

Machine Tool Research Group – Xi'an Jiaotong University

THÈSE / PhD Thesis

présentée par / presented by : **Xiang XU**

soutenue le / defended in : **25 Novembre 2022**

pour obtenir le grade de / to obtain the degree of : **Docteur d'HESAM Université**

et de / and of : **Doctor of Xi'an Jiaotong University**

préparée à / prepared at : **École Nationale Supérieure d'Arts et Métiers**

et à / and at : **Xi'an Jiaotong University**

Spécialité / Speciality : **Génie Mécanique – Procédés de Fabrication**
Mechanical Engineering – Manufacturing Processes

Modélisation de l'évolution de la microstructure et de l'intégrité de surface en usinage à grande vitesse du Ti-6Al-4V

Modelling of microstructure evolution and surface integrity in high speed machining of Ti-6Al-4V alloy

THÈSE dirigée par / PhD Thesis supervised by :
M. José OUTEIRO et/and **M. Jun ZHANG**

Jury :

M. Mohammed NOUARI, Professor, University of Lorraine	Président
M. Domenico UMBRELLO, Professor, University of Calabria	Rapporteur
M. Min WAN, Professor, Northwestern Polytechnical University	Rapporteur
Mme. Madalina CALAMAZ, Associate Professor, Arts et Métiers Institute of Technology	Examinatrice
M. Ke HUANG, Professor, Xi'an Jiaotong University	Examinateur
M. Qinghua SONG, Professor, Shandong University	Examinateur
M. Jun ZHANG, Professor, Xi'an Jiaotong University	Examinateur
M. José OUTEIRO, Assoc. Professor HDR/Habil., Arts et Métiers Institute of Technology	Examinateur

T H E S I S

Modelling of microstructure evolution and surface integrity in high speed machining of Ti-6Al-4V alloy

Xiang XU

Arts et Métier Institute of Technology

and

Xi’an Jiaotong University

DOCTORAL DISSERTATION

Confidential until:
31/12/2022

Acknowledgement

This thesis was carried at the LaBoMaP (Laboratoire Bourguignon des Matériaux et Procédés) laboratory of the Arts et Metiers Institute of Technology and MTRG (Machine Tool Research Group) of the Xi'an Jiaotong University (XJTU), with the financial support from National Natural Science Foundation (No. 51375373), Shaanxi Science Foundation for Distinguished Young Scholars (2019JC08), and China Scholarship Council (NO. 201906280422).

This work would not have been possible without the support of my supervisors as a co-supervised doctoral student. I would like to thank my supervisor, Prof. José Outeiro, for his guidance and advice throughout my thesis work. What impresses me is his innovative ideas and energetic motivation to do research work. His scientific expertise in modeling and simulation of machining operations especially considering constitutive models gives me great help to improve my work. He shares a lot of his experience with me about how to manage the research work, cooperation and daily life, which benefits to my personal abilities to better continue any future work. I would also like to thank my supervisor, Prof. Jun Zhang, for his support and supervision during my whole PhD stage. He pays a lot of attention with great patience and encouragement to teach me how to complete a meaningful research work and improve it continuously. What he always teaches me is that, when I am working hard, I shouldn't forget to look up at the sky and stars. Special thanks must be given to Prof. Wanhua Zhao, the leader of MTRG, for his lifetime contribution to provide a better laboratory and scientific atmosphere to help us study and conduct research work.

I would like to thank Dr. Rachid M'Saoubi from SECO Tools company for his critical support in designing my cutting experiments and providing the cutting inserts. I would like to thank Dr. Lamice Denguir for her valuable advice in developing the CEL approach and modeling. My gratitude is also given to Prof. Viktor Astakhov to improve the proposed numerical approaches. I would like to thank Dr. Betrand Marcon from Arts et Metiers Institute of Technology for the preparations of machining tests. I would like also to thank Mr. Baochen Li and Dr. Hongguang Liu from Xi'an Jiaotong University for their help in the high-speed machining experiments and material microstructural observation.

I would like to thank all my colleagues in LaBoMaP and XJTU for their help in my work and their company in daily life. I am thankful to my friends with wonderful memories with them: Guangchao Nie, Wenyu Cheng, Yutao Zhang, Wudi Li, Iheb Cherif, Rabiae Arif, Edouard Ducroux, Bastien Toubhans, Come Legrand, Ivan Hamm, Yong He, Binbin Xu, Zhechao Liu, Xiaojie Li, Wei Feng, Yangguang Zhang and Xin Liu.

I am grateful to my dear wife, Zhihui Li, for her support and understanding during my doctoral study, which enables me to focus on my research work and thesis. She always gives me spiritual strength when I am in the most difficult time. Special thanks to my parents and other family members for taking care of me for a long time to support me doing research work without any hesitancy, and finally complete my thesis.

Résumé

Le développement rapide de l'industrie aérospatiale est la motivation pour augmenter la productivité lors de la fabrication des pièces en conservant la même qualité ou performance. L'usinage à grande vitesse (UGV) des matériaux difficiles à découper comme les alliages à base de titane est un moyen d'atteindre une productivité élevée. Cependant, les mécanismes d'enlèvement de matière sont différents de l'usinage conventionnel, ce qui affecte les propriétés des surfaces et sous-couches de la pièce usinée connues sous le nom d'intégrité de surface. Jusqu'à présent, la plupart des travaux de recherche sur l'intégrité de surface dans l'usinage sont basés sur l'analyse phénoménologique et impliquent rarement une analyse théorique des phénomènes physiques responsables de la modification des propriétés des sous-couches.

Dans ces travaaux de recherche, l'évolution de la microstructure et d'autres caractéristiques de l'intégrité de surface (contraintes résiduelles, déformations plastiques et topographie) induites par UGV de l'alliage Ti-6Al-4V sont étudiées en utilisant une modélisation multiéchelles et des approches expérimentales. L'approche de modélisation multiéchelles combine la simulation du procédé de coupe orthogonale à l'échelle mésoscopique en utilisant la méthode des éléments finis (MEF) et la simulation de la morphologie du grain à l'échelle microscopique en utilisant la méthode des automates cellulaires (AC).

Cette approche de modélisation à plusieurs échelles est particulièrement utilisée pour simuler l'évolution de la microstructure et son influence sur la microdureté dans la zone de coupe, y compris la microstructure dans la bande de cisaillement dans les copeaux et le gradient de microstructure dans la sous-couche usinée. Les observations expérimentales des copeaux et des surfaces usinées à l'aide du microscope électronique à balayage (MEB) et du microscope électronique à transmission (MET) ont permis d'identifier la recristallisation dynamique (DRX) comme mécanisme principal de raffinement du grain dans l'usinage du Ti-6Al-4V. Par conséquent, la morphologie du grain induite par le DRX a été simulée en utilisant la méthode AC en considérant comme données d'entrée les distributions de déformations, de vitesses de déformations et de températures obtenues à partir des simulations EF du procédé de coupe. Pour mener ces simulations, des modèles de coupe UGV de l'alliage Ti-6Al-4V sont développés en utilisant la méthode EF et les approches lagrangienne et eulérienne couplées (CEL). Ces modèles de coupe comprennent une loi de comportement proposée (plasticité et endommagement) tenant compte de l'état de contrainte (triaxialité et paramètre de

Lode) en plus de la déformation, de la vitesse de déformation et de la température. En outre, une procédure numérique a été proposée pour simuler efficacement la formation des contraintes résiduelles dans l'usinage. Cette procédure est basée sur l'approche CEL pour simuler les phases de chargement et de déchargement, et sur l'approche lagrangienne pour simuler la phase de refroidissement.

Les modèles de coupe proposés ont permis de simuler avec précision les copeaux festonnés, les forces, les contraintes résiduelles, la déformation plastique, la microstructure, la microdureté et la topographie des surfaces dans la coupe orthogonale de l'alliage Ti-6Al-4V, pour une large gamme de conditions de coupe. En particulier, la fluctuation périodique des résultats d'usinage (forces, topographie de surface, contraintes résiduelles, déformation plastique, etc.) souvent observée dans l'usinage d'alliages de titane a été prédite avec précision en utilisant cette approche de modélisation multiéchelle.

Mots clés : Modélisation, Usinage à Grande Vitesse, Ti-6Al-4V, Microstructure, Recristallisation Dynamique, Intégrité de Surface.

Abstract

The rapid development of aerospace industry is the motivation for increasing the manufacturing productivity keeping the same part quality or event improve it. High-Speed Machining (HSM) of difficult-to-cut materials like Titanium-based alloys is a way to achieve a high productivity. However, the mechanisms of material removal are different from conventional machining, which affects the proprieties of the near surface layers of the machined part also called the surface integrity. So far, most of research works on surface integrity in machining are based on the phenomenological analysis and rarely involve a theoretical analysis of the physical phenomena responsible for the modification of the near surface layer properties.

In this research work, the microstructure evolution and other surface integrity features (residual stresses, plastic strain, and surface topography) induced by HSM of Ti-6Al-4V alloy are investigated using multiscale modelling and experimental approaches. The multiscale modelling approach combines the simulation of the orthogonal cutting process at meso-scale using Finite Element Method (FEM) and the simulation of the grain morphology at the micro-scale using Cellular Automata (CA) method.

This multiscale modelling approach is particularly used to simulate the microstructure evolution and its influence on the microhardness in the cutting zone, including the microstructure in the shear band in the chips and the microstructure gradient in the machined subsurface. Experimental observations of the chips and machined subsurfaces using scanning electron microscope (SEM) and transmission electron microscope (TEM) permitted to identify the dynamic recrystallization (DRX) as the main mechanism of grain refinement in machining of Ti-6Al-4V. Therefore, grain morphology induced by DRX was simulated using CA method by considering as input data the strain, strain rate and temperature distributions obtained from FE simulations of the cutting process. To conduct these FE simulations, cutting models of HSM of Ti-6Al-4V alloy are developed using FE method and both Lagrangian and Coupled Eulerian and Lagrangian (CEL) approaches. These cutting models included a proposed constitutive model (plasticity and damage) considering the state of stress (triaxiality and Lode parameter) in addition of the strain, strain rate, and temperature. In addition, a numerical procedure was proposed to efficiently simulate the residual stresses formation in machining. This procedure is based on CEL approach to simulate the loading and unloading phases, and the Lagrangian approach to simulate the cooling phase.

The proposed cutting models permitted to accurate simulate serrated chips, forces, residual stresses, plastic

strain, microstructure, microhardness and surface topography in orthogonal cutting of Ti-6Al-4V alloy, for a wide range of cutting conditions. In particular, the periodic fluctuation of the machining outcomes (forces, surface topography, residual stresses, plastic strain, etc.) often seen in machining Titanium alloys were accurately predicted using this multiscale modelling approach.

Keywords: Modelling, High Speed Machining, Ti-6Al-4V, Microstructure, Dynamic Recrystallization, Surface Integrity.

Table of Contents

List of tables

List of figures

Glossary

Abbreviation

ABOP	Analytical bond order potential
ALE	Arbitrary Lagrangian-Eulerian
ASB	Adiabatic shear band
BCC	Body-centered cubic
CA	Cellular automata
CCR	Chip compression ratio
cDRX	Continuous dynamic recrystallization
CEL	Coupled Eulerian and Lagrangian
CRSS	Critical resolved shear stress
DDB	Dislocation density based
dDRX	Discontinuous dynamic recrystallization
DEM	Discrete element method
Depth_MRS	Depth of the maximum compressive residual stress
DIC	Digital Image Correlation
DRV	Dynamic recovery
DRX	Dynamic recrystallization
EAM	Embedded atom method
EBSD	Electron back scattering diffraction
EDX	Energy Dispersive X-ray Detector
EVF	Eulerian Volume Fraction
FCC	Face-centered cubic
FDZ	First deformation zone
FE	Finite element
FEM	Finite element method
FFT	Fourier transform
FIB	Focused ion beam
FSI	Fluid-structure interaction
GB	Grain boundary
GND	Geometrical necessary dislocation
HAGB	High angle grain boundary
HCP	Hexagonal close packed
HR	High resolution
HSM	High speed machining
IFFT	Inverse Fourier transform
IPF	inverse pole-figure
JC	Johnson-Cook

JMAK	Johnson–Mehl–Avrami–Kolmogorov
LAG	Lagrangian
LAGB	Low angle grain boundary
Layer_RS	Depth of the layer affected by residual stress
LM	Lattice model
MD	Molecular dynamics
MRS	Maximum compressive residual stress beneath the surface
MTS	Mechanical threshold stress
OR	Orientation relationship
PCD	Polycrystalline diamond
PED	Precession electron diffraction
PSZ	Primary shear zone
SAED	Selected area electron diffraction
SCM	Self-consistent method
SDV	User-defined variables
SDZ	Secondary deformation zone
SEM	Scanning electron microscope
SF	Schmid factors
SPD	Severe plastic deformation
SPH	Smoothed particle hydrodynamics
SRS	Residual stress at the machined surface
STEM	Scanning transmission electron microscope
TB	Twin boundary
TDZ	Third deformation zone
TEM	Transmission electron microscope
ZH	Zener-Hollomon
XRD	X-ray difraction

Nomenclature

a	(mm)	Lattice size
A_s and D_s	(-)	Material constants to determine Austenite phase transformation
A_{JC}, B_{JC}, n_{JC}, C_{JC}, m_{JC}	(-)	Coefficients of the JC plasticity model
A, m, n, B, C, E, h	(-)	Coefficients of the proposed plasticity model
a_1, h_1, m_1, c_1 and Q_1	(-)	Material parameters to determine the critical strain for DRX
a_5, h_5, m_5, c_5 and Q_5	(-)	Material parameters to determine the DRX volume fraction
a_8, h_8, m_8, c_8 and	(-)	Material parameters to determine the DRX grain size

Q_8		
b	(-)	Burgers vector
b_i^k	(-)	Burgers vector of the kth dislocation type
C_n	(-)	A material constant
c_l	(-)	A material constant
c_0 and c_1	(-)	Material constants to determine microhardness
c^s_θ, c^{ax}_θ, c^t_θ, c^c_θ, f_{Lode}	(-)	Lode angle parameter related coefficients
c_η	(-)	Stress triaxiality coefficient
D_f	(-)	Stiffness degradation of the material
d	(μm)	Initial grain size
D, P, d_C, b_C	(-)	Coefficients of the TANH plasticity model
d_0	(μm)	Initial grain size of twins
D_1 - D_8	(-)	Damage coefficients for the BW model
D_b	(m^2 s^{-1})	Boundary self-diffusion coefficient
d_{Cell}	(μm)	Average cell size
d_{cr}	(μm)	Average dislocation cell size
d_{drex}	(μm)	DRX grain size
d_f	(μm)	Recrystallized grain size
d_i	(μm)	Current grain size
dP	(MPa)	Local stress
d_t	(μm)	Grain size of effective twins
f_s	(-)	Saturated volume fraction of deformation twinning
f	(-)	Fraction of cell wall dislocation density in total dislocation density
F	(N)	Driving force of grain boundaries
f'	(-)	Ratio of β phase precipitation
F_i	(N)	Driving force of the newly formed DRX grain
f_t	(-)	Volume fraction of deformation twinning
f_t	(-)	Volume fraction of twinning phase
f_{t0}	(-)	Initial volume fraction of twinning phase
f_{TW}	(-)	Twin volume fraction
f_{tw}	(-)	Volume fraction of twinning
f_β	(-)	Volume fraction of β-Ti
$f_{\alpha''}$	(-)	Volume fraction of the α'' phase
G	(-)	Shear modulus
g_0	(J)	Normalized activation energy at 0 K
G_f	(J)	Fracture energy
Gs	(-)	Serrated degree

H	(mm)	Peak of serrated chips
h	(mm)	Valley of serrated chips
h_{total}	(HV)	Total microhardness
H_0	(-)	A material constant
h_0	(HV)	Initial microhardness of material
h_0, h_i	(-)	Recrystallization related parameters for modified JC model
h_1	(mm)	Uncut chip thickness
K	(m^2 kg s^{-2} K^{-1})	Boltzmann's constant
K, m	(-)	Material constants
K_0	(-)	Material constant
k_1, c_1	(-)	Coefficient related to the work hardening
k_2, c_2	(-)	Coefficient related to the DRV
k_B	(-)	Boltzmann constant
k_c	(-)	Hall-Petch coefficient for twinning
k_t	(-)	Parameter related to tool-chip contact property
l_{TW}	(μm)	Mean spacing of the twin lamellae
L	(-)	Characteristic length of the element
l	(m)	Dislocation mean free path
l_{PED}	(mm)	Step size of PED
l_c	(m)	Tool-chip contact length
L_{CA}	(mm)	Length of a CA cell
m	(-)	Constant related to strain rate sensitivity
M	(-)	Mobility of grain boundary
M_s	(℃)	Initial temperature of martensitic transformation
N_i	(-)	Lattice number that makes up the current grain
$\dot{n}$	(-)	nucleation rate of dDRX
P	(-)	Nucleation probability of dDRX
Q	(kJ mol^{-1})	Activation energy
Q_b	(kJ mol^{-1})	Boundary-diffusion activation energy
R	(J mol^{-1} K^{-1})	Gas constant
r_i	(μm)	Grain radius of the current DRX grain
R_{lim}	(μm)	Critical grain size
$\mathbf{S}$	(-)	Deviatoric stress tensor
S_{CA}	(mm^2)	Area of a CA cell
t	(μm)	Thickness of the twin lamellae
t_j^k	(-)	Unit line direction of the kth dislocation type
T	(K)	Temperature
T_e	(℃)	Temperature when the phase transformation is complete
T_m	(K)	Melting temperature
T_r	(K)	Room temperature

T_s	(°C)	Initial temperature of the phase transformation
t_{tw}	(μm)	Mean thickness of twin lamella
V_c	(m min^{-1})	Cutting speed
V_i	(m s^{-1})	Grain growth velocity of the current DRX grain
V_s	(m/s)	Sliding speed of the chip over the tool
w	(-)	Damage initiation variable
w^k	(-)	Weighted factor of the kth dislocation
X_{drex}	(-)	DRX volume fraction
Z	(-)	Zener-Hollomon parameter
α	(-)	Numerical constant for shear stress
α^*, β^*, k_0	(-)	Controlling parameters for evolution rates of dislocation density
α_1	(°)	direction angle between the principal stress and X-axis
α_{ij}	(-)	Nye tensor
β_d and k_d	(-)	Material constants
γ	(-)	difference between von Mises and Tresca equivalent stress in the deviatoric stress plane
γ_m	(J)	Grain boundary energy
δ	(m)	Characteristic grain-boundary thickness
Δh_d, Δh_{HP}, Δh_{PT}, and Δh_t	(HV)	Increments of microhardness caused by dislocation density change, HP effect of grain size change, phase transformation and twin strengthening
ΔH_{tr}	(-)	Enthalpy of phase transition
ΔV_{tr}	(mm^3)	Volume change caused by phase transition
ε	(-)	Strain
$\varepsilon_{0.5}$	(-)	Strain with the DRX volume fraction of 0.5
ε_{init}	(-)	Critical strain of twin excitation
ε_r	(-)	Critical plastic strain
$\Delta\bar{\varepsilon}^{pl}$	(-)	Increment of the equivalent plastic strain
$\bar{\varepsilon}_0^{pl}$	(-)	Equivalent plastic strain at damage initiation
$\bar{\varepsilon}_f^{pl}$	(-)	Equivalent plastic strain at failure
$\dot{\varepsilon}$	(-)	Strain rate
η	(-)	Stress triaxiality
η_0	(-)	Reference stress triaxiality
θ	(rad)	Local misorientation
$\bar{\theta}$	(-)	Lode angle parameter
λ	(-)	Coefficient to control the material degradation rate
μ	(-)	Coulomb's friction coefficient

ξ_1, ξ_2	(-)	Fractions transferred from cell wall to GNDs
ρ	(mm^{-2})	Dislocation density
ρ_0	(mm^{-2})	Initial dislocation density
ρ_c	(mm^{-2})	Critical dislocation density
ρ_c	(mm^{-2})	Dislocation densities of cell interiors
ρ_d	(mm^{-2})	Dislocation density of the DRX grain
ρ_{gnd}	(μm)	Final total GND density
ρ^k	(mm^{-2})	GND density of the *k*th dislocation type
ρ_m	(mm^{-2})	Dislocation density of the original grain
ρ_{tot}	(mm^{-2})	Total dislocation density
ρ_{wg}	(mm^{-2})	Geometrically necessary dislocation densities of cell walls
ρ_{ws}	(mm^{-2})	Statistically stored dislocation densities of cell walls
σ	(MPa)	Flow stress
σ_1, σ_2, σ_3	(MPa)	Three principal stresses
σ_a	(MPa)	Stress components from rate-dependent interactions of dislocations with long-range barriers
σ_c	(MPa)	Critical resolved shear stress
σ_d	(MPa)	Stress components for dislocation drag
σ_G	(MPa)	Stress components for grain size effects
σ_m	(MPa)	Mean principal stress
σ_n	(MPa)	Normal stress at the tool-chip interface
σ_s	(MPa)	Corresponding saturated flow stress
σ_{th}	(MPa)	Stress components for thermal effects
σ_{tw}	(MPa)	Stress components for mechanical twinning
τ	(J)	Dislocation line energy
τ_{CRSS}	(MPa)	Critical shear stress
τ_f	(MPa)	Tangential contact stress
τ_{max}	(MPa)	Maximum shear stress
τ_Y	(MPa)	Yield shear stress
φ	(°)	Interaction angle between precipitation and GB
ϕ	(°)	Angle between principal stress direction and twinning shear direction
χ	(-)	Material constant

1 Introduction

This chapter presents an introduction to the research background and significance in the field of metal cutting and surface integrity, and then based on this introduction, the current main research challenges are discussed, and the research objectives are proposed. Finally, the structure of the dissertation is described.

1.1 Research background and significance

High speed machining (HSM) is widely used in many industrial sectors including in the aerospace and automotive industries for increasing the productivity due to its high materials removal rates. The machining process has great influence on the machined surface topography, and on the mechanical and microstructural properties of the near surface layers of machined components, also called surface integrity. With the rapid increase of the cutting speed, the mechanism affecting the surface integrity has changed and there are still some details remaining unclear.

As a severe plastic deformation (SPD) process, HSM can induce dynamic recrystallization and phase transformation due to the intense thermo-mechanical coupling generated by the cutting process. During HSM, the complex loading conditions, such as high strain rate, dynamic stress state and localized thermo-mechanical coupling, make the microstructure evolution quite different from other SPD processes. With the change of cutting conditions (cutting speed, feed, depth of cut, tool geometry, etc.), the internal loads (stress, strain rate, temperature, etc.) of the materials will change accordingly. So, the complex loading conditions and the correlation between them and the microstructure have become a key point to reveal the mechanisms of microstructure evolution in HSM.

To accurate modeling the microstructure in metal cutting an in-depth understandings of physical mechanisms controlling this microstructure is required. Amongst these mechanisms there are the grain refinement induced by SPD, grain refinement and grain growth inducted by dynamic recrystallisation (DRX) and dynamic recovery (DRV), mechanical twinning and phase transformation. These mechanisms are essential to be incorporated into machining simulation in order to better predict the microstructure evolution in metal cutting. To improve the functional performance and life of components, the cutting process needs to be optimized to obtain an enhanced surface integrity. In the long-term research process, surface roughness, strain hardening and residual stress are considered to be the most important factors affecting the functional performance and life of components. However, failure and damage of parts are not only affected by these factors. It is found

that the microstructure of machined surface is also a crucial factor affecting the functional performance and life of components. A severe plastically deformed layer near the machined surface can be formed during HSM, in which the deformation of grains, the increase of dislocation and crystal defects have a remarkable impact on the physical and mechanical properties of parts.

As a typical parameter to represent the residual mechanical state of components, residual stress is generated from the complex thermo-mechanical loading history induced by machining operations, which includes mechanical loading and unloading, rapid temperature rise and cooling, and combined effect acting on the workpiece [1]. The influence of residual stress on functional performance and life of components depends on its nature and distribution. For example, compressive residual stress will increase the fatigue lifespan by delaying the crack initiation and propagation in the part [2]. However, the distribution of residual stress in the machined subsurface can also bring instability to the in-service behavior of parts [3].

To sum up, not only the surface roughness, strain hardening and the residual stress but also the microstructure of the machined surface and subsurface has an important influence on the functional performance and life of components (fatigue lifespan, corrosion resistance, etc.). Most of the research works found in the literature on the microstructure evolution in the machined parts and chips induced by machining operations are based on an experimental approach. Therefore, it is of great significance to develop a physics-based modelling approach able to accurately predict the microstructure evolution induced by machining, which is helpful for optimizing the process parameters for an improved functional performance and life of parts.

1.2 Research challenges

Based on the above introduction about the research background and significance, both experimental and modeling approaches are used in the present PhD dissertation to investigate the surface integrity in HSM, including the microstructure evolution. A major challenge towards future manufacturing science and technology is how to produce highly reliable components with enhanced functional performance and lifespan. Traditionally, the research work on manufacturing regarding the surface integrity aims to find the correlation between machining process parameters and final part's performance. Research works on materials response, including the internal loadings and metallurgical changes, are still insufficient to achieve a comprehensive understanding of the influence of manufacturing processes on part quality, and underlying physic-based mechanisms. As a consequence, the properties of machined surface obtained after HSM cannot be accurately predicted and then improved. Therefore, the main research challenges are described as follows:

(a) Numerical approach and constitutive modelling of the cutting process.

Lagrangian (LAG) approach and sacrificial layer to allows chip formation are often used in the numerical simulation of the metal cutting process, which results in mesh distortion, and consequently in the difficulty to accurate predict the surface integrity in the machined surface. Therefore, a numerical method that can solve the mesh distortion problem is very important for predicting the cutting process accurately. Moreover, the constitutive model for the description of the stress-strain relationship strong affects the accuracy of the cutting model predictions. In particular, the state of stress on the material effects the damage and fracture behaviors, but unfortunately most of the constitutive models used in metal cutting simulation are ignoring this important factor.

(b) Microstructure characterization and mechanisms in metal cutting.

As far as the microstructure evolution in HSM is concerned, many researchers have investigated the effect of the cutting process parameters on the grain deformation, grain refinement and phase transformation for different materials. However, the research work on the dynamic recrystallization, phase transformation behavior and constitutive model research is separated, which lacks of certain links. For the particular case of HSM, the effect of high strain rate on microstructure evolution is not clear, which needs to be further investigated due to the coupling relationship of multi-mechanism. The evolution of microstructure in cutting process is correlated with the macroscopic mechanical properties of materials, and the effect of microstructure evolution on the mechanical behavior of materials in cutting process under the mechanical-thermal coupling loading needs to be further revealed.

(c) Modeling of microstructure evolution in metal cutting.

Microstructure modeling and simulation based on the finite element method (FEM) and phenomenological laws including the Zener-Hollomon (ZH) and Johnson-Mehl-Avrami-Kolmogorov (JMAK) are widely used in cutting models, because they can provide good computation efficiency. However, they are unable to accurate describe the real physics of the microstructure generation in real manufacturing processes. Therefore, the development of a simulation approach combining multi scale models is of great significance to provide more physical fundamentals for modeling and better predict ability.

(d) Influence of microstructure evolution in metal cutting in the material mechanical behavior and surface integrity.

Machining can induce significant microstructural modifications in the machined surface and subsurface, characterized by phase changes, formation of grains of different sizes and shapes, etc. These microstructural modifications may also affect other surface integrity characteristics like microhardness and residual stresses,

thus the functional performance and lifespan of components. Moreover, the integration of the microstructure evolution mechanisms in the material constitutive models contributes for a better description of the mechanical behavior in metal cutting, thus for a better prediction of the surface integrity characteristics. So far, limited number of research works have considered the microstructure evolution in metal cutting and their impact on the mechanical behavior and surface integrity.

1.3 Objectives

This Ph.D dissertation aims to investigate the microstructure evolution and the surface integrity in HSM of Ti-6Al-4V titanium alloy, using multiscale modelling and experimental approaches. Moreover, based on the previous research challenges, the following objectives of this Ph.D work are formulated:

1) Conduct orthogonal cutting experiments and characterization of microstructure evolution in the chips and machined surfaces:
   (a) To design and conduct orthogonal cutting tests on Ti-6Al-4V titanium alloy using cemented carbide and PCD cutting tools;
   (b) To investigate the crystalline structure and the mechanisms of microstructure formation in the machined surface and chips using a novel characterization technique, precession electron diffraction (PED). This technique is applied for a quantitative characterization of the nano-scaled microstructures of the machined surfaces, including: phase distribution, grain size, grain boundary, grain orientation and geometrical necessary dislocation (GND) density distribution.
2) Modelling and simulation of HSM using CEL approach and a constitutive model considering the state of stress:
   (a) To use the Coupled Eulerian and Lagrangian (CEL) approach to overcome the problem of severe mesh distortion found in metal cutting simulations using pure Lagrangian approach;
   (b) To propose a constitutive model considering the state of stress and evaluate the accuracy of this model to describe the mechanical behavior of the Ti-6Al-4V alloy in HSM;
   (c) To develop a 3D orthogonal cutting model based on the CEL approach and the proposed constitutive model. Apply this cutting model to investigate the surface integrity in HSM of Ti-6Al-4V alloy.
3) Multiscale modelling and simulation of grain refinement induced by dynamic recrystallization (DRX)
   (a) To develop a microstructure evolution model based on continuous DRX (cDRX) and discontinuous DRX (dDRX) mechanisms;

(b) To develop a multiscale model using coupled FEM and cellular automata (CA) methods, which is used to predict the microstructure evolution in the deformation zone in HSM;

(c) To analysis of the effect of grain refinement induced by DRX on the strain softening phenomenon.

4) Assessment of other surface integrity characteristics using both experimental and modelling approaches

(a) To predict the surface topography by numerical simulation and to compare it with the experimental measurements;

(b) To predict the residual stresses and plastic strain induced by the cyclic thermomechanical loading applied on the workpiece, which are caused by the cyclic nature of chip formation. To propose an efficient FE-based approach to predict the residual stress in the machined surface and subsurface;

(c) To model the microhardness distribution in the machined surface and subsurface by considering the influence of dislocation density and grain size.

1.4 Structure of the dissertation

The structure of this Ph.D dissertation is organized in seven chapters, described as follows:

Chapter 1 provides an introduction to the research background and significance in the field of metal cutting and surface integrity. Then, the research challenges are presented and the research objectives are formulated. Finally, the structure of the Ph.D dissertation is described.

Chapter 2 reviews the state-of-the-art about the metal cutting process, surface integrity and microstructure evolution in metal cutting divided in six sections: fundamentals of metal cutting mechanics, cutting modeling and simulation, microstructure evolution in metal cutting, microstructure based property transformation in cutting process, constitutive model for metal cutting, and surface integrity.

Chapter 3 describes the proposed model of HSM based on CEL approach and the constitutive model considering the effect of the state of stress in the material plasticity and damage. When compared with a model using Lagrangian approach and the Johnson-Cook (JC) constitutive model, the accuracy of the proposed cutting model to predict the metal cutting outcomes (including the surface integrity) is evaluated. Then, the influence of state of stress on the chip formation is analyzed. Besides that, the phenomenon of material side flow and lateral burr formation is simulated.

Chapter 4 describes the proposed multiscale model combining the FEM and CA methods considering the grain refinement caused by dynamic recrystallization (DRX). A grain size prediction subroutine is developed and integrated into the FE model based on the dynamic recrystallization theory model. Then, the deformation conditions (strain, strain rate and temperature) obtained by FE simulation are transferred into the CA model

to predict the microstructure evolution during the cutting process, which considers both cDRX and dDRX mechanisms. The accuracy of this multiscale model is confirmed through material characterization experiments. The effect of the cutting speed on DRX behavior is investigated.

Chapter 5 describes the mechanisms of microstructure formation in machined subsurface using the multiscale model developed in chapter 4 and experimental characterization techniques. Two layers with different grain structure are found: (1) a layer of "Nano grains" with continuous dynamic recrystallization (cDRX) grains characteristics, and (2) a layer of "Micro grains" with discontinuous dynamic recrystallization (dDRX) grains characteristics. By combining the effect of dislocation density evolution, mechanical twinning, and the precipitation of second phase particle, the grain refinement mechanism in machined surface under the high strain rate condition is revealed.

Chapter 6 presents an improved version of the cutting model described in chapter 3, in order to investigate other surface integrity characteristics. This model is used to investigate the influence of chip geometry on the periodic fluctuation of cutting force and surface morphology. Considering the effects of dislocation density, grain size, twinning and phase transformation on the microhardness of materials, a model for predicting the microhardness in the machined subsurface is proposed and integrated in the improved cutting model. Considering the residual stresses formation due to the workpiece loading, unloading and cooling, CEL approach is adopted to simulate the cutting process (loading), while Lagrangian approach is used to simulate the residual stress formation (unloading and cooling). Data transfer and mesh rebuilding techniques are utilized to extract the data from the cutting model using the CEL approach and to apply this data in the residual stress calculation model using Lagrangian approach. Using this numerical simulation approach, the effects of cutting parameters and tool geometry on the temperature, forces, equivalent plastic strain and residual stress are studied.

Chapter 7 presents the main conclusions and recommendations for future work.

Fig. 1 shows a flowchart of the main research work presented in each chapter and their relationship.

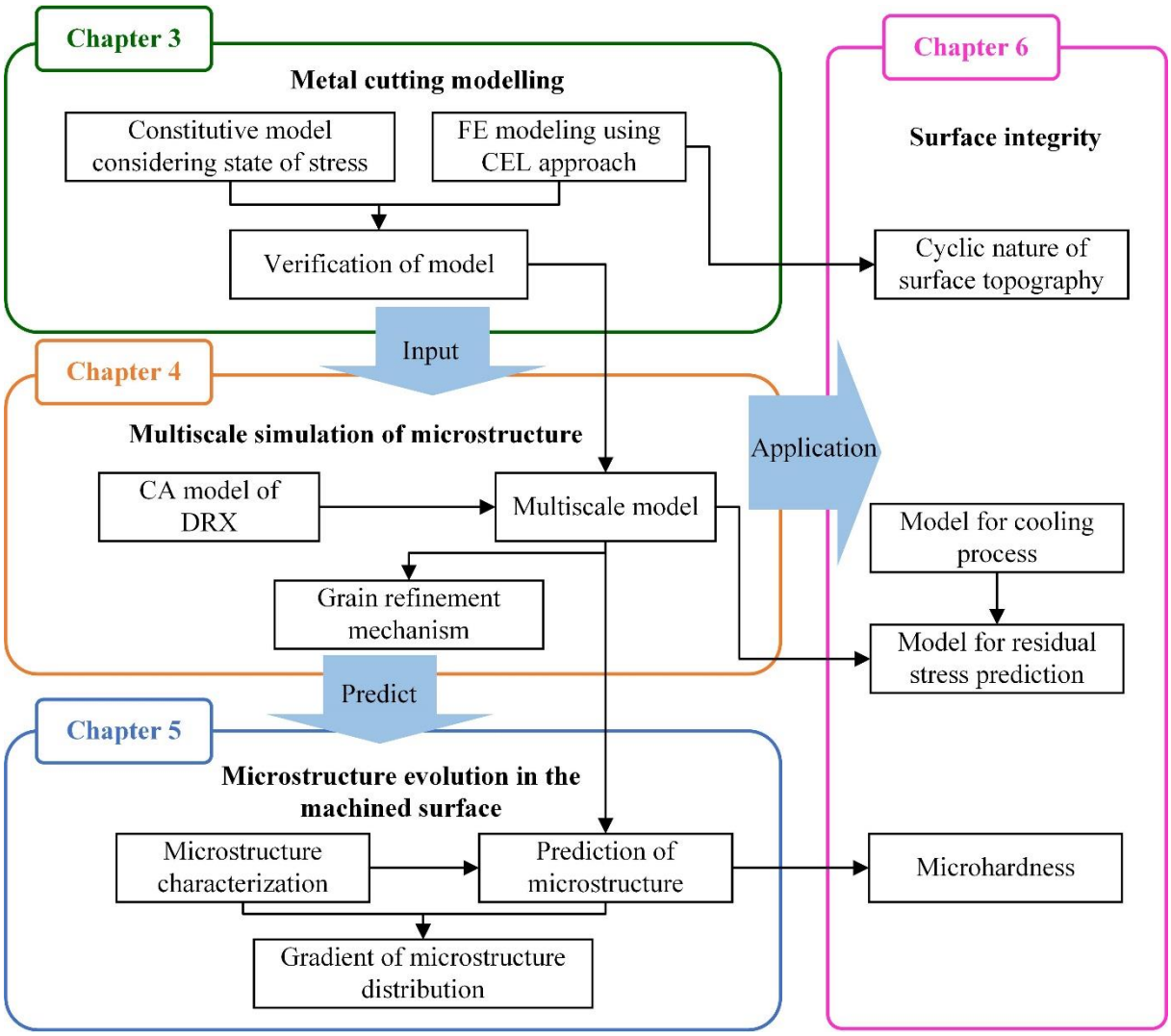

Fig. 1 Flowchart of the contents of each chapter and their relationship.

2 State of the art

2.1 Fundamentals of metal cutting mechanics

Metal cutting is one of the most widely used processes to shape the functional components with specifically designed geometries, dimensions, and surface conditions by removing an unwanted material layer resulting into chip formation. Common cutting processes include turning, milling, drilling, boring, shaping, broaching, reaming and others. The basic two-dimensional orthogonal cutting process is first analyzed in details followed by considering representative three-dimensional cutting operations. Special attention is directed towards cutting forces, cutting temperatures, tool wear, and the surface integrity of machined components. Machining optimization can be conducted in terms of high efficiency, high quality and low consumption. Cutting processes are unusually considered as complex thermo-plastic deformation processes due to the boundary conditions limiting the material making two basic operations occur simultaneously with strong interaction:

- Three/four deformation zones with large plastic strain under different types of deformation mode (e.g. shear, friction, tension, compression, and mixed mode)
- Material flow along the contact interface with a heavily local deformation between chip/workpiece and tool.

In general, several simplified models that emphasize different aspects of the problem such as thermal, material, and surface condition are produced simultaneously, and their importance depends on the specific machining parameters. Because of the complexity of the problem, a general prediction theory is impossible. Instead of seeking the impossible, a more practical approach is adopted to explain the fundamental terms by conducting a wide variety of experiences.

1) Three deformation zones

The geometrical complexity of the actual machining operations brings difficulties to lead a comprehensive understanding of the material removal mechanics. By definition, a simplified model, called orthogonal cutting, is proposed using a wedge-shaped tool whose cutting edge is perpendicular to the cutting direction. After shear plastic deformation, the material flow occurs in the plane of tool rake face. And then the friction behavior in the interface between chip and tool results in the further plastic deformation in the local zone of the chip, which produces a resulting ploughing force perpendicular to the workpiece surface. The ploughing effect from cutting tool would introduce a thermo-mechanical gradient of loading in the workpiece surface.

Due to the above different deformation resources to characterize the mechanical behavior towards the chip flow and surface generation, deformation zone can be divided into three parts as shown in Fig. 2:

Zone I: Primary shear zone (PSZ), severe shear deformation takes place in this region to form the chips, which always extends from tool cutting edge to the workpiece top free surface. The plastic deformation is the main mechanism of cutting consuming energy accounting for 60~80%, which performs as the variation of cutting force and temperature. According to the heat produced from severe plastic deformation, the temperature in this region can rise up rapidly, which would induce the material softening and influence the mechanical response.

Zone II: Secondary deformation zone (SDZ), local shear deformation is introduced due to the friction between the tool and chip bottom surface. Large amount of heat is generated in this region, which shows great influence on the tool wear, built-up edge formation, and the tangential cutting force to form the machined surface.

Zone III: Third deformation zone (TDZ), after the chip is separated from the workpiece with a specific material fracture, the stretching effect and friction behavior leads to the plastic deformation in the surface and subsurface. The thermo-mechanical loadings in-depth show a gradient distribution until the bulk materials' state is reached, which shows a significant influence on the surface integrity of components (e.g. microstructural characteristics, microhardness and residual stresses).

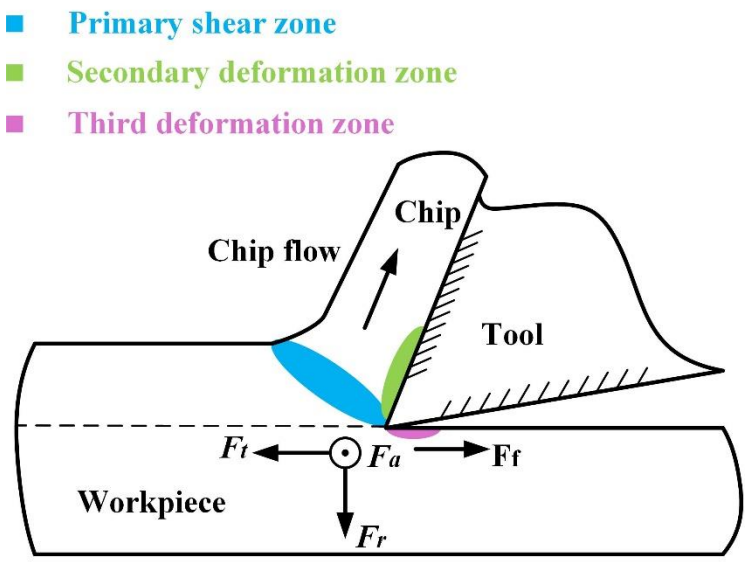

Fig. 2 Schematic of three deformation zones in metal cutting process.

2) Chip formation mechanism

The chip formation process is the mechanical response of work material under the influence of tool geometry, cutting parameters, and material properties. In general, the chip is continuous as shown in Fig. 3 (a) with a steady state as the shear deformation occurs, which is characterized with a chip compression ratio (CCR). When the cutting speed increases or the conductivity of the work material (especially difficult-to-cut material) is too low, the generated heat cannot be spread out of the shear zone, which induces the adiabatic shear behavior in a localized region. It is identified as an unsteady cutting process, which produces serrated chips as in Fig. 3 (b). While cutting brittle materials with a relative low cutting speed, the crack initiation and propagation induce the formation of discontinuous chips as in Fig. 3 (c) due to the poor ductility. So the chip formation under different cutting conditions and materials occurs due to one of these three types of mechanisms, which are called "shear slip theory", "adiabatic shear theory", and "cyclic crack propagation theory", respectively.

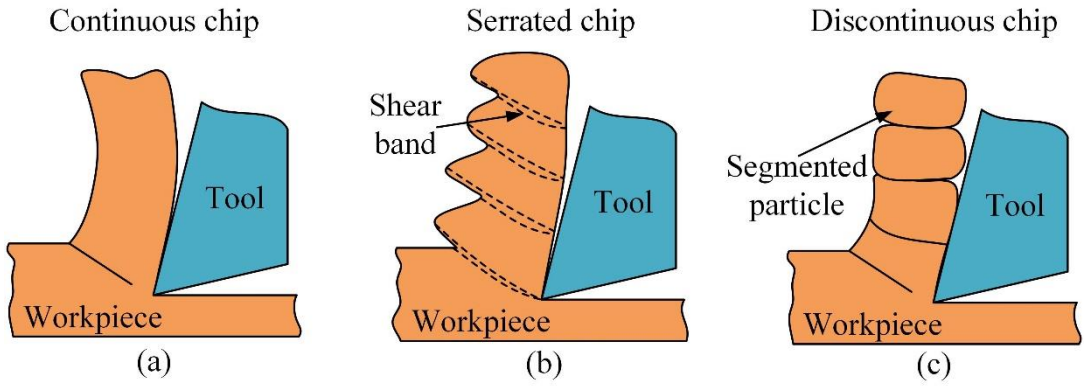

Fig. 3 Schematic of three different types of chip formation: (a) continuous, (b) serrated, and (c) discontinuous.

3) Cutting forces and heat generation

For orthogonal cutting process, the cutting speed, uncut chip thickness, width of cut, tool rake angle, and friction coefficient between the tool and the workpiece material, are the key factors to determine the cutting forces, while in conventional machining operations, e.g. milling, drilling, and turning, other related parameters, such as helix angle, depth of cut, and feed should affect the force direction and amplitude. The cutting forces reflect not only the mechanical stresses during the cutting process, but the global stress during the surface generation. Alongside the elasto-plastic energy generated by the mechanical stresses, heat generated from the thermal stresses will introduce the material softening behavior, which can cause tool life reduction and local volume expansion of the materials.

2.2 Metal cutting modelling and simulation

To model the machining process, state variables such as tool wear [4], forces [5], and surface integrity [6], including microstructure evolution [7] in metal cutting, characterization of thermomechanical conditions during the cutting process are of great significance to improve the component performance and the manufacturing efficiency. Considering the high cost and time consumption of experimental tests and the difficulties of obtaining some machining process data (e.g. strain, cutting temperature and residual stresses), the application of the numerical simulation to predict the performance of the machining process has outstanding advantages. The most generalized method in modelling of metal cutting process is FEM, where a detailed distribution of strains, strain rates and temperatures can be obtained simultaneously. However, there are also some weaknesses of FEM such as mesh distortions, difficulty to model cracks initiation and propagation, etc. As an alternative, mesh-free methods show high potential to be used for this purpose. The dominant approaches of numerical modelling in this case are summarized as following:

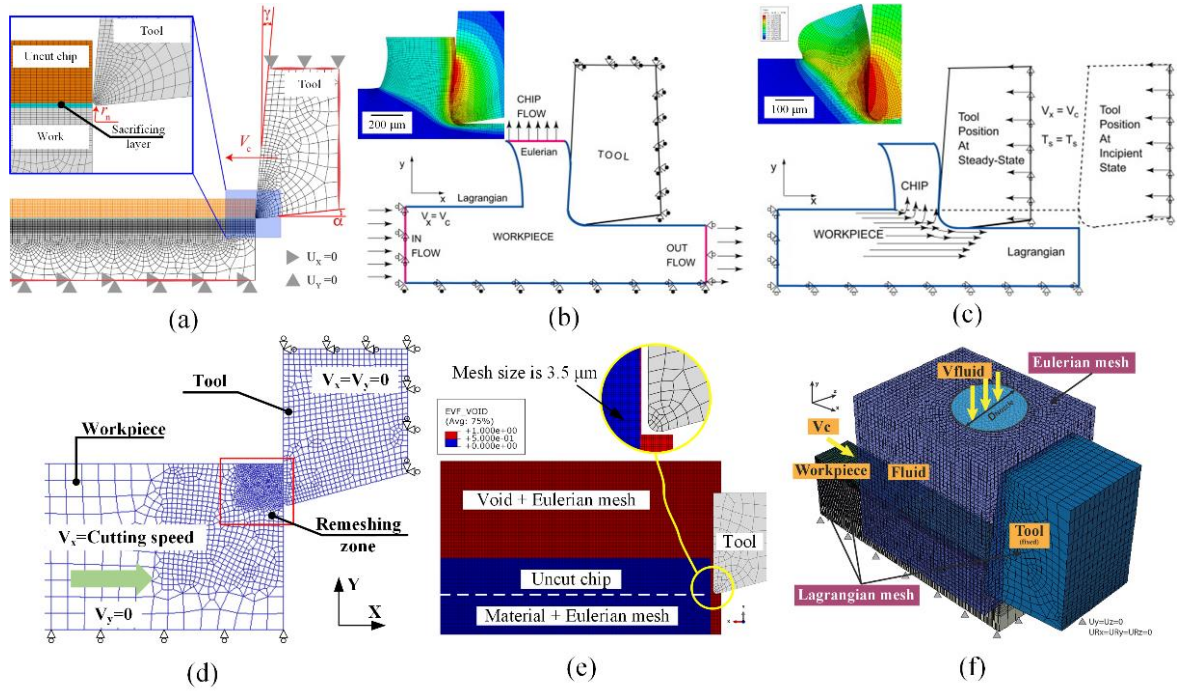

Fig. 4 Boundary conditions of cutting simulations through conventional FEM models: (a) LAG model with sacrificing layer [8]. *(b) and (c) are applications of ALE approach* [9]*: (b) Modelling with Eulerian and Lagrangian boundaries; (c) Modelling with pure Lagrangian boundaries. (d) Remeshing* [10]. *(e) and (f) are CEL model configurations: (e) Modelling work material as Eulerian body, only available for dry cutting condition* [11]*; (f) Modelling work material as Lagrangian body and coolants as Eulerian body, eligible for wet cutting condition* [12].

1) FEM method

As far as the simulation methods applied to machining processes are concerned, the traditional Lagrangian approach is widely adopted, in which the presetting of sacrificial layer and control of element distortion and deletion shown in Fig. 4 (a) are required. The critical issue of this approach is the element distortion due to the severe plastic deformation induced by cutting. To overcome this issue, in order to solve the problem of element distortion associated to the Lagrangian approach, three methods/hybrid approaches are developed: Lagrangian with remeshing [13], Arbitrary Lagrangian-Eulerian (ALE) [14,15], and Coupled Eulerian-Lagrangian (CEL) [16,17]. The main problem of remeshing approach is the accumulation of calculation errors caused by node migration [18]. Taking the advantages of both Lagrangian and Eulerian approaches, ALE describes the chip formation like a material flow around the tool cutting edge, which does not require a sacrificial layer neither a fracture criterion. The detailed description of this method is shown in Fig. 4 (b) and (c). However, the computational costs of this technique are higher due to the higher sweeping frequency required for maintaining a better mesh shape, which significantly increases the time consumption. ALE approach is suitable for simulating continuous chip formation [14,19], but it is unable to simulate serrated chips, like those observed in machining of difficult-to-cut materials. Concerning the remeshing method shown in Fig. 4 (d), an updated Lagrangian-based method with remeshing technique was proposed for the simulation of metal cutting processes. It can automatically change the mesh sizes and shapes within deformation area to achieve chip formation and separation, and excessive distortion can be fully avoided, which is suitable for both 2D [20,21] and 3D cases [22,23]. The results showed that local remeshing technique could provide results that are more accurate and avoid wrong predictions in deformation zones. Regarding the CEL approach, it can avoid the mesh distortion, and the stable time increment is not reduced when compared to the ALE one. This method shown in Fig. 4 (e) separates the spatial coordinates of the meshes by material points, and the material can flow through the mesh. Ducobu et al. [17] proposed a cutting model of Ti-6Al-4V using the CEL approach, which considers the workpiece as an Eulerian region and the tool as a Lagrangian one. They analyzed the effect of element size and shape on the simulation results. However, they could only simulate continuous chips, partially due to the low cutting speed (30 m/min) used in their machining simulations [24,25]. Later, Shuang et al. [26] successfully simulated serrated chips under extremely high cutting speed of 1200 m/min. Unfortunately, the simulated chip was continuous for a cutting speed of 60 m/min, while in reality the chip must be serrated. Moreover, it is worth noting that the plastic strain in the shear band of chip is extremely high when compared to strain at fracture. If work material is

modelled as a Lagrangian body, CEL model provides another possibility of fluid-structure interaction (FSI), which can be used to describe cutting processes with supply of coolants, as shown in Fig. 4 (f). This approach was developed by Ayed et al. [45] towards high pressure waterjet assisted machining, where a script was used to realize heat transfer between solid phase and liquid phase. It is beneficial towards future application in predicting microstructure evolution in wet cutting processes, which is more practical for industries.

Although modeling and simulation using two-dimensional (2D) Finite Element Method (FEM) have significantly improved and helped to understand the fundamental mechanisms of the cutting process during the past decades [27], it is based on the assumption of the plane strain conditions. Therefore, it cannot be used to describe the cutting process mechanics in real 3D machining operations, such as turning, drilling, and milling. As a result, three-dimensional (3D) cutting models of those machining operations have been developed to predict forces, temperatures, tool wear, and surface integrity [28–31]. Attanasio et al. [32] developed a 3D model to simulate tool wear in drilling of Inconel by updating the geometry of the worn tool using a new algorithm considering the tool wear rate. Niu et al. [33] established a 3D model of the milling of Ti-6Al-4V titanium alloy to predict the cutting force, cutting temperature, and residual stresses. Liu et al. [34] developed a 3D model of turning using a new designed micro-textured cutting tool to investigate its cutting performance. Outeiro et al. [35] developed a 3D model of turning of Inconel 718 and AISI 316L stainless steel to investigate the thermomechanical phenomena in machining these two difficult-to-cut materials, and correlate these phenomena with the residual stresses in the machined surfaces. It is worth noting that none of these 3D models was able to simulate serrated chips, and thus they could not reproduce the cyclic variation of the plastic strain and topography of the machined surface observed experimentally [36]. Therefore, there is a need to develop a model of cutting to accurately reproduce the cyclic nature of the chip formation process, and its influence on the thermomechanical phenomena and surface integrity.

2) Mesh-free methods

In order to characterize the material removal behavior due to the transformation from continuity to discontinuity during fracture, mesh-free method is considered as an effective method to model the workpiece by avoiding the spatial discontinuity [37]. Through mesh-free methods, fracture is modelled in a more natural way without additional treatments of elements like remeshing or element deletion. In this case, crack initiation and propagation are modelled more precisely [38,39]. Mesh-free methods also show a good ability in considerations from micro-scale perspectives. Discrete element method (DEM), smoothed particle hydrodynamics (SPH) and molecular dynamics (MD) are the most popular mesh-free methods applied in

cutting.

DEM approaches are mainly divided into two categories depending on the interactions between discrete elements, which are contacted type and connected type, respectively. Contacted type DEM is very flexible for definitions of initial conditions of discrete elements [40]. In this case, each element has a contact rule only with its contacted elements. Connected type DEM was primarily proposed by Hrennikoff [41] and was referred as Lattice model (LM) in the beginning. For this approach, elements are connected with each other by springs along the normal direction, and the connecting parameters are derived through equivalence of material strain energy and spring potential energy within unit volume [42,43]. Concerning initial application of connected type DEM in metal cutting processes, materials were assumed as homogeneous without consideration of microstructure effects. Jiang et al. [44] developed a DEM cutting model towards homogeneous material polycarbonate as a preliminary study, where the initiation and propagation of stress wave induced by the high-speed impact from cutting tool were analyzed. Following, Liu et al. [45] developed a continuum-based DEM approach towards better application in cutting, which shows better performance in terms of the transition from continuum to dis-continuum.

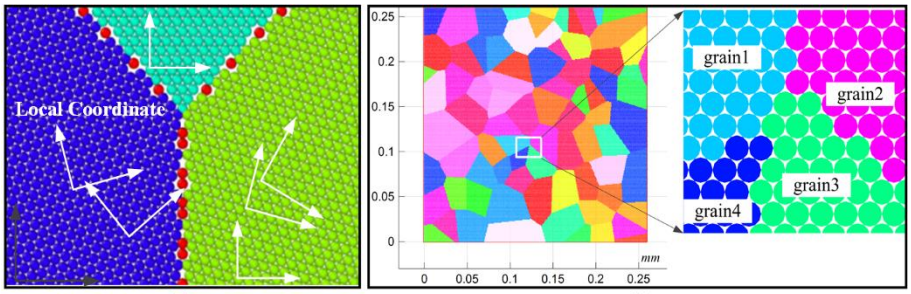

Fig. 5 Characterization of microstructure effects in DEM approach: (a) The method of rotating local coordinate [46]. *(b) The approach of changing interaction coefficients* [47].

DEM approach also provides the possibility to describe heterogeneity of materials induced by microstructures. Voronoi tessellation is always applied in order to obtain materials with randomly distributed grains and phases. Horie and Case [46] and Chen [46] maintained same interaction coefficients during modelling, and expressed different grain orientations through rotating local coordinates in a local reference system with respect to global coordinates in the global reference system, so that the normal direction of element can be the same as grain orientation, as shown in Fig. 5 (a). Another method was proposed by He et

al. [47]. In their cases, the local coordinate of element pair is fixed with global coordinate, and the directions of interaction rules and pertinent coefficients of elements within each individual Voronoi tessellation (partition into regions close to each of the given set of elements) are changed, as shown in Fig. 5 (b). The former method can be used to express any directions as desired, while initial stresses are easily formed at grain boundary due to elements piling. The latter method is more convenient, although limited orientations can be characterized.

Furthermore, a DEM model representing cutting spheroidal graphite cast iron was developed by He et al. [38] through particle flow codes in two dimensions (PFC2D) , as shown in Fig. 6. The discrepancies of mechanical properties provided by graphite phase and ferrite phase were considered, and their influences on cutting performances were investigated. In their model, graphite phase was randomly distributed inside ferrite grains with sphere shape, and grain boundaries were formed due to different grain orientations. They performed cutting simulations at different speeds through this model, which shows the deformation of microstructures with respect to variation of cutting speeds, and a good agreement was obtained between simulation and experimental results in terms of chip formation. However, the drawback still lies in the constitutive modelling of plasticity. In this case, they applied a simplified bilinear behavior instead of nonlinear plasticity models fairly accurate for cutting processes.

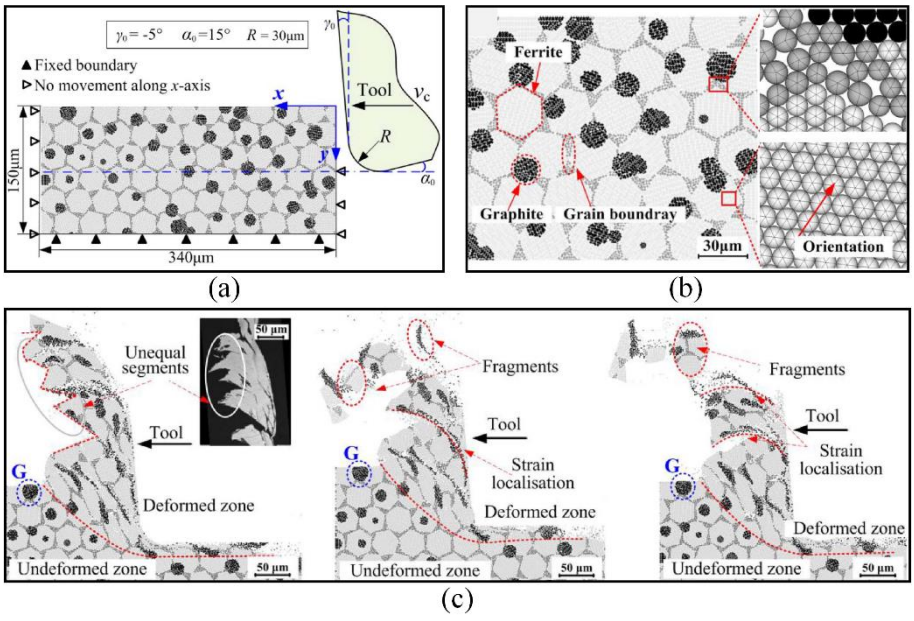

Fig. 6 DEM simulation of cutting spheroidal graphite cast iron with consideration of heterogeneity induced by microstructure features [38]: (a) Boundary conditions. (b) Arrangement of particles within grain boundaries and inside ferrite grains. (c) Simulated chip morphologies at 2259 m/min, 3000 m/min and 3780 m/min, respectively.

SPH is a method suitable for solving large deformation problems and material discontinuity, which is firstly developed to simulate the mechanical responses in solid mechanics [49]. By introducing deviatoric stresses, SPH method is then extended for simulation of metal cutting process due to its simplicity, robustness, and ease to apply physics [50]. The algorithm proposed by Heisel et al. [51] towards optimization of SPH coefficients also provides more opportunities while applied in cutting simulation. However, concerning the effect of microstructure and evolution, rare publications were reported using SPH. An attempt was proposed by Zahedi et al. [52] to introduce consideration of microstructures into SPH simulation, where they implemented the theory of crystal plasticity and developed an FE/SPH model through subroutine VUMAT in commercial software Abaqus/Explicit. It reveals the mechanisms of material removal at micro-scale, and illustrates the influences of crystal orientation on cutting performance of face-centered cubic metals. Takabi et al. [53] enhanced the theory of SPH approach through introducing a damage criteria into numerical model. And they compared the performances of cutting simulation with respect to undamageable SPH, damageable SPH and damageable FEM, as shown in Fig. 7. The results show that the fluctuation of cutting forces can be decreased with the help of SPH model, which is beneficial towards simulation of brittle materials. However, the forces and stresses obtained from SPH model are lower than those from FEM model, and chip curving cannot be well characterized as FEM model.

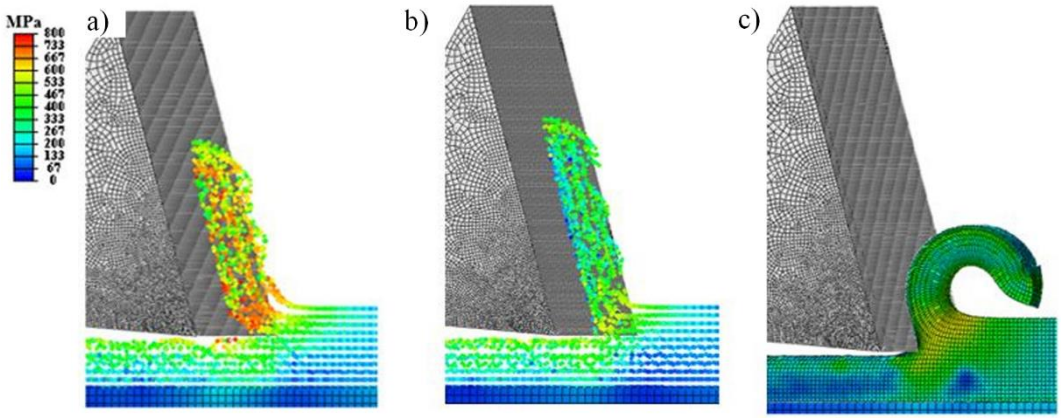

Fig. 7 Effects of simulation methods on chip formation in orthogonal cutting aluminum, a) undamageable SPH, b) damageable SPH and c) damageable FEM [53].

To summarize, both DEM and SPH approaches provide a good capability of describing fracture behaviors in cutting, especially in terms of problems regarding to crack initiation and propagation when compared to

continuum-based methods like FEM. They are suitable for simulating cutting processes at both micro- and meso-scales. For DEM, it shows a good performance in accounting for microstructure effects, however, the nonlinear plastic behaviors are difficult to be accurately modeled. For SPH, it has a better compatibility with plastic behaviors, while less with microstructure features, and convergence is a major issue as well. As a result, compared to FEM models, they are less practical in terms of modelling microstructure effects and evolution in cutting processes.

3) Molecular dynamics (MD)

Molecular dynamics (MD) is a method for analyzing multi-particle behaviors at the atomic scale or at the nanoscale. This method is a physical based approach aiming to characterize the interactions between atoms. Considering that microstructure is fundamentally determined by the atomic arrangements, this method can analyze the effects and the evolution of microstructures. However, due to the limitations of time and space scalars, it was initially introduced to investigate the cutting process at a nanoscale.

Executions of a MD simulation are mainly dependent on the potential function. In terms of the cutting simulation, the Morse potential and the embedded atom method (EAM) potential are the most commonly used potentials, but some other ones like the Tresoff potential and the analytical bond order potential (ABOP) have also been reported. Pei et al. [54] compared the Morse potential and EAM potential in chip morphology and a machined surface through a nano-cutting process for copper. They pointed out that the EAM had a better performance in terms of describing the behaviors of metals. With the EAM potential, Sharma et al. [55] proposed a nano-cutting simulation subjected to single crystal copper with different orientations, as shown in Fig. 8. The results showed that the evolution of the dislocation density was strongly dependent on the crystal orientations, which could also induce discrepancies in terms of the cutting forces, specific cutting energy, and surface quality. Due to the limitations of the space scalars, MD simulation is always applied to nano-cutting within a single grain, which shows the strong dependency of the cutting performances on orientations, as illustrated in Fig. 8. However, the interactions of multi-grains or behaviors at grain boundaries cannot be addressed, which minimizes the feasibility of MD simulation for conventional cutting processes. Multi-scale approaches may be a good solution to utilize the advantages of MD simulations in terms of revealing the in-depth mechanisms in the local area involved in cutting.

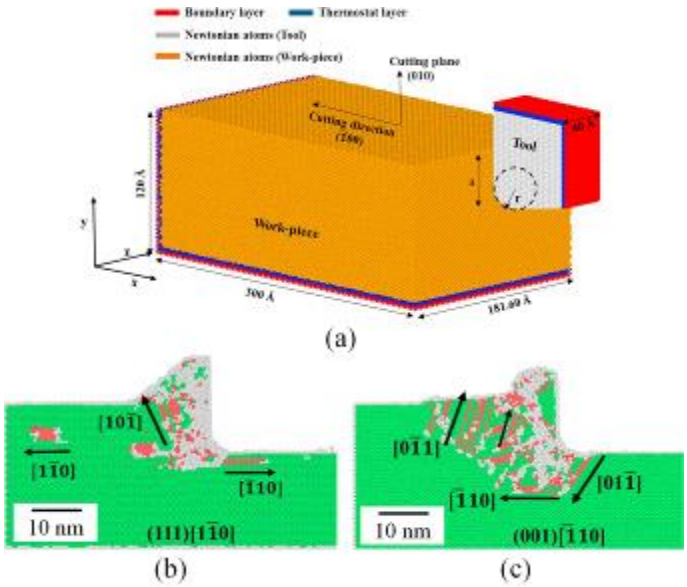

Fig. 8 MD simulation of nano-cutting single crystal copper [55]: (a) Boundary conditions. (b) and (c) are chip formations at different orientations with the same ratio of uncut chip thickness to edge radius.

2.3 Microstructure effects and its evolution in metal cutting

Predicting microstructure evolution in machining process is of great significance to improve production efficiency and obtain components with high performance. A review by Pan et al. [56] indicated that the material microstructure evolution induced by machining results from the thermal and mechanical loading processes, and the altered microstructure have an inverse influence on materials flow stress behavior, machining forces and surface integrity. The development of microstructure modeling is gaining rising interest, and Arrazola et al. [27] indicated that a constitutive model including the microstructure effects would more accurately reflect the mechanical behavior of workpiece during machining. The review presented by Melkote et al. [57] shows that several models for predicting the microstructure evolution in metal cutting using FE simulations have been proposed. It is worth to notice that the limitation and accuracy of microstructure models in FE simulations are based on the phenomenological description and many microstructure parameters cannot be represented. Huang and Logé [58] reviewed the dynamic recrystallization in metals. They showed that microstructure evolution under severe plastic deformation can include dislocation density, grain deformation, grain nucleation and growth. The final microstructure morphology is strongly dependent on deformation condition. The mechanical properties are influenced by both grain size and grain morphology. Therefore, simulation methods that can improve the accuracy in predicting microstructure evolution and consider the influence on mechanical behavior in metal cutting are required.

As reported by Fanfoni and Tomellini [59], two major types of DRX were dominant mechanisms appearing during metal deformation, which are discontinuous dynamic recrystallization (dDRX) and continuous dynamic recrystallization (cDRX), respectively. DRX is a key factor resulting in grain size evolution during metal cutting processes. In terms of predicting grain sizes induced by DRX in cutting process, Zener-Hollomon (ZH) and Johnson–Mehl–Avrami–Kolmogorov (JMAK) models are mostly used with phenomenological laws as shown in Fig. 9.

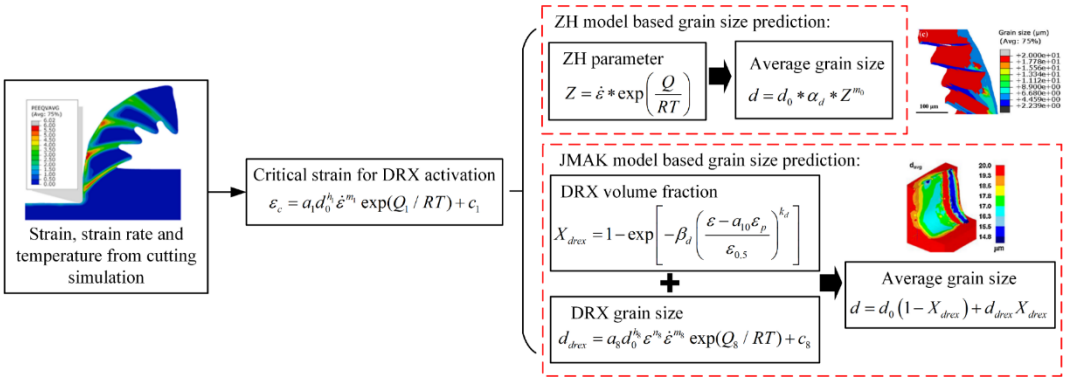

Fig. 9 Prediction of grain size evolution in metal cutting processes through ZH and JMAK models.

[c] **Nomenclature**: a_1, h_1, m_1, c_1, α_d, m_0 , a_8, h_8, n_8, m_8, and c_8 - material constants; Q_1 - modified activation energy at current time step; Z - Zener-Hollomon parameter; ε_c, $\varepsilon_{0.5}$, ε_p - critical strain, half-fraction strain and peak strain for DRX of JMAK model; X_{drex}, d_{drex} - DRX volume fraction and grain size; β_d, k_d - material constants related to DRX.

Both models require a critical strain to determine the occurrence of DRX. For ZH model [60], a ZH parameter should be determined firstly according to the strain, strain rate and temperature, then a simplified term is used to estimate grain sizes. Based on this approach, Caruso et al. [61] simulated the grain size alteration in chips and machined surface during hard turning AISI 52100. By extending their previous work, the white layer and dark layer appearing as surface modifications are predicted and compared with the experimental data through microstructure characterization, which shows a good agreement [62]. Further modifications of this model were then achieved by combining ZH and Hall-Petch equations, which is verified as a reliable approach to predict refined grain sizes during machining processes by Wang et al. [63] and Umbrello et al. [30]. Pertinent results are as shown in Fig. 10.

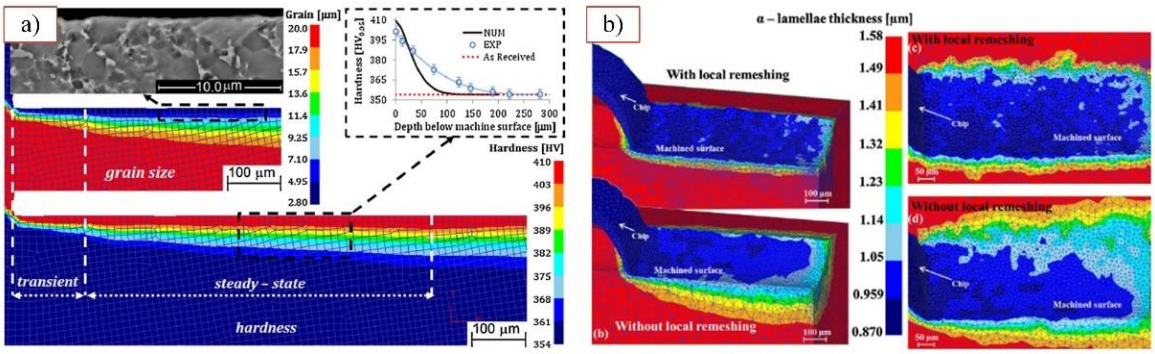

Fig. 10 Predicted grain size distribution in machined surface for a) 2D case [64] and b) 3D case [30].

Based on the framework of deformation–microstructure correlation shown in Fig. 11 proposed by Guo et al. [65], several different models of grain size prediction have been developed. After Estrin and Kim [66] proposed the dislocation density based microstructure evolution model, Ding et al. [67] conducted FE simulations by integrating microstructure-based subroutines to investigate the grain size evolution of Al 6061 T6 alloy and OFHC Copper in cutting process. They showed that low strain, high strain rate or high cutting temperature could result in a coarse and elongated grain structure. Liu et al. [68] proposed a unified dislocation density-based model by considering dislocation drag effect at high strain rate. This model was calibrated in order to obtain a good agreement with experimental measured results from low to high cutting speeds. Physical-based microstructure models are preferred as they can reveal the materials nature of deformation and mechanical properties. However, the values of the microstructure parameters of these models are difficult to be identified experimentally. Depending on the research of mechanism of dynamic recrystallization (DRX) in metal deformation process [59], two types of DRX can occur in metals: discontinuous dynamic recrystallization (dDRX) and continuous dynamic recrystallization (cDRX). Zener-Hollomon [60] and Johnson–Mehl–Avrami–Kolmogorov (JMAK) models [59] are mostly used to predict grain size evolution. Rotella et al. [22] utilized the Hall–Petch [69,70] and Zener–Hollomon models [60] developed a subroutine to predict the grain size and surface hardness in turning of AA7075 alloy. Wang et al. [71] conducted the simulation of grain size and microhardness in chips and machined surfaces by combining Hall-Petch and Zener-Hollomon equations in machining Ti-6Al-4V. JMAK model and its application were reviewed by Fanfoni and Tomellini [59] to successfully describe the DRX kinetics. Arisoy and Özel [72] used the JMAK model by conducting 3D FE simulation in turning of Ti-6Al-4V alloy to predict DRX and grain size. The results showed an alteration of microstructure and grain size in machined subsurface due to DRX.

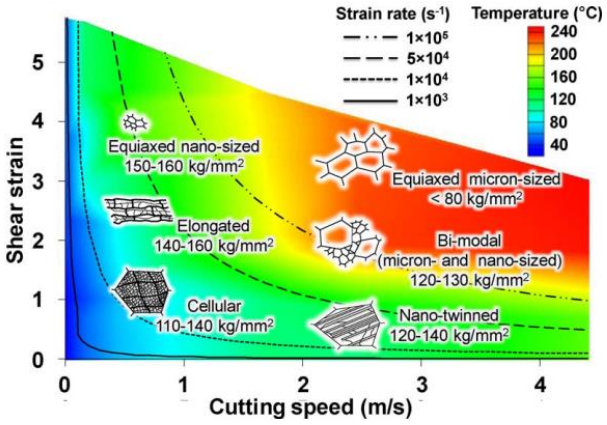

Fig. 11 Deformation–microstructure map for copper derived from machining experiments [73].

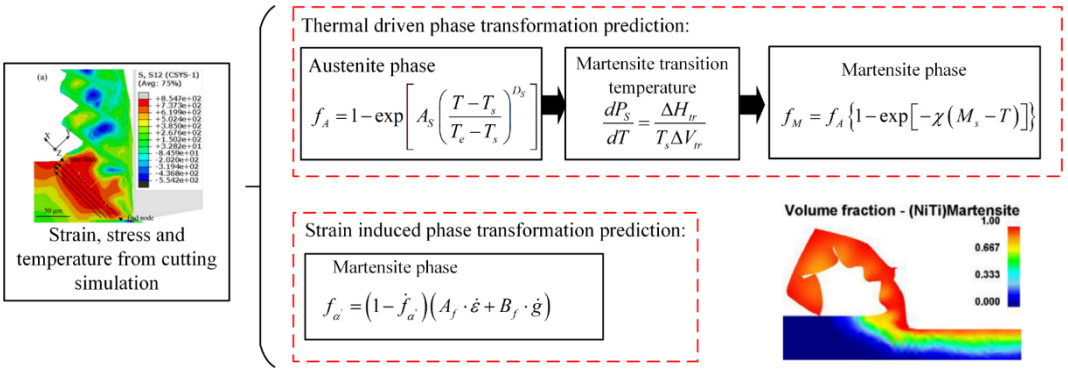

Fig. 12 Prediction of phase fractions in metal cutting processes through thermal-driven and strain induced models.

[d] **Nomenclature**: f_A, f_M - volume fraction of austenite phase and austenite-martensite phase transformation in heating process; T_s, T_e - starting and ending temperatures for phase transformation; A_s, D_s, χ- material constants; P_S - the equivalent stress; ΔH_{tr} - heat change involved in phase transformation; ΔV_{tr} - the volume change per mole due to phase transformation; T_P - the phase transformation temperature; M_s – the martensite transformation temperature; $\dot{f}_{\alpha'}$ - the increasing rate of martensite volume fraction; $\dot{g}$ - the rate of martensitic transformation driving force.

During machining processes, high temperature, rapid temperature rises and quenching usually occur. Therefore, phase transformation is easily activated under these conditions. Due to the material properties and crystal structures, different phase transformation mechanisms may also be involved [74]. The metallographic characteristics of chips and machined surfaces have shown significant phase transition features in both shear

bands and tool-chip interface of serrated chips, and the formation of white layer in machined surface is also considered to be tightly related to a phase transition [57]. For the prediction of phase fractions, the thermal-driven phase transformation and strain induced transformation models are applied in metal cutting processes as shown in Fig. 12.

A thermal-driven phase change dynamics is always used to describe the evolutions of phase volume, phase plasticity and volume expansion. Based on this formula, the thickness of the white layer in machined surface is firstly predicted by Han et al. [75]. In this case, the volume fraction of austenite phase is dependent on the time-temperature transformation behavior and Avrami model. By using the above theoretical models in a cutting simulation, Ramesh et al. [76] investigated the thermal changes induced phase transformation and white layer formation shown in Fig. 13 (a). In this developed model, two critical judgements were used: 1) the temperature of material points should exceed the Austenite transition temperature, which are remarked as "transformed" point, 2) the temperature of these points fall below the martensite transition temperature. In this developed model, the effects of stress on the martensite transition temperature were considered and the phase transformation fraction was calculated using an incremental method to improve its precision. Then, the volume fraction of austenite-martensite phase transformation in cooling process is determined. This model was further applied by multiple research works in different cutting cases, which showed a good capability to predict the depths of white layer and dark layer in machined surfaces [77–80]. As most constitutive models ignore the effect of phase transformation on material dynamic response, Zhang et al. [81] developed a new constitutive model combining the mechanical responses of alpha and beta phases based on a self-consistent method (SCM) during cutting Ti-6Al-4V alloy, as shown in Fig. 13 (b).

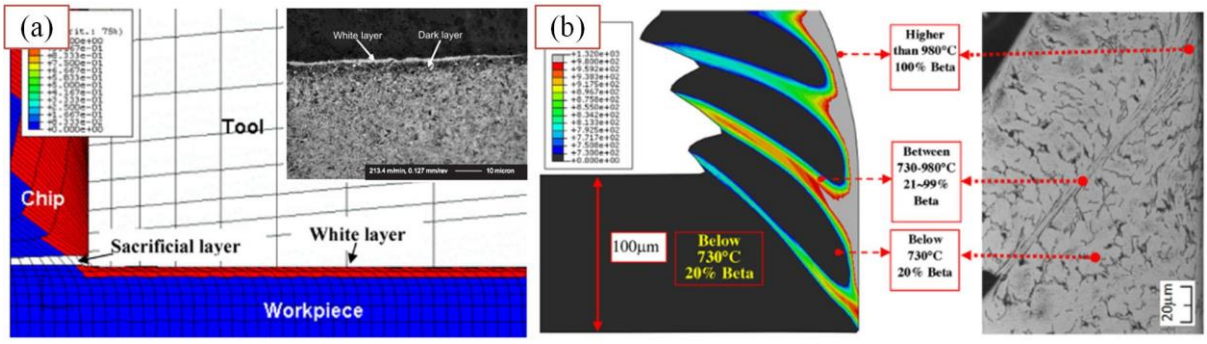

Fig. 13 Simulated phase volume fraction to predict the white layer formation in machined surface[76] *and (b) Estimation of beta volume fraction in chip segmentation by SCM-based flow stress model* [81].

Besides the thermal-driven phase transformation model, stress assisted and strain induced transformation are found to be a dominant mechanism involved in martensitic transformation [82]. Until now, the theoretical model for stress assisted transformation mechanism has not been well established to predict the phase transformation during machining processes, although this phenomenon has been observed and verified by multiple researchers as a fundamental mechanism during machining processes with complex stress states [83,84]. Zhang et al. [85] proposed a strain induced model for martensite phase transformation. It is based on an initial phase transformation model considering the effect of adiabatic shear behavior, high temperature and high strain rate with the assumption that strain-induced phase transformation is the dominant mechanism [86]. Kaynak et al. [87] took into account the impacts of strain rate and temperature on the driving force of phase transformation, and then developed a machining induced phase transformation model by modifying Helmholtz free energy-based model.

Although dislocation slip is considered to be the dominant form of plastic flow of materials, twinning deformation, including coordinating deformation and providing more possible slip systems, plays a fundamental role in conditions of high strain rates and low temperatures, or when cutting materials with poor crystal symmetry. This important mechanism of plastic deformation is generally neglected during the machining process, and few studies have considered its influence on machining process. Recently, the evolution of twinning and its influence on mechanical behavior have been preliminarily explored by Shen et al.[88,89], Wang et al. [90] and Sergio et al. [91]. Referring to the Hall-Petch effect, the evolution of twinning is described as the function of volume fraction and grain size of deformation twinning by Wang et al. [90]. A critical resolved shear stress (CRSS) for the motivation of twinning mechanism during high speed machining Ti-6Al-4V alloy, which can be defined as:

$$\sigma_c = K\dot{\varepsilon}^{(-1/m+1)} e^{Q/(m+1)RT} + k_c d^{-0.5} \tag{1}$$

where K and m are material constants, k_c is the Hall-Petch coefficient for twinning, and d is the initial grain size. When the flow stress is higher than CRSS, the calculation of twinning is generated. The volume fraction of deformation twinning f_t is expressed by

$$f_t = f_s \times \tanh\left(\pi \frac{\langle \sigma - \sigma_c \rangle}{\sigma_s - \sigma_c}\right) \tag{2}$$

where f_s is the saturated volume fraction of deformation twinning, and σ_s is the corresponding saturated flow

stress. The grain size d_t of effective twins is defined as

$$d_t = (d - d_0) \times \tanh\left(\pi \frac{\langle \sigma - \sigma_c \rangle}{\sigma_s - \sigma_c}\right) + d_0 \tag{3}$$

where d_0 is the initial grain size of the twins.

Sergio et al. [91] adopted the mean spacing of the twin lamellae and twin volume fraction to the dynamic recrystallization terms in describing the twinning evolution. The mean spacing of the twin lamellae is given by

$$\frac{1}{l_{TW}} = \frac{1}{2t} * \frac{f_{TW}}{1 - f_{TW}} \tag{4}$$

where t is the thickness of the twin lamellae, f_{TW} is the twin volume fraction, which is expressed by

$$f_{TW} = \frac{0.417}{1 + \exp(-27.15 * (\varepsilon - 0.183))} \tag{5}$$

After utilizing the above theoretical model of deformation twins in FE platform, the simulated results in Fig. 14 shows that the twin bands affected layer in the machined surface can be identified, which enhances the mechanical properties in machined surface.

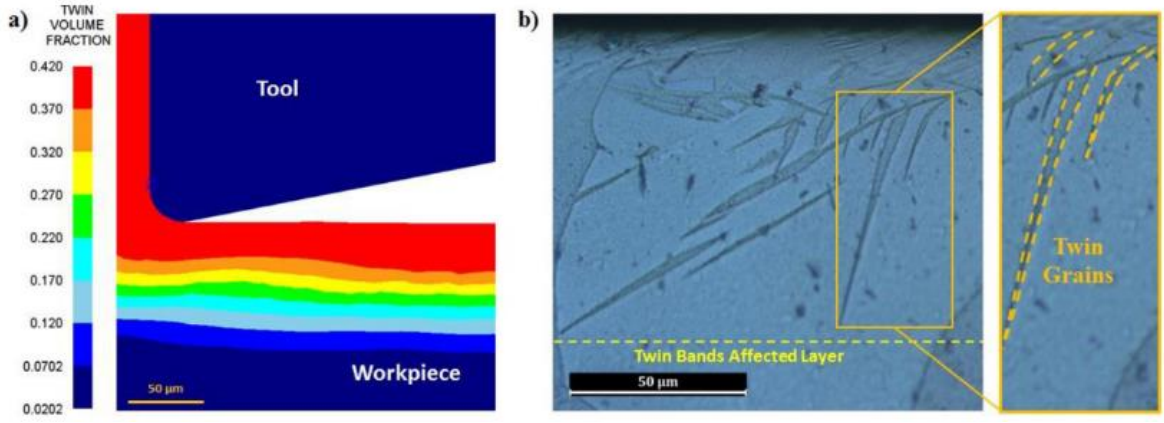

Fig. 14 Comparison of (a) numerically predicted and (b) optical microscope observed twinning affected layer thickness beneath the machined surface [91].

Due to the simplification of microstructure predicting model in FE simulation, many microstructure

parameters cannot be included to study the effect of microstructure evolution on plastic deformation mechanism. Although FE microstructure predicting models have been successfully applied to obtain the dislocation density and grain size distributions, these models cannot describe the grain refinement evolution and final microstructure characteristics. To compare the difference between different approaches to predict microstructure evolution, the approach by developing subroutine in FE platform to predict microstructure evolution is assigned as conventional approach. This microstructure evolution can be described by using the dislocation density evolution model established by Goetz and Seetharaman [92]. Using this model, Cellular automata (CA) method has been used to simulate the grains nucleation and growth process induced by DRX, under large plastic deformation at mesoscale. Ding and Guo [93] studied the DRX phenomenon of OFHC copper under low strain rate thermomechanical processing. They proposed a theoretical model of grain nucleation, grain growth and grain boundary migration. CA method has been applied successfully to simulate the DRX process for titanium alloys by Song et al. [95]. Therefore, the CA method is suitable to conduct simulations of microstructure evolution during thermomechanical processing at a mesoscale. Shen et al. [94] were probably the first to investigate the microstructure evolution in machining process using CA method. However, since then, few studies continued to use this method for studying the microstructure of the cutting process.

The literature review described above shows that previous works were mostly focused on the use of the microstructure-based constitutive models in FE simulation to investigate the microstructure evolution in metal cutting at a macroscale. The shortcoming of these models is their inability to reproduce the grain structure at mesoscale or even microscale. Moreover, very few research treating microstructure evolution simulation in metal cutting by multiscale methods are available in literature. Therefore, the aim of this study is to propose a multiscale simulation approach to predict the grain refinement induced by DRX during HSM of Ti-6Al-4V.

Transmission electron microscopy (TEM) was used to qualitatively analyze the deformed microstructure in machining pure Copper [73]. They show that the extent of grain refinement is greater induced by larger strains with a typical minimum size of 150 nm for pure metals. Duan and Zhang [95] found that the adiabatic shear bands (ASBs) consist of fine equiaxed grains and high dislocation density, and the equiaxed grains in ASBs result from the dynamic rotational recrystallization. This phenomenon is also found in chips during machining of AISI 1045 by using EBSD techniques, which is shown in Fig. 15. Residual stress and surface alteration, such as white layers and working hardened layers, play critical roles in the functional performance

and life of components [96,97]. Therefore, it is essential to understand the mechanism of microstructure evolution in HSM surface in order to propose an effective control strategy of the surface integrity.

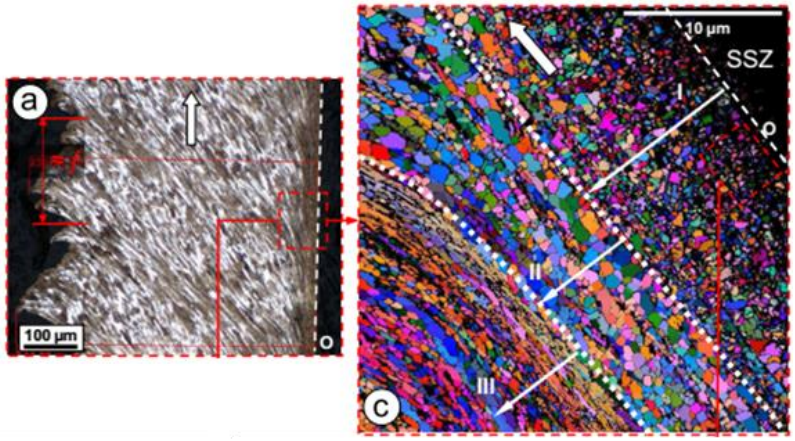

Fig. 15 EBSD characterization of the grain structure in the deformation zones (chip, AISI 1045) [98].

In the cutting process, chip formation is significantly affected by the microstructure evolution [99–101]. With the increase of cutting speed, the evolution law of adiabatic shear band (ASB) turns from deformed banding to transformed banding [102], which is mainly resulted from the phase transformation under high strain rate and temperature. In turn, the microstructure evolution of chips will influence the mechanical property and fracture process of materials [99,103]. With the increase of cutting speed, some surface defects, such as dimples, are formed in the machined surface [36], and its relationship with the microstructure of surface remains to be studied. The surface obtained by HSM of Ti-6Al-4V alloy can be divided into two different layers: highly perturbed layer and plastically deformed layer [71,104–106]. In addition, there are two opinions about the reason for the formation of the observed white layer on the machined surface. On one hand, the generation of white layer is the result of phase transformation or surface oxidation [105,107]. On the other hand, the grains are refined to the nanoscale [108]. Till now, there is no irrevocable explanation for the formation of white layer. The lack of correlation between analysis of deformation process and microstructure evolution besides the limitation of testing techniques are considered to be the main reasons.

In order to obtain the microstructure information regarding the highly perturbed surface layer, the focused ion beam (FIB) was adopted to acquire transmission electron microscope (TEM) samples as its thickness doesn't exceed 15~30μm. TEM testing results showed that highly perturbed layer presents a nanocrystalline structure [104]. As the overall quality of electron backscattered patterns degrade when the crystal lattice is

highly deformed, the resolution of EBSD shown in Fig. 16 is too low for severely deformed surface of titanium and Ni-based alloys [106,109,110]. As an emerging TEM-based orientation microscopy technique, precession electron diffraction (PED) offers ideal spatial resolution (~2nm) and reasonable angular resolution (~0.8°), which provide possibilities to study nanoscale features of severe deformed crystalline materials [111,112].

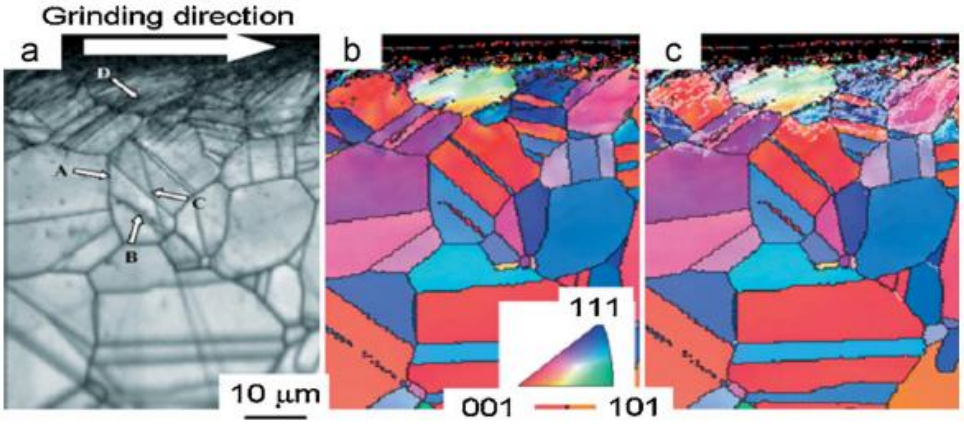

Fig. 16 EBSD analysis of the grinding surface [36].

In this study, HSM experiments of Ti-6Al-4V alloy are carried out and physical deformation conditions of surface are analyzed to establish process-microstructure relation. TEM and PED technologies are applied to characterize crystal information such as grain size, phase distribution, GND density, twins and phase transformation. Finally, the effects of high strain rates during HSM on dislocation generation, twining and secondary phase precipitation are analyzed, and formation mechanisms of nanoscale grains are revealed.

2.4 Constitutive model for cutting process

The numerical simulation of the machining process is highly dependent on the constitutive model, which describes the material behavior under various loading conditions found in metal cutting [57]. Johnson-Cook (J-C) constitutive model is often applied in the simulation of manufacturing processes including machining [113]. J-C model was proposed by Johnson and Cook [114] in 1983, which integrates the effects of strain hardening, strain rate hardening and thermal softening, and it can be expressed as

$$\sigma = \left(A + B \cdot \varepsilon^{n}\right) \cdot \left(1 + C \cdot \ln \frac{\dot{\varepsilon}}{\dot{\varepsilon}_0}\right) \cdot \left[1 - \left(\frac{T - T_0}{T_m - T_0}\right)^{m}\right] \tag{6}$$

This function rapidly turns to be the most widely used model in terms of metal cutting simulation since its

establishment, due to its good performance in describing coupled thermomechanical behaviors during plastic deformation. Moreover, it provides a good compromise between computational efficiency and simplicity of implementation, benefiting from a good compatibility with most of engineering alloys. The drawback is that a number of different J-C plasticity model coefficients can be found in the literature for the same material[115]. A sensitivity analysis of these coefficients shows that they have a significant influence on the simulations results. Often researchers select and test several sets of J-C model coefficients to determine which is the best set to use in their particular case [115,116]. Several studies have also shown that the J-C constitutive model is not suitable to represent the mechanical behavior of the work material in machining adequately [57]. Therefore, the J-C model has been modified or new constitutive models have been proposed to achieve an accurate description of the mechanical behavior of the work material in machining [117–119]. To address the difficulty of the J-C plasticity model to capture the serrated chip formation, Calamaz et al. [117] proposed a constitutive model (called the TANH model) to better predict serrated chips, which considers the effect of strain softening on the flow stress. Sima and Özel [118] made some improvements to this model to better control strain softening behavior. However, the accuracy of this model is verified only through orthogonal cutting tests rather than mechanical tests. Compared to original JC model, this modified model describes serrated chip formation for Ti-6Al-4V alloys in a better manner. It is also worth noting that, this modified JC model with a TANH term was reported to be suitable towards heat resistant alloys, especially Ti-6Al-4V. However, it is rarely reported to be applied for other material categories. Nevertheless, it provides a good compatibility with modifications, thus, Rotella and Umbrello [120] introduced some physical terms into this model to explain the composition of yielding stress, which is calculated depending on microstructure components. They also explained the phenomenon of stress decrease at high strains through dynamic recovery (DRV) and DRX theories. This is an early attempt of introducing microstructure-related concerns by the modification of J-C model, however, initial yielding stress is the only variable related to the initial microstructure, while the evolution of mechanical responses is not directly linked to physical aspects.

To introduce microstructural effects into constitutive behaviors with a strong dependency, Denguir et al. [121] proposed a new modified JC model. The effects induced by DRV and DRX are formulated by a phenomenological term to be added to original JC model. Similarly, another new modified J-C model considering the state of stress was proposed by Cheng et al. [122]. In their model, a term regarding Lode angle was used to describe the state of stress, and only strain-rate effects were implemented. Thermal softening was neglected in their original form. Both models from Denguir et al. [121] and Cheng et al. [122]

introduced the mechanisms regarding to stress triaxiality, which is used to optimize material plasticity with respect to cutting. The formation of cracks in chip formation (tearing) and cyclic nature of chip formation were recognized by the most noticeable classical work in metal cutting by Time [123], Nicolson [124], Taylor [125], Okoshi and Fucui [126]. In modern terminology, it is considered as cyclic fracture in chip formation [98,103,127,128]. Childs et al. [129] proposed a combined flow stress and failure model to simulate the serrated chip formation process of Ti-6Al-4V alloy over a wide cutting speed range, which improved the prediction accuracy of FE cutting models. Therefore, work material damage and fracture as state of stress dependent phenomena must be considered when modelling material behavior. Bai and Wierzbicki [18,130] proposed a constitutive model considering the effect of the state of stress (stress triaxiality and Lode parameter) on the material plasticity and damage. Wang et al. [128,131] found that the stress triaxiality in the first deformation zone (FDZ) gradually increased from negative near the tool cutting edge to positive in the chip free surface, which has a great influence on the formation of serrated chips and fracture strain distribution. Therefore, a constitutive model considering the effect of the state of stress is essential for describing the mechanical behavior of the work material in cutting as its use greatly increases the prediction accuracy. However, only few constitutive models used in metal cutting consider the state of stress. Cheng et al. [122] proposed a constitutive model that considers the effect of strain hardening, strain-rate, and the state of stress on the mechanical behavior of Ti-6Al-4V alloy. The accuracy of this model is verified for different samples geometries and loading conditions (thus different state of stress), by comparing the predicted force-displacement curves obtained using this constitutive model and the experimental curves. This accuracy is not reached using the J-C model.

The model proposed by Denguir et al. [6] provides a better dependency on physics-based concerns and microstructures, however, the microstructure-based term treats DRX as an equivalented effect depending on critical strains and temperatures, and no physical parameters are introduced for explicit calculation towards updating flow stresses. As a result, although these modified J-C models provide more comprehensive understandings with respect to different concerns, they are still attributed to the category of phenomenological laws due to the lack of explicit description and updating of physics-based matters. This type of modified J-C models are always realized through introducing add-on terms to the original shape, and the detailed functions are listed as shown in Table 1.

Table 1 Several featured modified JC models with special add-on terms

References	Constitutive laws	Remarks
Calamaz et al. [117], Sima and Özel [118]	$\begin{cases} \sigma = \left[A + B\cdot\varepsilon^{n}\cdot\left(\dfrac{1}{\exp\left(\varepsilon^{a}\right)}\right)\right]\left(1 + C\cdot\ln\dfrac{\dot{\varepsilon}}{\dot{\varepsilon}_0}\right)\left[1-\left(\dfrac{T-T_0}{T_m-T_0}\right)^{m}\right] \\ \qquad \times\left[D + (1-D)\left(\tanh\left(\dfrac{1}{(\varepsilon+P)^{c}}\right)\right)\right] \\ D = 1-\left(\dfrac{T}{T_m}\right)^{d_C} \\ P = \left(\dfrac{T}{T_m}\right)^{b_C} \end{cases}$	Decrease of flow stress at high strains is introduced to original JC model through a TANH term. This term is strain and temperature dependent.
Rotella and Umbrello [120]	$\sigma = \left[\left(A + \dfrac{K}{\sqrt{t}}\right) + B\cdot\varepsilon^{n}\right]\left(1 + C\cdot\ln\dfrac{\dot{\varepsilon}}{\dot{\varepsilon}_0}\right)\left[1-\left(\dfrac{T-T_0}{T_m-T_0}\right)^{m}\right] \times\left[D + (1-D)\left(\tanh\left(\dfrac{1}{(\varepsilon+P)^{r}}\right)\right)^{s}\right]$	Initial yielding stress is calculated based on lamella thickness. TANH term is used to describe the strain softening behavior.
Denguir et al. [6]	$\begin{cases} \sigma = \left(A + B\varepsilon^{n}\right)\left[1 + C\ln\left(\dfrac{\dot{\varepsilon}}{\dot{\varepsilon}_0}\right)\right]\left[1-\left(\dfrac{T-T_{room}}{T_m-T_{room}}\right)^{m}\right] \\ \qquad \times H(\varepsilon,\dot{\varepsilon},T)\left(1-c_\eta\left(\eta-\eta_0\right)\right) \\ H(\varepsilon,\dot{\varepsilon},T) = \dfrac{1}{1-\hat{H}(\varepsilon,\dot{\varepsilon})u(\varepsilon,T)} \\ u(\varepsilon,T) = \begin{cases} 0 & when\ \varepsilon < \varepsilon_r(\varepsilon,T) \\ 1 & when\ \varepsilon \geq \varepsilon_r(\varepsilon,T) \end{cases} \\ \hat{H}(\varepsilon,\dot{\varepsilon}) = H_1(\varepsilon) - H_2(\varepsilon)\exp(\dot{\varepsilon}) \\ \hat{H}_i(\varepsilon) = \dfrac{h_0}{\varepsilon} + h_i \quad with\ i = 1, 2... \end{cases}$	DRX and DRV induced material behaviors are introduced to original JC model through an add-on term. Stress triaxiality is introduced to original JC model to modify the stress state for cutting conditions.
Cheng et al. [122]	$\begin{cases} \sigma = \left(A + B\varepsilon^{n}\right)\left[L + C\ln\left(E + \dfrac{\dot{\varepsilon}}{\dot{\varepsilon}_0}\right)\right]\left[1-c_\eta\left(\eta-\eta_0\right)\right] \\ \qquad \times\left[c_\theta^{s} + \left(c_\theta^{ax} - c_\theta^{s}\right)\left(\gamma - \dfrac{\gamma^{f_{Lode}+1}}{f_{Lode}+1}\right)\right] \\ \gamma = 6.464\times[\sec(\bar{\theta}\pi/6) - 1] \\ c_\theta^{ax} = \begin{cases} c_\theta^{t} & for\ \bar{\theta} > 0 \\ c_\theta^{c} & for\ \bar{\theta} \leq 0 \end{cases} \end{cases}$	Both stress triaxiality and Lode angle are added to original JC model to describe the effects of the state of stress on material behaviors during cutting.

[a] **Nomenclature**: A, B, n, C, m - yielding stress, strain hardening rate, strain hardening coefficient, strain rate hardening coefficient, thermal softening coefficient for JC model; D, P, d_C, b_C - Temperature related coefficients for JC-TANH model; t - α phase lamella thickness for JC-TANH model; K - material constant; η - stress triaxiality; η_0 - the reference triaxiality; c_η - the triaxiality coefficient; ε_r - critical plastic strain; γ - difference between von Mises and Tresca equivalent stress in the deviatoric stress plane; $H(\varepsilon, \dot{\varepsilon}, T)$ - microstructural effect term for modified JC model; $u(\varepsilon, T)$ - strain and temperature related term for modified JC model; h_0, h_i - recrystallization related parameters for modified JC model; E - plastic strain rate related coefficient for modified Johnson–Cook model; c^{s}_{θ}, c^{ax}_{θ}, c^{t}_{θ}, c^{c}_{θ}, f_{Lode} - Lode angle parameter related

coefficients; $\bar{\theta}$ - Lode angle parameter.

Following J-C model, another generalized constitutive model was proposed by Zerilli and Armstrong [132] in 1987, which emerges the consideration of crystalline structures into the description of constitutive behaviors. In this model, they differentiated material behaviors depending on face-centered cubic (FCC) and body-centered cubic (BCC), respectively. Moreover, the effect of average grain size was also implemented. The general expression of this model can be used as:

$$\begin{cases} \sigma = \Delta\sigma_G^{'} + c_2\varepsilon^{1/2}\exp\left(-c_3T + c_4T\ln\dot{\varepsilon}\right) + kd^{-1/2} & \text{for FCC} \\ \sigma = \Delta\sigma_G^{'} + c_1\exp\left(-c_3T + c_4T\ln\dot{\varepsilon}\right) + c_5\varepsilon^n + kd^{-1/2} & \text{for BCC} \end{cases} \tag{7}$$

In this model, d denotes the average grain size, which contributes to a certain part of the flow stress. However, no evolution law was introduced to describe the progressive alteration of grain sizes during the deformation process. So it only contributes to the initial yielding stress. Moreover, the difference between FCC and BCC materials is mainly towards the relationship between strain effects and strain rate effects. This model was then developed by Zerilli [133] through incorporating the calculation of a new effective grain size through the consideration of deformation twinning, which makes the model eligible for hexagonal close packed (HCP) materials. He further commented that an excellent fit of the constitutive law may be obtained through implementing dislocation density-based strain-hardening law. Compared to modified J-C model, ZA model starts to move from phenomenological to introducing more physics, where the difference induced by crystal structures has been considered and emerged into models. However, these physics work only for a specific or determined condition, without progressive evolution.

The constitutive model considering microstructure effect plays a significant role in predicting the microstructure alterations in severe plastic deformation. A shear flow stress in terms of microstructure by considering the dislocation density was proposed [134]. Estrin and Kim [66] proposed a the dislocation density based (DDB) flow stress model considering dislocation density evolution at cells interior and cells walls. This model was firstly used for simulation of cutting process by Ding et al. [67], they proposed a Taylor factor M from the idea of Estrin et al. [135] towards testing models. Generally, DDB model is more reliable compared to other phenomenological models, especially within the strain range out of calibration, as it updates material behaviors based on physical considerations instead of purely fitted parameters. However, drawbacks still exist in DDB model. Indeed, only dislocation mobility and evolution are accounted, which is not well performed in terms of multi-mechanisms dominated deformation and limited to single phase

materials. Imbrogno et al. [136] investigated the deformation mechanism of Waspaloy under different cutting condition and developed a physic-based constitutive model which consists of additive long-range and short-range contributions as shown in Fig. 17. This model was used in FE orthogonal cutting simulation to predict the surface integrity. The main problems encountered are: (1) great difficulties to obtain the microstructure properties of a given work material to determine the constitutive model coefficients; (2) intricacy to assure the stability of the microstructural properties over various regions of the workpiece material.

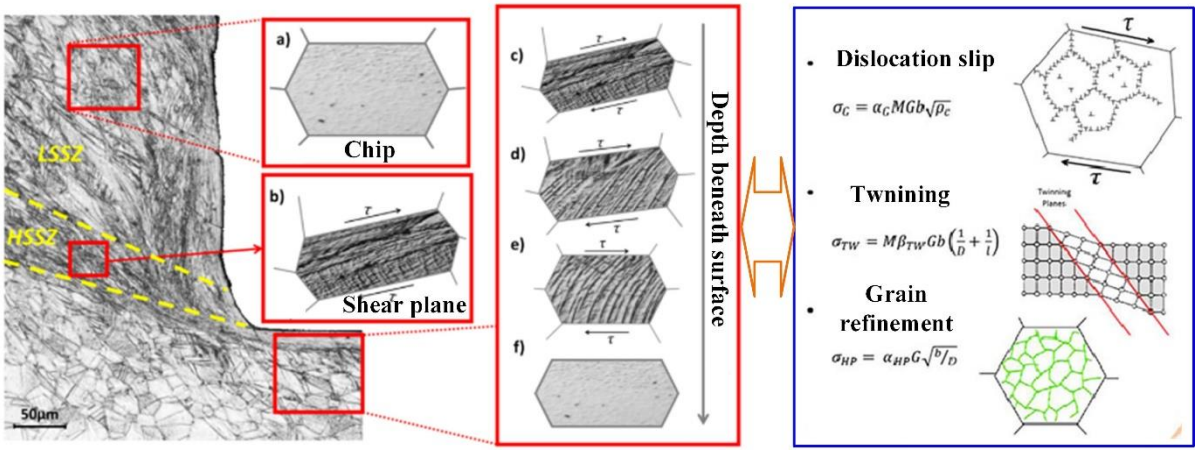

Fig. 17 Microstructural-based constitutive model based on the long-range and short-range contributions to simulate the serrated chip formation in the machining of Waspaloy.

Mechanical threshold stress (MTS) model [137] is composed of several components, which represents the integration of multiple behaviors at microstructure-level, including dislocation density evolution, dislocation drag, grain size effects, mechanical twinning, etc. Its initial function only contains the term σ_a (adiabatic shear stress) for stress components from rate-dependent interactions of dislocations with long-range barriers, and σ_{th} (thermal stress) for the initial stress induced by interactions between mobile dislocations and short-range barriers following Kocks and Mechking (KM) model [134]. In terms of calculation of σ_a, a simplified dislocation evolution law is normally involved, which can describe its contribution to flow stress by a relatively low computational cost. Compared to DDB model, the most prominent advantage of MTS model as a physics-based law is the capability to incorporate more comprehensive physical mechanisms with adding terms. Liu et al. [7] introduced the contributions of grain size effects and dislocation drag to update flow stress. In their case, the contribution from grain size to flow stress follows a Hall-Petch relationship, and grain size evolution is expressed based on the mechanisms of DRX and DRV [59]. With implementations of

pertinent functions, the constitutive model is now available towards predicting multiple factors involved in microstructure evolution simultaneously with the materials deformation during metal cutting process. This model can present the average grain size instead of sub-grain size from DDB model, which is more reasonable and practical in terms of observation from microscopy. Rinaldi et al. [91] investigated orthogonal cutting of commercially pure titanium, which is a typical HCP crystal. For this material, twinning is a non-negligible mechanism in deformation, especially at high strain rates. In their case, σ_{tw} is used to denote the stress component coming from mechanical twinning, which is calculated by the mean space of twin lamella and average grain size, where the twin volume fraction is calculated as following. This model successfully introduces modelling of twinning into metal cutting simulation. However, the major drawback is that the thickness of twinning lamella is used as a constant value instead of a progressive one following material deformation and fracture. Moreover, volume fraction of twinning is influenced by the single variable of plastic strain, and other factors are all neglected. This parameter is not provided by experimental data, as a result, the twinning portion of this constitutive modelling is more of a qualitative term instead of quantitative description, which still require to be validated. The comparison of different physic-based constitutive models is presented in Table 2. Although physics-based models are more profound in terms of physics and they have gained increasing attention for cutting simulations, these physical parameters significantly reduce the computational efficiency and are difficult to identify.

It can be seen from the above description of phenomenological and physics-based constitutive models that each one has its strict scope of application and its boundary conditions to use. The selection of the constitutive model depends on the research purpose. On the premise of ensuring the accuracy to describe the mechanical behavior, higher computational efficiency and revealing more physical nature of machining process a constitutive model has to be achieved.

Table 2 Several physic-based constitutive models considering different microstructure effects

References	Constitutive laws	Remarks
Ding et al. [67]	$\tau_c^r = \alpha Gb\sqrt{\rho_c}\left(\frac{\dot{\gamma}_c^r}{\dot{\gamma}_0}\right)^{1/m}$ $\tau_w^r = \alpha Gb\sqrt{\rho_w}\left(\frac{\dot{\gamma}_w^r}{\dot{\gamma}_0}\right)^{1/m}$ $\tau^r = f\tau_w^r + (1-f)\tau_c^r$ $\dot{\rho}_w = \frac{\sqrt{3}\beta^*(1-f)\sqrt{\rho_w}}{fb}\dot{\gamma}_c^r + \frac{6\beta^*(1-f)^{2/3}}{bdf}\dot{\gamma}_c^r - k_0\left(\frac{\dot{\gamma}}{\dot{\gamma}_0}\right)^{-1/n}\rho_w\dot{\gamma}_w^r$ $\dot{\rho}_c = \alpha^*\frac{1}{\sqrt{3}}\frac{\sqrt{\rho_w}}{b}\dot{\gamma}_w^r - \beta^*\frac{6}{bd(1-f)^{1/3}}\dot{\gamma}_c^r - k_0\left(\frac{\dot{\gamma}}{\dot{\gamma}_0}\right)^{-1/n}\rho_c\dot{\gamma}_c^r$	Dislocation density evolution in cell interior and wall induced strain hardening behavior.
Imbrogno et al. [136]	$\sigma = \sigma^* + \sigma_G + \sigma_{HP}$ $\sigma^* = \sigma_0\left(1-\left(\frac{k_bT}{\Delta f_0 Gb^3}\ln\left(\frac{\dot{\varepsilon}_r}{\dot{\varepsilon}^p}\right)\right)^{1/q}\right)^{1/p}$ $\sigma_G = M\alpha Gb\sqrt{\rho}$ $\sigma_{HP} = k_{HP}/\sqrt{D}$	Short-range effect induced by dislocation density and long-range effect induced by grain size evolution are introduced.
Zhang et al. [127]	$\sigma_{\alpha+\beta} = f\sigma_\alpha + (1-f)\sigma_\beta$ $\sigma^{1/m'} = K\exp(Q/RT)\dot{\varepsilon}$ $\sigma_{\alpha+\beta} = fk_\alpha\dot{\varepsilon}_{\alpha+\beta}^{m'} + (1-f)k_\beta\dot{\varepsilon}_{\alpha+\beta}^{m'} = fk_\alpha\dot{\varepsilon}_{\alpha+\beta}^{m'}\left\{1+\left[(1-f)/f\right]\left(k_\beta/k_\alpha\right)\right\}$ $k_{\alpha+\beta}/k_\alpha = f\left(\dot{\varepsilon}_\alpha/\dot{\varepsilon}_{ov}\right)^{m'} + \left[(1-f)^{(1-m')}\left(k_\beta/k_\alpha\right)\left(1-f\left(\dot{\varepsilon}_\alpha/\dot{\varepsilon}_{ov}\right)^{m'}\right)\right]$	Effect of phase transformation on the flow stress is described by a mixed approach.
Umbrello et al. [91]	$\sigma = \sigma_G + \sigma_{TW} + \sigma_{TH} + \sigma_{HP} + \sigma_D$ $\sigma_G = \alpha MGb\sqrt{\rho}$ $\sigma_{TW} = M\beta_{TW}Gb\left(\frac{1}{D}+\frac{1}{l}\right)$ $\sigma_{TH} = \sigma_0\left(\alpha_{TH}T\ln\left(\frac{\dot{\varepsilon}}{\dot{\varepsilon}_0}\right)\right)\left(1-\left(-\beta_{TH}T\ln\left(\frac{\dot{\varepsilon}}{\dot{\varepsilon}_0}\right)\right)^{1/q}\right)^{1/p}$ $\sigma_{HP} = \alpha_{HP}G\sqrt{b/D}$ $\sigma_D = \alpha_D\dot{\varepsilon}$	Both dislocation slip and twinning are added to describe the effects of high strain rate on material behaviors during cutting.

[b] **Nomenclature**: ρ_c, ρ_{ws}, ρ_{wg} and ρ_{tot} are the dislocation densities of cell interiors, statistically stored dislocation densities (SSDs) of cell walls, GNDs of cell walls and the total dislocation density, respectively; f denotes the fraction of cell wall dislocation density in total dislocation density, d_{Cell} is the average cell size; α^*, β^* and k_0 are the controlling parameters for evolution rates of dislocation density, K_0 a material constant, ξ_1 and ξ_2 denote the fractions transferred from cell wall to GNDs; σ_a - stress components from rate-dependent interactions of dislocations with long-range barriers; σ_{th}, σ_G, σ_d, σ_{tw} - stress components for thermal effects, grain size effects, dislocation drag and mechanical twinning; α - numerical constant for shear stress; G - shear modulus; b - Burgers vector; k_B - Boltzmann constant; g_0 - the normalized activation energy at 0 K; ε_r - the critical strain for DRX; d_0, d_f - initial and recrystallized grain sizes; t_{tw} - the mean thickness of twin lamella; f_{tw} - the volume fraction of twinning.

Phenomenological and physics-based laws are both effective approaches in terms of modeling the microstructure effects and the evolutions developed during the cutting processes. Concerning phenomenological laws, additional terms are introduced to account for the effect of the microstructure instead of merging the entirety of the concerns about the microstructure evolution. In this case, the generalized models are generally introduced to describe the effect of the microstructure. For physics-based models, physical matters can be explicitly calculated and used to update the flow stress. As a result, both the effect of the microstructure and its evolution can be visualized based on their good performances for cutting simulation. However, although physics-based models are more profound in terms of physics and they have gained increasing attention for cutting simulations, some limitations still exist:

1) Physics-based models are mainly developed based on a single crystal structure, which is not applicable for dual-phase systems and phase transformation cases due to the limitations of fundamental assumptions.
2) Physics-based models introduce a large number of physical parameters into the calculation. These parameters significantly reduce the computational efficiency and are difficult to identify. In this case, some variables are still determined through fitting against phenomenological models, which makes the models lose some realism in terms of physics. We recommend identifying these microscale factors through approaches like the first principle and molecular dynamics. However, this also increases the difficulty of handling the model and makes it less suitable for industrial application.

The summary of advantages and drawbacks of different constitutive models is summarized in Table 3. As a result, currently, phenomenological laws cannot be completely replaced by physics-based laws, and they are working in more of a relationship of compensating for each other. However, there is still high potential for more frequent usage of physics-based laws instead of phenomenological laws following the continuously increasing development during the last decade, although only small modifications and developments have been reported for phenomenological laws recently. Thus, by solving the urgent problems of computational costs and implementing more mechanisms to make physics-based laws applicable for multi-phase materials and phase transformation problems, physics- based laws are expected to be used more often in the future.

Table 3 Summary of advantages and drawbacks of different constitutive models

Researchers	Numerical approach	Advantages	Drawbacks
Calamaz et al. [117] Sima and Özel [118] Rotella and Umbrello [120] Denguir et al. [6] Cheng et al. [122]	Phenomenological-based model	Low computational cost Good convenience Small modification for traditional constitutive law Easy to application	Less physical meaning Low accuracy
Ding et al. [67] Imbrogno et al. [136] Zhang et al. [127] Umbrello et al. [91]	physics-based model	Good accuracy More microstructure feature are addressed	High level complexity Low calculation efficiency Difficulty to validation

2.5 Surface integrity in metal cutting

The functional performance of machined components is determined by the surface integrity of machined surface. The definition of surface integrity was first proposed by Field and Kahles [138] in 1964. compared with the traditional machining surface quality evaluation method, the evaluation parameters for surface integrity shown in Table 4 requires that the surface geometric features, mechanical and physical properties and metallographic structure can meet the requirements of application. Besides that, due to the physical nature of material removal and surface alteration from machining process, the service performance of components has changed greatly, which includes the wear resistance, corrosion resistance, compatibility stability and reliability, and fatigue resistance of the components. Therefore, a comprehensive evaluation of the surface quality of the workpiece after machining is required [139].

Table 4 Evaluation parameters for surface integrity after machining process

Basic data	Standard data	Generalized data
1. Geometric features	**Basic data +**	**Standard data +**
2. Physical features	5. Residual stress	7. Stress corrosion
3. Microstructures	6. microscale mechanical test	8. Fatigue life
4. Hardness		9. Supplementary mechanical test

The changes in geometric and physical characteristics of machined surfaces caused by mechanical processing vary from the nanoscale to the macro-scale. High speed cutting is a highly nonlinear mechanical-thermal coupling process of workpiece material under the interaction of cutting tool and workpiece which includes large deformation, high strain rate, high temperature and complex friction in cutting deformation zone. Under such extreme conditions, the processed surface of the workpiece produces complex metamorphic layer. The deformation of grain, the increase of dislocation and the microstructure evolution of the complex crystal have a direct impact on the macroscopic physical and mechanical properties of the workpiece. According to the theory of molecular-mechanical friction, Grzesik [140] used the Brammertz equation to calculate the surface roughness theory and compared the experimental results under different cutting parameters. According to the theory of molecular-mechanical friction, it was pointed out that the difference between the theoretical calculation and experimental results was mainly caused by the tool-chip adhesion. And then, Korkut et al. [141] studied the feed rate and cutting speed in face milling and pointed out that the cutting speed had a significant impact on built-up edge and scales, which both led to the increase of surface roughness. Therefore, the cutting parameters are an important part of the factors affecting the surface integrity, and the material removal plays an important role in the surface integrity.

Through the analysis of plastic deformation during machining nickel-based alloy, Yıldız et al. [31] pointed out that the distribution of surface plastic shear strain was similar to the distribution of residual stress on the machined surface. Furthermore, Nie et al. [142] presented the relationship between the cutting resistance and the compressive stress of the machined surface by investigating the surface hardening behavior. The depth of hardened layer on machined surface is quantified by the relation between cutting force and stress of machined surface. Since then, the influence of the surface integrity of the cutting process on the performance of parts is gradually taken into account. For example, Obikawa et al. [143] shows that when cutting carbon steel, a typical two-phase alloy, the phase content and distribution presents a great influence on the distribution of the final residual stress. Residual stress on the machined surface will affect the mechanical properties of the workpiece such as corrosion, cracking and fatigue strength. Through experiments on cutting of AZ31B magnesium alloy with different parameters, Pu et al. [144] found that the corrosion resistance of the surface would be improved when the grain was refined and the substrate texture was generated. Denguir et al. [145] attempted to establish the correlation between surface roughness, residual stress, grain size and surface corrosion resistance by studying the microscale corrosion mechanism of the surface, and to improve surface corrosion resistance by optimizing cutting parameters and tool geometries. The influence of grain

refinement and phase transformation on the surface microhardness after machining of Ti-6Al-4V alloy by Umbrello [30] and it is found that the grain refinement and increase of β phase content improves the microhardness of machined surface. The surface integrity has a significant influence on the fatigue life of aircraft engine components under severe cyclic loadings. Yang et al. [146] revealed the mapping relationship between the machined surface integrity and fatigue life by comprehensively analyzing the formation mechanism of surface integrity of milling Ti-6Al-4V alloy and the characterization of low-cycle fatigue life of parts. Herbert et al. [104] improved the fatigue life of machining RR1000 components twice by increasing the thickness of white layer and residual compressive stress on the surface through shot peening technology, thus preventing crack initiation and propagation. Liu et al. [147] induced martensitic transformation and residual compressive stress on the surface by adjusting the processing parameters to improve the fatigue strength of the workpiece. To sum up, cutting the surface integrity and the relationship between the load and performance as shown in Fig. 18, the mapping relationship between cutting parameters and the part b performance, through the analysis to reveal the influence of load on the microstructure and microstructure on the physical and mechanical properties, can build a complete system to evaluate the performance of workpiece, the microstructure is the response of the load, As the key factor connecting the whole cutting process in series, the surface integrity of machined surfaces is of great significance to the prediction and evaluation of the functional performance and life of parts.

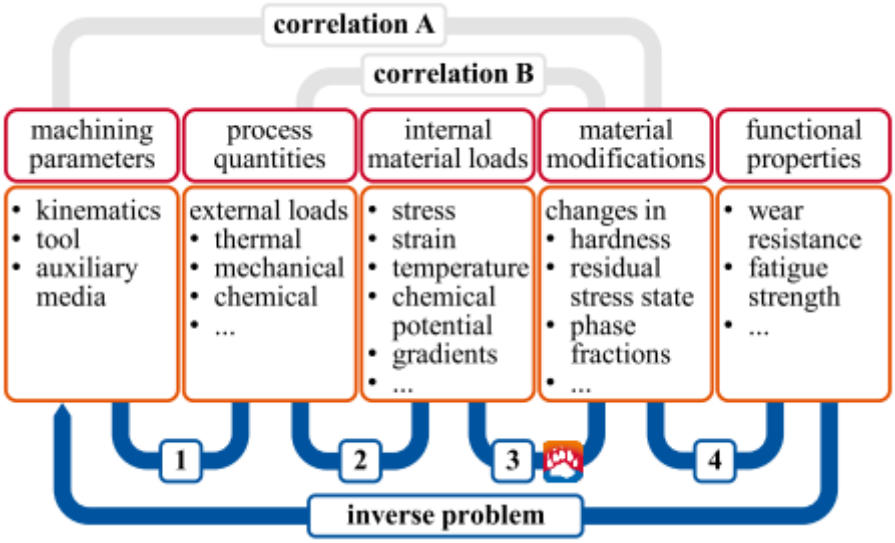

Fig. 18 Process signature for surface integrity prediction [148].

2.6 Summary of the chapter

Based on the review of the above research status, the experimental research and numerical modeling of the microstructure and surface integrity under the influence of high-speed cutting are targeted. Nowadays research on high speed cutting mechanics has made certain progress, but most of it is limited to use experimental observation. Therefore, the properties of the machined surfaces obtained by high-speed cutting cannot be accurately evaluated and predicted. Therefore, the main problems existing in current research are as follows:

(1) Numerical modeling and constitutive model for metal cutting process

In view of the present application of the most common finite element modeling methods to machining, traditional Lagrangian (LAG) model is the most widely used, and a preset sacrificial layer is needed Mesh distortion control and removal conditions, under the influence of mesh distortion, has become extremely difficult, So a finite element technique which can solve the mesh distortion problem is very important for predicting the cutting process accurately. Numerical simulation of the process, material constitutive model for the description of the stress-strain relationship define the accuracy of the simulation results. In the process of cutting, stress state on the material, fracture and damage evolution behavior are very significant, but the current development of constitutive models often ignored these important factors.

(2) Microstructure characterization and evolution mechanism in cutting deformation zone

Materials used in high speed cutting presented metallurgical change: many scholars used different materials with different cutting parameters, and observed deformation, grain refining, and phase transformation phenomena during their exploratory research. The evolution of the microstructure during the cutting process is correlated with the macroscopic mechanical properties of materials, and the effect of microstructure evolution on the mechanical behavior of materials in cutting process under the mechanical and thermal constraints needs to be furtherly revealed.

(3) Numerical modelling of microstructure effects and evolution

Due to the several assumptions and hypothesis used to simplify the microstructure prediction model, besides the difficulties to achieve accurate description of microstructure evolution mechanisms, the predicted results cannot meet those issued from experimentation. As a result, it is difficult to accurately predict the surface quality in high speed cutting and to optimize the process in order to improve the workpiece performance. This is due to the scale of the simulation model, the adequacy of each model to the operation's scale.

(4) Study of the surface integrity considering the influence of the microstructure

At present most of research used phenomenological modelling calibrated using experimental results to predict surface integrity. Hence, it is difficult to find a material model integrating microstructure allowing to perform simulations with accurate predictions, especially while the assumptions on which the model is based ignore a lot of microstructure parameters, the influence of the state of stress, and the interaction with the environment (the cooling process if there is any, and the contact with the cutting tool).

3 Metal cutting modelling using CEL approach and constitutive model considering the state of stress

3.1 Constitutive model considering the state of stress

3.1.1 Definition of the state of stress

The proposed constitutive model considers the effect of state of stress on both material plasticity and damage. This state of stress is characterized by the stress triaxiality and the Lode parameter [18]. Three invariants of the stress tensor are defined by:

$$p = -\sigma_m = -\frac{1}{3}(\sigma_1 + \sigma_2 + \sigma_3) \tag{8}$$

$$q = \bar{\sigma} = \sqrt{\frac{3}{2}\mathbf{S}:\mathbf{S}} = \sqrt{\frac{1}{2}\left[(\sigma_1 - \sigma_2)^2 + (\sigma_2 - \sigma_3)^2 + (\sigma_3 - \sigma_1)^2\right]} \tag{9}$$

$$r = \left(\frac{9}{2}\mathbf{S}:\mathbf{S}:\mathbf{S}\right)^{1/3} = \left[\frac{27}{2}(\sigma_1 - \sigma_m)(\sigma_2 - \sigma_m)(\sigma_3 - \sigma_m)\right]^{1/3} \tag{10}$$

where σ_1, σ_2 and σ_3 denote the three principal stresses, σ_m is the mean principal stress, **S** is the deviatoric stress tensor. Stress triaxiality η and Lode parameter are defined as follows:

$$\eta = \frac{-p}{q} = \frac{\sigma_m}{\bar{\sigma}} \tag{11}$$

$$\begin{cases} \xi = \left(\dfrac{r}{q}\right)^3 = \cos(3\theta) \\ \bar{\theta} = 1 - \dfrac{6\theta}{\pi} = 1 - \dfrac{2}{\pi}\arccos\xi \end{cases} \tag{12}$$

where ξ and $\bar{\theta}$ are the normalized third deviatoric stress invariant and the normalized Lode angle (also called Lode parameter). The range of $\bar{\theta}$ is between [-1, 1].

3.1.2 Plasticity

An accurate and reliable constitutive model is very important to describe the mechanical response of the work material in machining. The J-C constitutive model [113] is widely used to describe the mechanical behavior of the work under different strain-rates and temperatures but is not accurate for relatively small strains and

complex state of stress. Therefore, a constitutive model considering the effect of strain hardening, thermal softening, strain rate, and state of stress are proposed in this study. This model is an extension of the constitutive model of Cheng et al. [122] by including the effect of the temperature on the material plasticity and damage.

The plasticity part of the proposed model is given by equation (13), where the strain hardening, strain rate, and temperature terms are based on the Dos Santos et al. [149] and Johnson and Cook [113] models, respectively. As far as the state of stress term is concerned, it is based on the Bai and Wierzbicki [18] and Cheng et al. [122] model.

$$\begin{aligned}\bar{\sigma} = \left(A + m\varepsilon^{n}\right)\left[B + C\ln\left(E + \frac{\dot{\varepsilon}}{\dot{\varepsilon}_0}\right)\right]\left[1 - \left(\frac{T - T_r}{T_m - T_r}\right)^{h}\right] \\ \times\left[1 - c_\eta\left(\eta - \eta_0\right)\right]\left[c_\theta^{s} + \left(c_\theta^{ax} - c_\theta^{s}\right)\left(\gamma - \frac{\gamma^{a+1}}{a+1}\right)\right]\end{aligned} \tag{13}$$

$$\gamma = 6.464\left[\sec\left(\bar{\theta}\pi/6\right) - 1\right] \tag{14}$$

$$c_\theta^{ax} = \begin{cases} c_\theta^{t} & \text{when } \bar{\theta} > 0 \\ c_\theta^{c} & \text{when } \bar{\theta} \le 0 \end{cases} \tag{15}$$

In these equations: i) $\bar{\sigma}$ is the equivalent stress; ii) ε and $\dot{\varepsilon}$ are the equivalent plastic strain and strain rate, respectively; iii) T is temperature; iv) η is the stress triaxiality; v) η_0 is the reference stress triaxiality; vi) $\dot{\varepsilon}_0$ is the reference strain rate; and vii) T_r and T_m are the room and melting temperatures, respectively, A, m, n, B, C, E, and h are the associated to the strain hardening, strain rate, and temperature terms, while c_η, c_θ^{s}, c_θ^{c}, c_θ^{t} and a are the coefficients associated to the state of stress (stress triaxiality and Lode parameter) term. The values of these coefficients are given in Table 5, which are determined by Cheng et.al [122].

Table 5: Coefficients of the plasticity part of the proposed constitutive model of Ti-6Al-4V alloy taken from the work of Cheng et al [122].

Coefficient	A (MPa)	m (MPa)	n	B	C	E	$\dot{\varepsilon}_0$ (s^{-1})	T_r (°C)
Value	812.1	625.7	0.176	0.4	0.073	3949	0.05	20
Coefficient	T_m (°C)	h	η_0	c_η	c_θ^{s}	c_θ^{t}	c_θ^{c}	a
Value	1620	1	-1/3	0.212	0.795	1.061	1	4

Fig. 19 shows the stress-strain curves obtained by plotting the proposed constitutive model given by equations

8-10 and the coefficients presented in Table 5, for the work material in FDZ with a temperature of 350 °C, strain rate of 10^5 s^{-1}, and several values of stress triaxiality and Lode parameter. $\bar{\varepsilon}_0^{pl}$ is the strain at damage initiation, calculated using Eq. 17 that will be described later, and the coefficients presented in Table 6. As can be seen in this figure, the stress-strain curves are affected by the stress triaxiality and the Lode parameter.

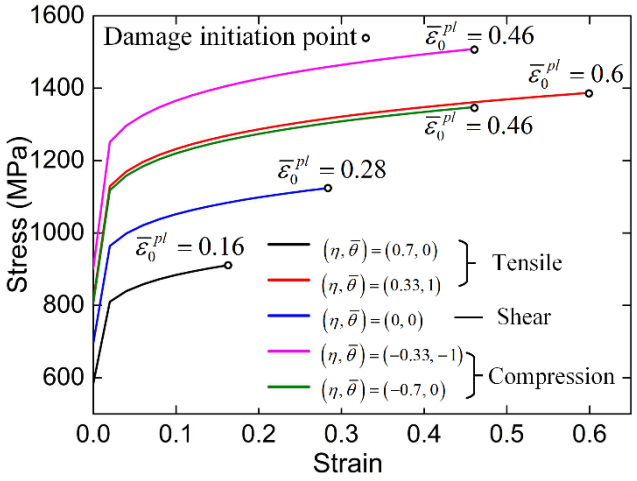

Fig. 19: Stress-strain curves of the proposed constitutive model of Ti-6Al-4V titanium alloy in the FDZ (temperature = 350 °C, strain rate = 10^5 s^{-1}, and several values of stress triaxiality and Lode parameter).

3.1.3 Damage initiation and evolution

To describe the material behavior in machining properly, the constitutive model must also consider material failure. This permits more realistic modeling of the chip formation (chip serration and the localized shear strain in the shear bands) in the machining of Ti-6Al-4V [150]. In this study, an energy-based ductile fracture criterion is adopted, which is composed of two stages, i.e. damage initiation and damage evolution [122]. The damage initiation is described by the variable W defined as:

$$w = \sum \frac{\Delta \bar{\varepsilon}^{pl}}{\bar{\varepsilon}_0^{pl}} \tag{16}$$

where $\bar{\varepsilon}_0^{pl}$ is the equivalent plastic strain at damage initiation and $\Delta \bar{\varepsilon}^{pl}$ is an increment of the equivalent plastic strain. As shown in Fig. 20, W increases continuously with plastic deformation, and when it is equal to 1, damage evolution is activated. $\bar{\varepsilon}_0^{pl}$ can be calculated by Eq.(17), based on Bai and Wierzbicki [18] and Johnson-Cook [151] constitutive models depending upon the stress triaxiality, Lode parameter, strain rate,

and temperature.

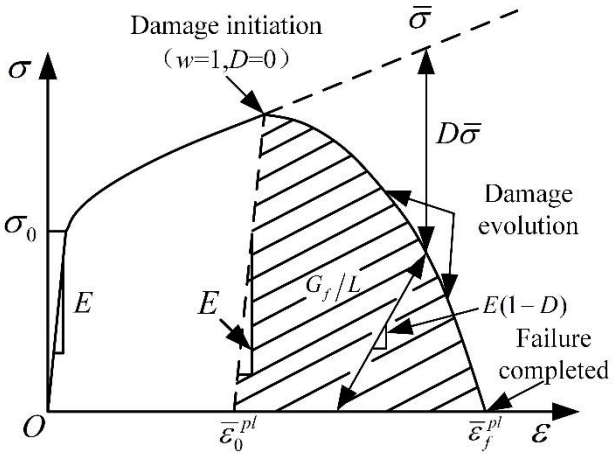

Fig. 20: Schematic representation of the stress-strain curve showing the material damage.

$$\bar{\varepsilon}_0^{pl}=\left\{\left[\frac{1}{2}\left(D_1e^{-D_2\eta}+D_5e^{-D6\eta}\right)-D_3e^{-D_4\eta}\right]\bar{\theta}^2+\frac{1}{2}\left(D_1e^{-D_2\eta}-D_5e^{-D_6\eta}\right)\bar{\theta}+D_3e^{-D_4\eta}\right\} \times\left[1+D_7\ln\left(\frac{\dot{\varepsilon}}{\dot{\varepsilon}_0}\right)\right]\left(1+D_8\frac{T-T_r}{T_m-T_r}\right) \tag{17}$$

In this equation, D_1 to D_6 are coefficients as in the Bai and Wierzbicki model, while D_7 and D_8 are as in the J-C one. These coefficients are determined by Cheng et al. [122] and given in Table 6. Moreover, the damage initiation point is calculated and given in Fig. 19 according to the above damage initiation model, which reveals that the damage initiation starts at different equivalent strains depending upon the state of stress.

Table 6: Coefficients of the damage initiation of Ti-6Al-4V alloy taken from the work of Cheng et al [122].

D_1	D_2	D_3	D_4	D_5	D_6	D_7	D_8
0.694	0.608	0.263	0.734	0.43	0.04	-0.028	3.87

The equivalent strain at damage initiation $\bar{\varepsilon}_0^{pl}$ as a function of the state of stress $\left(\eta, \bar{\theta}\right)$ for the Ti-6Al-4V alloy in FDZ at temperature of 350 °C and a strain rate of 10^5 s^{-1} are calculated and presented in Fig. 21. As can be seen, when the stress triaxiality is 1 and the Lode parameter is 0, the minimum of the plastic strain at damage initiation is the case obtained. Decreasing the Lode parameter from 0 to -1 or increasing it from 0 to 1 results in increasing the plastic strain at damage initiation. However, the plastic strain at damage initiation decreases as the stress triaxiality increases from -1 to 1.

In Fig. 20, $\bar{\varepsilon}_f^{pl}$ is the plastic strain at the point where the material has lost all its stiffness and dissipated all the fracture energy. Therefore, $\bar{\varepsilon}_f^{pl}$ can be calculated using the following equation:

$$G_f = \int_{\bar{\varepsilon}_0^{pl}}^{\bar{\varepsilon}_f^{pl}} L\sigma_y d\bar{\varepsilon}^{pl} \tag{18}$$

where G_f is the fracture energy, L is the characteristic length of the element. The stiffness degradation of the material can be described by D_f, which varies from 0 (damage initiation) to 1 (failure) [152]. D can be calculated as follows:

$$D_f = \frac{1-\exp\left(\lambda\varepsilon^*\right)}{1-\exp\left(\lambda\right)}, \quad \varepsilon^* = \frac{\bar{\varepsilon}^{pl} - \bar{\varepsilon}_0^{pl}}{\bar{\varepsilon}_f^{pl} - \bar{\varepsilon}_0^{pl}} \tag{19}$$

where λ is a coefficient to control the material degradation rate, $\bar{\varepsilon}_0^{pl}$ is the equivalent plastic strain at damage initiation, and $\bar{\varepsilon}_f^{pl}$ is the equivalent plastic strain at failure. G_f and λ are equal to 18.5 kJ/m^2 and 9.4, respectively [122]. Therefore, the stress at the damage stage is calculated by the following equation:

$$\tilde{\sigma} = \left(1 - D_f\right)\bar{\sigma} \tag{20}$$

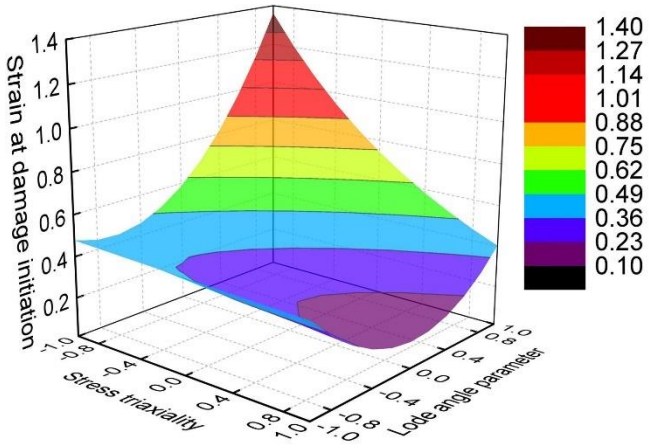

Fig. 21: Strain at damage initiation for the Ti-6Al-4V alloy in FDZ in function of the stress triaxiality and Lode parameter (temperature of 350 °C and a strain rate of 10^5 s^{-1}).

The proposed constitutive model including both plasticity and damage parts is implemented into Abaqus/Explicit through a VUHARD subroutine using FORTRAN language. It is worth noting that the

maximum value of parameter D_f is limited to be 0.99 because the element deletion cannot occur in the CEL cutting model.

3.1.4 Johnson-Cook constitutive model

To evaluate the accuracy of the proposed constitutive model in modeling the cutting process, J-C [153] model (plasticity and damage) is also used in orthogonal cutting simulations using CEL approach. This model describes the material flow stress (equation(21)) and plastic strain at damage initiation (equation(22)) as a function of the strain, strain rate, stress triaxiality and temperature. The corresponding equations are represented as follows:

$$\bar{\sigma} = \left(A_{J-C} + B_{J-C}\varepsilon^{n_{J-C}}\right)\left(1 + C_{J-C}\ln\left(\frac{\dot{\varepsilon}}{\dot{\varepsilon}_0}\right)\right)\left[1 - \left(\frac{T - T_0}{T_m - T_0}\right)^{m_{J-C}}\right] \tag{21}$$

$$\varepsilon_0^{pl} = \left[D_{1J-C} + D_{2J-C}\exp\left(D_{3J-C}\frac{\sigma_p}{\bar{\sigma}}\right)\right]\left[1 + D_{4J-C}\ln\left(\frac{\dot{\varepsilon}}{\dot{\varepsilon}_0}\right)\right]\left[1 + D_{5J-C}\frac{T - T_r}{T_m - T_r}\right] \tag{22}$$

where: $\bar{\sigma}$ is the equivalent stress; ε_0^{pl} is the equivalent plastic strain at damage initiation; ε and $\dot{\varepsilon}$ are the equivalent plastic strain and strain rate, respectively; T is the temperature; η is the stress triaxiality; $\dot{\varepsilon}_0$ is the reference strain rate; T_r and T_m are the room and melting temperatures, respectively. $A_{J\text{-}C}$, $B_{J\text{-}C}$, $n_{J\text{-}C}$, $m_{J\text{-}C}$, and $C_{J\text{-}C}$ are the coefficients of the J-C plasticity model, while $D_{1J\text{-}C} \sim D_{5J\text{-}C}$ are the coefficients of J-C damage initiation model. The values of these coefficients for the Ti-6Al-4V titanium alloy are shown in Table 7. The equations of the damage evolution and the related coefficients (G_f and λ) are the same of the above proposed constitutive model (from equation (18) to equation (20)). They are determined by Cheng et al. [122] using the same data used to determine the coefficients of the proposed damage model.

Table 7: Coefficients of the Johnson-Cook constitutive model for Ti-6Al-4V taken from the work of Cheng et al [122].

Coefficient	$A_{J\text{-}C}$ (MPa)	$B_{J\text{-}C}$ (MPa)	$n_{J\text{-}C}$	$m_{J\text{-}C}$	$C_{J\text{-}C}$	$D_{1J\text{-}C}$	$D_{2J\text{-}C}$	$D_{3J\text{-}C}$	$D_{4J\text{-}C}$	$D_{5J\text{-}C}$
Value	812	844	0.261	1.0	0.015	0.245	0.081	-1.276	-0.028	3.87

3.1.5 Flowchart of subroutine development

Using ABAQUS/Explicit solver, in order to realize the development of constitutive model considering stress

state on this platform, it is necessary to extract the stress state of nodes under each work step in the calculation process, and solve the stress triaxiality and Lode Angle, and apply it to the stress solving subroutine. In this subroutine development, VUHARD and VUSDFLD subroutines are used jointly to realize the implementation. The key parameters used in reading and writing parameters of the subroutine on the ABAQUS platform are shown in Table 8. Variables such as stress state are stored, transmitted, updated and outputted by user-defined variables. By solving and updating yield stress, hardening rate related to strain, temperature and strain rate, the stress state of the material can be updated, and then the whole cutting process can be solved.

Table 8: Types and purposes of main parameters used in VUHARD and VUSDFLD subroutines.

Subroutine	Types	Purpose of main parameters
VUSDFLD	Read-Only （Read from ABAQUS）	**stateOld**：User-defined state variables for the last incremental step **vgetvrm**：Obtain the node variable under the current time increment step
	Write-Only （Write into ABAQUS）	**stateNew**：User-defined state variables under the current time increment step **field**：Field variable under the current time increment step
VUHARD	Read-Only （Read from ABAQUS）	**props**：User-defined material properties **tempOld**：Temperature of the last incremental step **stateOld**：User-defined state variables for the last incremental step **eqps**：Equivalent plastic strain under current time increment step **eqpsRate**：Equivalent plastic strain rate at current time increment step
	Write-Only （Write into ABAQUS）	**yield**：Yield stress at current time increment step **dyieldDtemp**：Derivative of yield stress with respect to temperature at current time increment step **dyieldDeqps**：Derivative of yield stress with respect to strain and strain rate at current time increment step **stateNew**：User-defined state variables under the current time increment step

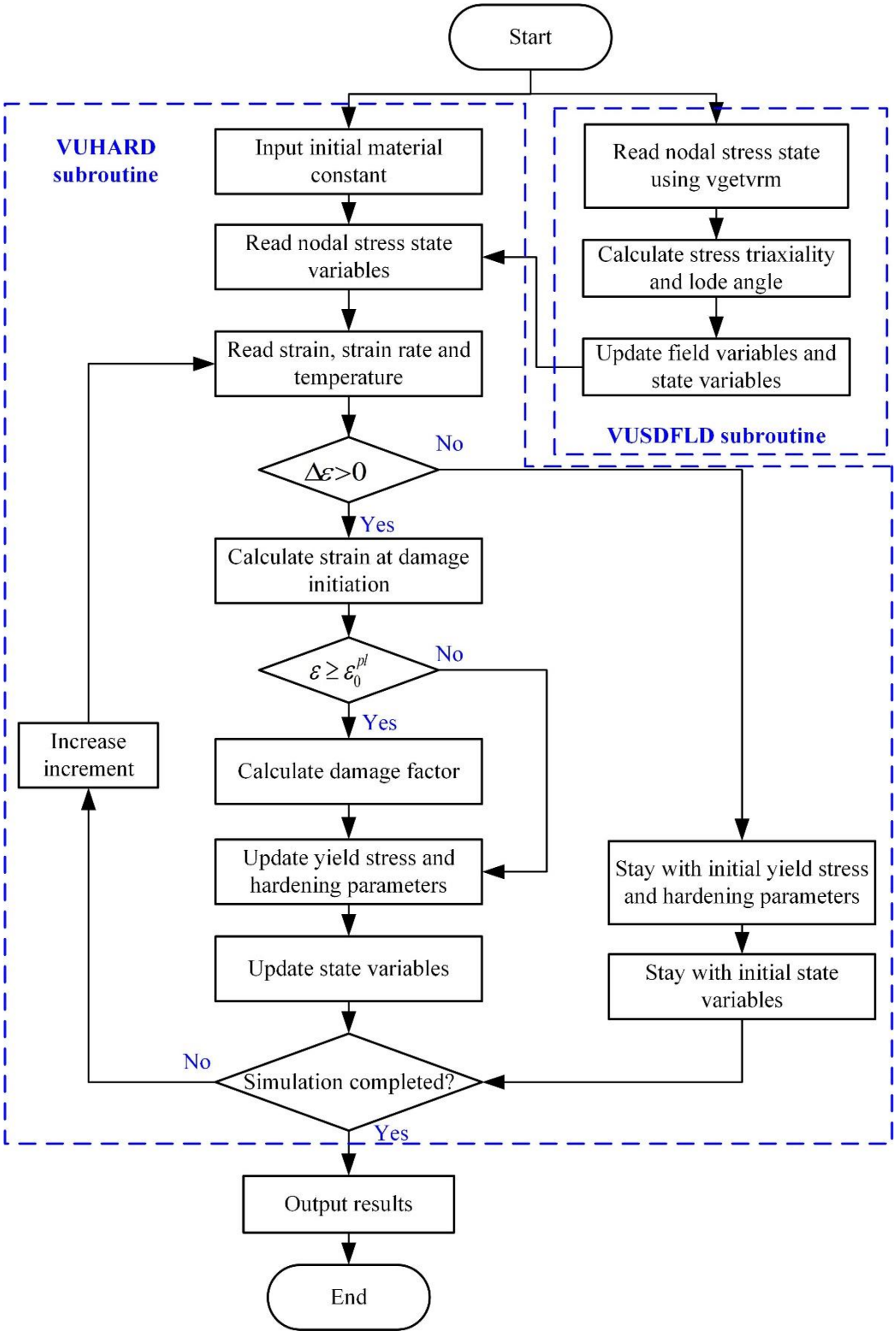

Fig. 22 Subroutine development and flow chart of constitutive model considering stress state.

The mechanical behavior of materials (including plastic yield stress and fracture damage evolution) is calculated based on the stress state parameters of materials and the judgment of critical conditions. Therefore,

in the form of user-defined variables, the initial stress state is stored, transmitted and updated in the form of field variables and the stress triaxiality and Lode Angle obtained based on this calculation are stored, transmitted and updated in the form of user-defined variables (SDV). It is important to note that due to the follow-up of this article is to build artifacts material model, using the Lagrangian and Eulerian grid, in the artifact damage fracture description, when the Lagrangian mesh stiffness damage reaches 1, to describe the material fracture behavior of the grid are deleted, and the characteristics of Euler grid because it could not be deleted, the material stiffness damage factor should be set as 0.99 to avoid convergence of numerical calculation. The process of constitutive model subroutine development and calculation is shown in Fig. 22. Firstly, VUSDFLD is used to read the node stress components of the cutting model, and the stress triaxiality and Lode Angle are calculated, and the calculated results are transmitted to VUHARD subroutine through field variables and state variables. Secondly, through input the initial material model parameters, read the current step analysis of strain, temperature and strain rate values of plastic strain increment as the conditions for determining whether to enter fracture damage calculation program, finally according to whether the hardening, whether into damage to enter different update yield stress, hardening parameters and state variables, Until the end of the simulation and output the calculation results.

3.2 Design and setup of orthogonal cutting tests for cutting models validation

To validate the developed FE model using CEL approach in chapter 2 and the multiscale model for microstructure evolution in chapter 3 and chapter 4, a five-axis DMG MORI milling center, model DMU 50, was used to carry out the orthogonal cutting tests, as milling operation is a better way to obtain high cutting speed than other operations. As shown in Fig. 23, the thickness and width of workpiece were 3mm and 20 mm, respectively. The diameter of the face milling cutter was 80 mm and up milling was used to conduct high speeds orthogonal cutting. A feed per tooth of 0.1 mm/z was applied and the axis of the cutter was parallel to the left edge of workpiece. Uncoated cemented carbide inserts (Sandvik N 331.1A) having the same geometry of FE model were used. Tool geometry in the tool-in-hand system according to the ISO standard 3002-1:1982/AMD 1:1992 was carefully inspected using an Alicona InfiniteFocusSL microscope. This geometry is represented by a rake angle (γ) of 0°±0.30°, a clearance angle (α) of 15°±0.23°, and a cutting edge radius (r_n) of 10 μm±1.2 μm. To ensure that tool wear was not affecting the machining tests results, the total cutting length was reduced (100 mm) and new tool cutting edges were used at each test. Cutting forces were measured using Kistler dynamometer, model 9265B.

The uncut chip thickness (h) was kept constant and equal to 0.1 mm, while the cutting speed (V_c) was varied

from 50 m/min to 500 m/min to investigate the effect of cutting speeds on the chip geometry, cutting force, microstructure and surface roughness. The cutting conditions are summarized in Table 8. Dry conditions are applied in all the tests. Samples containing several chips are prepared for observing at the optical microscope to measure their geometries. All samples are prepared by grinding, polishing, and etching with 1 ml HF + 6 ml HNO_3 + 193 ml H_2O solution and observed under an optical microscope and SEM. Cross-section samples in shear band of chips were prepared by using Focused Ion Beam (FIB). The FEI Tecnai G2 F20 S-TWIN microscope at 200 KV was adopted to conduct TEM and PED testing.

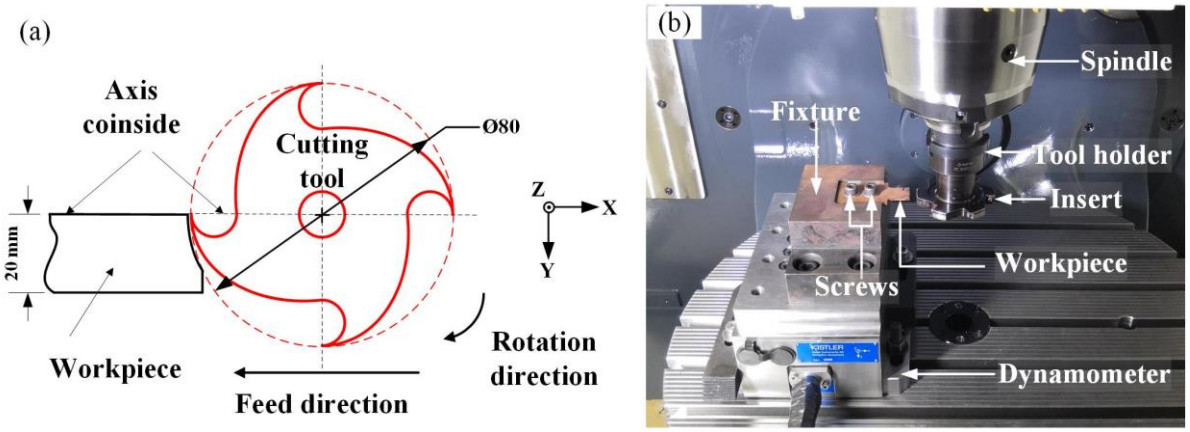

Fig. 23: Experimental tests using CNC milling machine: (a) schematic representation of orthogonal cutting configuration, and (b) experimental setup.

Table 9 Cutting conditions for orthogonal cutting of Ti-6Al-4V alloy using CNC milling machine.

Cutting condition (case number)	Cutting tool	Cutting speed (m/min)	Uncut chip thickness (mm)	Analysis
No.C1	WC-Co	50	0.1	Chip geometry, Microstructure, Surface roughness
No.C2	$\gamma = 0° \pm 0.30°$	125	0.1	
No.C3	$\alpha = 15° \pm 0.23°$	250	0.1	
No.C4	$r_n = 10 \pm 1.2$ µm	500	0.1	

3.3 Cutting modelling using Lagrangian and coupled Eulerian and Lagrangian (CEL) approaches

3.3.1 Description of orthogonal cutting models

Orthogonal cutting models of HSM of Ti-6Al-4V titanium alloy are developed and simulated by FEM using the (CEL) and Lagrangian approaches, available in ABAQUS/Explicit software. Fig. 24 shows the orthogonal cutting model using the CEL approach, which can only be used for 3D simulations [154]. This

3D model has an extremely small width of cut (only 4 µm) when compared to the workpiece length and height (hereby called CEL1 model). In this model, the tool is described by the Lagrangian approach while the workpiece is described by the Eulerian one. Eulerian Volume Fraction (EVF) plays an important role in CEL simulations, so it will be tracked to measure the ratio of material inside the element. Fig. 24a shows the initial state of the model, where the blue color of elements means that they are filled with material (EVF = 1), while the red colored elements are empty (EVF ≈ 0).

Because the displacement of the Eulerian element cannot be constrained, a zero-velocity boundary condition will be used. As shown in Fig. 24b, the workpiece movement is constrained in the vertical (the Y-direction) and horizontal (the X-direction) by applying the zero-velocity boundary condition at the bottom and right-side surfaces of the model. The tool is constrained to have zero displacements along the Y-direction and the velocity equal to the cutting speed in the positive X-direction. To avoid the material flow out of the Eulerian region, the zero velocity boundary condition is applied in front and back surfaces of the model in the Z-direction. The Lagrangian region (tool) is in contact with Eulerian one (workpiece) inside the Eulerian mesh [17,154].

The workpiece, including both void and material regions, is meshed using the 8-node thermo-mechanical coupled linear Eulerian brick elements (EC3D8RT) with reduced integration and hourglass control features. The tool is meshed as the 8-node linear thermo-mechanical coupled brick elements (C3D8RT). The cutting time and cutting length need to be determined carefully to make sure that the material flow is all inside the Eulerian mesh boundaries for all the cutting conditions.

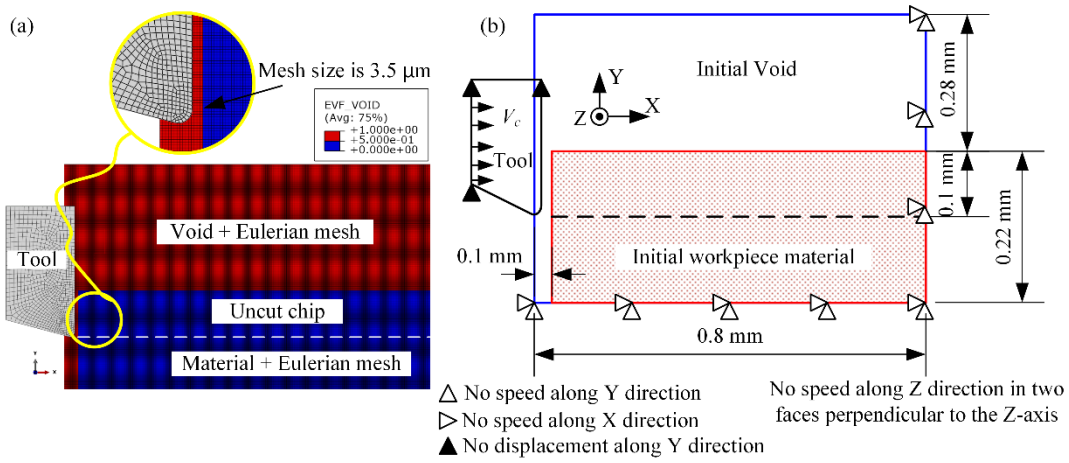

Fig. 24: Orthogonal cutting model having an extremely small width of cut (only 4 µm) using the CEL approach (CEL1 model): (a) boundary conditions and (b) mesh.

The element size and element orientation of the workpiece directly determine the convergence of the calculation process and has a great impact on the results. To balance the accuracy and efficiency of the simulation, the effect of the element size and element orientation angle on simulation results will be investigated. Besides that, the element size of the tool in the tool-chip contact zone is chosen to be similar to the workpiece. Initial homogeneous temperature distribution of 20°C is applied to the workpiece and tool.

Since only 3D models can be developed using CEL approach [154], the calculation time is higher compared to the traditional 2D models using Lagrangian or ALE approaches. For this reason, the previous orthogonal cutting model using CEL approach uses an extremely small width of cut (only 4 μm) to minimize this calculation time. However, very small with of cut does not allow the material to flow freely in the Z-direction, thus it cannot reproduce the lateral burr formation and a larger chip width used in orthogonal cutting tests of several work materials [155,156]. Therefore, a second 3D orthogonal cutting model with a larger width of cut equal to 3 mm is proposed (hereby called CEL2 model). To reduce the computation time, a symmetry plane perpendicular to the Z-direction is applied, thus the width of the workpiece is equal to 1.5 mm. This model is shown in Fig. 25, where a volume of void having 0.5 mm of width is used in the back side of the workpiece to allow material side flow freely in the Z-direction. The workpiece movement is constrained in the vertical (Y- direction) and horizontal (X-direction) by applying a zero-velocity boundary condition at the bottom and right surfaces of the model. The workpiece including the void and material regions is meshed using the 8-node thermo-mechanical coupled linear Eulerian brick elements (EC3D8RT) with reduced integration and hourglass control features. The tool is meshed as the 8-node linear thermo-mechanical coupled brick elements (C3D8RT). According to Liu et al. [157], the stress and strain distributions are uniform in the interior of the chip/machined part, while in the border (the interface between the material and the void in the CEL model) these distributions changes significantly. Pednekar et al. [158] show that, when the ratio between the width of cut and the uncut chip thickness reaches a critical value of 20, more than 90% of the chip width can undergo plane strain conditions. The model shows in Fig. 25 has a ratio of 30, so most of the workpiece is in plane strain conditions. Therefore, a coarser element size in the interior of the workpiece does not reduce the simulation accuracy and increases the calculation efficiency. The element size of this model in the XY plane is 3.5 μm (the same as in the CEL1 model), while this size in Z-direction ranges from 3.5 μm to 100 μm (finer mesh near the interface between the material and the void, and coarser mesh in the other zones).

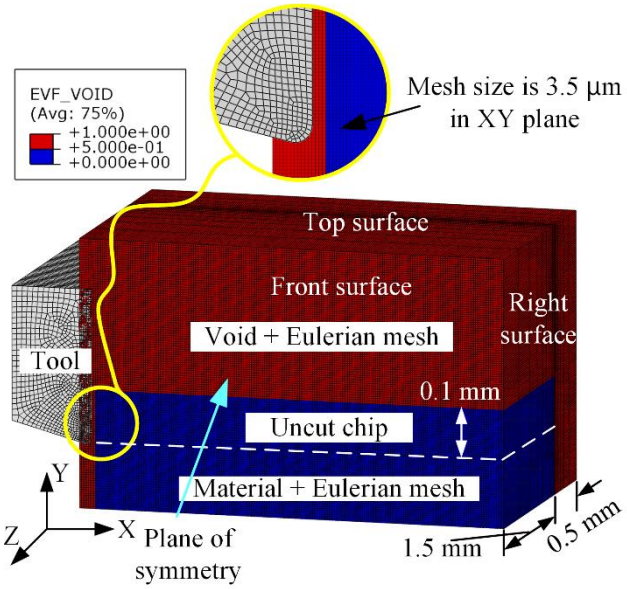

Fig. 25: Orthogonal cutting model having a larger width of cut (3 mm) using the CEL approach (CEL2 model).

Finally, a 2D model of orthogonal cutting using the Lagrangian approach is also developed (hereby called LAG model), as shown in Fig. 26. This figure shows the workpiece composed by the uncut chip layer, sacrificial layer, and remaining part of the workpiece. The workpiece is meshed using the planar quadrilateral continuum elements (CPE4RT) with four-node, plane strain, with reduced integration features suitable for large deformation analysis. The tool is meshed as three-node linear displacement and temperature elements (CPE3T) with plane strain features. The element sizes in the uncut chip and sacrificial layers are determined by a sensitivity analysis on the influence of this parameter in the forces and chip geometry. The obtained values are 5 µm and 2.5 µm, respectively. The bottom of the workpiece is fixed and the tool is moving along the X-direction only, from right to left at a constant cutting speed. Besides that, element size of the tool in the tool-chip contact zone is set less than that of the workpiece.

The geometry of finite elements used in the CEL simulations (element size and its orientation/shape) was determined based on the sensitive analysis of the influence of this geometry on the forces and chip geometry. This analysis is presented and discussed in section 3.3.2. Similar study was already conducted by the authors using the Lagrangian approach [159].

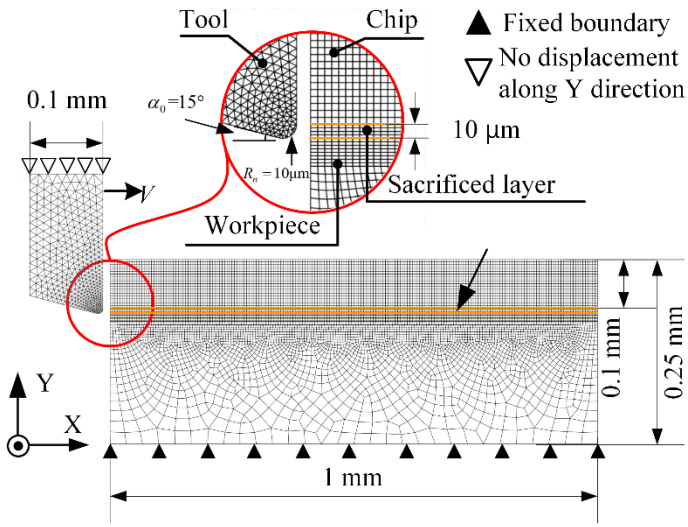

Fig. 26: Mesh and boundary conditions of 2D orthogonal cutting model using Lagrangian approach (LAG model).

Cutting conditions, contact model, material properties and constitutive model are the same for the three models. Four values of the cutting speed were used: 50, 125, 250 and 500 m/min. The uncut chip thickness and width of cut are set constant equal to 0.1 mm and 3 mm, respectively. The physical, thermal, and elastic properties of the work material are shown in Table 10. Uncoated cemented carbide (WC-Co) cutting tools are used, and the corresponding physical, thermal, and elastic properties are given in Table 10. Tool geometry is represented by the rake angle of 0°, a clearance angle of 15°, and cutting edge radius of 10 µm. In machining practice, the maximum recommended cutting speed for machining of Ti-6Al-4V titanium alloy using a cemented carbide tool is about 120 m/min.

Table 10: Physical, thermal, and elastic properties of the work and tool materials [160–163].

Material	Density (kg m^{-3})	Elastic modulus (GPa)	Poisson's ratio	Specific heat (J $kg^{-1}K^{-1}$)	Thermal conductivity (W $m^{-1}K^{-1}$)	Expansion (K^{-1})
WC-Co	11900	534	0.22	400	50	-
Ti-6Al-4V	4430	109	0.34	611	6.8	1E-5

For higher cutting speed such as those speeds used in this research work, polycrystalline diamond (PCD) is the suitable tool material for machining of Ti-6Al-4V titanium alloy. However, uncoated cemented carbide

tools are used in the present study, keeping the cutting length extremely short and one cutting edge per tests, to avoid tool wear effects on the results.

As far as the tool-chip contact is concerned, Zorev's model [164] is used, which considers two contact regions: i) a plastic region near the cutting edge, with a limit shear stress equal to the yield shear stress of the chip material, and; ii) a sliding region near the end of the tool-chip contact, where the tangential contact stress τ_f is proportional to the normal stress σ_n at the tool-chip interface. Zorev's model can be represented by the following equation:

$$\tau_f = \begin{cases} \tau_Y & if \quad \mu\sigma_n \geq \tau_Y \quad (plastic \text{ region}) \\ \mu\sigma_n & if \quad \mu\sigma_n < \tau_Y \quad (sliding \text{ region}) \end{cases} \tag{23}$$

where μ is the coulomb's friction coefficient, and τ_Y is the yield shear stress of the work material. Yield shear stress can be correlated with the yield stress using for instance the Von Mises criterion, thus $\tau_Y = \sigma_Y / \sqrt{3}$ under various state of stress. The friction coefficient depends on the contact conditions, including the temperature, contact pressure, and sliding speed. Courbon et al. [165] showed that the friction coefficient between the Ti-6Al-4V alloy and the cemented carbide tool depends mainly on the sliding speed, and can be given by the following equation:

$$\mu = 0.48 \times V_s^{-0.1904} \tag{24}$$

where V_s is the sliding speed of the chip over the tool. The thermal conductance in the tool-workpiece contact interface is equal to 1000 kW/(m^{2}K) according to Sima and Ozel [118].

3.3.2 Element sensitivity analysis

In this section, simulations using the proposed constitutive model and the CEL approach (the CEL1 model) are conducted to determine the influence of the geometry of the finite element (the element size and its orientation/shape) on the results. This step is essential to determine a suitable element geometry for further CEL simulations.

(1) Influence of the CEL element size on the results

Due to the existence of Eulerian elements with the void in the Eulerian approach, the same computational space requires more elements when compared to the Lagrangian one, which takes more computing time for every incremental step. Besides, it can be deduced from Eq. (18) that the plastic strain at damage evolution

depends on the characteristic length of the element, L. So, a decrease of the element size can lead to an unexpected increase of plastic strain. Therefore, the key point is the determination of the element size which ensures an accurate prediction without significantly penalize the calculation efficiency.

A square element is used, and the element size are varied from 10 µm to 2.5 µm. The simulated chip morphology and equivalent plastic strain distribution with different element sizes are presented in Fig. 27.

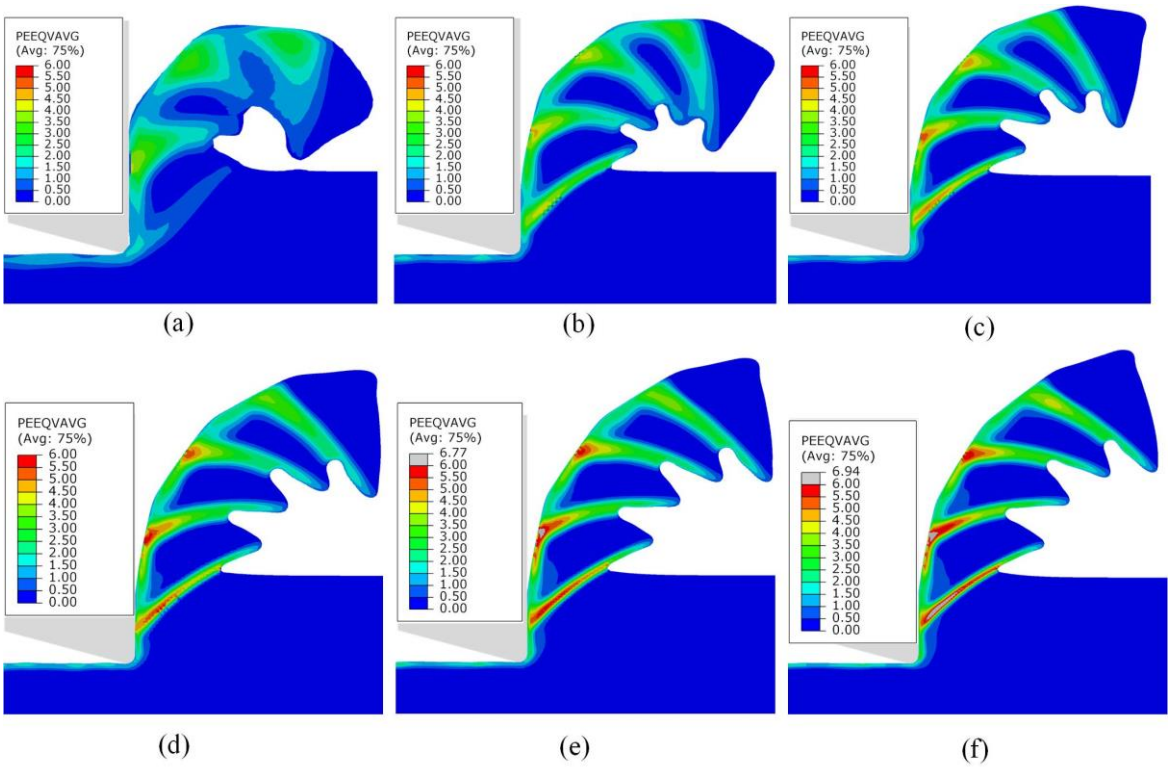

Fig. 27: Chip morphology and distribution of the equivalent plastic strain (PEEQVAVG) obtained using CEL approached with element size of (a) 10 µm, (b) 5 µm, (c) 4 µm, (d) 3.5 µm, (e) 3 µm and (f) 2.5 µm (cutting speed of 250 m/min).

As shown in Fig. 27a, when the element size is 10 µm, the chip morphology is almost continuous, while experimentally the chips are serrated as shown in Fig. 36i. When the element size is reduced to 5 µm (Fig. 27b), the chip morphology become serrated, but its geometry is still far from that observed experimentally. Only when the element size is reduced to 3.5 µm (Fig. 27d), the serrated chip morphology becomes close to the experimentally obtained geometry. To quantitatively investigate the influence of the element size on the simulated chip geometry, the chip geometry parameters (peak, valley and spacing) obtained by CEL simulation for several element sizes and experimentally are shown in Fig. 28. The differences between

CEL simulations with different element size and experimentally is presented in Table 5.

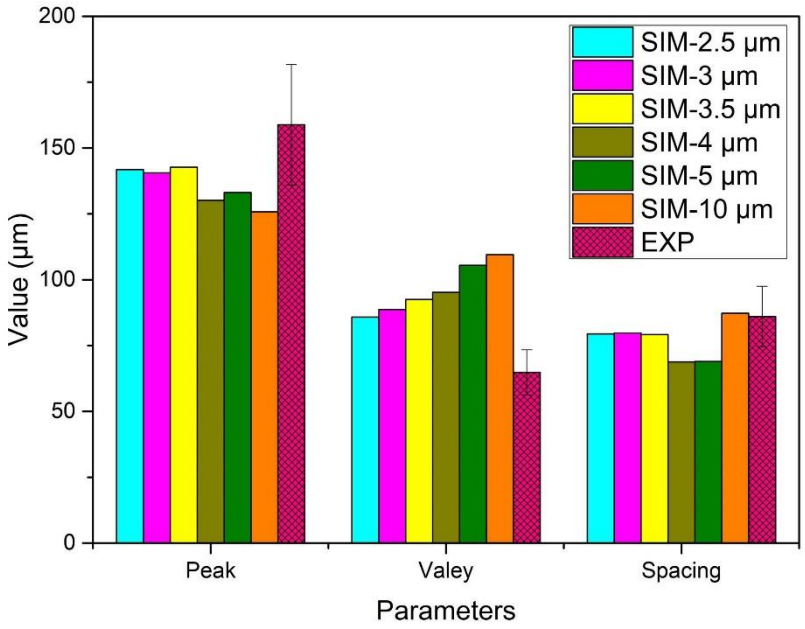

Fig. 28: Chip geometry obtained by CEL simulations for several element sizes and experimentally (cutting speed of 250 m/min).

Table 11: Differences in chip geometry between CEL simulations with different element size and experimentally (cutting speed of 250 m/min).

Element size	10 µm			5 µm			4 µm		
Difference	Peak	Valley	Spacing	Peak	Valley	Spacing	Peak	Valley	Spacing
	23.2%	62.2%	9.7%	18.7%	56.3%	28.6%	20.5%	41%	28.8%
Element size	3.5 µm			3 µm			2.5 µm		
Difference	Peak	Valley	Spacing	Peak	Valley	Spacing	Peak	Valley	Spacing
	12.8%	37%	18%	14.1%	31.4%	17.4%	13.4%	27.1%	17.8%

From Fig. 28 and Table 5, it can be deduced that when the element size decreases from 4 µm to 3.5 µm, the difference between simulated and experimental chip geometry reduces from: 20.5% to 12.8% for the peak; 41% to 37% for the valley; and 28.8% to 18% for the spacing. Further reduction of the element size to 3 µm (Fig. 27e) and even further to 2.5 µm (Fig. 27f) do not improve the simulation results, since it does not affect the chip geometry significantly, and the plastic strain in the shear band unreasonable increases.

The predicted cutting force vs. time is plotted in Fig. 29 for different element sizes. This figure puts in evidence the influence of the cyclic nature of the chip formation in the forces. These forces are not constant, but they vary cyclically along the chip formation process [166].

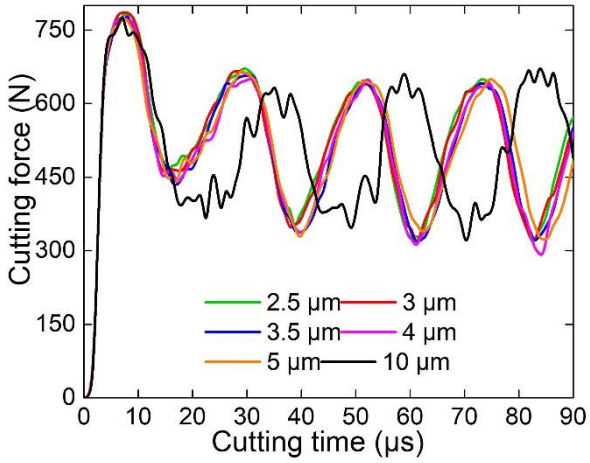

Fig. 29: Cutting force in function of the time for different element size used in CEL simulations.

When the element size is 10 μm, the evolution of cutting force is not smooth, which is very different from that obtained using smaller element sizes. However, cutting force does not change when the element size is less than or equal to 5 μm. It can be deduced that the element size of 5 μm for the CEL simulations is small enough to accurately predict the cutting force. Based on this analysis of the chip morphology and cutting force, the element size of 3.5 μm is selected for the CEL simulations in this study, which allows a balance between calculation accuracy and efficiency.

(2) Influence of the CEL element shape/orientation on the results

The element orientation along the direction of the deformation in FDZ is used in several FE simulations of cutting to facilitate the formation of serrated chips, and to reduce element distortion when using the Lagrangian approach [163,167]. Therefore, it is important to determine the suitable element shape/orientation to be used in the FE simulation of cutting using the CEL approach.

To determine the element shape/orientation, the angle between two adjacent edges of the element is used, as shown in Fig. 30. This figure shows the chip morphology and the equivalent plastic strain distribution for the cutting speed of 250 m/min for three angles of elements namely 90°, 60°, and 45°. When the element orientation angle is changed from 90° to 60° and then to 45°, the plastic strain in the chip increases significantly, reaching extremely high values. These phenomena are related to the uniqueness of the CEL approach, in which the plastic strain is calculated based on the Eulerian Volume Fraction (EVF). In addition, according to the Abaqus user's manual [154] the contact between the Lagrangian region and the Eulerian need to be smooth. In the current simulations using the tool rake angle of 0º, when the element orientation

angle is 60° or 45°, the contact between Eulerian and Lagrangian components appears as point contact and acute angle contact, which will cause the calculation distortion of EVF and an abrupt change during the calculation of the plastic strain. In the CEL simulation, the selection of element shape/orientation depends on the boundary conditions and contact geometry. Therefore, elements with an orientation angle of 90° are used in CEL simulations of orthogonal cutting of Ti-6Al-4V using a tool rake angle of 0°.

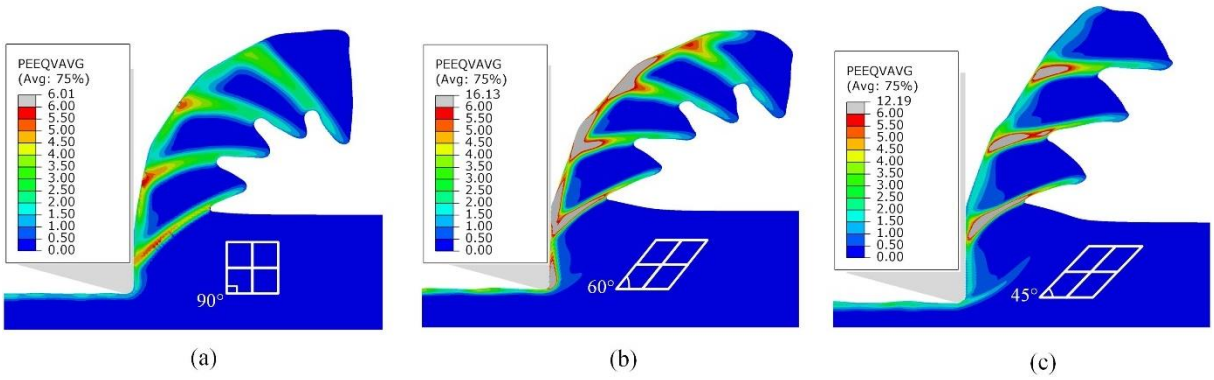

(a) (b) (c)

Fig. 30: Chip morphology and distribution of the equivalent plastic strain (PEEQVAVG) obtained using CEL approach with the element angle of (a) 90°, (b) 60°, and (c) 45° (cutting speed of 250 m/min).

(3) Verification of plane strain conditions for CEL1 model

CEL1 model was developed based on the assumption of plane strain conditions, which need to be verified. The distributions of plastic strain and stress components over the X, Y and Z axes are shown in Fig. 31. As can be seen in Fig. 31 (a), (b) and (c), the plastic strain over the X and Y axes in deformation zone ranges from -1 to 1, while the plastic strain over the Z axis in this zone is approximately zero. Fig. 31 (d), (e) and (f) show that the stress exists over the X, Y and Z axes, especially over the Z axis. This confirms that the 3D CEL1 model is in a plane strain conditions, thus its results can be compared with those obtained by the 2D LAG model, also under plane strain conditions.

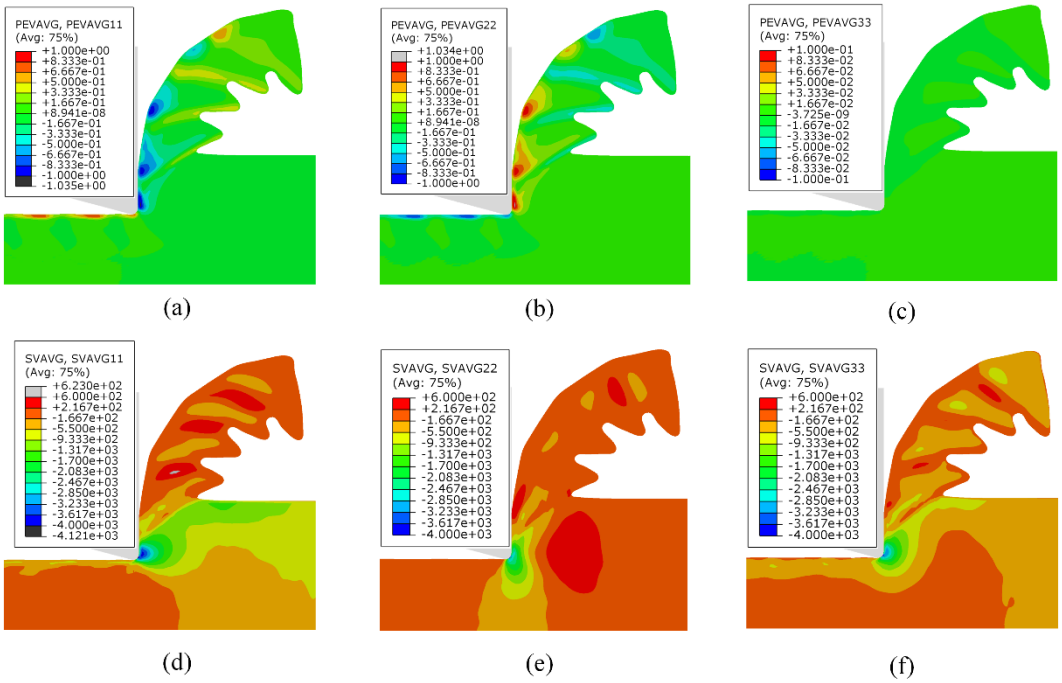

Fig. 31: Plastic strain components ((a) X-axis, (b) Y-axis, and (c) Z-axis) and stress components((d) X-axis, (e) Y-axis, and (f) Z-axis) obtained using CEL1 approach (the cutting speed of 250 m/min).

3.3.3 Comparison between Lagrangian and CEL approaches

Simulations using the proposed constitutive model and CEL approach (CEL1 model) are performed, and the results are compared with those obtained using the Lagrangian approach (LAG model). The previous section compares the state of stress and strain at damage initiation obtained using the CEL approach with the Lagrangian one. To complete this analyses, other more practical machining outcomes should also be compared, including the chip geometry, tool-chip contact length, strain, temperature, and forces.

The simulated chip shape and morphologies using both the CEL (CEL1 model) and Lagrangian (LAG model) approaches are shown in Fig. 33a and Fig. 33b, respectively. Both approaches generate similar chip morphologies but predict different tool-chip contact lengths (0.086 mm for the CEL1 model and 0.176 mm for the LAG model). Fig. 32 shows the simulated tool-chip contact length using CEL1 and LAG models in function of the cutting speed and compares with the tool-chip contact length calculated by Poletica equation [168]. This equation is proposed by Poletica [168] after analyzing the tool-chip contact length for a wide range of work materials and cutting conditions, as it is represented by:

$$l_c = h_1 \cdot \zeta^{k_t} \tag{25}$$

where ζ is the chip compression ratio, h_1 is the uncut chip thickness and $k_t = 1.5$ when $\zeta < 4$, and $k_t = 1.3$ when $\zeta \geq 4$.

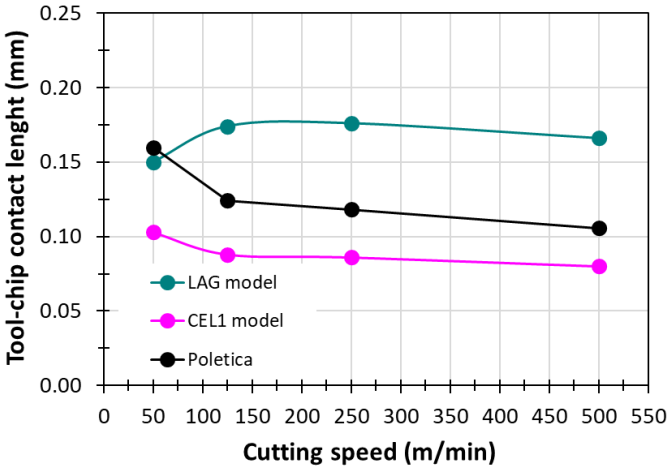

Fig. 32: Simulated tool-chip contact length using CEL1 and LAG models, and comparison with tool-chip contact length calculated by Poletica equation [168].

As shown in this figure, tool-chip contact length in function of the cutting speed obtained by CEL model have the same trend as the tool-chip contact length calculated by Poletica equation. Moreover, when comparing to the LAG model, the tool-chip contact length obtained by CEL model is closer to that calculated by Poletica equation. Since both CEL1 and LAG models used the same input physical data, this is probably due to the different numerical approaches used to simulate the separation of the material from the workpiece. Fig. 33 also shows that many distorted elements are generated near the machined surface and in the chip shear band when the Lagrangian approach is used. This does not happen when the CEL approach is used.

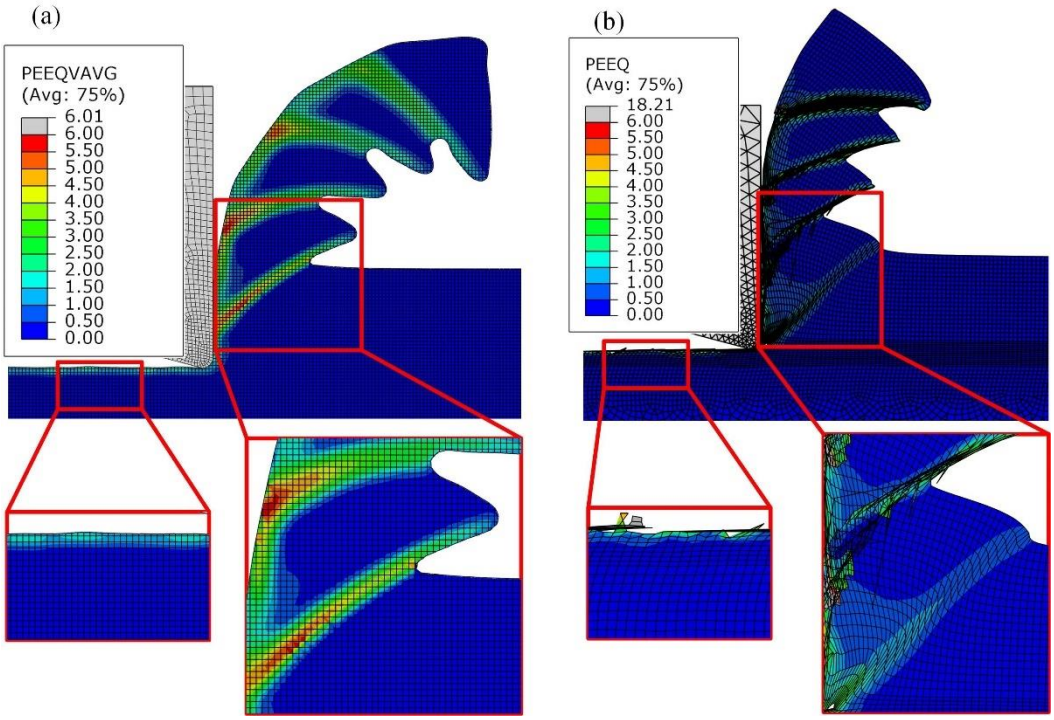

Fig. 33: Chip morphology and distribution of the equivalent plastic strain (PEEQVAVG) obtained using (a) CEL and (b) Lagrangian approaches (cutting speed of 250 m/min).

The distributions of the equivalent plastic strain and temperature in cutting of Ti-6Al-4V alloy, obtained using the CEL and Lagrangian approaches, are shown in Fig. 34. As can be seen in Fig. 34a and Fig. 34b, the CEL approach generates the equivalent plastic strain distribution in the shear band of the chips that gradually decreases from the tool cutting edge zone to the chip free surface, while this distribution is relatively uniform when the Lagrangian approach is used. It can be seen in Fig. 34b that the plastic strain of the distorted elements is extremely high, and thus several elements are deleted too early, which has an influence on the final simulated results. Similar results are observed for the temperature distribution, i.e., the CEL approach (Fig. 34c) generates a high localized temperature at the tool-chip interface on the rake face, which is consistent with experimental data [169]. On the contrary, the Lagrangian approach (Fig. 34d) generates a quasi-uniform temperature in the chip over the tool-chip interface, and a high localized temperature in the chip root near the cutting edge. Since the temperature is associated to the thermal energy generated by plastic deformation and friction, the greater plastic strain in the secondary deformation zone compared to other zones obtained by the CEL approach leads to a higher temperature. In Fig. 34d, the temperature in the chip root near the tool cutting edge radius reaches 800°C when the Lagrangian approach is used, but with the deletion of elements in the sacrificial layer, the temperature drops quickly as the deleted elements are no longer

involved in the calculation. Besides that, the existence of several elements with extremely high temperatures can lead to a misinterpretation of simulation results.

The cutting forces obtained using both CEL and Lagrangian approaches are plotted in Fig. 35. Both cutting forces vary cyclically in function of the cutting time. However, when the Lagrangian approach is used, this cyclic variation shows small fluctuations, compared to those when CEL approach is used. These fluctuations in the Lagrangian approach are not related to the cutting process itself, but to the element distortion and element deletion in the sacrificed layer.

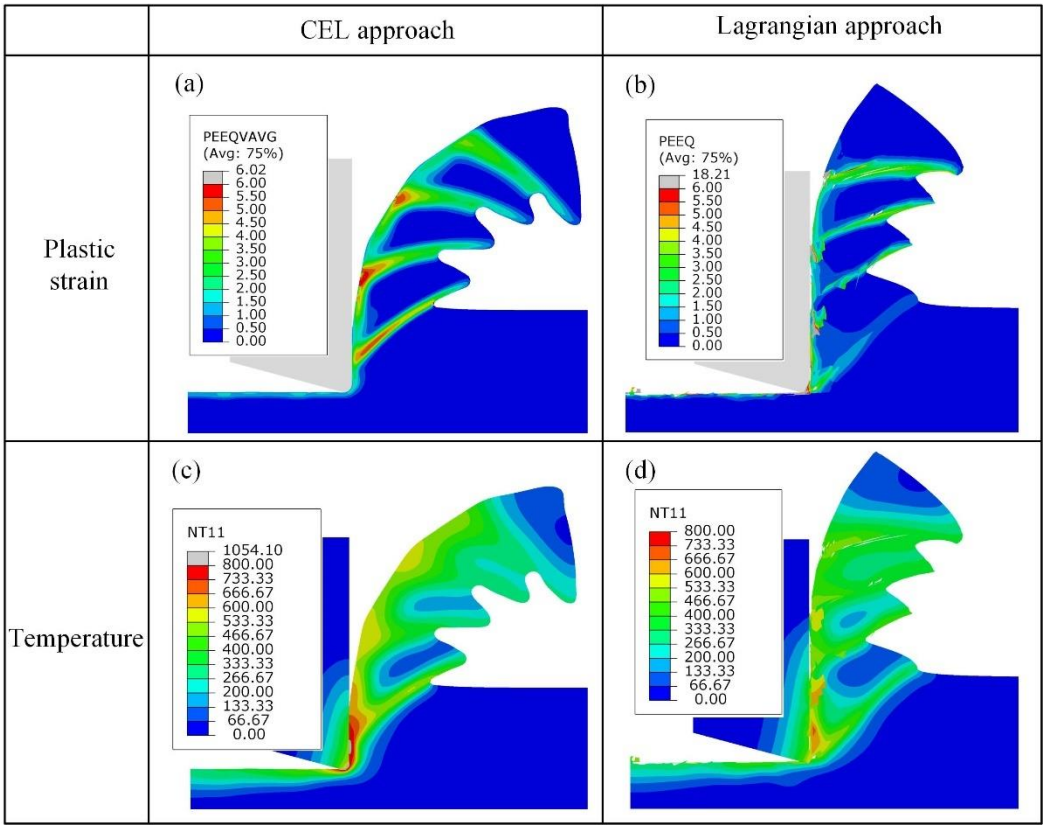

Fig. 34: Distributions of the equivalent plastic strain ((a) and (b)) and temperature ((c) and (d)) obtained using CEL (CEL1 model) ((a) and (c)) and Lagrangian (LAG model) ((b) and (d)) approaches (cutting speed of 250 m/min).

Element distortion generated by the Lagrangian approach can results in an incorrect calculation of the nodal forces and displacements [98]. Moreover, element deletion (element will no longer participate in the calculation) causes a discontinuity in the calculated stress, strain, and temperature fields. This can significantly affect the predicted results, in particular the surface integrity of the machined surface. This is

because the thickness of the layer affected by machining in the workpiece can be shallow (in this work is about 10~25 μm), so that if there are a large number of distorted elements in this thickness, the extraction and interpretation of the results become very difficult. Therefore, the cutting model including the CEL approach combined with the proposed constitutive model has great advantages in machining simulation of Ti-6Al-4V titanium alloy since it avoids element distortion, thus can better predict the serrated chip geometry, forces, and plastic strain.

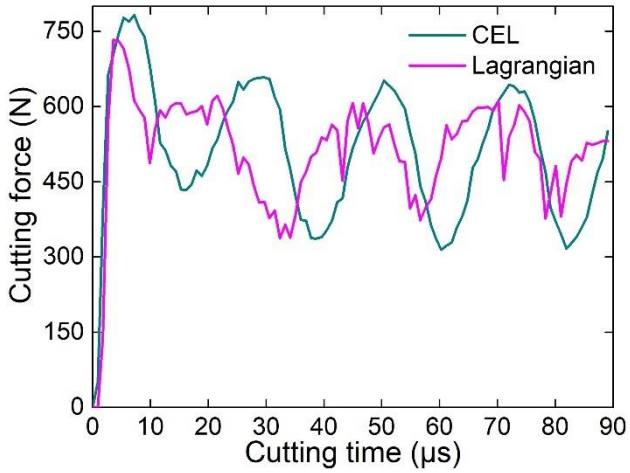

Fig. 35: Cutting force in function of the time obtained by CEL and Lagrangian approaches (cutting speed of 250 m/min).

The durations of the calculations of these three proposed models were obtained for the same cutting conditions, corresponding to the cutting speed of 250 m/min and using the same computation environment. The results show that CEL2 model needed 23.4 hours to complete the simulation, while CEL1 just needed 2.6 hours and LAG – 1.7 hours. Although the CEL2 is closer to the actual cutting process, the long time, and thus high computation cost is the major inconvenient. It is worth noting that the computation cost of CEL2 model can be reduced by decreasing the total number of elements. Thus, a mesh optimization is required to decrease the computation cost without compromising the accuracy of the simulated results. From the computation efficiency perspective, CEL1 model is preferred due to the low computation cost, but it should be used with cautions under the assumption of plane strain condition.

3.4 Analysis of chip formation mechanism and surface generation

3.4.1 Comparison between the proposed constitutive model and the Johnson-Cook model

To verify the accuracy of the cutting model using the CEL approach (CEL1) together with the proposed

constitutive model, the predicted and measured cutting force and chip morphology are compared for several cutting speeds. Fig. 36 shows the experimental and simulated chip morphology using J-C and the proposed constitutive models obtained varying the cutting speeds from 50 m/min to 500 m/min.

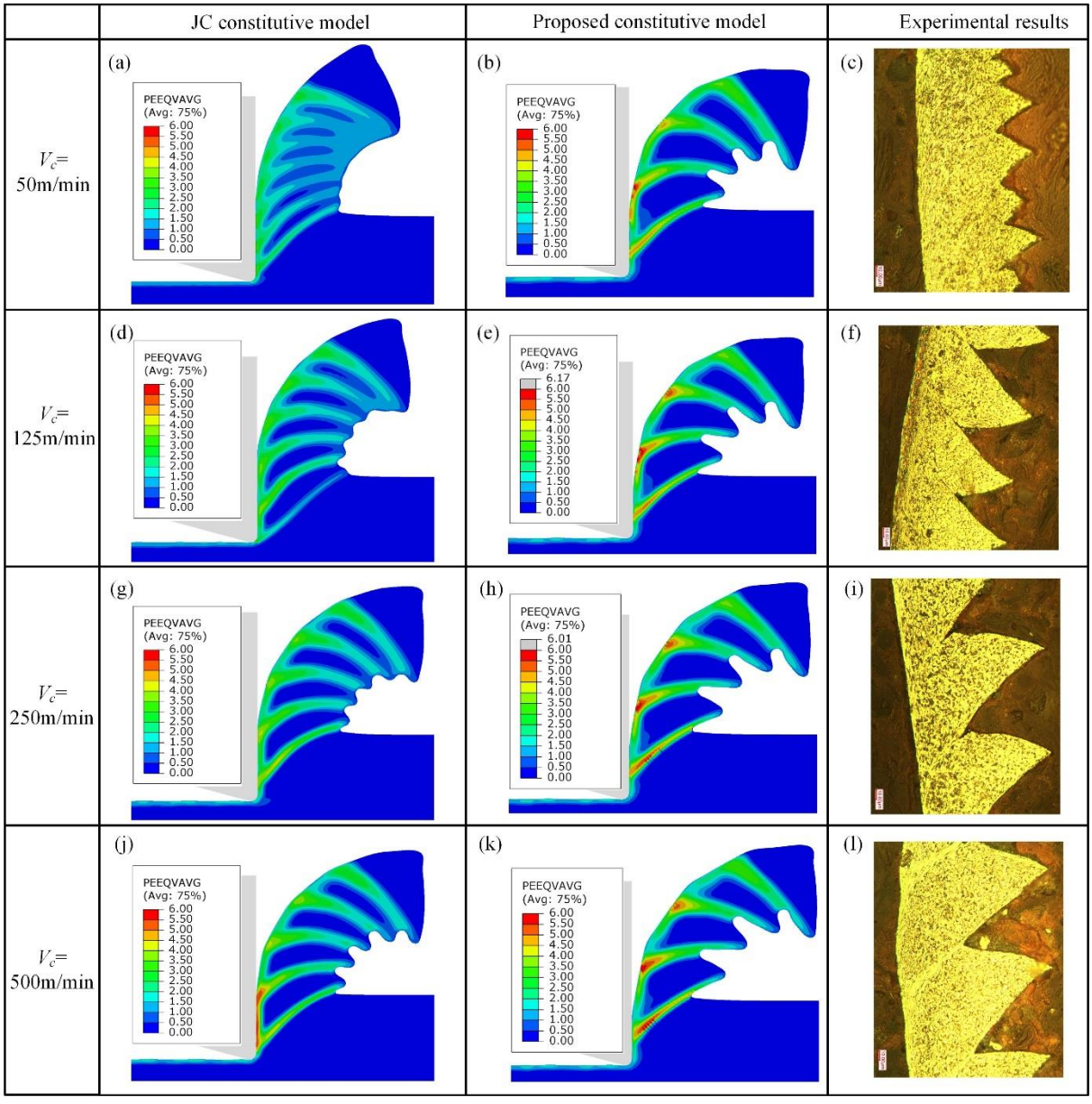

Fig. 36: Simulated chip morphology and distribution of the equivalent plastic strain (PEEQVAVG) obtained using CEL approach, using the Johnson-Cook and the proposed constitutive models at several cutting speeds (50, 125, 250 and 500 m/min). Experimental chip morphology.

The J-C model generates a chip morphology almost continuous, and it does not change significantly with the cutting speed, being quite different from the chip morphology observed experimentally. Shear localization in

the chip gradually increases with the cutting speed. Moreover, the serrated chips are observed using the proposed constitutive model, and the chip geometry changes significantly with the cutting speed. It can be deduced from Fig. 36 that the chip morphology predicted by the proposed constitutive model is closer to the experimental one when compared to the chip morphology predicted by the J-C constitutive model. To compare the chip geometry obtained by CEL simulations and experimentally, the geometric characteristics of the serrated chips are presented. The chip peak, valley, and spacing (see Fig. 37) are measured and the obtained results are shown in Fig. 38 and listed in Table 12. If was found that the differences between simulated and experimental values of the peak and spacing are within the range of the experimental error. It can also be seen that the differences between simulated and measured values of the valley are a bit higher, in particular for the cutting speeds of 250 m/min and 500 m/min.

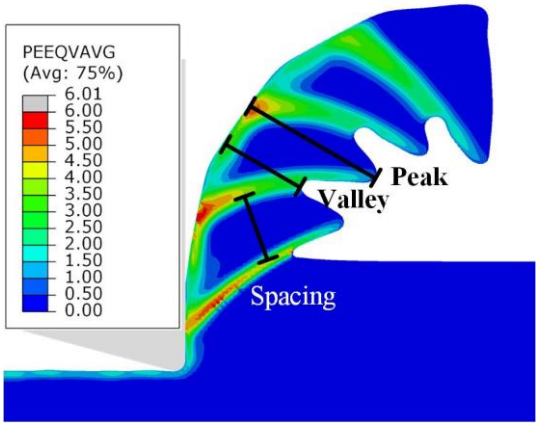

Fig. 37: Distribution of the equivalent plastic strain (PEEQVAVG) and parameters of chip geometry obtained using CEL approach (cutting speed of 250 m/min).

Table 12: Chip geometry differences between CEL simulated and experimentally obtained chips for several cutting speeds.

Cutting speed	50 m/min			125 m/min		
Difference	Peak	Valley	Spacing	Peak	Valley	Spacing
	4.3%	14.2%	9.8%	10.4%	20%	16.8%
Cutting speed	250m/min			500m/min		
Difference	Peak	Valley	Spacing	Peak	Valley	Spacing
	12.7%	36.6%	19.1%	6.7%	38.3%	12%

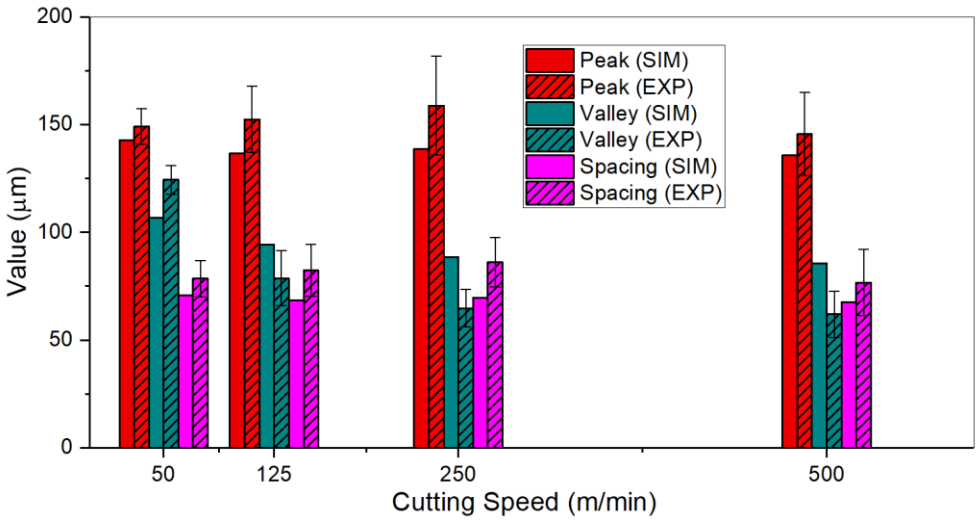

Fig. 38: Chip geometry obtained by CEL simulations and experimentally for several cutting speeds.

Fig. 39 shows the evolution of the cutting force as a function of time obtained by CEL simulations using both J-C and the proposed constitutive model at the cutting speed of 250 m/min. The amplitude and frequency of the cutting force are related to the cyclic nature of chip formation. As can be seen, the amplitude of the cutting force generated using the J-C constitutive model is smaller than that of the proposed one, while the opposite is true for the frequency. As far as the average cutting force is concerned, The J-C constitutive model generates higher force compared to the proposed constitutive model and the experimental results (see also Table 13). Moreover, the proposed constitutive model generates an average cutting force close to that obtained experimentally.

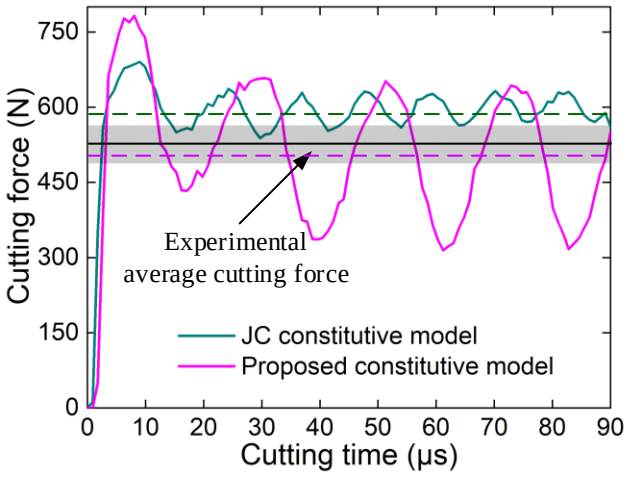

Fig. 39: Simulated cutting force as a function of the time obtained using both J-C (green) and the proposed (magenta) constitutive model (cutting speed of 250 m/min), and the comparison with the average cutting force (black line with gray region indicating the standard deviation).

Table 13: Comparison between simulated and experimental cutting force

Cutting Speed (m/min)	Simulated force F_t (N)	Experimental force F_t (N)	Difference (%)
	Average	Average	
50 m/min	519.5	541.4±20.9	4%
125 m/min	505.1	523.2±25.3	3.5%
250 m/min	493.8	512.1±24.7	3.6%
500 m/min	474.2	480.6±32.1	1.2%

Therefore, the proposed constitutive model is more accurate than the J-C model in the prediction of chip geometry and cutting force during HSM of Ti-6Al-4V alloy. Fig. 40 and Fig. 41 can be used to explain the reasons for the better predictability of the proposed constitutive model. Fig. 40 shows the simulated distributions of the equivalent plastic strain (PEEQVAVG) and von Mises stress (SVAVG) using the CEL approach (CEL1 model), for both the J-C and the proposed constitutive model.

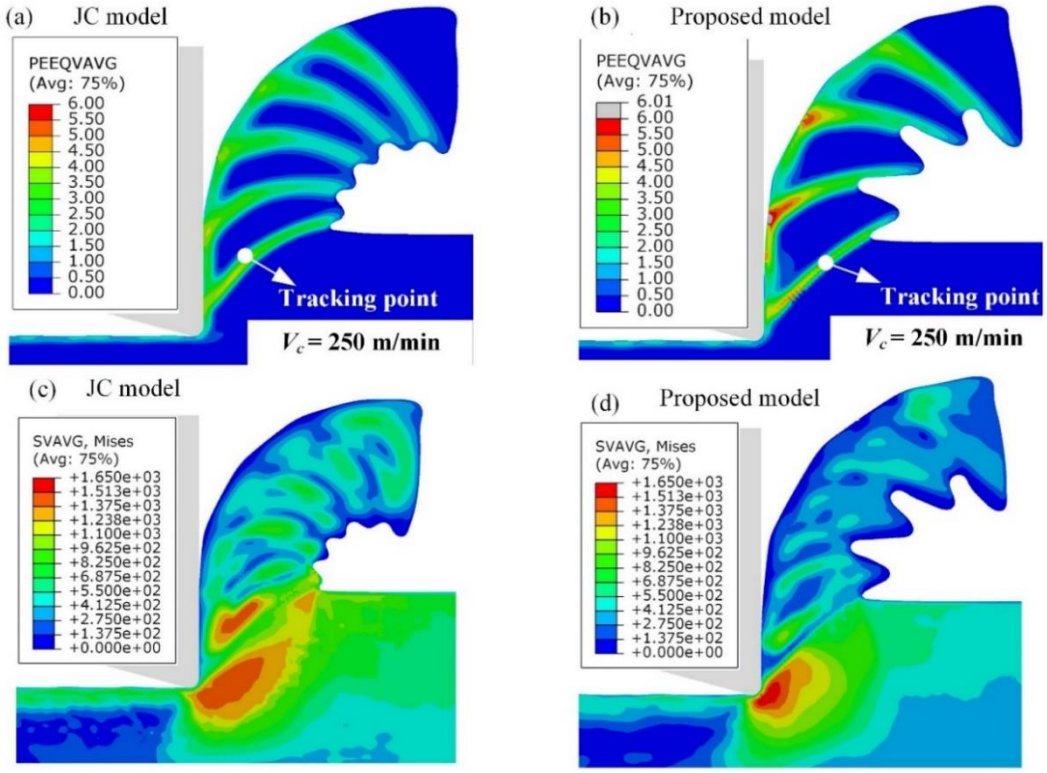

Fig. 40: Results of CEL simulations: (a) Plastic strain distribution using J-C constitutive model, (b) plastic strain distribution using the proposed constitutive model, (c) von Mises stress distribution using J-C constitutive model, (d) von Mises stress distribution using the proposed constitutive model.

Fig. 41a and Fig. 41b show the von Mises stress as a function of the plastic strain for a tracking point in the

middle of the shear band of FDZ (see Fig. 40a and Fig. 40b) obtained using the CEL approach with the J-C model and the proposed constitutive model at the cutting speed of 250 m/min.

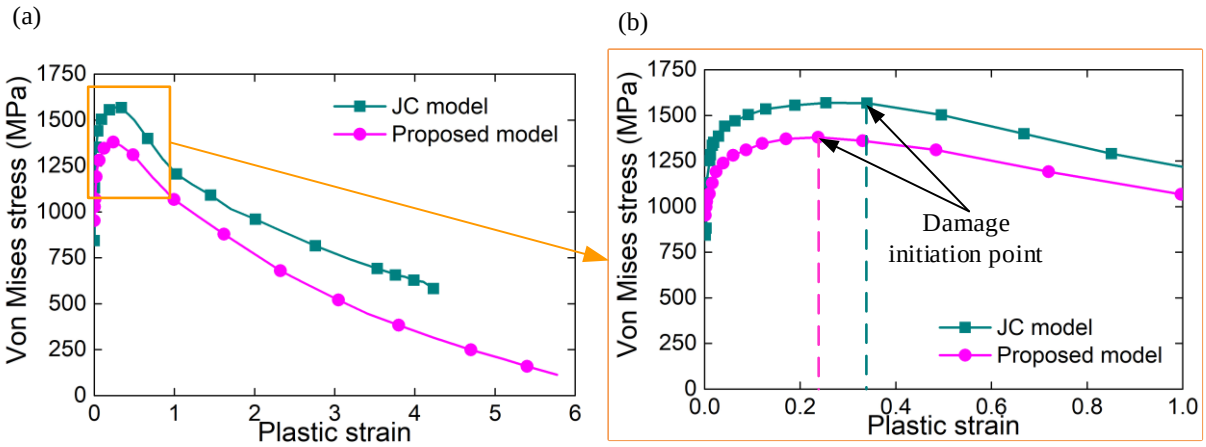

Fig. 41: von Mises stress in function of the plastic strain for a tracking point in the middle of the shear band of FDZ shown in Fig. 40, for the J-C and the proposed constitutive models, respectively (the cutting speed of 250 m/min).

In Fig. 41a, the von Mises stress generated by the J-C model is higher than that of the proposed model for the same strain. This is also confirmed by observing the distribution of the von Mises stress in FDZ (Fig. 40c and Fig. 40d). Due to this higher stress, the cutting force generated using the J-C model is higher than that using the proposed model (see Fig. 39). It can be seen in Fig. 41b that the plastic strain at damage initiation using the proposed model is lower than that using the J-C model.

Fig. 42 shows von Mises stress as a function of the plastic strain for a tracking point in the middle of the shear band of FDZ, obtained by CEL approach using the proposed constitutive model at different cutting speeds. As can be seen, the maximum stress increases with the cutting speed due to the combined influence of the strain rate and temperature, and the stress triaxiality. However, the plastic strain at damage initiation decreases with the cutting speed due to the increased stress triaxiality (Fig. 44a) whereas the Lode parameter is zero near the cutting edge where the material is separated from the workpiece to form the chip (Fig. 44b).

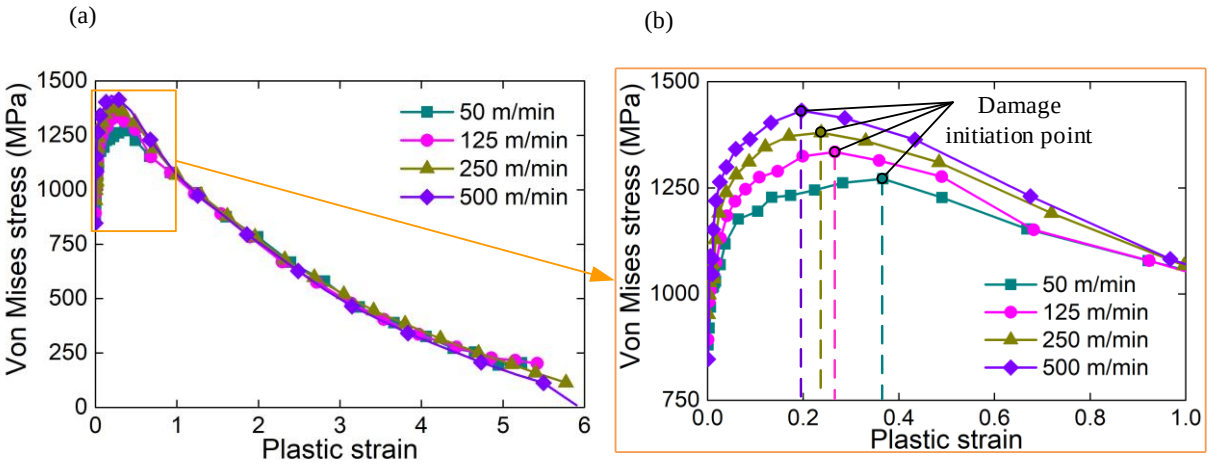

Fig. 42: von Mises stress vs. of the plastic strain using the proposed constitutive model in CEL simulations at different cutting speeds (50, 125, 250 and 500 m/min).

3.4.2 State of stress and strain at damage initiation at the beginning of a chip formation cycle

According to the proposed constitutive model (Eqs. (13) and (17)), the state of stress affects the flow stress and the strain at damage initiation of the work material, and consequently the chip formation, forces, surface integrity and so on. In this section, both the CEL1 and LAG cutting models are used to analyze the state of stress in FDZ at the beginning of a chip formation cycle, and how the cutting speed affects this state.

Considering the CEL1 model, Fig. 43 shows the distributions of the stress triaxiality (Fig. 43a) and Lode parameter (Fig. 43b) in the workpiece and chip, for a cutting speed of 50 m/min. Fig. 44 shows the evolution of the stress triaxiality (Fig. 44a) and Lode parameter (Fig. 44b) along the shear band in FDZ represented in Fig. 43 (path from point 1 to point 10), for several cutting speeds. It follows from Fig. 44a that the values of stress triaxiality along the shear band in FDZ increases from negative near the cutting edge (point 1) to positive at the chip free surface (point 10). This means that, according to Fig. 21, the strain at damage initiation decrease from the tool cutting edge (point 1) to the chip free surface (point 10). This figure also shows that increasing the cutting speed from 50 m/min to 500 m/min, the stress triaxiality becomes less negative near the tool cutting edge, and more positive in the chip free surface. This means that the strain at damage initiation will decrease with the increase of the cutting speed, so less energy is required to remove a layer or material from the workpiece to form the chip [170].

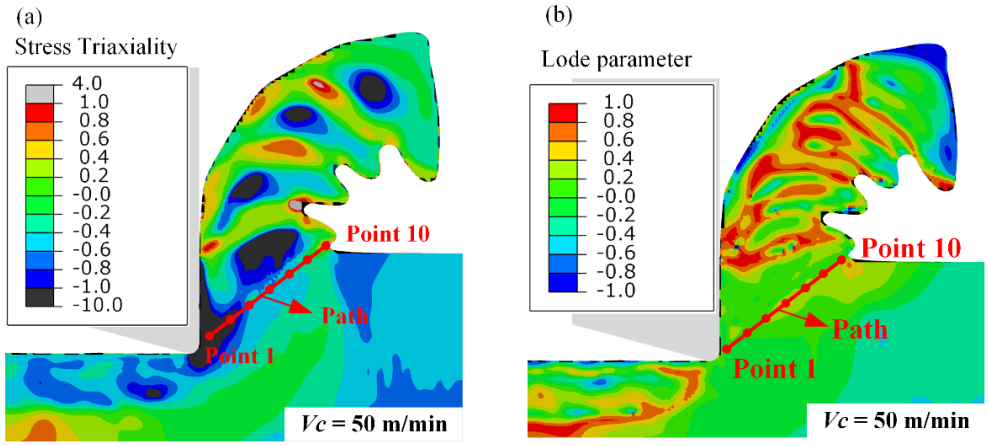

Fig. 43: Distribution of (a) stress triaxiality and (b) Lode parameter, obtained using CEL1 model for a cutting speed of 50 m/min.

As far as the Lode parameter is concerned, Fig. 44b shows that the Lode parameter increases from zero near the tool cutting edge, to a maximum value of about 0.6-0.8 at the chip free surface. The influence of the cutting speed on the Lode parameter is not so evident as the stress triaxiality. Three zones can be identified along the path from point 1 to point 10: near the cutting edge, in the middle of FDZ, and near the chip free surface. In the zone near the cutting edge, there are no evident influence of the cutting speed on the Lode parameter. Moreover, independently of the cutting speed, the Lode parameter is zero at the chip root. In the middle of FDZ, the Lode parameter decrease as the cutting speed increases. Finally, the Lode parameter increases with the cutting speed near the chip free surface.

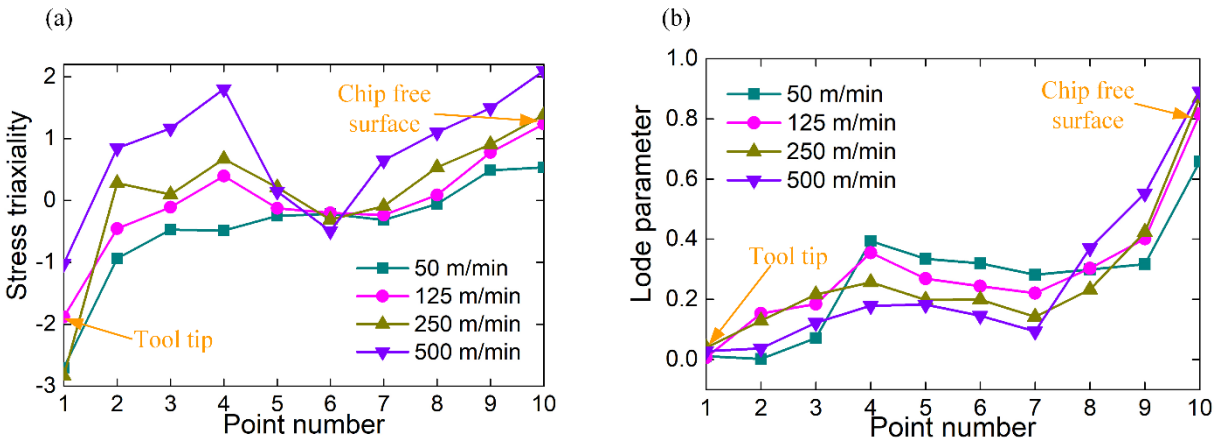

Fig. 44: Evolution of the (a) stress triaxiality and (b) Lode parameter, along the path shows in Fig. 43, obtained using CEL1 model for several cutting speeds (50, 125, 250 and 500 m/min).

According to Fig. 21, the increase of the Lode parameter from zero to both negative and positive ranges lead to an increase of the strain at damage initiation. So, near the tool tip where the Lode parameter is zero, the strain at damage initiation will be lower than that at the chip free surface, where the Lode parameter is maximum.

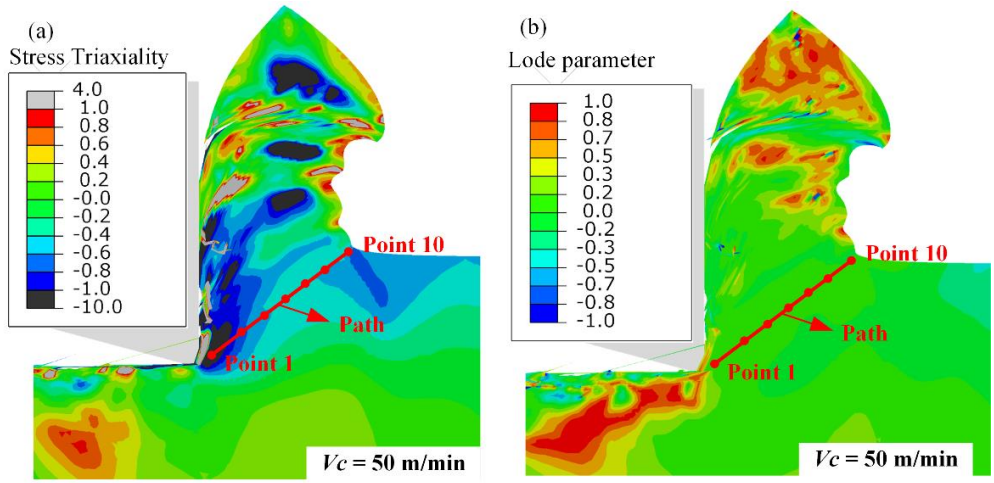

Fig. 45: Distribution of (a) stress triaxiality and (b) Lode parameter, obtained using LAG model for a cutting speed of 50 m/min.

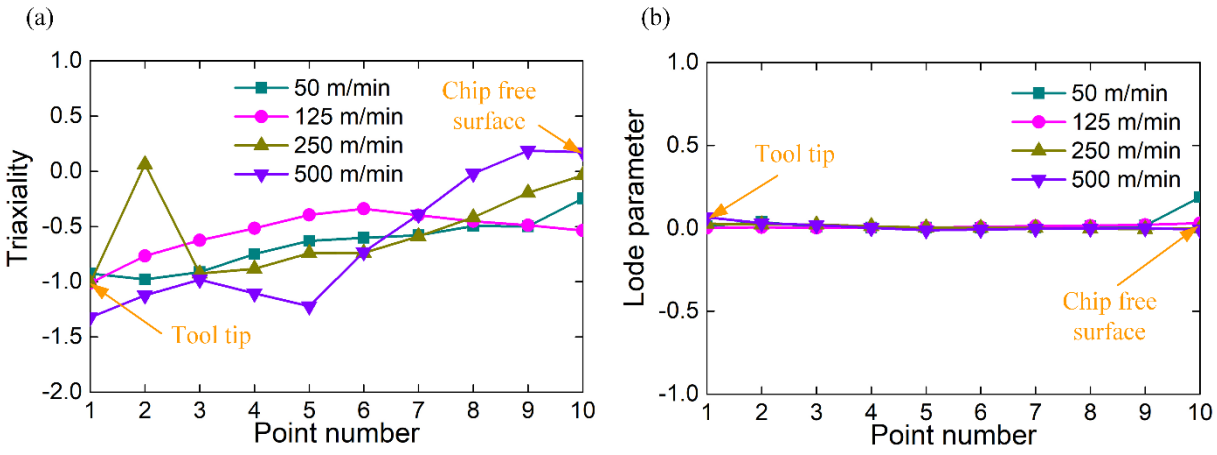

Fig. 46: Evolution of the (a) stress triaxiality and (b) Lode parameter, along the path shows in Fig. 45, obtained using LAG model for several cutting speeds (50, 125, 250 and 500 m/min).

Fig. 45 and Fig. 46 show the distributions of the state of stress (stress triaxiality and Lode parameter) (Fig. 45), and the evolution of this state of stress along the shear band (Fig. 46), obtained using the LAG model for the same conditions as used in the CEL1 model. These figures show that the stress triaxiality is mainly

negative in FDZ, and its magnitude reduces when moving to the chip free surface (Fig. 45a and Fig. 46a). Moreover, its magnitude is lower than that obtained using the CEL1 model, and there is no evident influence of the cutting speed on the stress triaxiality. This negative stress triaxiality in FDZ is associated with the compressive state of the material at the beginning of the chip formation cycle [123–125]. As far the Lode parameter is concerned, since plane strain conditions are applied in the LAG model, this parameter is almost zero in FDZ (Fig. 46b), while it increases from the cutting edge to the chip free surface in the case when the CEL1 model is used (Fig. 44b).

The strain at damage initiation depends on both stress triaxiality and Lode parameter, as well as on the temperature and strain rate (equation (12)). Fig. 47 and Fig. 48 show the distribution of the strain at damage initiation for the cutting speed of 50 m/min (Fig. 47a and Fig. 48a), and the evolution of the strain at damage initiation along the shear band in FDZ (Fig. 47b and Fig. 48b) for several cutting speeds using both CEL1 and LAG models. As can be seen, the values of the strain at damage initiation decreases from chip free surface to near the tool tip, regardless the cutting speed value. However, this decrease, and the magnitude of the strain at damage initiation are lower when the LAG model is used compared to the results of the CEL1 model. This implies that less energy is required to separate the material from the workpiece to form the chip according to the LAG model, although the same input physical data was used in both models. This is probably due to the different numerical approaches used to simulate the separation of the material from the workpiece.

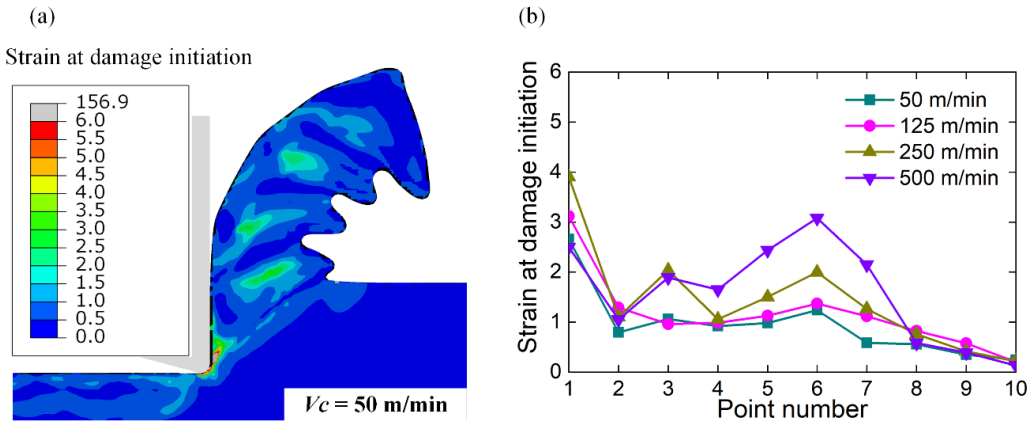

Fig. 47: (a) Distribution of the strain at damage initiation for a cutting speed of 50 m/min, and (b) evolution of the strain at damage initiation along the path shows in Fig. 43, obtained using CEL1 model for several cutting speeds (50, 125, 250 and 500 m/min).

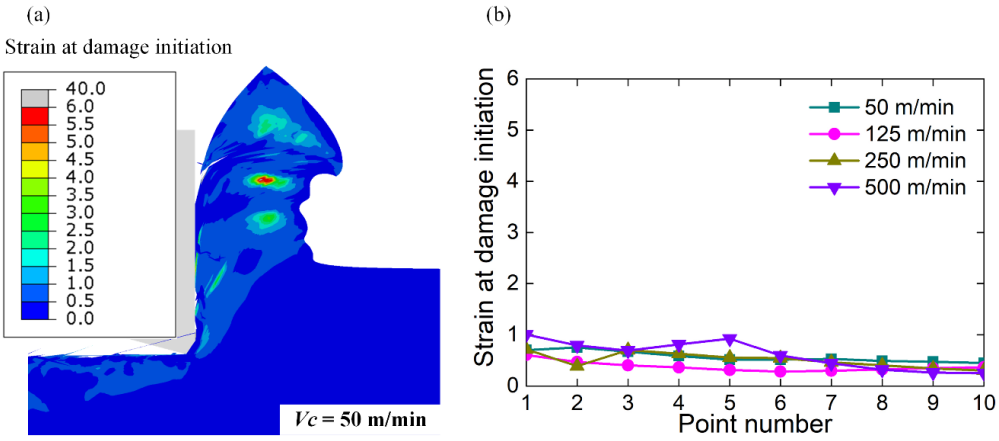

Fig. 48: (a) Distribution of the strain at damage initiation for a cutting speed of 50 m/min, and (b) evolution of the strain at damage initiation along the path shows in Fig. 45, obtained using LAG model for several cutting speeds (50, 125, 250 and 500 m/min).

3.5 Analysis of material side flow phenomenon

3.5.1 Effect of material side flow behavior on chip width and lateral burr formation

Previously predicted results are obtained using the 3D orthogonal cutting model using the CEL approach having a small width of cut (CEL1). However, this model does not permit to simulate the material side flow often observed experimentally. Therefore, a 3D orthogonal cutting model using the CEL approach with the actual width of cut (CEL2) of 3 mm is also developed, and the obtained results are compared with CEL1. Fig. 49 shows the plastic strain and temperature distributions extracted from: 1) the lateral surface of the workpiece of CEL1 model (designed in Fig. 49 by "CEL1 model"); 2) a plane passing through the middle of the workpiece of the CEL2 model (designed in Fig. 49 by "CEL2 model (middle surface)"); 3) the lateral surface of the workpiece of CEL2 model (designed in Fig. 49 by "CEL2 model (lateral surface)"). A comparison between the results over the middle surface obtained using the CEL1 and CEL2 models (see Fig. 49a, b, c, and d) shows that the strain and temperature have almost the same distributions, which verifies the consistency between the CEL1 and CEL2 models. However, a relatively lower strain and temperature are the case at the lateral surface when the CEL2 is used compared with the results in the middle surface as shown in Fig. 49c and Fig. 49f.

As shown in Fig. 49, the strain distribution over the middle surface is different from that distribution in the lateral surface of the workpiece. This implies that the deformation conditions in the middle section and lateral surface of the workpiece are not the same. Therefore, if plane strain conditions can be assumed in the middle

section, this is not the case for the lateral surface. In the testing practice, the temperature distribution during cutting is often obtained by thermal cameras and the strain distribution by high speed imaging cameras using the Digital Image Correlation (DIC) technique [171]. Both temperature and strain distributions are obtained only for the lateral surface of the workpiece and chip, whereas numerical simulation allows to assess temperatures and strains over the whole the width of the workpiece and chip. Therefore, 3D cutting models need to be developed to correctly compare the simulated strain distribution with that obtained experimentally by DIC. The same is applied when comparing the simulated temperature distribution and that measured by thermal cameras. Unfortunately, this is not taken into account in many known publications [172–174].

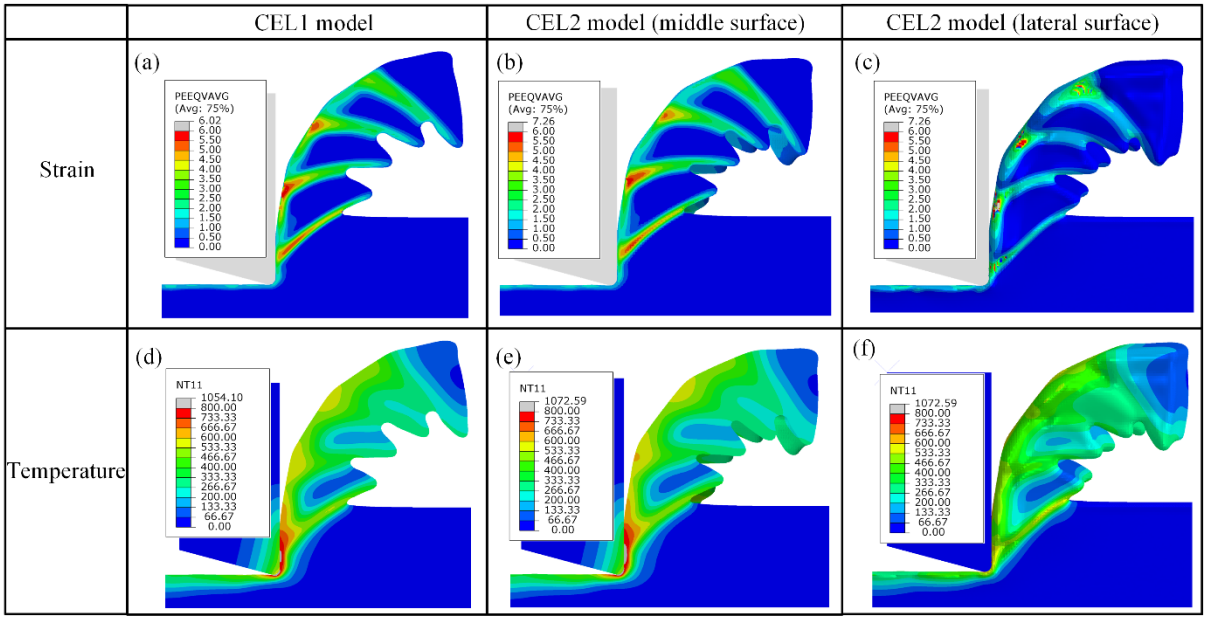

Fig. 49: Distributions of the plastic strain and temperature using the CEL1 ((a) and (d)) and CEL2 ((b), (c), (e) and (f)) models. Distributions are obtained in a plane passing through the middle of the workpiece of the CEL2 model and at the lateral surface of the workpiece of both CEL1 and CEL2 models. The cutting speed is constant and equal to 250 m/min.

As shown in Fig. 50, the material side flow (the red dotted line area) is found when the CEL2 model is used. This flow occurs in the chip (its width becomes greater than the width of cut) and in the machined surface in the form of side burr. Although the work material is constrained in the Z-direction in the front face (symmetry condition), it is free to move in the opposite side, resulting in an increase of chip width and formation of lateral burrs on the machined surface. The material side flow is observed experimentally in the chip and

machined surface using an optical microscope and SEM. Fig. 51 shows the experimental chip free surface for several cutting speeds. Table 14 shows a comparison between simulated and experimental chip width. For the same cutting speed, experimental and simulated values of the chip width are almost same. Depending on the cutting speed, the chips are wider about 50-140 µm than the width of cut (3mm). Fig. 52 shows the lateral burr on the machined surface observed using SEM.

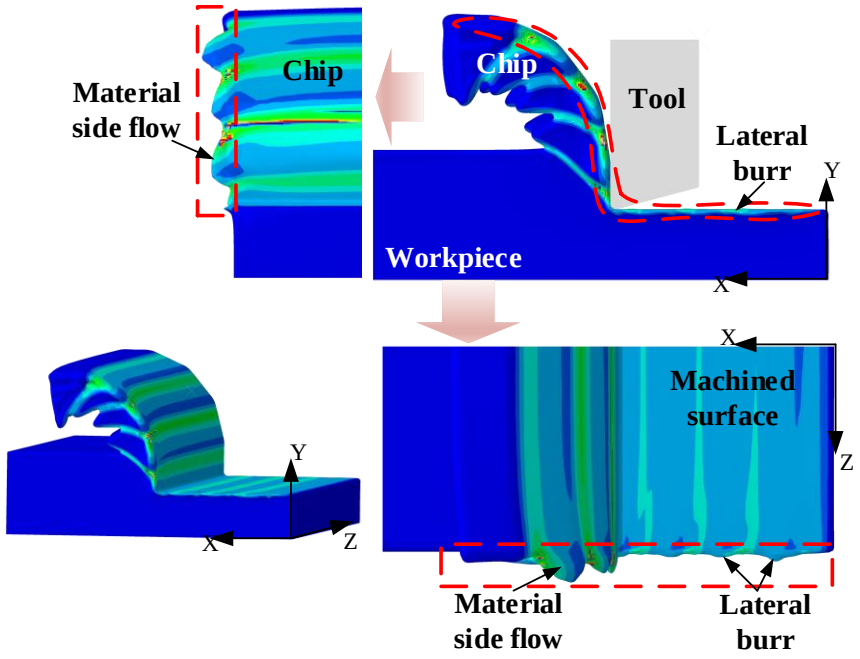

Fig. 50: Several projection views of serrated chip morphology and machined surface simulated using the CEL2 model at the cutting speed of 250 m/min. This figure put in evidence the formation of lateral burr in the machined surface and the increased chip width compared to the width of cut.

Table 14: Comparison between simulated and experimental chip width

Cutting Speed (m/min)	Simulated (SIM)		Experimental (EXP)		Difference between EXP and SIM (average) (%)	Difference between EXP chip width and the width of cut (average) (mm)
	Average	Maximum	Average	Maximum		
50 m/min	3.06±0.02	3.08	3.05±0.02	3.08	0.33%	0.05
125 m/min	3.08±0.02	3.10	3.08±0.03	3.12	0%	0.08
250 m/min	3.09±0.03	3.12	3.14±0.05	3.19	1.62%	0.14
500 m/min	3.10±0.03	3.13	3.13±0.07	3.21	0.97%	0.13

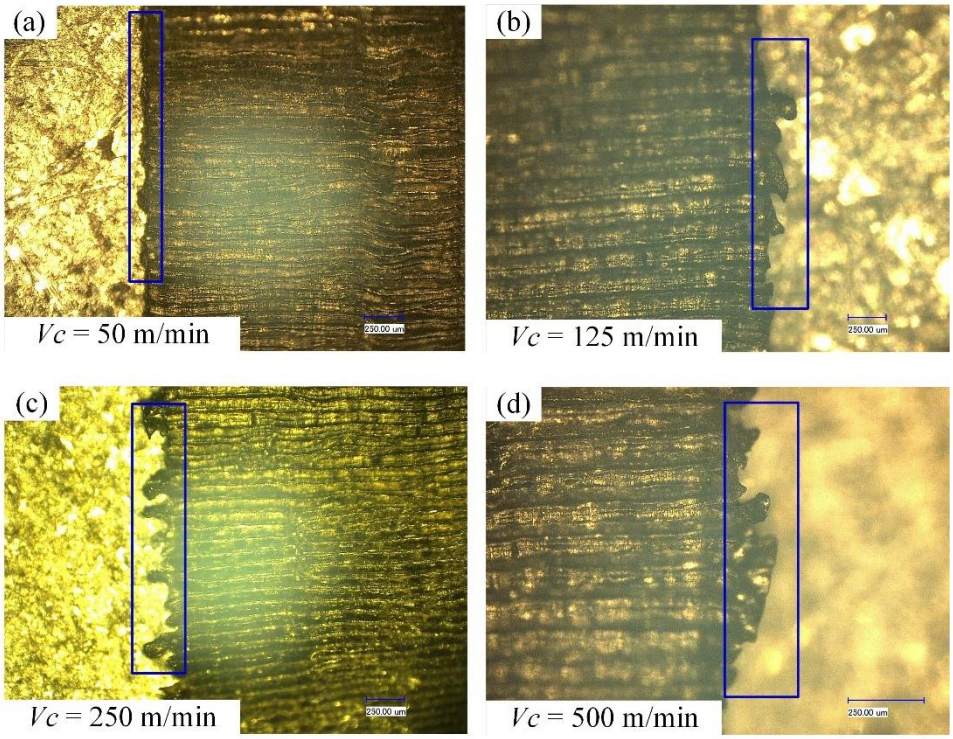

Fig. 51: Experimental chip free surface for several cutting speeds, observed at the optical microscope.

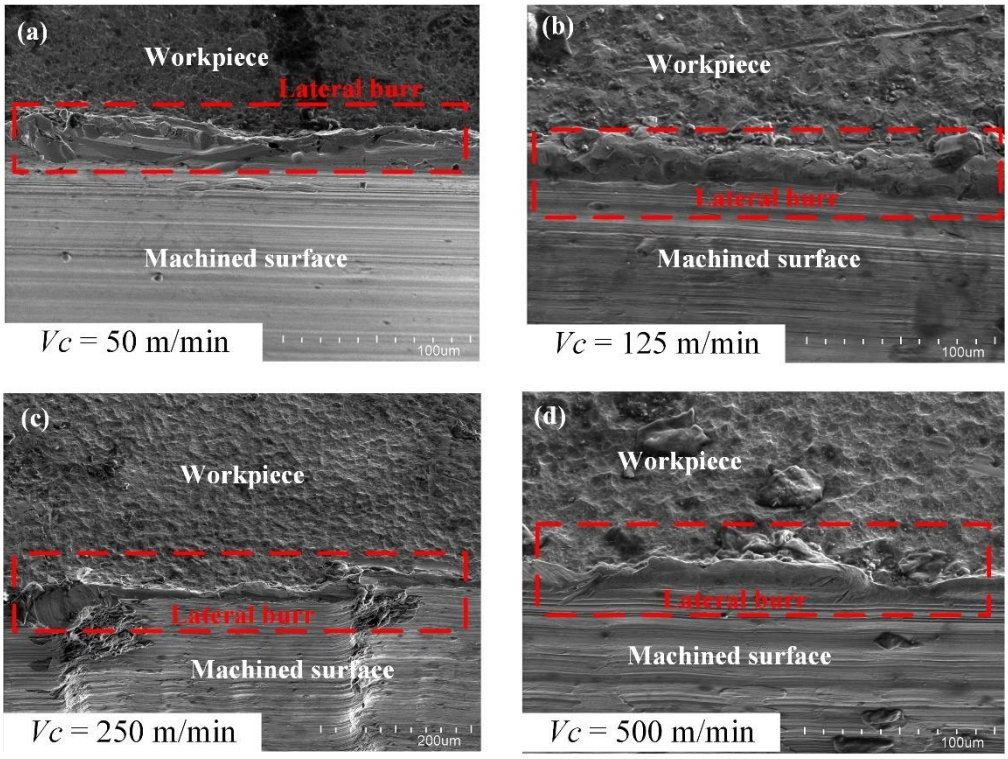

Fig. 52: SEM images of the lateral burr in the workpiece for several cutting speeds.

3.5.2 Formation mechanism of lateral burr

Due to lack of transversal constraint in the both side of workpiece, the material side flow under Poisson effect finally results in an increase of chip width and formation of lateral burrs in the workpiece after machining. To determine the geometry of the lateral burr, the cross section of workpiece is analyzed as shown in Fig. 53. Burr width and burr height are the geometrical parameters used to characterize the lateral burr. Burr width increases firstly into the maximum value and then decreases gradually along the surface depth direction. It is worth noting that the burr height is greater than the thickness of plastic deformed layer.

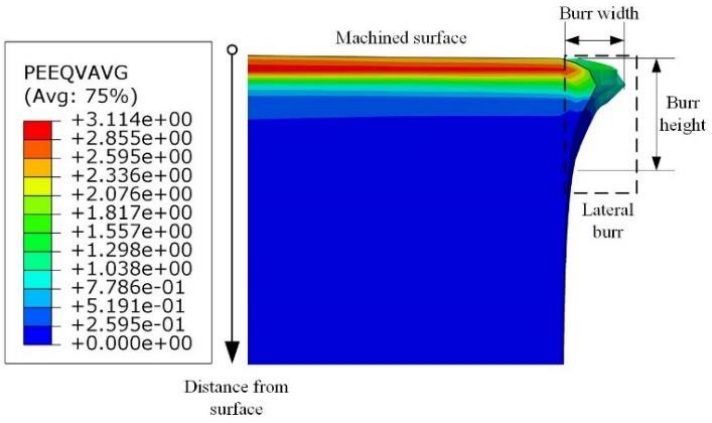

Fig. 53: Cross section of the workpiece showing the burr geometry at cutting speed of 250 m/min.

The plastic strain and burr width in function of distance beneath machined surface is shown in Fig. 7. The maximum plastic strain in subsurface is about 3.0 and the maximum burr width is about 15.0 μm. The maximum plastic strain locates in the near surface, while the maximum burr width locates in the depth of 6 μm from machined surface. Besides that, the thickness of plastic effected layer is about 6 μm, while the burr height is about 10 μm. It can be concluded that the lateral burr cannot be predicted simply from the relationship between plastic strain and burr width. According to the research of Pang et al. [175], the lateral burr is formed under the poison effect. So, the lateral burr generation is sensitive to the plastic strain, temperature of machined surface under different cutting parameters and material properties.

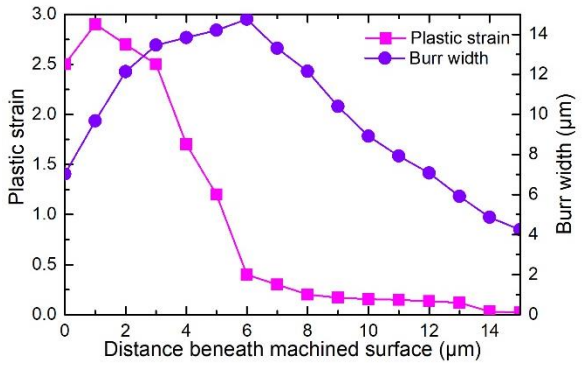

Fig. 54: The plastic strain and burr width in function of distance beneath machined surface shown in Fig. 53.

The material side flow always occurs during machining. The deformation is compression and the high contact stresses are generated in the machined surface and tool-chip contact zone, respectively. In the middle of the workpiece, the work material is constrained in the Z-direction, thus it mainly flows over the tool rake face. However, the work material near the lateral surface of workpiece is free to flow in the Z-direction. Due to the lower constraint from the surrounding material, the compression deformation can result in the material side flow under Poisson effect.

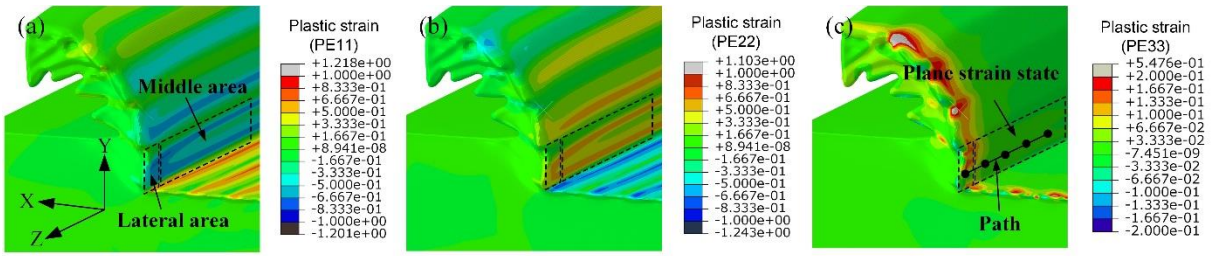

Fig. 55: Distribution of plastic strain components in (a) X, (b) Y, and (c) Z directions. This figure put in evidence the material in middle surface is in a plane strain state at cutting speed of 250 m/min.

To investigate why material side flow occurs in machining, the distribution of plastic strain components in X, Y and Z directions are obtained from 3D CEL simulation, and shown in Fig. 55. As shown in Fig. 55 (a) and (b), the plastic strain on X and Y directions in the middle of the workpiece is higher than that in lateral area. While Fig. 55 (c) shows that the plastic strain on Z axes in middle area is approximately zero (see the magenta curve in Fig. 57) and that in lateral area is positive. It is deduced that the material in middle area of

workpiece is in a plane strain state, while the material in lateral area of workpiece is not.

The distributions of stress components in X, Y and Z directions are shown in Fig. 56. As shown in Fig. 56 (a) and (b), the stress on X and Y direction in middle of the workpiece is more compressive than that in lateral area. Fig. 56 (c) shows that the stress on Z direction in lateral area is approximately zero (see the violet curve in Fig. 57) and that in middle of the workpiece is negative. It is deduced that the material in lateral area of workpiece is in a plane stress state, while the material in middle area of workpiece is not. Plastic strain and stress in Z-direction in function of distance along the path is obtained as shown in Fig. 57. From this figure, we can know that the workpiece changes from plane strain state in middle of the workpiece to plane stress state in lateral surface. The plane stress state allows the large deformation of workpiece in Z direction, which finally results in the formation of lateral burr.

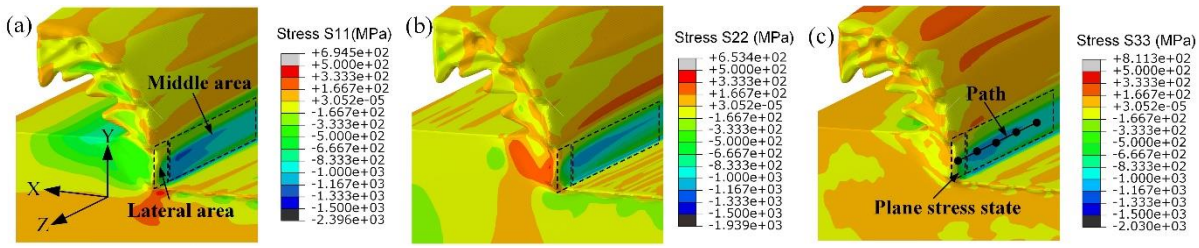

Fig. 56: Distribution of stress components in (a) X, (b) Y and (c) Z directions from 3D CEL simulation. This figure put in evidence the material in lateral surface is in a plane stress state at cutting speed of 250 m/min.

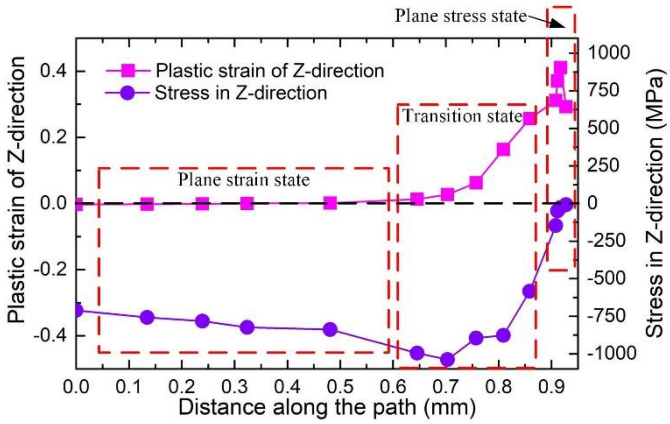

Fig. 57: Plastic strain and stress in Z-direction in function of distance along the path (shown in Fig. 55 and Fig. 56) to verify the transformation from plane strain state in middle surface to plane stress state in lateral surface.

According to the research from Liu et al. [157], when the uncut chip width is much greater than the uncut

chip thickness with a certain ratio, the effect of material side flow on cutting force and surface integrity can be neglected properly when more than 90% of the width of the chip undergoes plane strain deformation [158]. Because the material side flow behavior is strongly sensitive to the material ductility, so the critical ratio of the uncut chip width to thickness varies greatly when the material changes. For the titanium alloy used in this study, the expanded chip width is 3.14 mm when compared to 3 mm (the width of cut) and the lateral burr width is 15 μm, the influence of material side flow on cutting process is significantly small. However, when the ratio between the uncut chip width and uncut chip thickness is quite small or the ductility of material ductility is so high, the assumption of plane strain needs to be verified to be applied in analysis of cutting process.

3.6 Summary of the chapter

Models of HSM of Ti-6Al-4V alloy are developed and simulated using both the Lagrangian and CEL approaches, including the proposed constitutive model considering the state of stress in addition of the strain hardening, strain rate, and temperature. A sensitivity analysis of the mesh topography on the chip geometry and cutting force permitted to determine a maximum element size of 3.5 μm and an element orientation of 90° to be used in in CEL simulations. Compared with the traditional Lagrangian approach, the CEL approach has outstanding advantages by avoiding the element distortion, which is important for simulating the cutting process, in particular the HSM. In addition, the following conclusions can be drawn:

1) Cutting model using the CEL approach and the proposed constitutive model allow to simulate serrated chips in machining Ti-6Al-4V alloy for a wide range of cutting speeds, ranging from 50 m/min to 500 m/min.
2) CEL approach can better predict the strains and tool-chip contact length than the Lagrangian one.
3) Increasing the cutting speed increases the maximum stress and decreases the strain at damage initiation. This is due to the increase of the strain rate and the decrease of the stress triaxiality when the cutting speed increases.
4) The proposed constitutive model predicts the cutting force and chip geometry much closer to experimental results than J-C model, because it provides a more realistic thermomechanical behavior of the Ti-6Al-4V alloy in cutting.
5) CEL simulations using larger width of cut permitted to simulate the material side flow, which results in a larger width of chip when compared to the width of cut, and the formation of lateral burr in the workpiece This implies that the plane strain conditions often assumed in 2D simulations of orthogonal

cutting cannot accurately represent the reality.

6) The workpiece transforms from plane strain state in middle surface to plane stress state in lateral surface due to lack transverse constraint in lateral surfaces, which finally results in the formation of lateral burr.

4 Multiscale modelling and simulation of grain refinement induced by dynamic recrystallization (DRX)

4.1 Microstructure evolution model based on continuous DRX (cDRX) and discontinuous DRX (dDRX) mechanism

High plastic strain and rapid temperature increasing will occur in primary deformation zone in HSM, which could result in the dislocation density evolution. Dislocation density is generally regarded as the power for grain deformation, nucleation and growth of DRX process under thermomechanical processing. Work hardening from the severe plastic deformation will induce generation of dislocation tangles and result in the increasing of dislocation density. On the other hand, the inhabitation of dislocation would result in the rapid drop of dislocation density by the influence of dynamic recovery (DRV) softening in high temperature condition. The dislocation density evolution and hardening behavior are determined by the interaction of these two processes. The DRX process will be activated when dislocation density reaches the critical value, which is significantly dependent on temperature and strain rate.

4.1.1 Model of dislocation density evolution

Dislocation density ρ under the influence of work hardening and DRV process is proposed by Mecking and Kocks [134] (KM model), and it can be calculated as following,

$$\frac{d\rho}{d\varepsilon} = k_1\sqrt{\rho} - k_2\rho \tag{26}$$

where k_1 is related to the work hardening and k_2 to the DRV. Both k_1 and k_2 are temperature and strain rate dependent, and expressed by,

$$k_1 = c_1\dot{\varepsilon}^m \exp\left(\frac{mQ}{RT}\right) \tag{27}$$

$$k_2 = c_2\dot{\varepsilon}^{-m} \exp\left(-\frac{mQ}{RT}\right) \tag{28}$$

where c_1 is a reference constant related to work hardening, c_2 is a reference constant related to DRV, m is the constant related to strain rate sensitivity, R is the gas constant, Q is the activation energy. An initial dislocation

density, ρ_0, of the material is assumed to be uniform and nucleation of dDRX starts when it reaches the critical value. Littlewood et al. [176] measured the dislocation density with $10^{12}/m^2$ of undeformed Ti-6Al-4V alloy, which was applied in this study. For the new recrystallization grains, the dislocation density evolves from initial dislocation density.

4.1.2 Model of dDRX grain nucleation and growth

The nucleation rate $\dot{n}$ of dDRX depends on both the temperature T and the strain rate $\dot{\varepsilon}$, and can be represented as follows:

$$\dot{n} = C_n \dot{\varepsilon}^m \exp(-\frac{Q}{RT}) \tag{29}$$

which is proposed by Kugler and Turk [177], where C_n is a material constant. Considering the energy change, the critical dislocation density ρ_c of grain boundary is described by Ding and Guo [178], which can be expressed as follows,

$$\rho_c = \left(\frac{20\gamma_m \dot{\varepsilon}}{3bMl\tau^2} \right)^{1/3} \tag{30}$$

where l is the dislocation mean free path, M is the mobility of grain boundary, γ_m is the grain boundary energy, and τ is the dislocation line energy given by:

$$\tau = c_l \mu b^2 \tag{31}$$

where μ is the shear modulus, b is the Burger's vector and c_l is a material constant of 0.5.

The dislocation mean free path l is represented by Roberts and Ahlblom[179] expression as,

$$\frac{\sigma l}{\mu b} = G \tag{32}$$

where G is a constant, for which 10 is adopted for most metals [180].

The flow stress σ is a function of the dislocation density component, and calculated using the following equation [134]:

$$\sigma = \alpha \mu b \sqrt{\rho} \tag{33}$$

Dislocation density of a DRX grain and the original microstructure are generally different, which provide the

growth driving force of a DRX grain with reduction of grain storage energy. The grain growth velocity V_i of the current DRX grain is assumed directly proportional to the mobility of the boundary and driving force per cell [181], thus given by,

$$V_i = \frac{MF_i}{4\pi r_i^2} \tag{34}$$

where r_i represents the grain radius of the current DRX grain. The mobility of grain boundary M is given by Stüwe and Ortner [182],

$$M = \frac{\delta D_b b}{KT} \exp\left(-\frac{Q_b}{RT}\right) \tag{35}$$

where K is Boltzmann's constant, δ is the characteristic grain-boundary thickness, D_b is the boundary self-diffusion coefficient, Q_b is the boundary-diffusion activation energy.

The driving force F_i of the newly formed DRX grain is generated from the surface energy reduction proposed by Ding and Guo [183],

$$F_i = 4\pi r_i^2 \tau (\rho_m - \rho_d) - 8\pi r_i \gamma_m \tag{36}$$

where γ_m represents the grain boundary energy, which is derived from the grains misorientation, ρ_m and ρ_d are the dislocation density of the original grain and DRX grain.

Considering the effects of time step and cell size, the nucleation probability P in the CA model is described by the following equation:

$$P = \dot{n} \times \Delta t \times S_{CA} \tag{37}$$

where S_{CA} is the area of a CA cell. Current CA cells are assumed to be square, so $S_{CA} = L_{CA}^2$, where L_{CA} was the length of a CA cell.

The current grain size is calculated as,

$$d_i = \sqrt{\frac{4N_i a^2}{\pi}} \tag{38}$$

where N_i is the lattice number that makes up the current grain, a is the lattice size.

Table 15: Material parameters of CA model [180, 184].

Parameter	K_1	K_2	Q (kJ mol^{-1})	m	R (J mol^{-1} K^{-1})	C	μ_0 (MPa)	b (m)
Value	3.4×10^{9}	5.2	153	0.848	8.314	4×10^{13}	2.05×10^{4}	2.86×10^{-10}
Parameter	G	δD_b (m^3 s^{-1})	K (m^2 kg s^{-2} K^{-1})	Q_b (kJ mol^{-1})	ρ_0 (/m^2)	α	ν	θ_m (rad)
Value	10	5×10^{-15}	1.38×10^{-23}	108	10^{12}	0.5	0.34	$\pi/12$

Considering the Hall-Petch relation [69,70] between material strength and grain size, with the decreasing of grain size, the intense distribution of grain boundary with high energy induces the increasing of material strength, which makes grains harder to refine. According to Ding and Guo [180] and Song et al. [184], the values of the CA model coefficients for the Ti-6Al-4V are list in Table 15.

4.1.3 Model of cDRX grain rotation and partition

The formation of new refined grains with HAGBs can be achieved by gradual rotation of subgrains without grain nucleation and growth process. cDRX is resulted from the accumulation of dislocation at LAGBs. When LAGB increase to critical value of 15°, it becomes HAGB. It is generally considered that the average dislocation cell size d_{cr} is inversely proportional to the square root of the total dislocation density ρ [185]. The relationship between the average cell size and flow stress can be expressed by:

$$d_{cr} = \frac{H_0}{\sqrt{\rho}} = \frac{\alpha\mu b H_0}{\sigma} \tag{39}$$

where H_0 is a constant equal to 10 for Ti-6Al-4V alloy. If the current critical dislocation cell size calculated by dislocation density or flow stress is smaller than the current grain size, it is considered that the critical condition of cDRX is satisfied. According to the grain segmentation model proposed by Tóth et al. [186], several subgrains with a diameter of about D/3 and a misorientation angle of 3~5° are generated in the region satisfying the cDRX critical condition by the rapid grain growth method. The formation of these subgrains consumes parts of dislocation. From the orientation differences between neighboring cells [187], the lattice curvature and dislocation density tensor can be derived as:

$$\theta = b \cdot \rho \cdot L_{CA} \tag{40}$$

where θ is the local misorientation, ρ is dislocation density and L_{CA} is the cell size of CA model. With the continuous increase of the dislocation density, the subgrain will rotate and the misorientation between the subgrain and the matrix will increase. When this misorientation reaches the critical value of HAGB, the subgrain becomes an independent cDRX grain. If the dislocation density of the newly formed cDRX grains reaches the critical condition again, cDRX behavior can occur again. With the continuous refinement of grains, the required dislocation density to achieve cDRX behavior will become higher, which makes grains harder to refine further. It is worth noting that HAGB produced by cDRX process can provide the condition of grain boundary for dDRX grain nucleation.

4.1.4 Simplified grain size prediction model for FE

During HSM, the plastic deformation and heat generation result in microstructure evolution, especially severe plastic deformation results in grain refinement and DRX by thermal activation. Increasing the cutting speed, plastic strain, strain rate and temperature increase, while the time of thermal conduction decreases rapidly, which has significant influence on microstructure evolution. JMAK DRX model [59] was implemented in a VUHARD Fortran subroutine to predict the grain size distribution in machining metals using ABAQUS/Explicit FEA software. This model is represented by equations (41)-(45). DRX is activated when the strain reaches the critical strain, ε_c, defined by the following equation:

$$\varepsilon_c = a_1 d_0^{h_1} \dot{\varepsilon}^{m_1} \exp(Q_1 / RT) + c_1 \tag{41}$$

where a_1, h_1, m_1 and c_1 are material parameters, R is gas constant, Q_1 is current activation energy.

The review performed by Fanfoni and Tomellini [59] indicates that JMAK model is widely accepted for predicting grain size evolution which includes the effects of initial grain size, strain, strain rate and temperature . Based on the theory proposed by Zener and Hollomon [60], the evolution of DRX volume fraction and DRX grain size due to grain nucleation and growth process would be calculated.

The DRX volume fraction X_{drex} presented by Avrami [188] for dynamic recrystallization is defined as follows:

$$X_{drex} = 1 - \exp\left[-\beta_d \left(\frac{\varepsilon - a_{10}\varepsilon_p}{\varepsilon_{0.5}} \right)^{k_d} \right] \tag{42}$$

where β_d and k_d are material constants, $\varepsilon_{0.5}$ is the value of strain with the DRX volume fraction of 0.5, and its formula is shown as:

$$\varepsilon_{0.5} = a_5 d_0^{h_5} \varepsilon^{n_5} \dot{\varepsilon}^{m_5} \exp(Q_5 / RT) + c_5 \tag{43}$$

where a_5 , h_5 , n_5 , m_5 and c_5 are material parameters. After the DRX volume fraction is obtained, the corresponding DRX grain size is the size of new formed grains after nucleation and growth process of DRX, which is calculated as follows:

$$d_{drex} = a_8 d_0^{h_8} \varepsilon^{n_8} \dot{\varepsilon}^{m_8} \exp(Q_8 / RT) + c_8 \tag{44}$$

Similarly, a_8 , h_8, n_8 , m_8 and c_8 are material parameters. Finally, the average grain size is the average value of the remaining original grain size and new formed DRX grain size, which can be calculated by:

$$d = d_0 (1 - X_{drex}) + d_{drex} X_{drex} \tag{45}$$

where the initial grain size d_0 is 8 μm, initial DRX volume is 0. The coefficients of JMAK model [59] for Ti-6Al-4V are given in Table 16. They were extracted from the Pan et al. [79] and Wang et al. [189] research works.

Table 16: JMAK model coefficients of Ti-6Al-4V [79,189].

Peak strain	a_1	h_1		m_1	Q_1 (J mol^{-1})	c_1	a_2		
	0.0064	0		0.0801	30579	0	0.8		
DRX kinematics	a_5	h_5	n_5	m_5	Q_5 (J mol^{-1})	c_5	a_{10}	β_d	k_d
	0.022	0	0	0.11146	26430	0	0.0311	0.9339	0.5994
DRX grain size	a_8	h_8	n_8	m_8	Q_8 (J mol^{-1})	c_8			
	1280	0	0	-0.088	-36848	0			

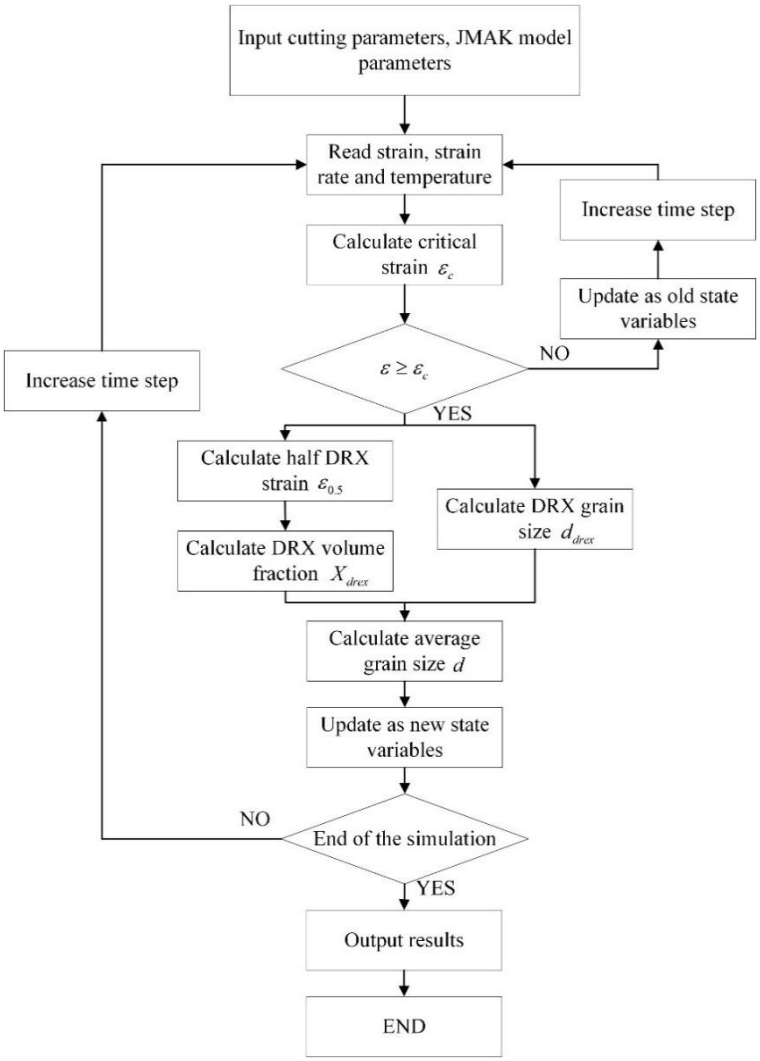

Fig. 58: Flowchart of subroutine VUHARD using JMAK model.

To predict the DRX kinetics and grain size, a user subroutine VUHARD is developed in FORTRAN by using JMAK model [59]. The flowchart of the calculating process of user subroutine VUHARD is shown in Fig. 58.

4.2 Multiscale model using coupled finite element (FE) and cellular automata (CA) approach

4.2.1 Description of CA simulation

The material in the deformation zone, during its cutting process, undergoes thermoplastic deformation, during which the evolution of dislocation density leads to dynamic recrystallization behavior. Due to the influence of different crystal structures, initial grain size, temperature and strain rate, two types of dynamic recrystallization (DRX) behavior are always observed: continuous dynamic recrystallization (cDRX) and discontinuous dynamic recrystallization (dDRX). As shown in Fig. 59, dDRX is driven by grain nucleation

and grain growth at grain boundary full of dislocation. When dislocation cell and subgrain structure with low angle grain boundaries (LAGBs) are generated within the grains, local misorientation may induce the progressive rotation of the grain to produce high angle grain boundaries (HAGBs) and new distinct grains, which is known as cDRX. There is no strict distinction between these two types of DRX, so the activation of these two behaviors depends on the current dislocation density and whether the required conditions are satisfied respectively.

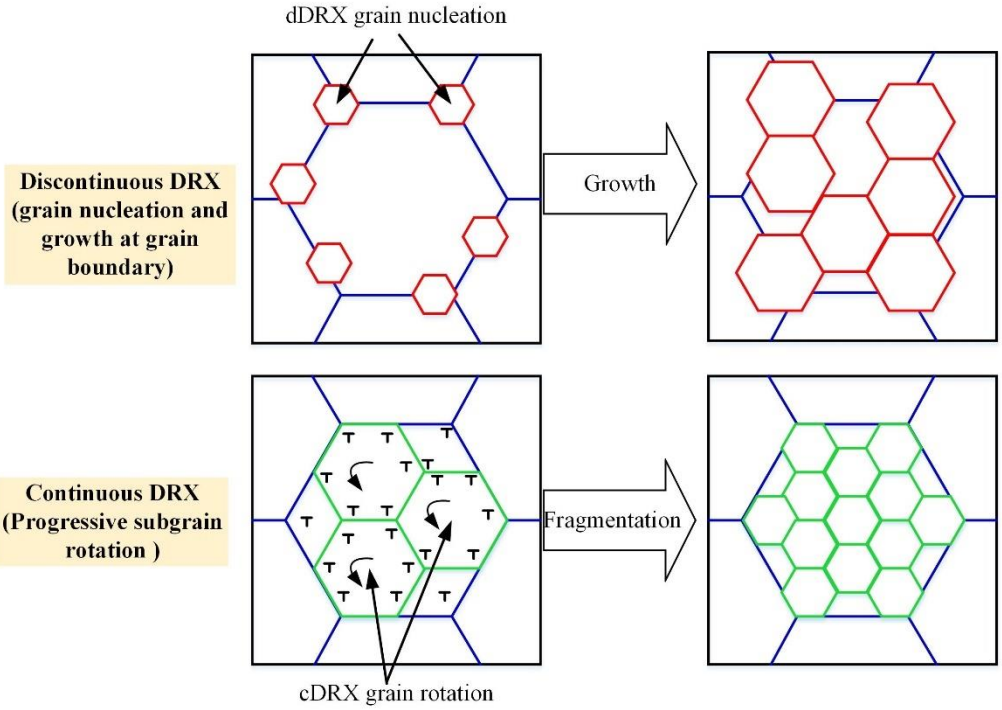

Fig. 59 Schematic of the grain refinement process of continuous and discontinuous DRX.

Based on the above theoretical model of DRX, a routine has been developed in MATLAB under the premise of CA transformation rules. Fig. 60 shows the initial grain distribution obtained by a natural grain growth algorithm based on the lowest energy principle [190]. The total energy is provided by the grain boundary in the CA space, and the energy of the interfacial cells depends on the number of the same state of central cell and neighboring cells. The driving force for the natural grain growth is derived from the reduction of the interfacial energy by state transition. The crystal structure of grains is hexagonal close packed (HCP) with average grain size of 8 μm measured by SEM. Different colors represent grains with different orientations.

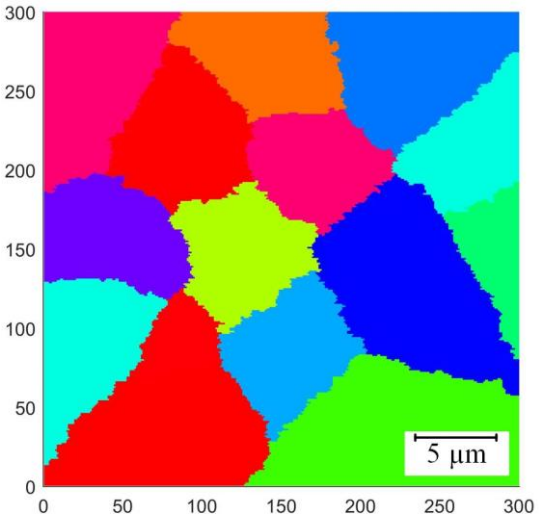

Fig. 60: Initial microstructure generated by a natural grain growth algorithm.

CA simulation of microstructure evolution is conducted with the increasing of strain, in which time step is $\Delta t = \varepsilon/(N\dot{\varepsilon})$, where N is the total iteration step and 300 steps are adopted in this study. During each time step, the whole lattice space is searched, and related judgement and calculation are carried out to update the lattice state at the next step. The above step loop in every step until the predetermined strain is achieved. After that, the results of dislocation density, grain size, grain distribution and DRX characteristics will be output. The flowchart of CA simulation is shown in Fig. 61. Five variables were assigned to each CA cell were selected to control the cell state during CA simulation: (1) dislocation density corresponds to the energy generated by thermal deformation, (2) grain orientation is used to distinguish different grains, (3) mark of grain boundary is used to identify whether the cell is on grain boundary, (4) mark of DRX represents the cell undergo the DRX process, (5) index of color is used to display grain characteristics distribution. CA simulation of microstructure evolution depends on the state transformation of each cell in CA domain which depends on its previous state and neighboring cells' sate. According to CA transformation rules, every CA cell has three probabilities to transform: (1) grain nucleation, (2) grain growth and (3) keep the previous state, as shown in Fig. 62. At the beginning of every simulation step, the dislocation density in whole CA domain was updated firstly based on the deformation condition calculated from FEM. And then the dislocation density was judged whether it exceed the critical value. If so a random number between 0 to 1 was generated along the grain boundary and when it was lower than the DRX nucleation probability, the cell was transformed to be a new DRX grain cell with updated state variables.

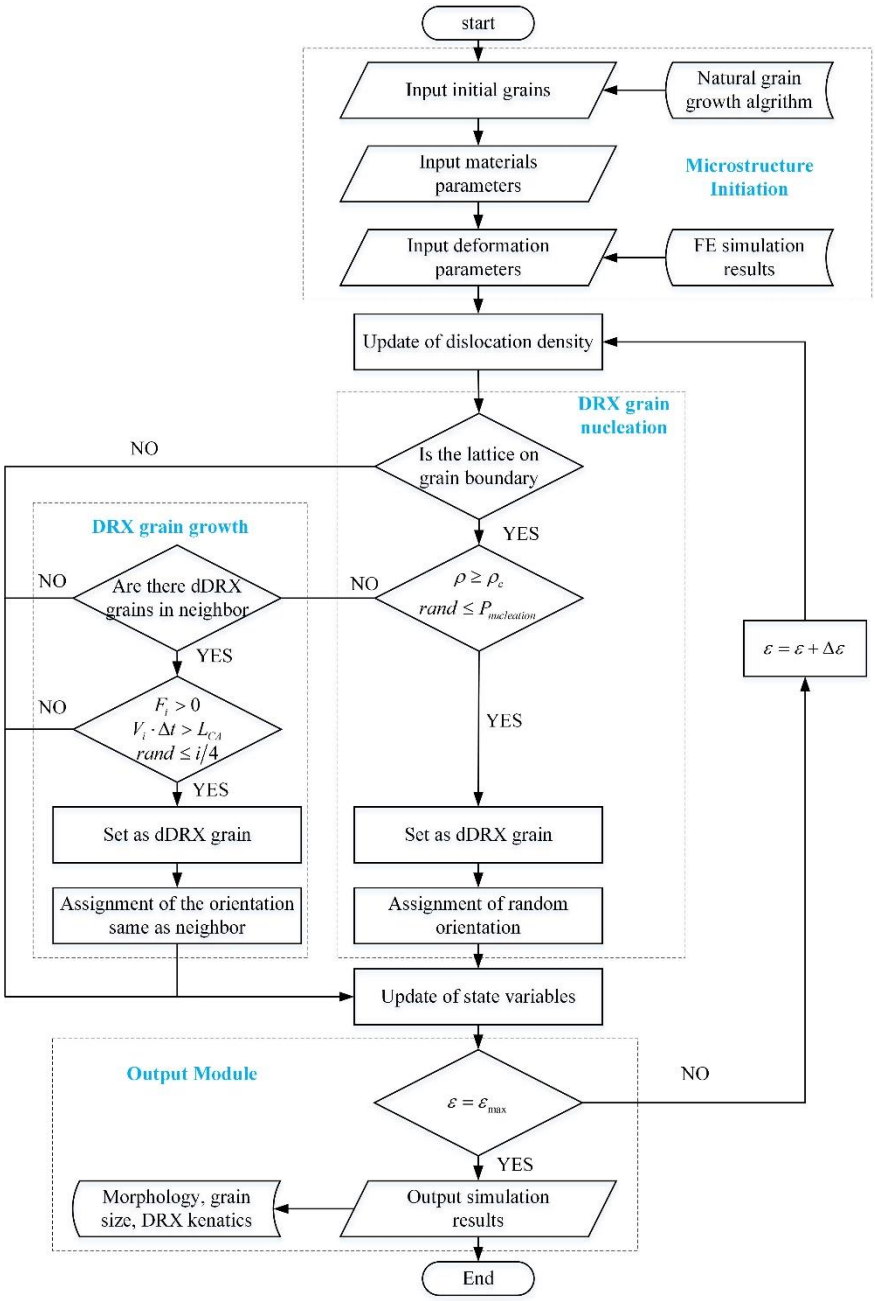

Fig. 61: Flowchart of CA simulation.

It's worth noting that the priority of grain nucleation is set higher than grain growth, which means that if a grain nucleation process of a cell has been satisfied, grain growth process was ignored by default. As for the grain growth process, the following several conditions need to be satisfied: (1) the cell is located at grain boundary, (2) the driving force of neighboring DRX grain is positive, (3) the migration distance of grain boundary is greater than cell size, (4) randomly generated number is smaller than transformation probability ($p = i/4$) where i represents the number of cells with same orientation. If any condition of grain nucleation

and growth cannot be matched, state variables of the cell would keep as the previous with continuous increasing dislocation density.

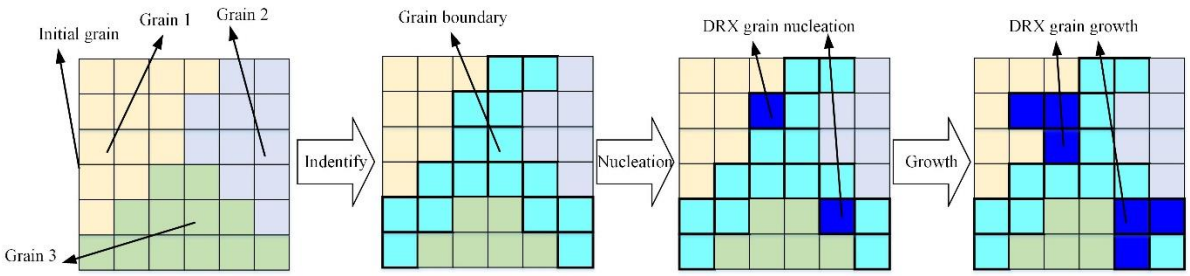

Fig. 62: The schematic diagram of state transformation process during CA simulation.

4.2.2 Multiscale simulation by combining FE and CA methods

The average grain size distribution simulated by FE and the grain morphology simulated by CA method are shown in Fig. 63. The simulated results and computational characteristics indicate that FE method is better at calculating speed and displaying the grain size distribution in different regions of workpiece in macroscale, while CA method is preferable to visualize the microstructure morphology at a certain point, which can reproduce the physical process of grain evolution and help to study the effect of microstructure evolution on mechanical behavior. The DRX kinetics results and average grain size simulated by FE and CA method are listed in Table 17. The results showed a reasonable agreement between these two methods.

As mentioned by Arrazola et al. [27], the main difficulty of the development of microstructure evolution model is the determination of the microstructure parameters. However, the development of advanced material testing technology like the EBSD, permitted to further investigate the grain refinement mechanism [191]. It's worth noting that the results of CA simulation can be compared with the materials testing results (e.g., TEM and EBSD) from experiments directly and its spatial scale is on mesoscale, so it is only suitable for exploring local microstructures evolution at present. As shown in Fig. 63 (a) and (c), the average grain size distribution of whole chip can be obtained from the FE simulation. In addition, the grain morphology in the selected point is presented in Fig. 63 (b) and (d). Compared to the single FE simulations of orthogonal cutting with microstructure evolution model, the implementation of CA model makes it possible to lead a direct comparison between simulation and materials testing results. Therefore, the combination of the FE subroutine and CA model in this study can achieve a more comprehensive and multiscale understanding of the microstructure evolution of machining and its influence on the cutting process.

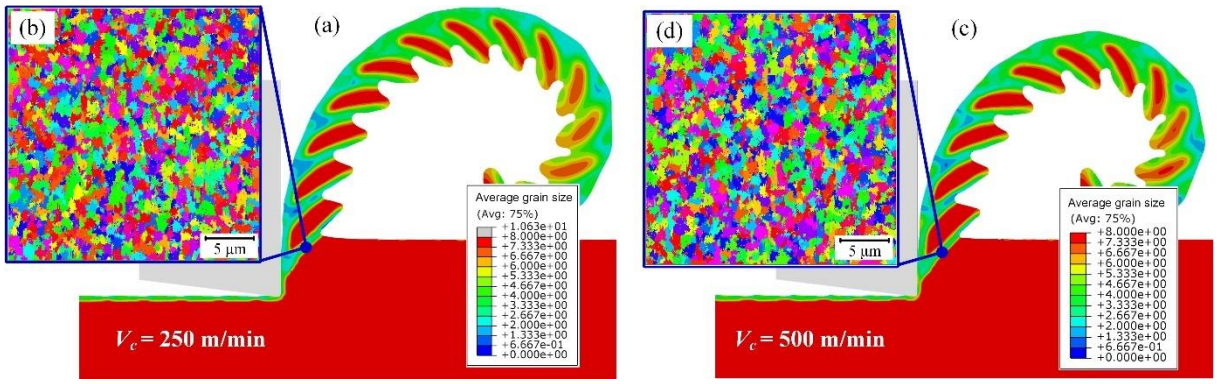

Fig. 63: Average grain size distribution simulated by FE (a and c) and the grain morphology simulated by CA method (b and d) at cutting speed of 250 m/min (a and b) and 500 m/min (c and d).

Table 17: Comparison of the DRX volume fraction, DRX grain size and average grain size between FE and CA simulations.

Simulation method	V_c = 250 m/min			V_c = 500 m/min		
	DRX volume fraction	DRX grain size (μm)	Average grain size (μm)	DRX volume fraction	DRX grain size (μm)	Average grain size (μm)
FE Simulation	0.82	0.93	1.33	0.91	1.07	1.18
CA Simulation	0.86	0.92	1.12	0.89	0.86	1.06
Difference	4.7%	5.1%	18.7%	2.2%	11.5%	11.3%

4.2.3 Validation of multiscale simulation results

To verify the accuracy of the FE machining model, the cutting force and chip morphology obtained from simulation and experiments under different cutting speeds were compared. When analyzing the experimental cutting force, the stable periods of each tooth cutting process were selected to calculate the average cutting forces. The average and standard deviation values of the simulated and experimental cutting force were calculated from 5 tests per cutting condition, as shown in Table 18. It can be summarized that cutting forces obtained by simulation is slightly larger than those of experiments, and the difference is within the reliable range. The difference between average simulated and experimental cutting force is less than 10%.

Table 18: Comparison of simulated and experimental cutting force.

Cutting speed	Simulated force F_t (N)	Experimental force F_t (N)		Difference
	Average	Average	Standard deviation	
V_c = 250 m/min	535.4	512.1	24.7	4.5%
V_c = 500 m/min	524.8	480.6	32.1	9.2%

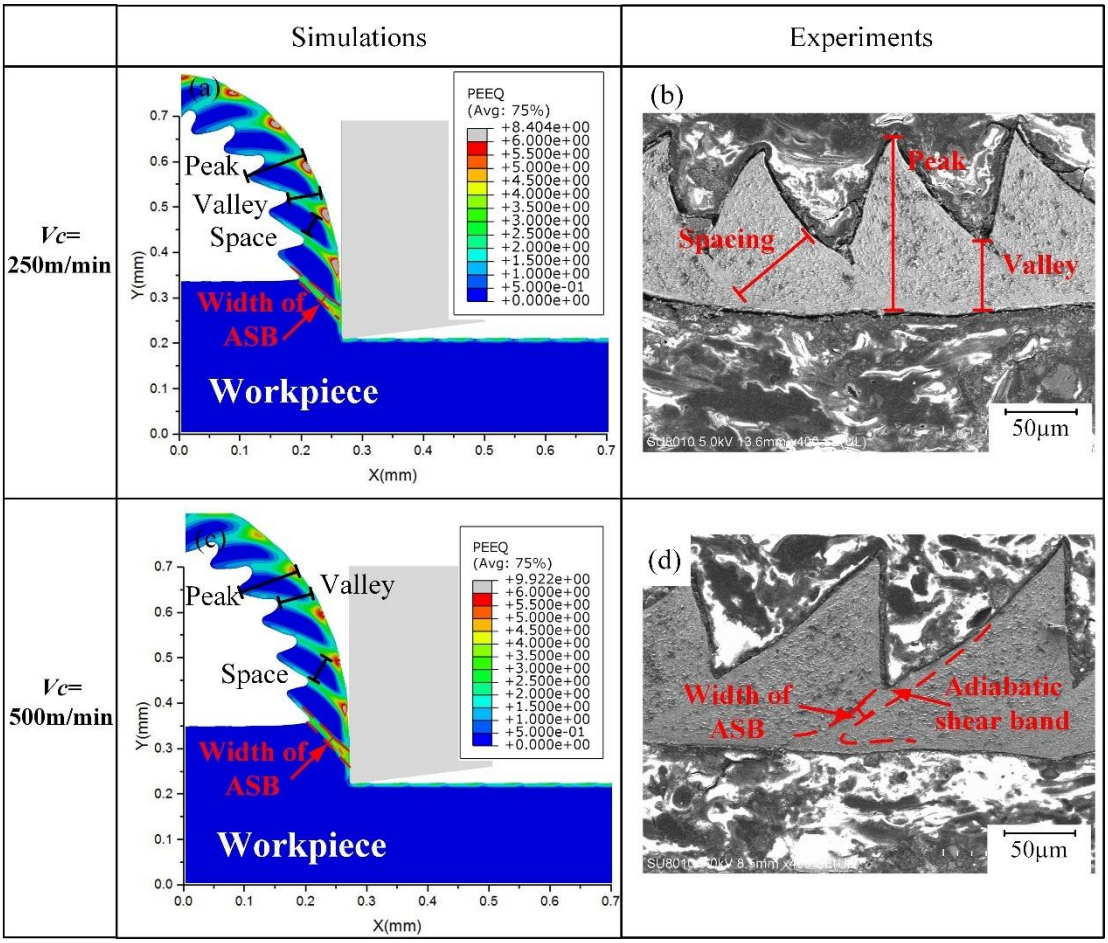

Fig. 64: The simulated equivalent strain (a and c) and SEM image of serrated chips (b and d) at 250 m/min and 500 m/min.

The serrated chips geometry obtained from simulation and experiments is shown in Fig. 9, and the morphology and structure of these serrated chips show similar characteristics. As for detailed features, the peak, valley, spacing and the width of adiabatic shear band (ASB) of serrated chips, which are noted in Fig. 64, are the commonly used typical characteristics proposed by Sutter and List [192] and Molinari et al. [193] for quantifying serrated chips dimension and the statistical results with multiple sampling and averaging are listed in Table 19. The difference of the peak, valley and spacing value of serrated chips between simulated and experimental results are within 30%. By the above comparison, the deformation parameters and

temperature calculated based on this FE machining model are considered to be reliable.

Table 19: Comparison of chip morphology between simulation and experimental tests.

	V_c = 250 m/min				V_c = 500 m/min			
	Peak (μm)	Valley (μm)	Spacing (μm)	Width of ASB (μm)	Peak (μm)	Valley (μm)	Spacing (μm)	Width of ASB (μm)
Simulation	141.5	80.8	60.2	5.9	128.3	73.7	62.7	6.5
Experimental	158.8	64.8	86	5.5	145.5	61.9	76.7	5.7
Difference	10.9%	24.7%	30%	6.8%	11.8%	19.1%	18.3%	12.3%

Fig. 65 shows the microstructure characteristics of the shear band of serrated chips obtained experimentally by Transmission Electron Microscopy (TEM) and simulated by CA model. Fine grains through DRX were observed in Fig. 65 (b) and (f), and the grain morphology and size vary with the deformation conditions at different cutting speeds. As shown in Fig. 65 (d) and (h), the simulated microstructure shows a reasonable agreement with experimental observed one. Besides that, deformed and elongated grains and twins were also observed in TEM images, which also could be formed at high strain rates, which according to the FE simulation it can reaches 10^5 /s. As a result, the TEM observed grain size was about 0.3-0.4 μm, which was smaller than CA simulated results of about 0.8-0.9 μm, since continuous DRX (cDRX) mechanism and twin formation theory were not included in this model. As shown in Fig. 66, the research work of Dargusch et al. [194] and our testing results shows that the twinning is formed in chips and machined surface, which could have direct influence on grain refinement and mechanical response. In general, this CA model was verified feasibly to predict DRX behavior of serrated chips in machining process, while a more accurate CA model considering the effect of cDRX, twinning and phase transformation behavior is expected to be developed in the future to predict the grain refinement of multiphase materials.

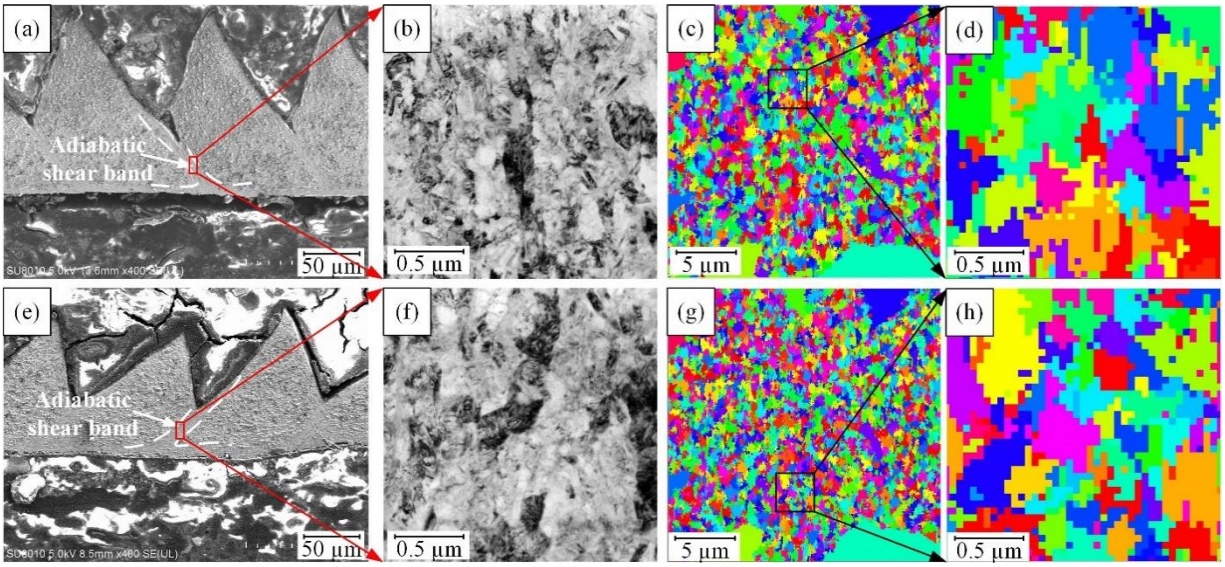

Fig. 65: (a) (e) SEM image, (b) (f)TEM image, (c) (g) simulated results and (d) (h) the enlarged image in the rectangle of (c) (g) of microstructure characteristics of serrated chips at cutting speed of 250 m/min and 500 m/min respectively.

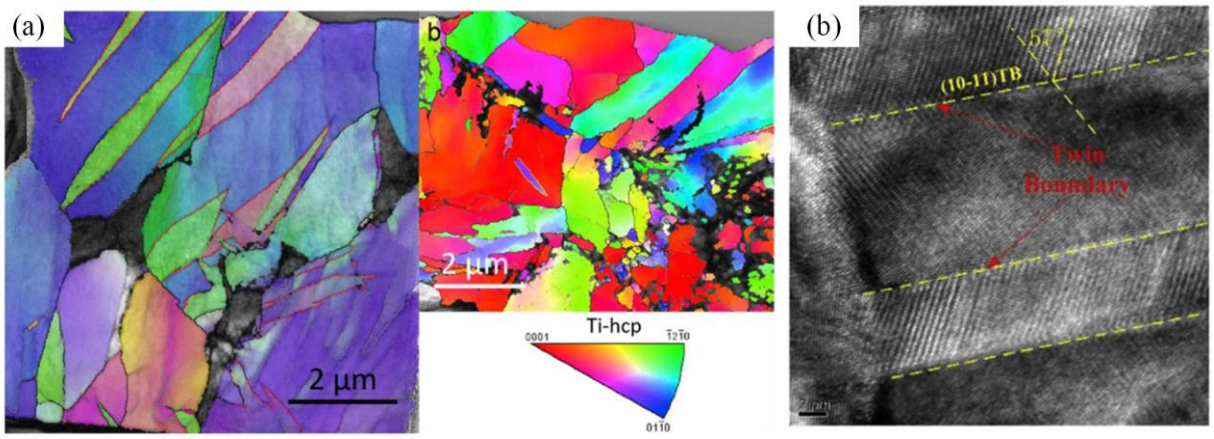

Fig. 66: (a) TKD image of twin boundaries in chips at cutting speed of 220 m/min conducted by Dargusch et al. (2018) and (b) the TEM image of twin boundaries in machined surface at cutting speed of 250 m/min conducted by our testing results during machining Ti-6Al-4V .

4.3 Analysis of grain refinement induced by DRX

4.3.1 Microstructure characteristics under different conditions

The simulated strain, strain rate and temperature in serrated chips at 250 m/min and 500 m/min are displayed in Fig. 67. It shows that the strain, strain rate and temperature of adiabatic shear band in chips at 500 m/min are higher than those generated at 250 m/min. Based on JMAK dynamic recrystallization model [59], the

distribution of DRX volume, DRX grain size and average grain size at cutting speed of 250m/min and 500m/min were obtained and shown in Fig. 68. The recrystallization behavior only occurs in the region of shear band and secondary deformation zone, which corresponding to the adiabatic shear of titanium alloy and friction between tool and chip respectively. From the DRX volume distribution in Fig. 68 (a) and (d), it can be deduced that the DRX volume fraction of shear band in chips at cutting speed of 500 m/min is higher than that of 250 m/min. And the DRX grain size of shear band at 500 m/min is also slightly bigger than that of 250 m/min which is shown in Fig. 68 (b) and (e). With increasing of cutting speed, the rise of both DRX volume fraction and DRX grain size finally leads to the decreasing of average grain size as Fig. 68 (c) and (f). From equation (42) and (44), the DRX behavior is closely related to the strain, strain rate and temperature.

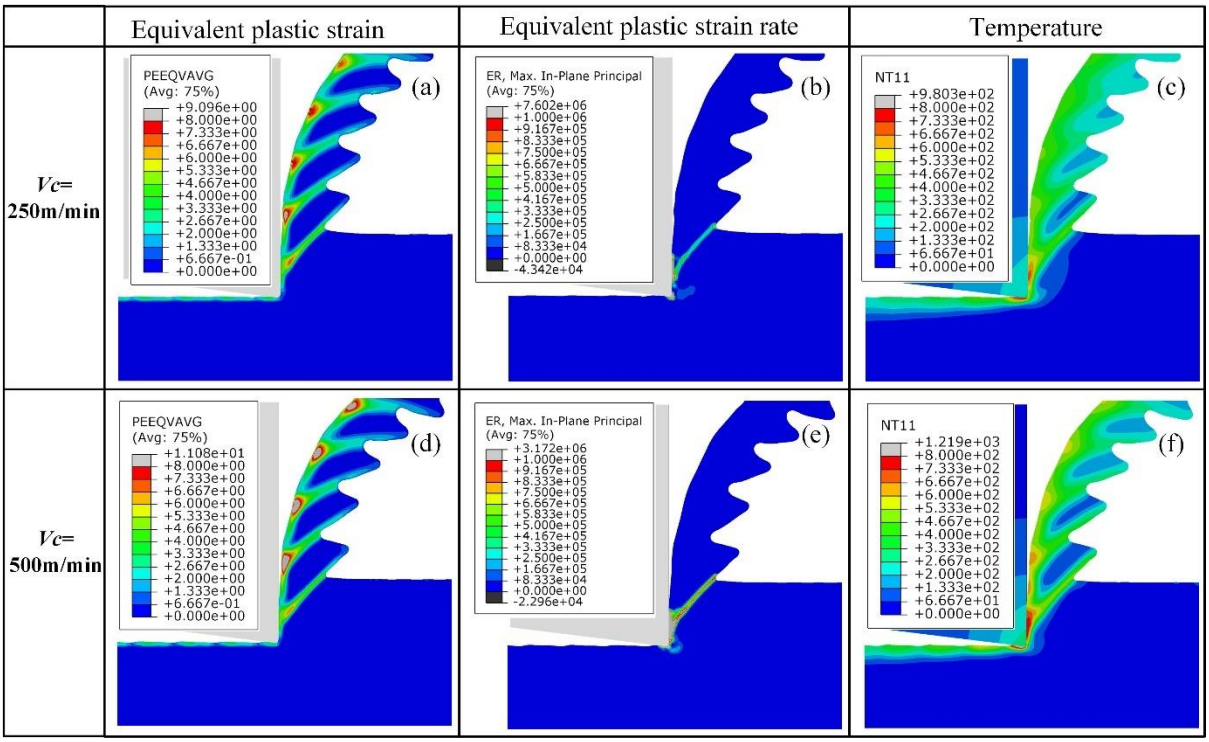

Fig. 67: The simulation results of the equivalent strain (a and d), equivalent strain rate (b and e) and the temperature (c and f) distributions in chips at a cutting speed of 250 m/min and 500 m/min.

Seen from Fig. 68, there are differences of the value of DRX volume fraction, DRX grain size and average grain size between different areas of the same shear band. In order to analyze the cause of these differences, three points are selected to compare the deformation parameters: point 1 close to the free surface, point 2 middle area, point 3 close to tool-chip contact area in shear band of chips. As shown in Fig. 68 (a) and (b), along the path from point 1 to point 3, the DRX volume fraction increases gradually, while the DRX grain

size decreases, which corresponding to the increasing of strain, strain rate and temperature in Fig. 67 (a)-(c). This phenomenon occurs because DRX behavior is based on thermal activation theory, so the DRX process can be fully completed only when the temperature exceeds the recrystallization temperature and lasts for a certain time and strain reaches a critical value. Higher strain rates enhance grain nucleation and inhibit grain growth, which relusts in smaller DRX grain size.

During cutting process, the DRX volume fraction will firstly increase, and then gradually become stable. The occurrence of adiabatic shear leads the strain in shear band to increase sharply and then decrease, which can be devided into two stages of loading and unloading. In the period of loading, the DRX is actived by large strain and high temperature, and the heterogeneous distribution of them in different regions is the essence for the differemce of DRX volume fraction and grain size. During unloading, temperature without the effect of plastic strain leads grains to a state of dynamic recovery, in which DRX volume fraction will decrease. When temperature decreases to a certain value, the microstructure evolution gradually weakens until it reaches a stable state.

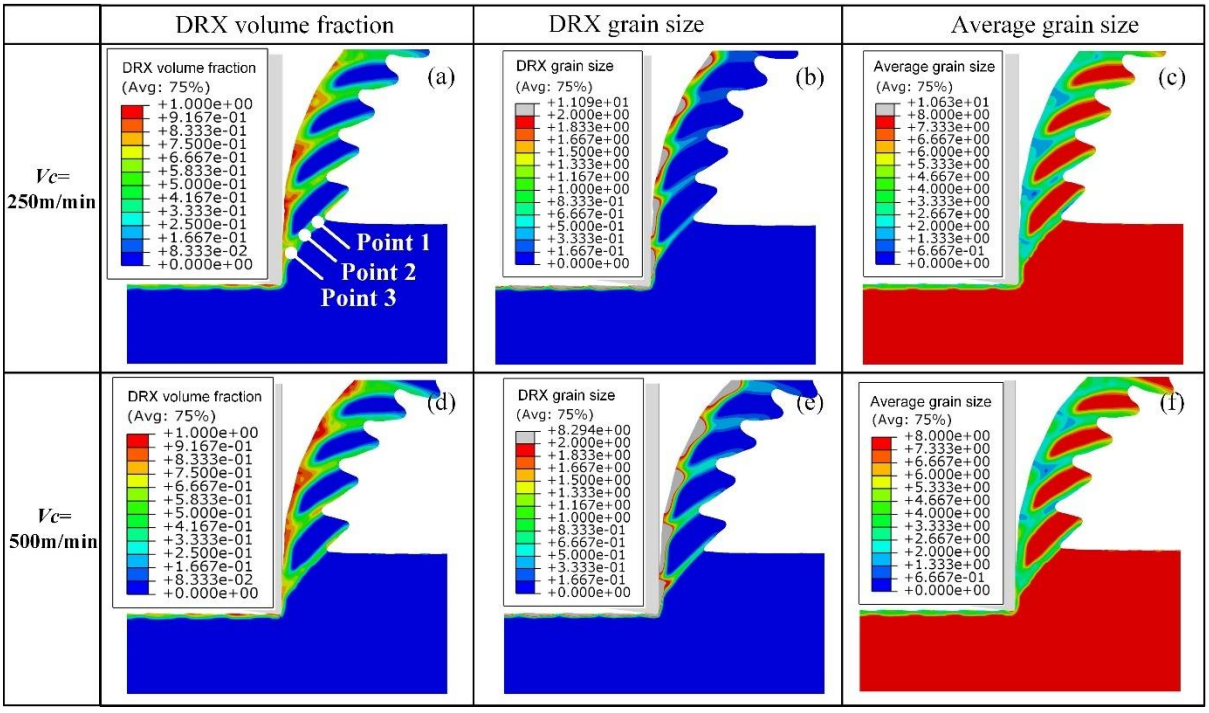

Fig. 68: Simulated results of DRX volume fraction (a and d), DRX grain size (μm) (b and e) and average grain size (μm) (c and f) distributions in chips at a cutting speed of 250 m/min and 500 m/min.

In order to compare the changes of DRX kenetics caused by cutting speed, point 2 in Fig. 68 (a) is selected

and the peak values of strain, strain rate, temperature and DRX kinetics are listed in Table 20. All of strain, strain rate and temperature rise with cutting speed increasing from 250 m/min to 500 m/min. Higher temperature is benefit for DRX behavior so that DRX volume fraction is higher at 500 m/min. The growth of DRX grain size is derived from higher temperature and longer growing time, and higher temperature and strain rate at 500 m/min eventually produce DRX grains with slightly greater size. Finally, lower average grain size of 1.18 μm is produced at 500 m/min compared to 1.33 μm at 250 m/min. The deformation condition provides the input parameters for CA simulation and the results of DRX kinetics are compared with CA results.

Table 20: Peak values of strain, strain rate, temperature and DRX kinetics at point 2 in shear band of chips in Fig. 67 and Fig. 68.

V_c (m/min)	Strain	Temperature (°C)	Strain rate (/s)	DRX volume fraction	DRX grain size (μm)	Average grain size (μm)
250	4.5	651	5×10^5	0.82	0.93	1.33
500	5.3	723	1.1×10^6	0.91	1.07	1.18

4.3.2 Strain softening behavior induced by DRX

The flow stress curve and corresponding microstructure morphology at cutting speed of 250 m/min are shown in Fig. 69. Only DRX grains are displayed in simulated microstructure morphology in which white region represents the original microstructure. The flow stress curve shows a typical DRX trend in which the strain softening phenomenon is obvious. Due to the microstructure morphology in strain of 1.1, the DRX grain nuclei begins to form at grain boundaries, and the strain hardening rate slows down when the lower dislocation density of DRX grains is introduced into the whole domain. With the increasing of strain to 2.2, the rise of DRX grains volume fraction and grain size results in the decrease of flow stress which is called strain softening effect. From the microstructure morphology in strain of 3.4, it is found that when the DRX grains grow to a certain size, the new DRX grain nuclei are formed at the previous DRX grain boundaries which cause grain size to a critical value. The continuous increasing of strain leads to DRX grains become dominant, and then the DRX grain size trend to become stable because of the dynamic equilibrium between grain nucleation and growth.

Calamaz et al. [160] proposed a constitutive model with the strain softening behavior. However, the

relationship between the grain refinement and constitutive model are not clearly investigated. Due to equation (13) and (20), the CA model including a flow stress equation based on dislocation density evolution can reflect the stress-strain response caused by dislocation density evolution during DRX process. As shown in Fig. 69, The DRX grain nuclei at grain boundaries could result in the decrease of dislocation density, which finally lead to the drop of flow stress. With the continuous increasing of strain, the rise of DRX grains volume fraction and grain size results in the decrease of flow stress due to the decrease of dislocation density.

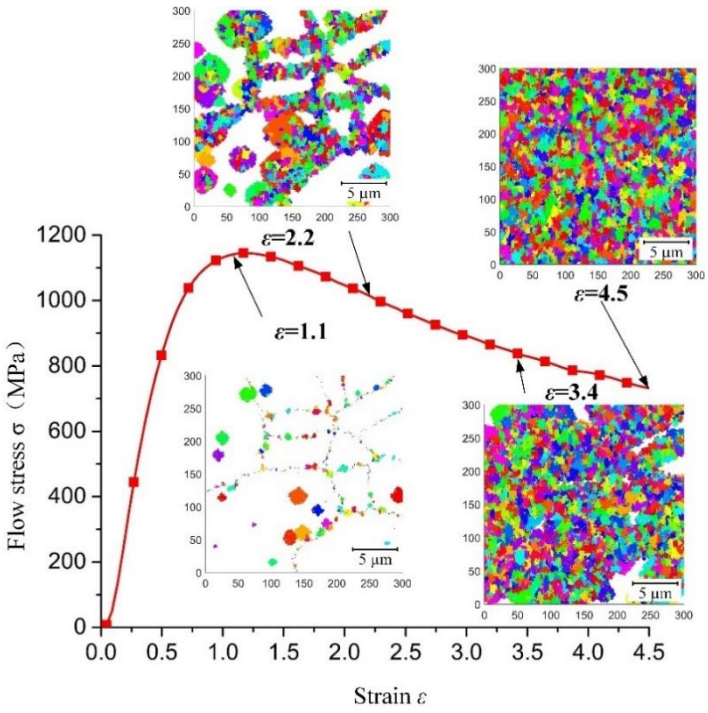

Fig. 69: Stress-strain curve and corresponding microstructure evolution at cutting speed of 250 m/min.

The flow stress curve and corresponding microstructure morphology at a cutting speed of 500 m/min are shown in Fig. 70. The flow stress at this cutting speed shows a similar trend with 250 m/min. However, the peak value of the flow stress at 500 m/min is 980 MPa, which is lower than 1150 MPa at 250 m/min due to thermal softening.

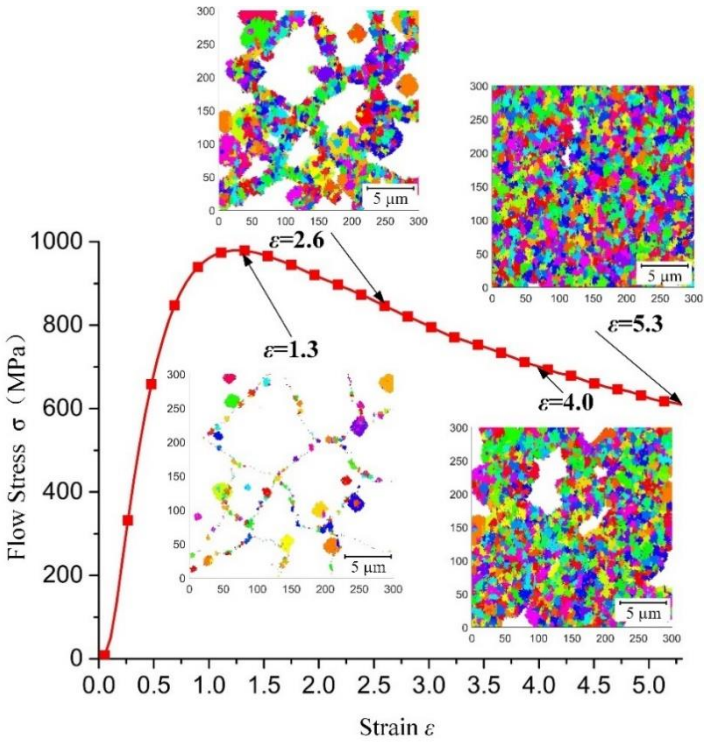

Fig. 70: Stress-strain curve and corresponding microstructure evolution at cutting speed of 500 m/min.

During the DRX process, finer DRX grains were generated and the DRX volume fraction increased, which leads to grain refinement. As shown in Fig. 71, the average grain size starts to decrease rapidly when the strain reaches the critical value of about 0.6 for DRX. Then, the decreasing rate of grain size slow down gradually due to a balance of grain nucleation and growth, which is strongly dependent on the deformation condition. The DRX volume fraction, average grain size and microstructure morphology from this CA simulation will be compared with the experimental observed results.

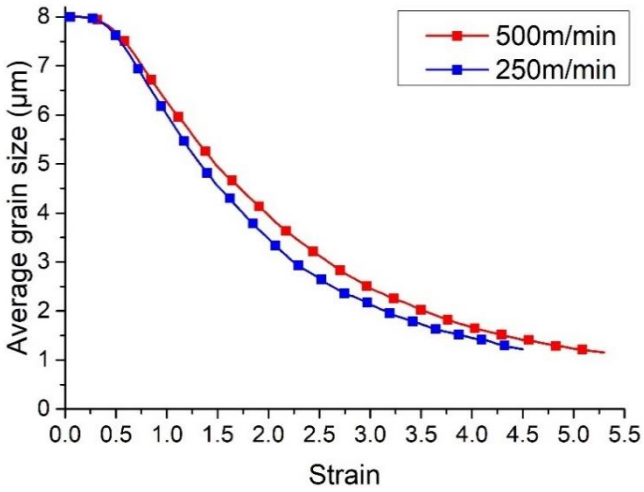

Fig. 71: Evolution of average grain size with increasing strain.

4.3.3 Effect of grain refinement on microhardness

When refined grains are generated, the physical and mechanical performance of materials would be improved, especially at the level of ultrafine grain size. The effect of grain refinement on microhardness, which is considered corresponding with the strength of the material performance, are also investigated. Picture in Table 11 shows the microhardness indentation performed in the adiabatic shear band of serrated chip, measured using HXD-1000TMC tester under the load of 50 gf for 10 s. As listed in Table 11, The microhardness in adiabatic shear band of serrated chip is higher (373-400 HV) compared with the original material (314 HV in average). According to Hall-Petch theory [69,70], the decreasing of grain size will result in the increasing of microhardness, as shown by the following equation,

$$HV = c_0 + c_1 d^{-1/2} \tag{46}$$

where c_0 and c_1 are material constants, d represents the average grain size.

Besides that, when the cutting speed increases from 250 m/min to 500 m/min, the average microhardness increases from 373 HV to 400 HV, which mainly results from higher level of grain refinement. Based on the Hall-Petch equation [69,70], the predicted microhardness by FE simulation is shown in Fig. 72. The results show that the predicted results are close to the experimental value, but slightly smaller.

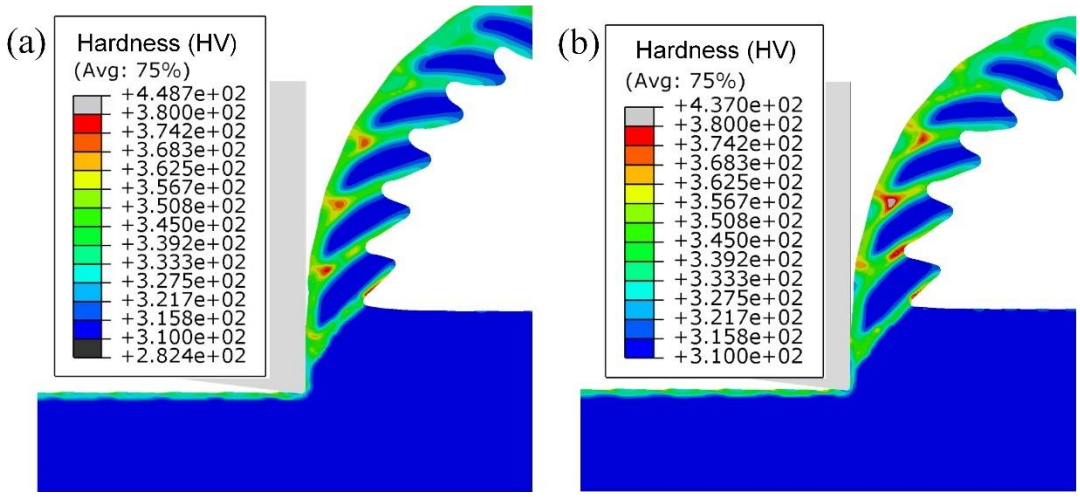

Fig. 72: Simulated microhardness using Hall-Petch equation at cutting speed of (a) 250 m/min and (b) 500 m/min.

Table 21: Experimental microhardness in adiabatic shear band of serrated chip.

		Microhardness (HV)			
		Point 1	Point 2	Point 3	Average
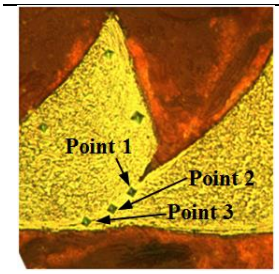	V_c = 250 m/min	386	376	356	373
	V_c = 500 m/min	408	396	396	400
	Original material	307	321	314	314

4.4 Summary of the chapter

Grain refinement process induced by DRX during HSM of Ti-6Al-4V titanium alloy was investigated experimentally and by simulation, in the last case using FE and CA methods. The JMAK grain size prediction models are used in the FE-based model to simulate the orthogonal cutting process. CA model is developed to calculate the microstructure evolution at mesoscopic level. This model considers the deformation parameters (strain, strain-rate and temperature) coming from the FE simulations as input parameters. Finally, the results from FE, CA and experiments are compared to validate the feasibility of combining FE and CA methods to investigate the grain refinement process induced by DRX of Ti-6Al-4V at high cutting speeds. The main conclusions are summarized as follows:

1) Compared to the conventional approach (defined in section 2.3) by developing subroutine in FE platform to predict microstructure evolution, the proposed multiscale microstructure model includes more physical mechanisms that are closer to the actual material deformation behavior to predict the distribution mapping of microstructure evolution, which improves the accuracy of the predicted results.
2) The results indicate that FE method is preferable for calculating the distribution of grain size in whole the workpiece and chip in macroscale, while CA method is suitable to calculate the microstructure morphology at a relatively small area at mesoscale. Therefore, the combination of the FE and CA methods can achieve a more comprehensive understanding of the microstructure evolution and its effect on the mechanical behavior of the material in the cutting process.
3) The distribution of grain size calculated by FE-based model shows that increasing the cutting speed, there are decrease of average grain size, which is induced by higher strain rate and temperature. The recrystallization behavior only occurs in the shear band region and secondary deformation zone, which corresponding to the adiabatic shear of titanium alloy and friction between tool and chip, respectively. There are differences of DRX kinetics in different areas along shear band of chips, because higher

temperature promotes the DRX, while higher strain rates enhance grain nucleation and inhibit grain growth. As a result, the decreasing of grain size resulted in the increasing of microhardness.

4) The results of microstructure evolution simulated by CA method shows a typical DRX trend of flow stress curve to reveal the strain softening phenomenon. When the DRX grain nuclei begin to form at grain boundaries, the increasing rate of flow stress slows down. With the continuous increasing of strain, the rise of DRX grains volume fraction and grain size results in the decrease of flow stress due to the decrease of dislocation density induced by DRX. At the end of the plastic deformation, the continuous increasing of strain leads to DRX grains become dominant, and the average grain size trend to become stable because of the dynamic equilibrium between grain nucleation and growth.

It should be noticed that the simulation results have an acceptable error when compared with the experimental results. A more accurate FE and CA model considering the effect of twinning and phase transformation should be developed to accurately predict the grain refinement in multiphase materials.

5 Microstructure evolution in machined surface and subsurface

5.1 Prediction of microstructure in machined surface and subsurface

5.1.1 Distribution of strain, temperature, and state of stress

The studies of subsurface plastic deformation and microstructure show that a thin layer (depth about 10~25 μm) is affected by the cutting process, which presents great challenges to research. Because the depth of this layer in machined surface is quite small, many studies directly assume that the mechanical and thermal load on the machined surface is uniform, which is far from the real situation. Therefore, as shown in Fig. 73, the distribution of plastic strain and temperature in machined surface along the depth direction is obtained by CEL cutting simulation. It can be seen from the figure that the temperature and strain gradually decrease along the depth direction of the machined surface and the depth subjected to significant thermo-mechanical effect is about 10 μm. Besides that, the effect of cutting speed on machined surface is considered in this study. The strain, strain rate and temperature along the path shown in Fig. 73 at different cutting speeds are extracted and drawn in Fig. 74. The strain and strain rate increase with the cutting speed at the same depth place from the surface. While as for the temperature, the temperature of the nearest surface at higher cutting speed is higher, but the temperature drops faster along the depth direction at higher cutting speed, which shows a more significant temperature gradient. Considering that dynamic behavior depends strongly on the strain, strain rate and temperature condition, different DRX modes can be activated in different depth zones of the same sample. The strain, strain rate and temperature distribution simulated by CEL cutting model will be applied as the input deformation condition of the following cellular automata (CA) model to predict the microstructure evolution.

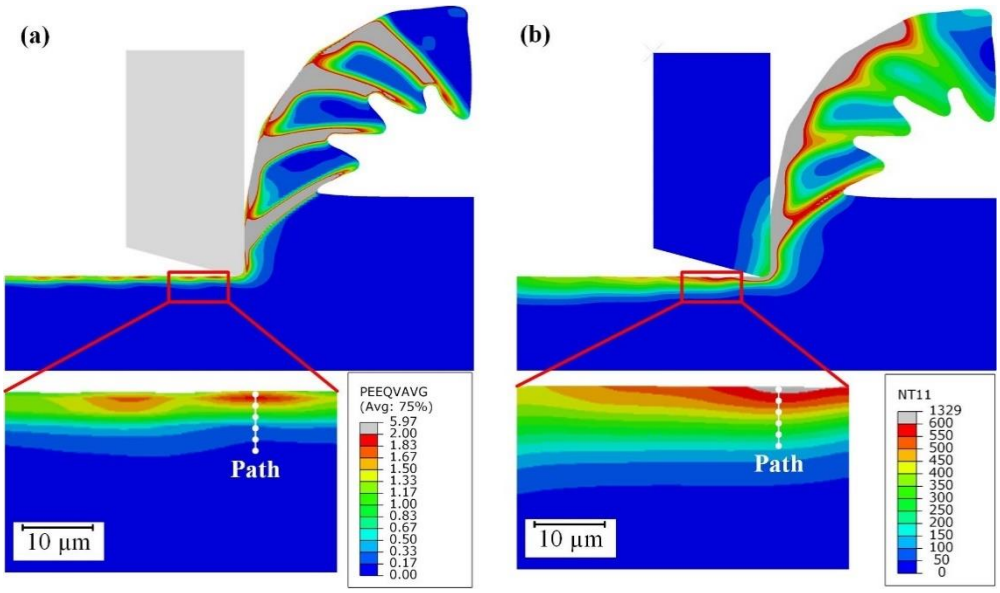

Fig. 73: The plastic strain and temperature distribution in machined subsurface obtained by FE simulation at cutting speed of 250 m/min.

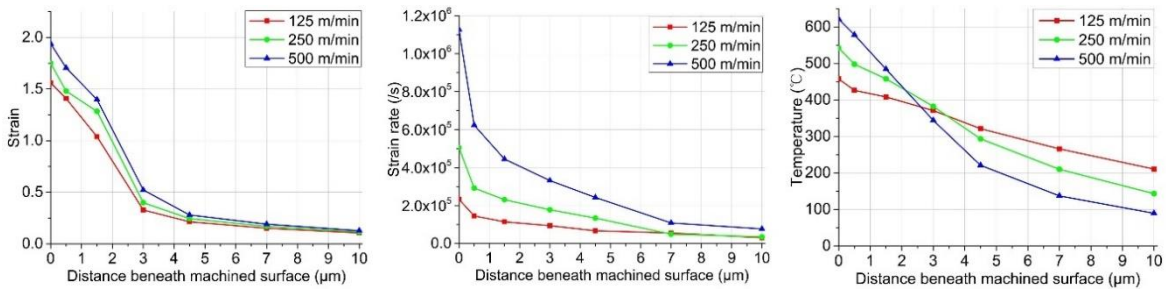

Fig. 74: The curve of plastic strain, strain rate and temperature distribution along the path in Fig. 73.

Fig. 75 (a) shows the distribution mapping of the principal stress in the XY plane, where the arrow vector represents the direction of the principal stress. The magnitude and direction of the principal stress in different regions, located at 1~10μm depth from machined surface, vary greatly. This phenomenon indicates that the stress at same region changes dynamically with the cutting process. The stress state of point A, 2μm depth from surface, is displayed in dotted rectangle of Fig. 75 (a), where the normal stress σ_α and shear stress τ_α of any section are calculated from the stress component (σ_x, σ_y, τ_{xy}) and α is the angle between σ_α and Y-axis. The two principal stresses of point A can be expressed as

$$\begin{matrix}\sigma_1 \\ \sigma_2\end{matrix} = \frac{\sigma_x + \sigma_y}{2} \pm \sqrt{\left(\frac{\sigma_x - \sigma_y}{2}\right)^2 + \tau_{xy}^2} \tag{47}$$

where the direction angle α_1 between the principal stress σ_1 and X-axis is defined by:

$$\tan 2\alpha_1 = -\frac{2\tau_{xy}}{\sigma_x - \sigma_y} \tag{48}$$

And the maximum shear stress is obtained from:

$$\tau_{\max} = \frac{1}{2}(\sigma_1 - \sigma_2) = \sqrt{\left(\frac{\sigma_x - \sigma_y}{2}\right)^2 + \tau_x^2} \tag{49}$$

The variation of above principal stresses and shear stress with cutting time is plotted in Fig. 75 (b). At the beginning, cutting process is in a stable stage, and the maximum principal stress and maximum shear stress in the XY plane are about -1000 MPa and 500 MPa, respectively. Then the amplitude of maximum principal stress and shear stress increase rapidly due to the impact between cutting tool and workpiece, and Fig. 75 (c) shows that the angle between the principal stress and Y-axis varies from 80° to 0°. The shear stress unloads rapidly after the peak value 760MPa is reached, while the principal stress keeps increasing continuously. As a result, the stress state transforms from composite stress with compressive stress along the X-axis and shear stress into compressive stress along the Y-axis until the unloading of stress.

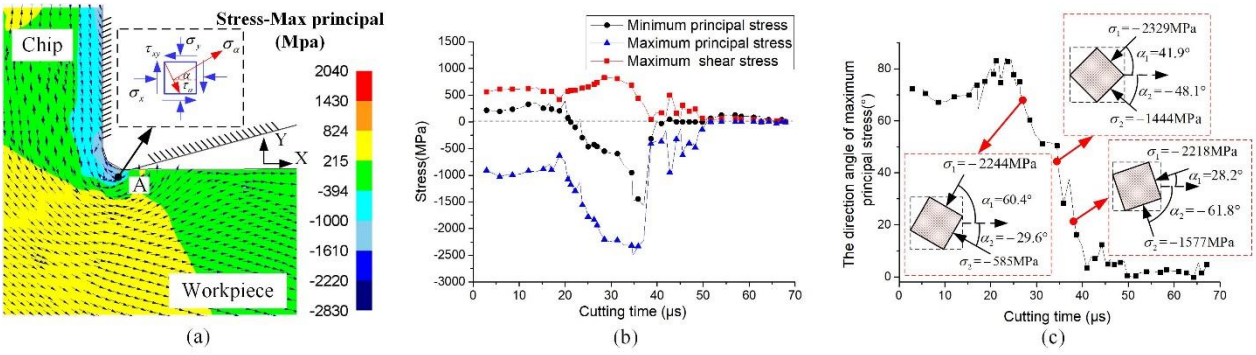

Fig. 75: Stress state of machined surface (a) distribution mapping of maximum principal stress in XY plane (b) variation of the stress component with cutting time (c) the direction angle variation of maximum principal stress at point A with cutting time

5.1.2 Experimental characterization of the distribution of the grain size

To better describe microstructure evolution in machined surface, white layer and deformed layer are defined to present the metallurgical characteristics observed in OM and SEM, while “nano grains” layer and “micro

grains" layer are used to describe the grain characteristics observed by TEM and PED. From the review of Huang et al. [195], it can be seen that the critical activation condition for different dynamic recrystallization modes of materials depends on the range of temperature and strain. By analyzing the metallurgical characteristics of the machined surface (as shown in Fig. 76), corresponding to the deformation conditions of the machined surface, two layers with different characteristics in different depths are generated, in which D3 zone with white layer characteristic and D2 zone with grain refinement and deformation. It is worth noting that there is an obvious boundary between D2 and D3 zone, which indicates that the microstructure has performed a significant transformation. Therefore, the TEM and PED techniques are applied to quantitatively characterize and analyze the microstructure in machined surface.

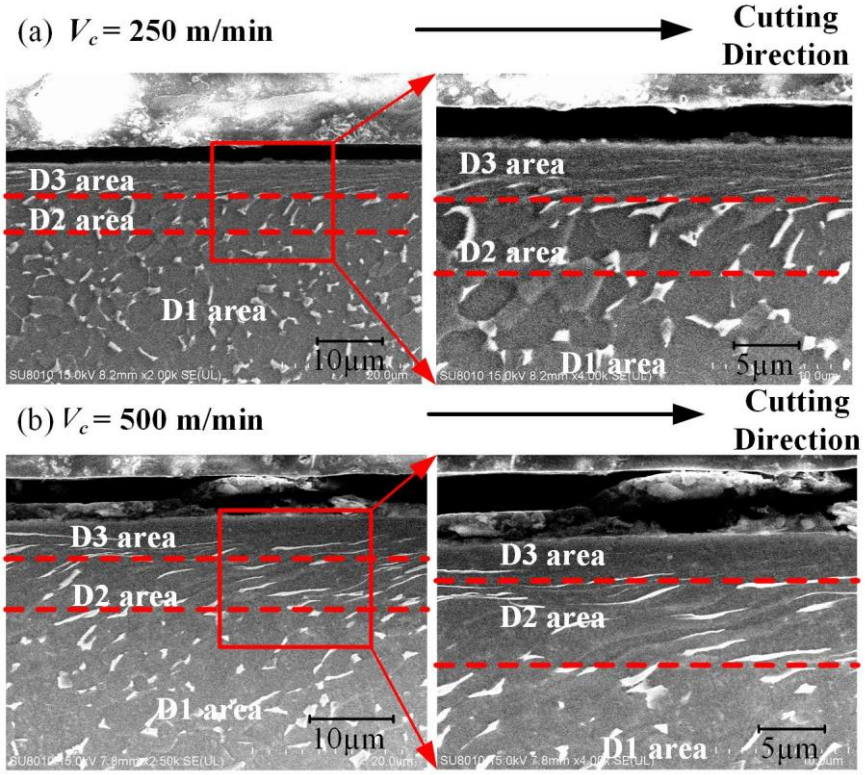

Fig. 76: Metallurgical characteristics of machined subsurface under cutting speed of 250 m/min and 500 m/min.

Fig. 77 is the microstructure distribution image obtained from TEM and PED techniques. From Fig. 77 (a) and (c), the grain morphology shows that the grain size in the nearest surface ranges from 100 to 200 nm and some equiaxed fine grains smaller than 50 nm are generated in the boundary of these grains. The grain structure in this layer shows typical discontinuous DRX characteristics. The grain size in deeper layer is much greater than that in the nearest layer. As shown in Fig. 77 (c), the color difference within the same grain

can be observed in the refined grains layer, in which different colors represent different orientations. Local misorientation and low angle grain boundary in grain interior is the typical continuous DRX characteristics. Fig. 77 (b) is the corresponding grain orientation distribution image without twins which is handled with the open-source software ATEX [196] and Fig. 77 (d) is the grain boundary distribution image including low angle boundary, high angle boundary and twin boundary. It can be seen from the figures that there are great numbers of twins in the nano-grains layer but almost no twins in the refined grain layer. Obviously, two different layers of twins distribution is also one of the characteristics for gradient distribution of microstructure evolution. However, considering that the model for twinning evolution has not been implemented in CA simulation and this study mainly considers the effect of different DRX modes induced grain refinement mechanism. So, the influence of twins is ignored temporarily, and the experimentally measured grain size is also obtained without considering twins.

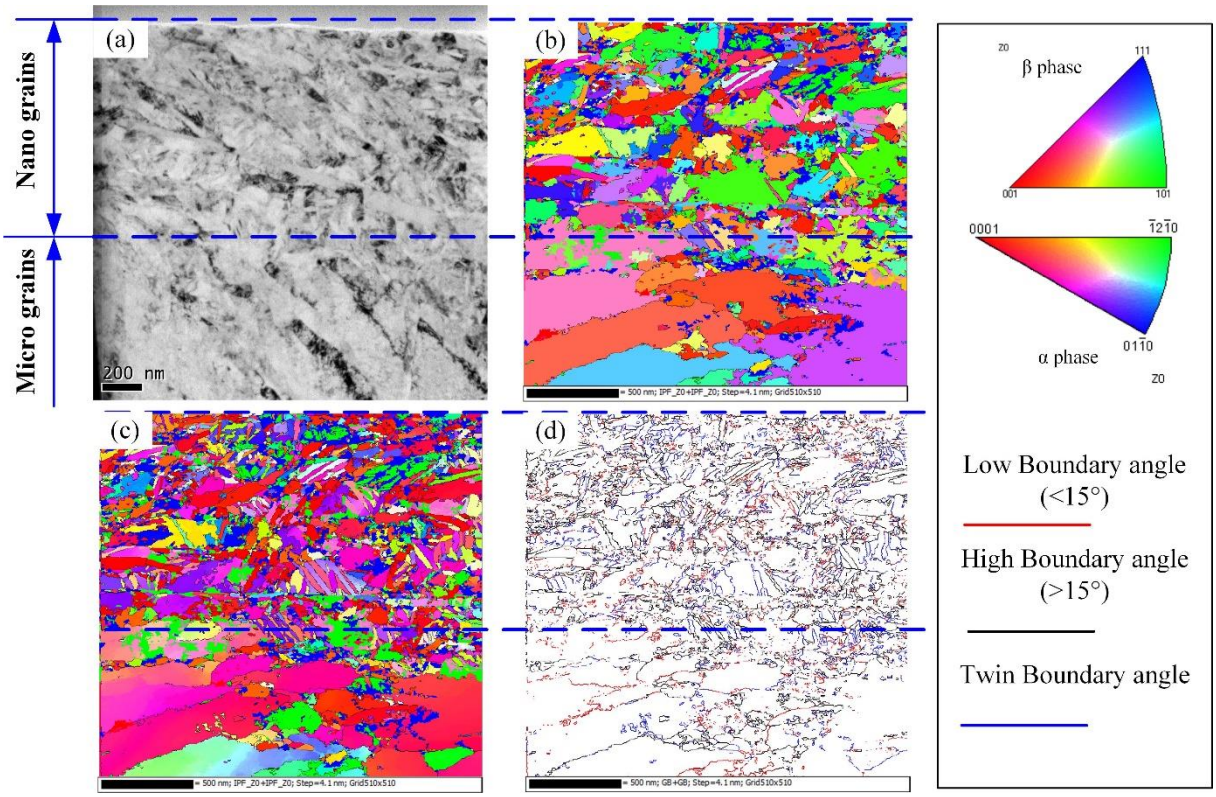

Fig. 77: (a) and (c) are TEM and PED images of grain distribution, respectively, (b) is the corresponding PED image without twins, and (d) is the grain boundary distribution in the machined subsurface at cutting speed of 250m/min.

The TEM observation of the "micro layer" (as shown in Fig. 78 (a) and (b)) shows that many dislocation

tangles and lines can are generated. And through the high resolution TEM (HRTEM) observation of these dislocations (Fig. 78 (c)), the existence of a large number of dislocations was further verified. After Fourier transform (FFT) and Inverse FFT (IFFT) of Fig. 78 (c), Fig. 78 (f) can help us determine the location of dislocation. The generation and pile-up of these dislocations would result in the local misorientation in the grain interior. And then the low angle boundary will form due to the accumulation of local misorientation, which shows the characteristic of subgrains in Fig. 78 (d) and (e). According to the review of Sakai et al. [197], the high dislocation density and a large number of subgrains are the main characteristics of continuous DRX. Therefore, the grain refinement in the refined grain layer mainly results from cDRX mechanism.

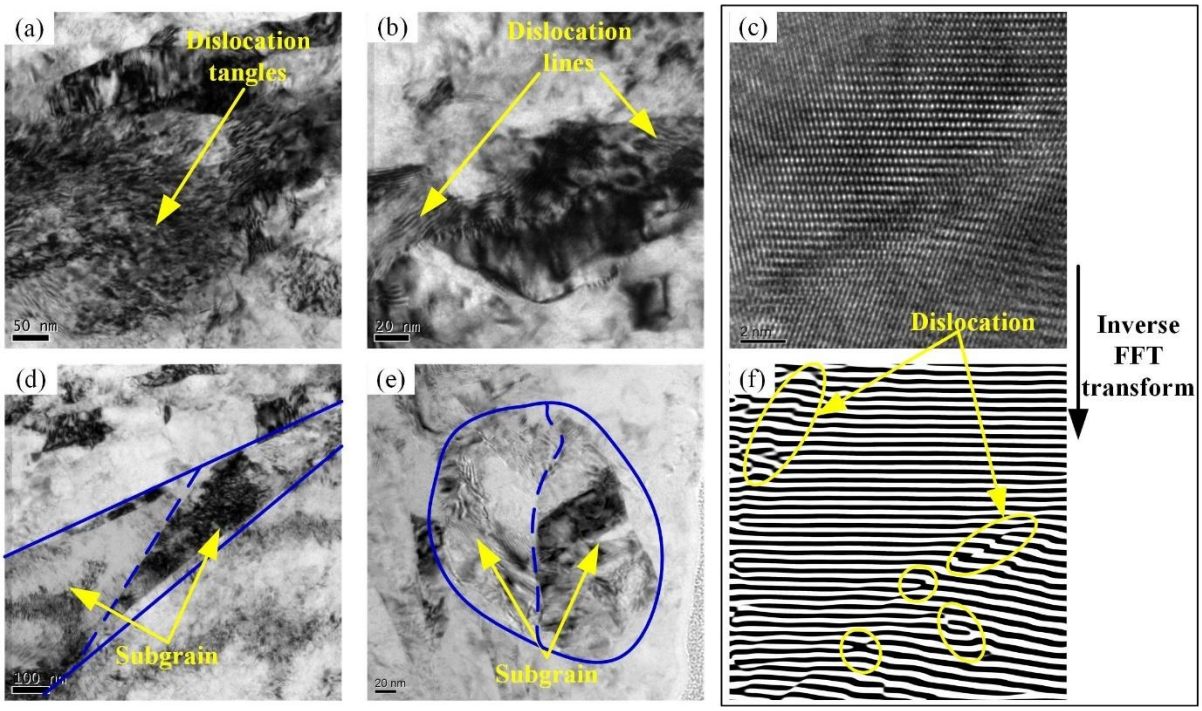

Fig. 78: TEM images of dislocation and cDRX grains characteristics in "refined grain" layer of machined subsurface at cutting speed of 250 m/min.

The TEM observation of the nano-grain layer (as shown in Fig. 79) shows that many equiaxed nanoscale grains can be found in the grain boundary of another larger grain, which is the typical characteristic of discontinuous DRX behavior. cDRX behavior is always activated by strong thermal plastic deformation. Besides that, cDRX behavior is sensitive to the grain boundary fraction of materials, which means that the increase of grain boundary fraction will enhance the nucleation of new grains. The grain size in the nano-grains layer (~50-200 nm) is quite smaller than the original grain size (~8 μm). In the absence of a large

number of grain boundaries in the original materials, how the grain refinement process can be achieved and the final microstructure show the cDRX characteristic cannot be analyzed only by present experimental observation. In addition, dDRX behavior needs to experience the process of grain nucleation and growth, so its evolution time is generally longer than that of cDRX behavior, so dDRX behavior is always accompanied by cDRX behavior. Its fundamental explanation will be discussed by combining the CA simulation results.

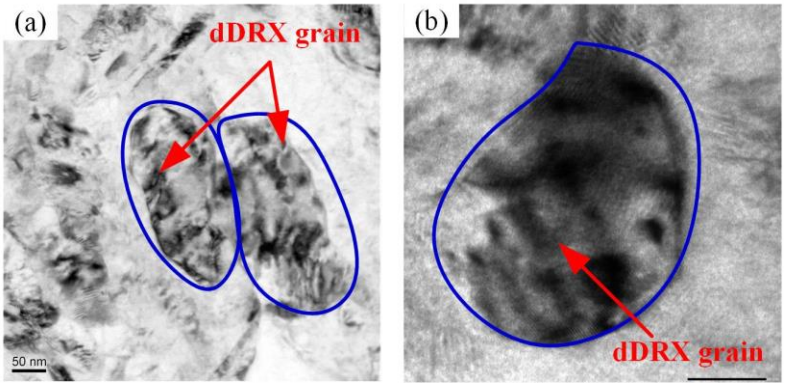

Fig. 79: TEM images of dDRX grains characteristics in machined subsurface in "Nano grains" layer of machined subsurface at cutting speed of 250 m/min.

5.1.3 Simulation of the microstructure

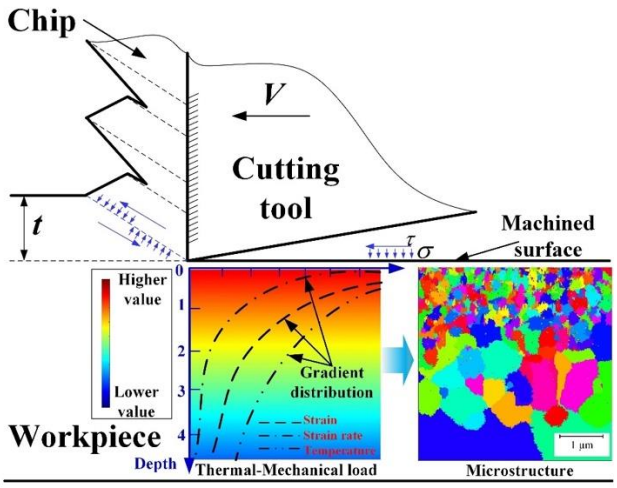

Fig. 80: The relationship between thermal-mechanical load and microstructure to present the formation mechanism of gradient of microstructure in the machined surface and subsurface.

The results of the above two section reveal that the deformation and microstructure of machined surface show gradient of microstructure along the distance beneath the machined. Fig. 80 presents the relation between

thermal-mechanical load and microstructure to show the formation of gradient of microstructure in the machined surface. As shown in the figure, after the loading of cutting force and heat in surface, the strain, strain rate and temperature start to decrease along the depth direction. The deformation and thermal conditions in different depths obtained by CEL cutting simulation are extracted as the input of the CA microstructure model. The image of grain morphology simulated by CA shows that the characteristics of microstructure in different depths are quite different. How does the decay of thermo-mechanical coupling lead to the gradient of microstructure and the mechanism of microstructure evolution will be analyzed.

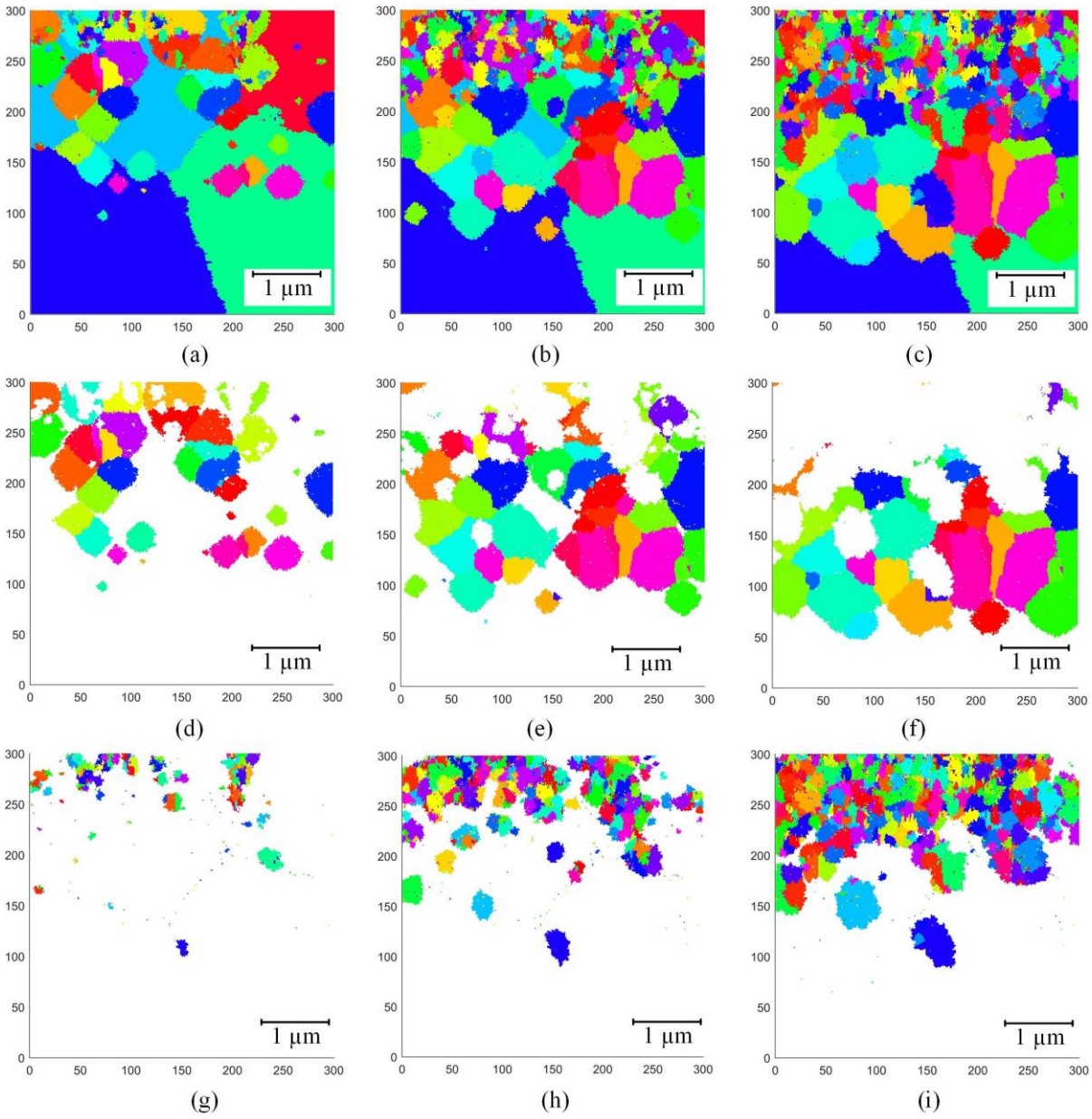

Fig. 81: Distribution of microstructure, cDRX grains and dDRX grains simulated by using CA model at different step time.

Distribution of total microstructure, only cDRX grains and only dDRX grains simulated by using CA model at different step times are shown in Fig. 81. In the beginning stage (Fig. 81 (a), (d) and (g)), cDRX grains (Fig. 81 (d)) form in most areas of the nearest machined surface, while in deeper area cDRX grains also start to form but relatively less. In this stage, the dDRX grains (Fig. 81 (g)) nucleation starts to occur in the grain boundary of cDRX grains in the nearest surface. When it comes to the intermediate stage (Fig. 81 (b), (e) and (h)), the fraction of cDRX grains (Fig. 81 (e)) in the nearest surface reduces while that in deeper surface rises. The decrease of cDRX grains in the nearest surface corresponds to the increase of dDRX grains (Fig. 81 (h)), in which more grown grains and newly nucleated grains can be found. In the near ending stage (Fig. 81 (c), (f) and (i)), most of the cDRX grains (Fig. 81 (f)) have disappeared in the nearest surface, which is instead mainly composed of dDRX grains (Fig. 81 (i)). And the fully cDRX grains are formed in a deeper surface and there are few dDRX grains in this layer.

5.1.4 Grain refinement mechanism at different layers beneath the surface

The formation mechanism of different layers in Fig. 81 is further analyzed in this part. From the previous analysis, it can be deduced that the dDRX grains nucleation in the nearest surface is derived from the formation of cDRX grain boundary. From the grain nucleation condition of dDRX grains described in section 4.2, we can know that dDRX grains only nucleate in the grain boundary. So, the formation of the cDRX grain in the nearest surface provides lots of grain boundary, which benefits the dDRX grains nucleation. A schematic diagram of microstructure evolution in different layers in machined surface with cutting process is drawn as Fig. 82 to reveal the grain refinement mechanism in different layers, which will be discussed with four steps. In step 1: the dislocation density within the grain interior in the refined grains layer is increasing, and the subgrains induced by the accumulation of dislocation have formed in the nano-grains layer. The higher strain, strain rate and temperature in the nano-grain layer induce a higher generation rate of dislocation than that in the refined grain layer, which makes the grain refinement process faster in the nano-grain layer. In step 2: due to the continuous generation and pile-up of dislocation, the local misorientation further increases until the low angle boundary becomes high angle boundary, which results in the formation of full cDRX grains in the nano-grain layer. While in this step, the subgrains just start to form in the refined grain layer. In step 3: in the nano-grain layer, the formation of cDRX grains provides a great number of grain boundaries for grain nucleation of dDRX, so lots of dDRX starts to nucleate in the grain boundary of cDRX grains. The subgrains evolve gradually into full cDRX grains. In step 4: the dDRX grains have grown in the nano-grains layer and the nucleation and growth of grains will reach a balanced state, which determines the

final dDRX grains morphology and size.

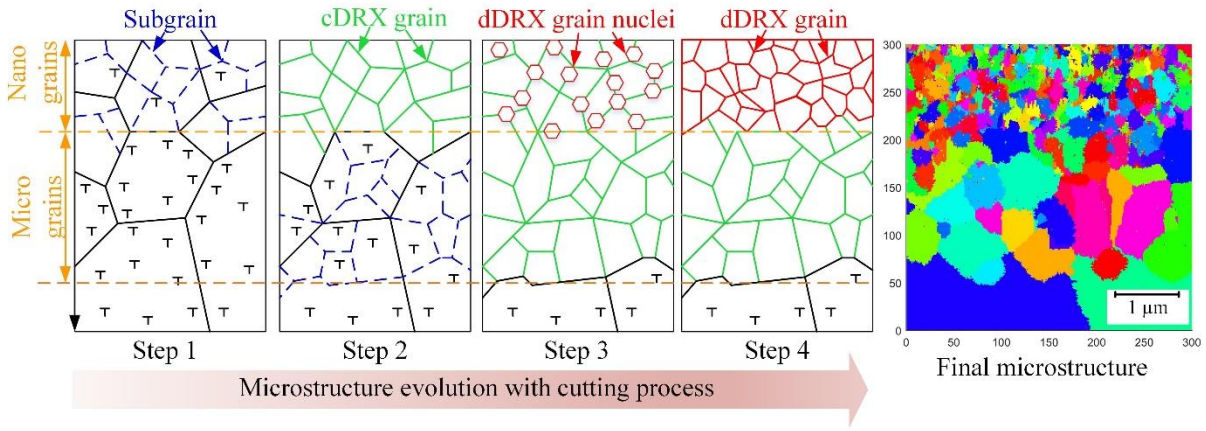

Fig. 82: Schematic diagram of microstructure evolution with cutting process showing different structures formation.

From the above analysis, it can be deduced that the refined grain layer is formed only by the cDRX mechanism and the nano-grain layer is resulted from a combined effect of cDRX and dDRX mechanism. The analysis of grain refinement mechanism of the nano-grain layer can provide a fundamental understanding of microstructure evolution in whole surface depth. The mechanism of the grain refinement process in the nano-grain layer is presented in Fig. 83. This process is divided into six steps: (a) a large number of dislocations are generated at the beginning of loading; (b) the dislocation accumulation induced by dislocation movement leads to the local misorientation of grains; (c) subgrains are formed with low angle boundary and step (a) and (b) provide the power for subgrains rotation; (d) when the misorientation between adjacent subgrains increases greater than 15 degrees, low angle boundary becomes high angle boundary and full cDRX grains is formed; (e) the refined cDRX grains generate lots of grain boundary and high dislocation density condition, which provide the favorable conditions for dDRX nucleation; (f) finally, full dDRX grains are formed after grain growth. This is the grain refinement mechanism of the nano-grain layer. While for refined grain layer, due to lower level of strain and temperature, the critical condition for nucleation cannot be met, so the refined grain layer only experience step (a), (b), (c) and (d) and full cDRX grains are formed.

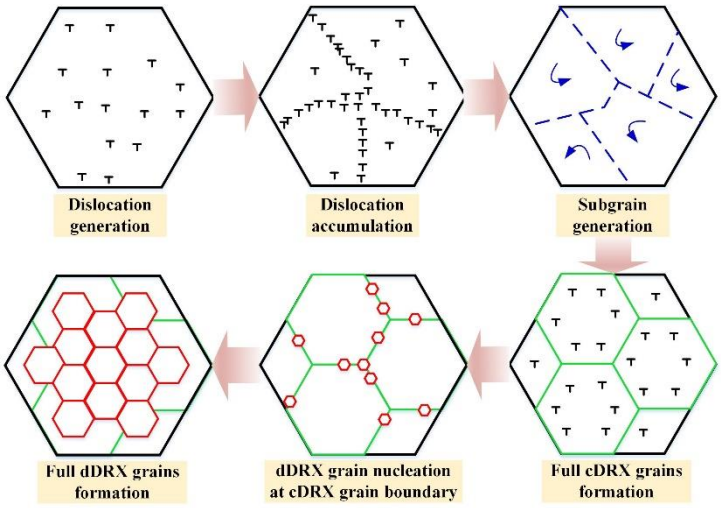

Fig. 83: Schematic to show the mechanism of the grain refinement process in the nano-grain layer of machine surface.

5.2 Experimental characterization of the microstructure in machined surface and subsurface

5.2.1 Metallurgical characteristics at different cutting speeds

The obtained SEM images (Fig. 84) of metallurgical characteristics in machined surface indicate that the depth of subsurface affected by HSM is about 10 μm. The deformed zone of subsurface could be divided into three zones marked as D1, D2 and D3: zone D1 displays the original structure, zone D2 presents the deformation and elongation of grains along cutting direction, and zone D3 shows the disappearance of the feature about original structure. The information of drastic crystalline modification is recorded by zone D3, the so called highly perturbed layer. In terms of the feature of microstructure and intense thermo-mechanical deformation, the results imply that high density dislocation motivation, grains refinement and phase transformation are generated most probably. As a result, it is further investigated by TEM and PED technology and selected area for FIB sample is shown in blue rectangle dotted line of Fig. 84.

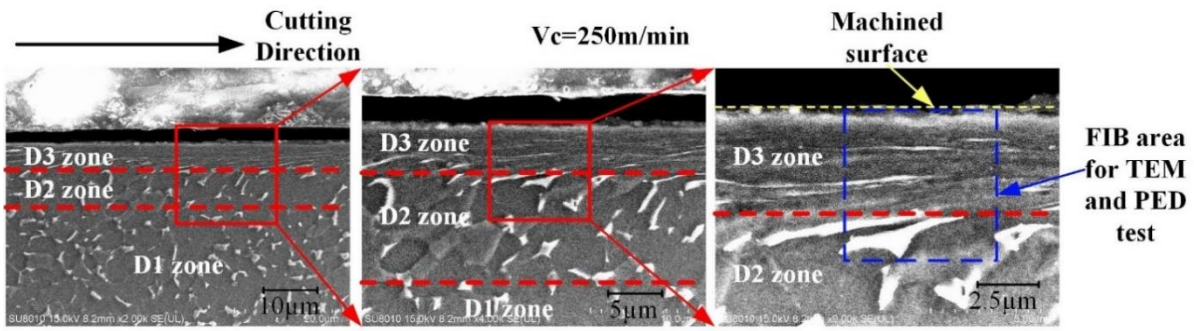

Fig. 84: SEM metallurgical characteristics image of machined subsurface at cutting speed of 250 m/min.

The comparison of microstructure characteristics in machined surface at cutting speed of 125 m/min and 250 m/min is shown in Fig. 85 and Fig. 86, respectively, in which several specific areas are selected for HRTEM observation to show the change of microstructure with the increase of cutting speed. From the TEM morphology and the corresponding SAED image shown in Fig. 85 (a), grains deformation has occurred and the grains are refined slightly at 125 m/min. Fig. 85 (c), (d) and (e) are TEM images of selected areas in Fig. 85 (a) showing the elongated and deformed grains, and (b), (f), (g) and (h) are HRTEM images showing the interior and boundary of grains consist of high density of dislocation and stacking fault. Twins are not found in the TEM observation at this cutting speed. As a result, it can be deduced that the grain deformation and refinement mechanism at this cutting speed results from evolution of dislocation density. Fig. 86 shows the TEM image of microstructure at 250 m/min, severe grain refinement can be observed from the TEM morphology and corresponding SAED image in Fig. 86. Moreover, the morphology (see Fig. 86 (c), (d) and (e)) shows the characteristics of twins, and the images of FFT (see Fig. 86 (b) and (f)) show the twin boundaries are $\{10\bar{1}1\}$ type. The interior of the twins contains dislocations with high density (see Fig. 86 (b) and (h)), and higher density dislocation still exist in grains free of twin boundaries as shown in Fig. 86 (g). Due to the generation of twins induced by high strain rate, the change of deformation mechanism of machined surface caused by high strain rate. Therefore, the grain refinement mechanism of machined surface at 250 m/min will be discussed in detail in the following.

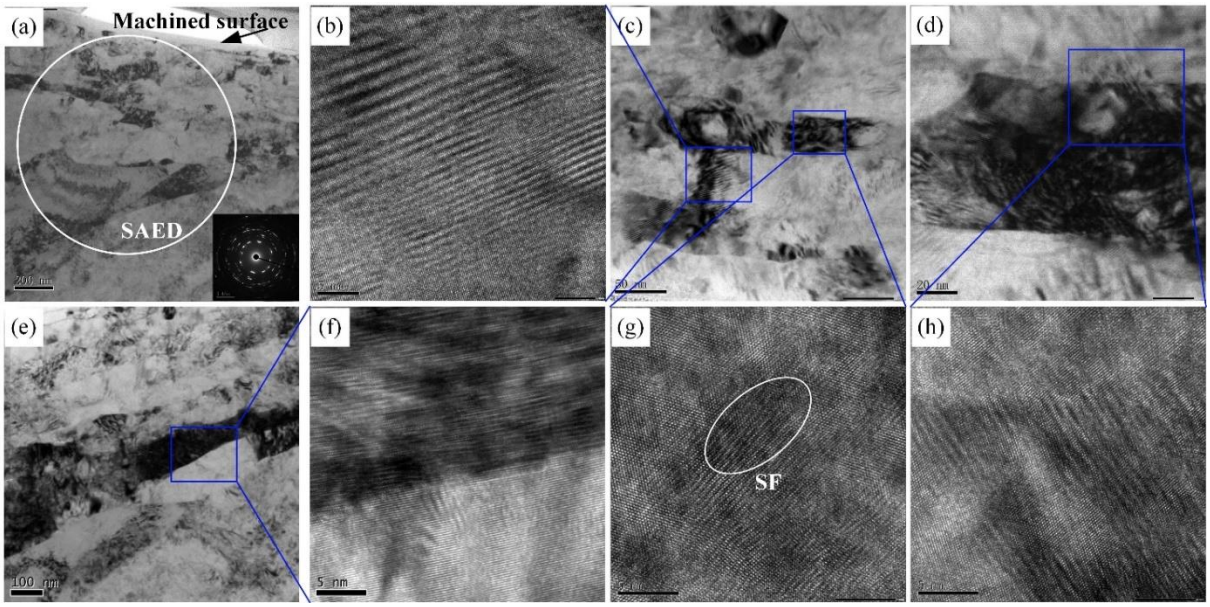

Fig. 85: Microstructure of machined surface at cutting speed of 125 m/min observed by TEM

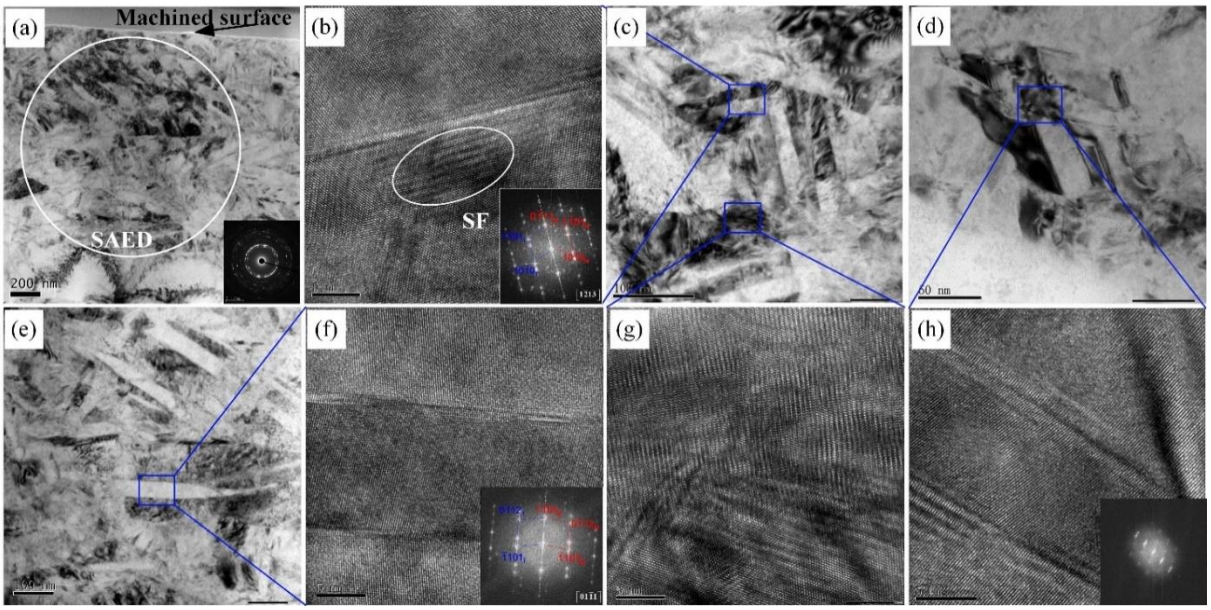

Fig. 86: Microstructure of machined surface at cutting speed of 250 m/min observed by TEM.

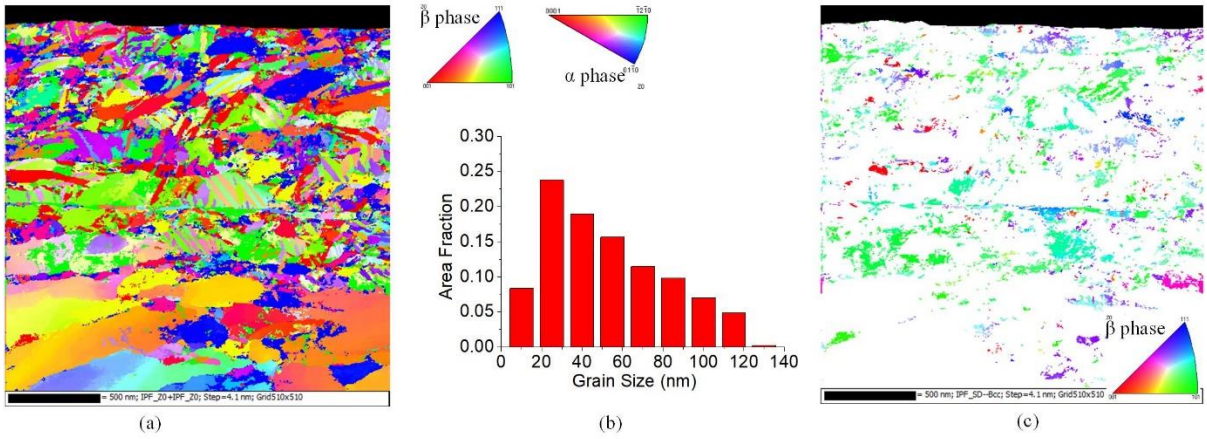

Fig. 87: Microstructure of machined subsurface observed by PED. (a) the PED orientation distribution map containing α and β phase observed by orientation indexing microscopy(OIM), (b) the area fraction distribution of grain size and (c) the orientation distribution map for β phase.

The TEM morphology and corresponding SAED image in Fig. 86 (a) demonstrates that plenty of nanoscale grains are generated in subsurface after HSM. The PED technology is applied successfully to quantitatively characterize the crystal orientations of nanoscale grains with a resolution higher than 95%, as shown in Fig. 87 (a). The inverse pole-figure (IPF) map of orientation distribution containing all α and β grains shows the grains are highly refined and deformed. The area fraction distribution of grain size in Fig. 87 (b) is the statistical results of Fig. 87 (a), in which twins are included. Fig. 87 (b) shows that most grains are with the

sizes between 20 to 70nm and some grains are even with average diameters less than 20nm. Fig. 87 (c) presents a dispersed distribution of β grains, which means that phase transformation may have occurred and have a certain effect on the dislocation evolution and grain refinement.

In Fig. 88 (a) and (b), low angle grain boundaries (LAGBs) with misorientations in the range 4°~15° account for over 20% which indicates that lots of dislocation has been piled up and many subgrains have not yet been transformed into high angle boundary grains. The most proportion and dense distribution of high angle grain boundaries (HAGBs) confirm that most grains of surface produced by HSM is complete nanoscale grains rather than subgrains. In Fig. 88 (b), it's worth noting that HABs arise peak values in around 35°, 60° and 80°, which probably represent large number of twin boundaries (TBs), maybe including types of $\{11\bar{2}1\}$, $\{10\bar{1}1\}$, $\{11\bar{2}2\}$and $\{10\bar{1}2\}$, is generated. As for dislocation and twinning conjointly account for plastic deformation under high strain rate, the formation mechanism of nanoscale grains is analyzed by considering dislocation motion and twinning in discussion.

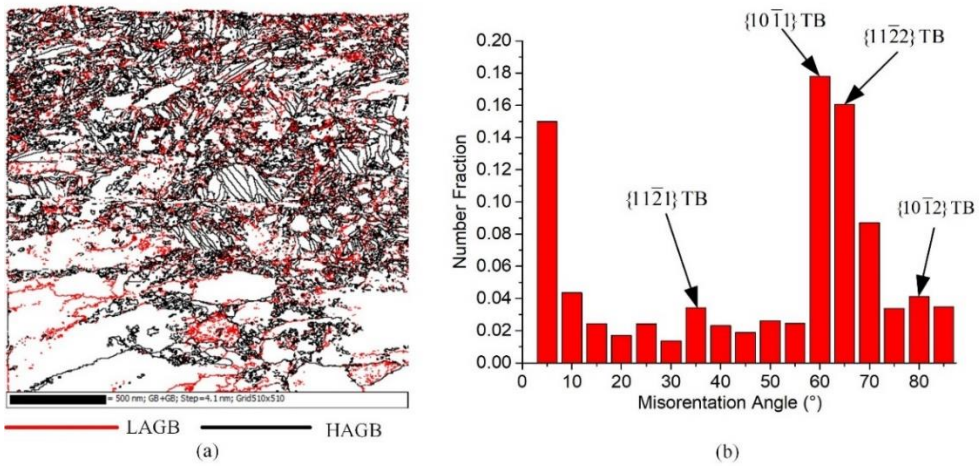

Fig. 88: (a) the distribution map of high angle grain boundary (HAGB) and low angle grain boundary (LAGB), (b) the fraction distribution histogram of misorientation angle.

5.2.2 Dislocation density

Geometrical necessary dislocation (GND) density is a key factor for analyzing the mechanism of grain refinement, as a result, GND densities are calculated based on crystal orientation data obtained from precession electron diffraction (PED) technique. From the orientation differences between neighboring points, the lattice curvature and dislocation density tensor can be derived [198]. The simplified equation can be written as [187]:

$$\rho = \frac{\theta}{b \cdot l_{PED}} \tag{50}$$

where θ is the local misorientation, and l_{PED} is the step size of PED. The simplified formula can be used to calculate GND efficiently, however the calculation accuracy is very limited without regard to Nye tensor. More accurate calculation of the dislocation density based on Nye tensor is applied [199].

The relationship between GND density and Nye tensor is expressed as:

$$\alpha_{ij} = \sum_{k=1}^{m} \left(\rho^k b_i^k t_j^k \right) \tag{51}$$

where α_{ij}, ρ^k, b_i^k and t_j^k are Nye tensor, the GND density, Burgers vector and unit line direction of the *k*th dislocation type respectively. The contribution of different types of dislocation in α phase of Ti-6Al-4V alloys to the lattice distortion is different, usually described by weighted factors [200]. The weighted factor of the *k*th dislocation is given by the following equation as:

$$w^k = c\mu \left(b^k \right)^2 \tag{52}$$

Where *c* is a constant, μ is the equation coefficient for which the value of edge dislocation is 1 and the value of screw dislocation is $1/(1-v)$. As for b^k, Burgers vector for <a>-type and <c+a>-type dislocation are 0.295nm and 0.553nm, respectively. Accordingly, the value of each weighted factor in α-Ti is estimated as: <a> screw 0.087, <a> edge 0.124, <c+a> screw 0.306, <c+a> edge 0.437 [201].

As the number of variables that need to be solved is more than equations, standard linear programming function is adopted to obtain a set of optimal solution which satisfies the lower boundary condition as the following equation:

$$L^1 = \sum_{k=1}^{N} \left| \rho^k w^k \right| \tag{53}$$

Then, the final total GND density is defined as

$$\rho_{gnd} = \sum_{k=1}^{N} \rho^k \tag{54}$$

As for the effects of indexing quality and step size on the calculating accuracy, a decrease in step size or increase in indexing quality could improve the accuracy [202], however, the step size of 4nm and indexing quality is close to the limitation of PED technique. So, the calculating GND density based on current step size and indexing quality is thought to be relatively reliable.

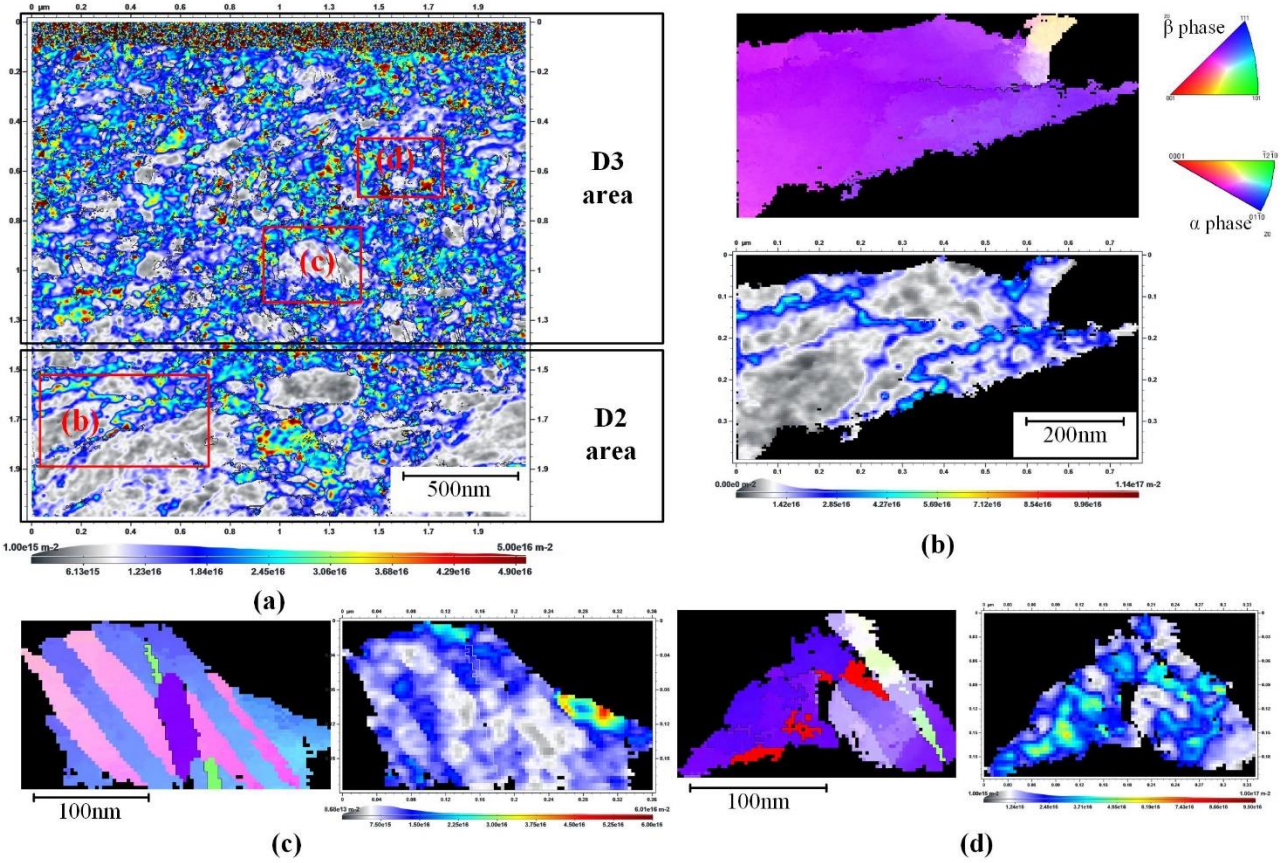

Fig. 89: (a) The GND density distribution map of machined subsurface, (b) (c) and (d) are the magnified GND density distribution maps and corresponding grain orientation maps of selected regions in (a).

The distribution of GND density is estimated based on the above GND density calculated procedure, for which the ATEX software is applied [196], and the calculated results is mapped as Fig. 89. As shown in Fig. 89 (a), the D3 and D2 areas are marked with black rectangles, the dislocation cell features are observed in wide-range and the GND density of D3 area is significantly higher than that of D2 area. And three selected areas are magnified and corresponding grain orientation maps is applied for detailed analysis. Fig. 89 (b) corresponding to D2 area show that the grain is deformed and elongated, and GND with density of $10^{15}/m^2$ is generated in interior of the grain, which is corresponding to the lower strain, strain rate and temperature

compared to D3 area. Moreover, the concentration of dislocation can be observed in some areas of the grain, which is benefit for the generation of LAGB. It's found from Fig. 89 (d) that the GND density of dislocation wall and dislocation interior reaches $1\times10^{16}/m^2$ and $1\times10^{15}/m^2$ respectively which demonstrates that the GND density of dislocation wall is much higher than dislocation interior and the grain refinement of HSM surface is mainly derived from continuous dynamic recrystallization (cDRX). As for the primary phase (α phase) is the close-packed hexagonal (HCP) structure, the dynamic recrystallization can be easily induced by high dislocation density. Lots of regions (see Fig. 89 (c)) with low dislocation density show the feature of twins which means that both dislocation slipping and twinning may be the contribution to deformation under HSM.

5.2.3 Precipitation of β phase induced by composite stress state and rapid heating

The precipitation of β phase particles often occurs under high temperature and large deformation of Ti-6Al-4V [203], which has great effects on the deformation and refinement of α phase. In order to obtain the characteristics of precipitations in HSM surface, the EDX scanning analysis was firstly performed to identify the elemental variation in Fig. 90. Fig. 90 (a) and (c) are STEM bright field images of two selected areas, in which two scanning paths are adopted to conduct the EDX analysis. The corresponding compositional profiles shown in Fig. 90 (b) and (d) indicate that the sharp drop in Ti and the rapid increase in V are related with the fact that V is a stabilizer of β grains.

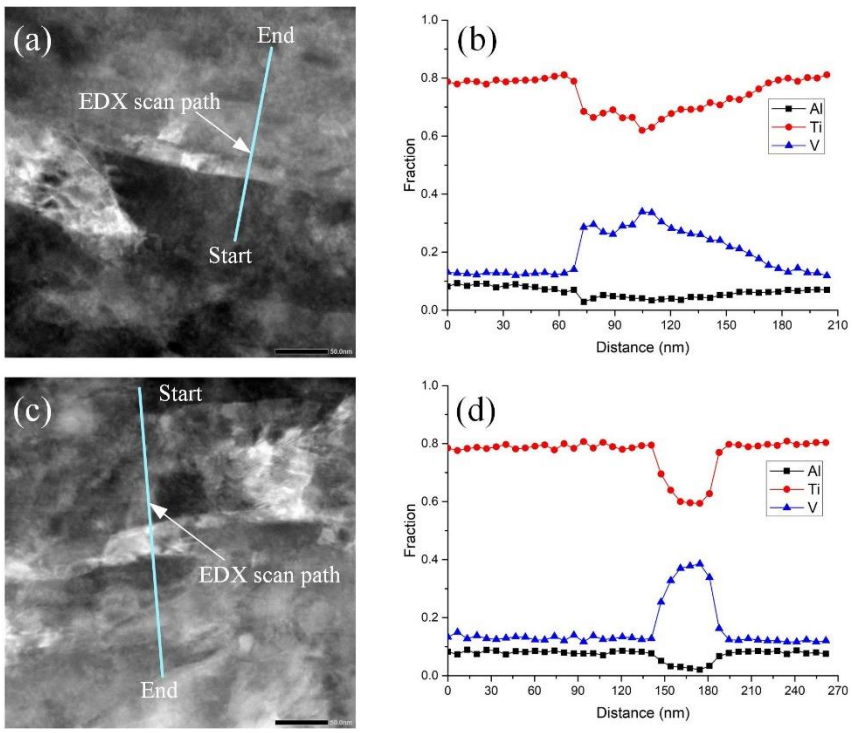

Fig. 90: (a) and (c) STEM bright field image of selected areas, (b) and (d) compositional profiles of the corresponding EDX scanning path.

Then the selected area electron diffraction (SAED) pattern based on TEM is adopted to observe the orientation relationship (OR) between α and β phase. Two types of crystallographic orientation has been found as$(0001)_\alpha//(110)_\beta$, $[11\bar{2}0]_\alpha//[1\bar{1}1]_\beta$and$(0\bar{1}10)_\alpha//(01\bar{1})_\beta$, $[0001]_\alpha//[111]_\beta$, which is shown in Fig. 91 (b) and (e), corresponding to areas A and B in Fig. 91 (a) and (d), respectively.α→β phase transformation can be activated by rapid heating and high stress state [102,204]. During HSM Ti-6Al-4V at 250m/min, the rising rate of temperature reaches 10^4℃/s, by which phase transformation with OR of $(0001)_\alpha//(110)_\beta$, $[11\bar{2}0]_\alpha//[1\bar{1}1]_\beta$ is motivated. From the stress state analysis in section 5.1.1, machined surface is under high composite stress state of shear and compressive stress, which leads to phase transformation with OR of $(0\bar{1}10)_\alpha//(01\bar{1})_\beta$, $[0001]_\alpha//[111]_\beta$.

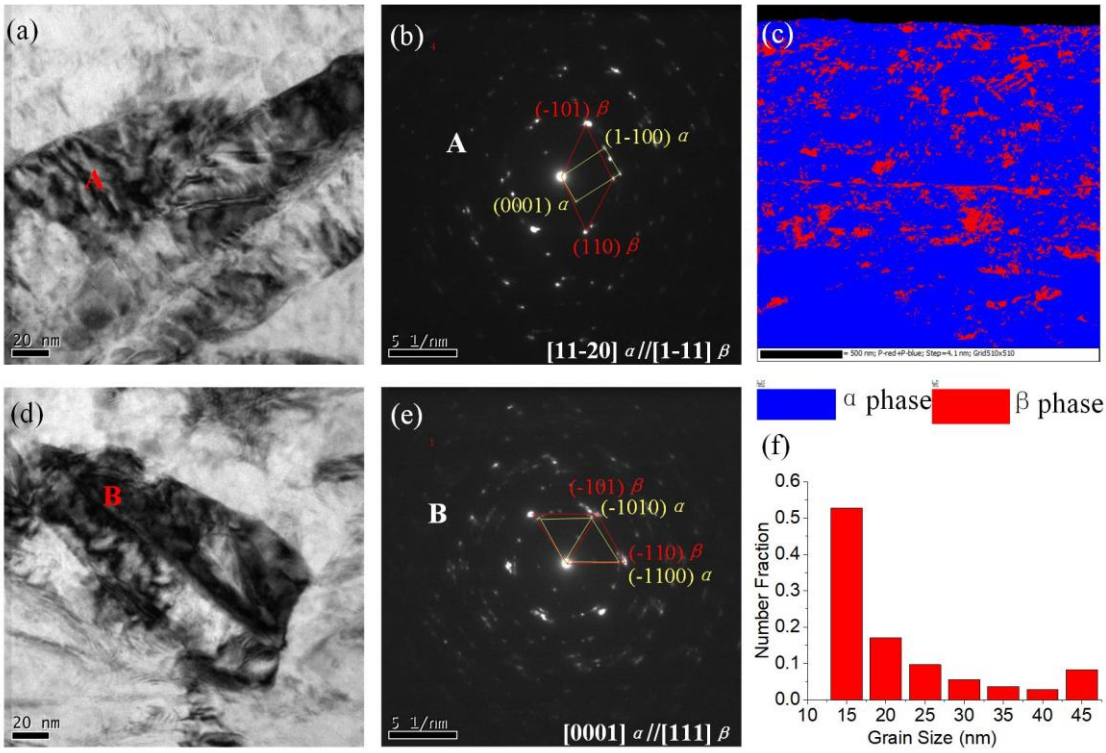

Fig. 91: (a) and (d) are TEM bright images of machined surface, b) and e) are SAED patterns of corresponding area of A and B respectively, c) and f) are the PED phase distribution map and number fraction histogram of β grain size.

The phase distribution mapping (Blue for α phase and red for β phase) and histogram of β phase size (see Fig. 91 (c) and (f)), obtained by PED technology, are adopted to analyze the effect of precipitation on evolution of microstructure. During HSM, most of the β phase with diameter of 10-25nm would precipitate

and present a random distribution, and β phase accounts for 10%. These fine and randomly distributed β phase will have great effects on the dislocation motion in α/β phase boundary and the grain growth [205]. Furthermore, the effects of the β precipitation on grain refinement of α phase will be further discussed in the following.

5.2.4 Twins size and fraction at different surface depth

The twin boundaries distribution, detected with misorientation angle and misorientation axis data of adjacent grains, is shown in Fig. 92, from which it can be observed that the main type of twin boundaries (TBs) are $\{10\bar{1}1\}$and $\{10\bar{1}2\}$TB and the length of TBs is mostly at nanoscale. When cutting temperature exceeds 400℃, and stress state is composed of compression and shear stress, $\{10\bar{1}1\}$and $\{10\bar{1}2\}$ types have become the main modes of deformation twinning, and TBs account for 14% of total grain boundaries, because the shear magnitudes of $\{10\bar{1}1\}$ and $\{10\bar{1}2\}$ twins are relatively lower (see Table 22). It's worth noting that junction and variant of twins which are found in Fig. 92 (a) are thought as the generation of secondary twins even tertiary twins[206,207].

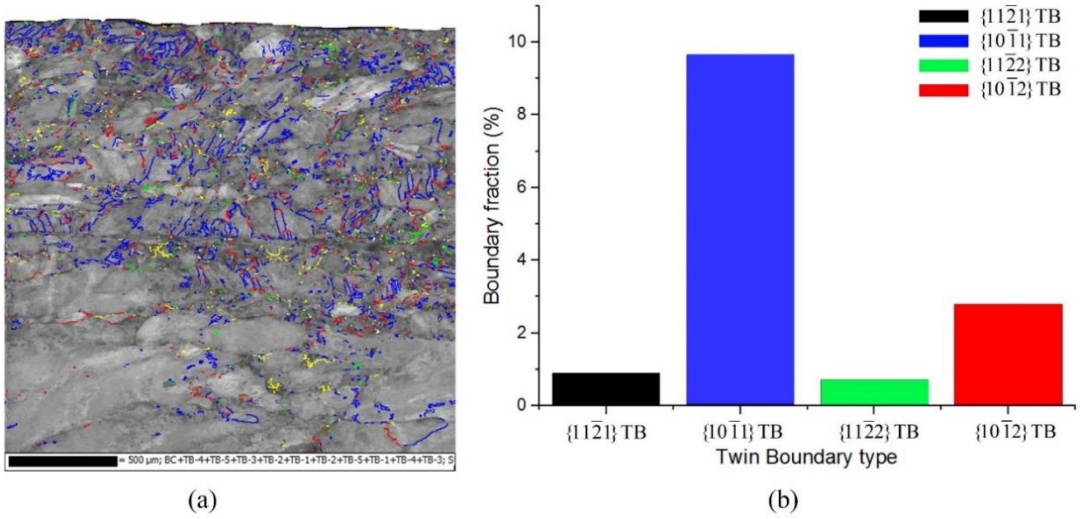

Fig. 92: (a) The distribution map and (b) fraction histogram of various twin boundaries.

Table 22: The twining system of common twins in α-Ti.

Twinning plane	Misorientation angle/axis	Twining type	The shear magnitude
$\{11\bar{2}1\}$	$35 \lessdot 1\bar{1}00 >$	Tension twins	0.638
$\{10\bar{1}1\}$	$57 \lessdot 11\bar{2}0 >$	Contraction twins	0.105
$\{11\bar{2}2\}$	$64 \lessdot 1\bar{1}00 >$	Contraction twins	0.225
$\{10\bar{1}2\}$	$85 \lessdot 11\bar{2}0 >$	Tension twins	0.167

5.3 Grain refinement mechanism based on a combined effect

5.3.1 Dislocation evolution based grain refinement considering pinning effect of β precipitation

The grain refinement of machined surface is based on dislocation density distribution and evolution, which could be regarded as the formation and evolution of dislocation cell structure. During grain refinement process, large number of dislocation cells are formed at initial stage and leads to local misorientation in grains interior, and then dislocation pile-up makes misorientation increasing until the grains are broken and new grains are formed[66,185]. The dislocation based model is adopted to describe grain refinement of HSM in this study. In the model, the dislocation cell structure is divided into two parts: the cell interior dislocation density ρ_c and the cell wall dislocation density ρ_w, which are expressed by the following equations:

$$\frac{d\rho_w}{d\gamma} = \frac{\sqrt{3}\beta^*(1-f)\sqrt{\rho_w}}{fb} + \frac{6\beta^*(1-f)^{2/3}}{bdf} - k_0\left(\frac{\dot{\gamma}}{\dot{\gamma}_0}\right)^{-1/n}\rho_w \tag{55}$$

$$\frac{d\rho_c}{d\gamma} = \alpha^*\frac{1}{\sqrt{3}}\frac{\sqrt{\rho_w}}{b} - \beta^*\frac{6}{bd(1-f)^{1/3}} - k_0\left(\frac{\dot{\gamma}}{\dot{\gamma}_0}\right)^{-1/n}\rho_c \tag{56}$$

Where γ is shear strain of cell interior and cell wall, b is the magnitude of Burgers vector, $\dot{\gamma}_0$ is the reference shear strain rate, f is the volume fraction of dislocation cell wall, α^*, β^* and k_0 are control parameters for dislocation evolution. The first terms of Eqs. (55) and (56) represent the dislocation generation by Frank-Read sources. The second terms describe the migration of dislocation from cell interior into cell wall. The last terms denote the annihilation of dislocation due to dynamic recovery. Because of α^* and β^* are constant, the generation and migration of dislocation are less affected by temperature and strain rate. Considering the annihilation of dislocation, k_0 increases with temperature and the value of $\dot{\gamma}$ decides the rate of dislocation annihilation. Lower temperature and higher strain rate can reduce the rate of annihilation which leads to higher dislocation density finally.

The average dislocation cell size d is inversely proportional to the square root of the total dislocation density ρ_{tot}. The total dislocation density ρ_{tot} and average dislocation cell size d are defined by

$$d = K/\sqrt{\rho_{tot}} \tag{57}$$

$$\rho_{tot} = f\rho_w + (1-f)\rho_c \tag{58}$$

Firstly large amounts of dislocations are generated due to high strain rate of HSM, and the dislocation distribution map (see Fig. 89) shows that obvious dislocation migration from cell interior to cell wall. As dislocation migration can be hindered by the subgrain boundaries, the dislocation pile-up in subgrain boundaries results in the increase of grain boundary angle until high angle grain boundaries are formed and grains are refined. Besides that, high strain rate is the significant factor for suppression of dislocation annihilation by dynamic recovery so that dislocation density can remain high level.

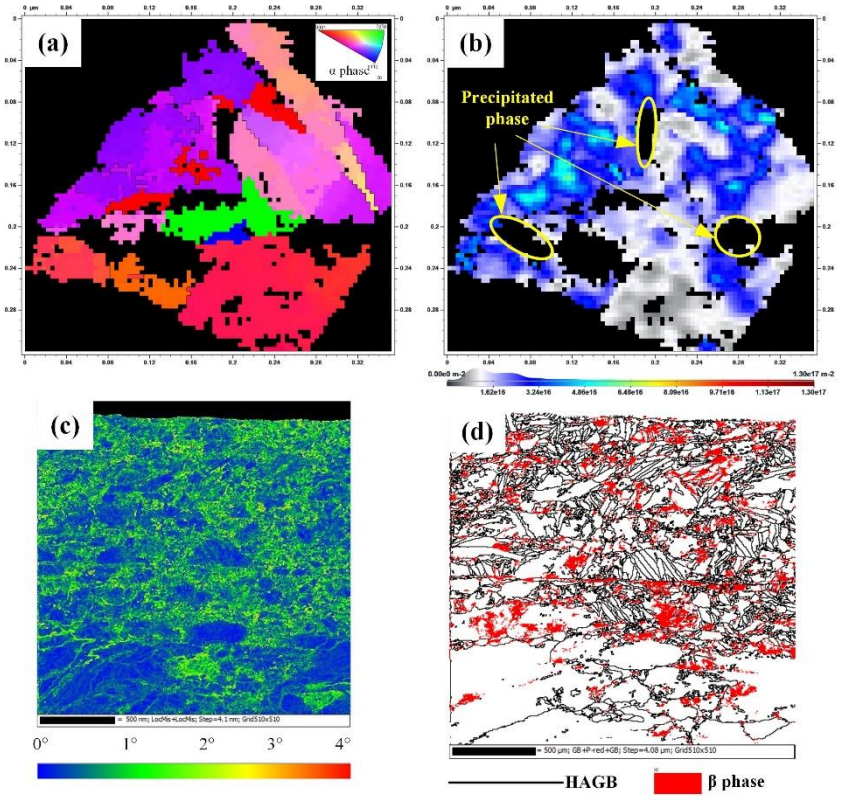

Fig. 93: (a) IPF image of α grains in selected areas, (b) GND density distribution of α grains in (a), (c) map of local misorientation angle, (d) map of high angle grain boundary and β precipitation

The β precipitation also has great effects on the pinning of dislocation and grain boundary. Twinning and dislocation slip leads to the formation of subgrains at the beginning of deformation, and LAGBs are the dominant form of grain boundaries in this case. Then β phase particles is precipitated (see Fig. 90 and Fig. 91) and high dislocation density occurs at grain boundaries and phase boundaries, and the extension of twins and migration of GBs are obviously hindered, which present the significant pinning effect of β precipitation

on dislocation until that LAGBs are transformed into HAGBs due to the accumulation of dislocation, as shown in Fig. 93 (a) and (b). The distribution of local misorientation angle in Fig.16(c) demonstrates that dislocation pile-up actually exists in GBs and phase boundaries. And mapping of HAGBs and β precipitation in Fig. 93 (d) displays the intersection of β precipitation and HAGBs, which demonstrates the pinning effect of β precipitation.

To better characterize the pinning effects of β precipitation on GBs, the models about driving force of GBs migration should be obtained firstly, which can be described as[208]:

$$F = -\frac{2\pi r^2 E}{3Rf'}\left(\frac{2}{Z_r} - \frac{3}{2}\right) \tag{59}$$

According to the research of interaction between precipitation and GBs, the pinning force formula of precipitation on GBs is written as[209,210]:

$$F_Z = \pi r E \sin 2\varphi \tag{60}$$

Where E is the GB energy caused by misorientation between two adjacent grains, and it can be seen that the driving force of GBs mainly comes from the reduction of interface energy. φ is the interaction angle between precipitation and GB. With the interaction angle increasing, grain boundary bending will lead to the increase of interface energy, while the increase of interface energy hinders the further migration of grain boundary. When grain growth is inhibited, a critical grain size $R_{\lim}$ depends on radius and volume fraction of β precipitation as[211]:

$$R_{\lim} = 4r/3f' \tag{61}$$

When the pinning force of β precipitation is equal to driving force of GB, dislocation would be pinned at GB and accumulation of dislocation occurs so that LAGBs between subgrains increase to generate several fine grains with HAGBs. According to Eq. (61), when the average radius of β precipitation ranges from 10 to 25 nm and the ratio of β phase is about 10%, it can be calculated that the critical grain size is in the range of 100-200nm. Since the effect of twinning on grain refinement is not included in this equation, the calculated grain size is much larger than experimental result (45-70 nm). The generation of dislocation and precipitation of β phase continue for loop to refine grains further. Because of inhibition of pinning effect on grain growth, nanoscale grains can be formed finally.

5.3.2 Effect of high strain rate and stress state on deformation nano-twins generation

It's generally believed that high strain rate and low temperature condition are the main factors to promote deformation twinning [212]. High strain rate deformation, as the primary feature of HSM, could lead to high twin activity [213]. The type and size of deformation twins are extremely sensitive to strain rate, which can be determined by Zener-Hollomon parameter (Z) as the following equation[214]:

$$\ln Z = \ln \dot{\varepsilon} + Q/RT \tag{62}$$

Where $\dot{\varepsilon}$ is the cutting strain rate, Q is the activation energy of self-diffusion, R is the gas constant，T is the cutting temperature.

From the Eq. (62), low temperature and high strain rate will lead to higher value of Z. When Z is greater than a certain critical value, the deformation twinning is thought to occur and Z even determines the types of twins [215]. Considering the influence of adiabatic temperature rise during HSM, the activation energy of self-diffusion is referred as 170kJ/mol [216] and the maximum value of lnZ is calculated as 33.6. The contribution ratio of twinning to plastic deformation depends on Z parameter, while the form of twins is resulted by Schmid factors (SF) and critical shear stress (CRSS) which is influenced by many factors such as stress direction, temperature, strain rate, texture and so on [217].

SF is estimated by equation as $m = \cos\phi \cdot \cos\lambda$, where ϕ is the angle between principal stress direction and twinning shear direction, λ is the angle between twinning plane and principal stress. And CRSS is estimated by equation as $\tau_{CRSS} = \gamma^t / \rho t + \tau^f$ [71], the value of CRSS in α-Ti are 125, 209 and 494 MPa for prismatic, basal and pyramidal glide, respectively[206]. According to the analysis of stress state in machined surface in section 5.1.1, the surface stress is much higher than CRSS and the value and direction of principal stress vary with cutting process, so it can be deduced based on SF and CRSS equation that deformation twins with different types and orientations would be generated.

Fig. 94 (a) is the high resolution (HR) TEM image of deformation twins, from which two types of twins are formed: one is nanoscale lamella twins named as primary twins, and the other is twin variants named as secondary twins. When the direction of shear stress is similar to c-axis of grains, multiple twins are formed simultaneously (see Fig. 94 (b)). Twin variants with $\{10\bar{1}1\} - \{10\bar{1}2\}$ double twinning, shown in Fig. 94 (c) and (f), are thought to be the results of changes in stress state in which the new orientation of primary twins is beneficial for the formation of secondary twins. The nucleation of twin variant is expected to be rather

difficult, so they occur under condition of large strain[218]. It's noted in Fig. 94 (d) that a junction domain is formed with three twins of almost same angle of 120° called double twins because twins impinge together on the extended path.

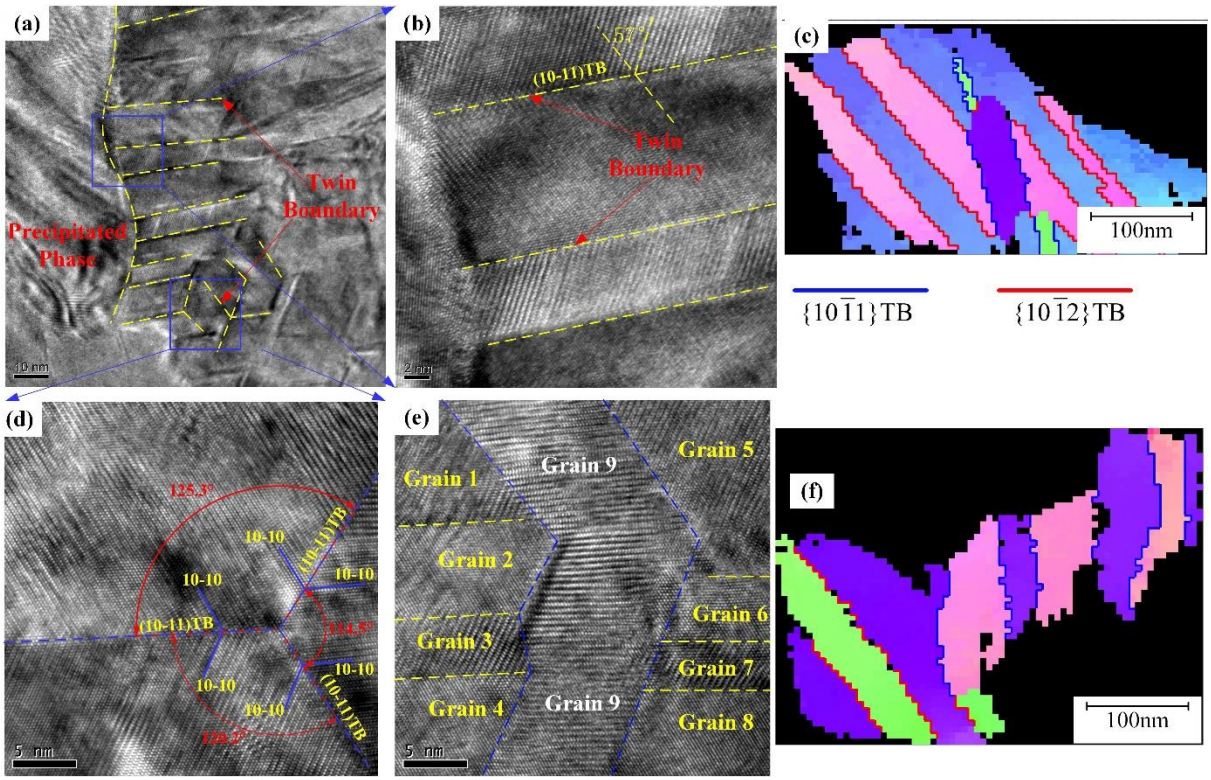

Fig. 94: (a), (b), (d) and (e) The HRTEM images of the nanoscale twins distribution with different types, (c) and (f) the PED IPF images of selected twins distribution.

According to Z parameter, with the increase of strain rate, the probability of twin nucleation increases rapidly and its extension is limited by cutting time. As shown in Fig. 94 (e), twins are nucleated in grains 1, 5, 4 and 8, and then twins 2, 6, 3 and 7 are generated and impinge together. According to the deformation process analysis in section3.3, the principal stress direction of subsurface has changed about 80°, and the stress state transforms from composite stress with compressive stress along X-axis and shear stress into compressive stress along Y-axis, secondary twin 9 is generated and passed through the above grains. The effect of secondary twins on TBs is shown in Fig. 95. When secondary twins are generated, the TBs impinge together and contacted TBs is formed, which hinders motion of TBs and makes the TBs more stability. In addition, the partial dislocation can travel across or along TBs which makes it possible for materials further deformation, so secondary twins restrain the extension of TBs and nanoscale twins are generated finally.

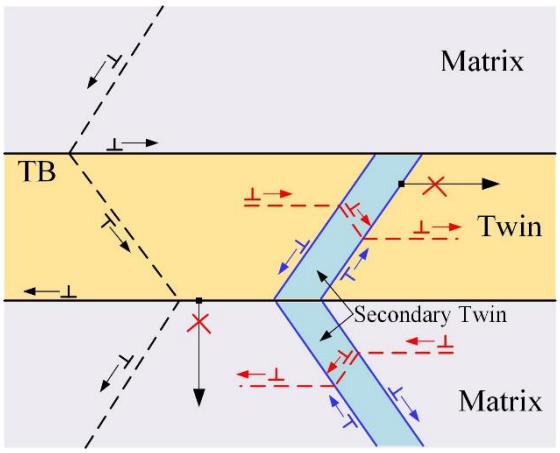

Fig. 95: The schematic of the effect of secondary twins on twin boundary and dislocation motion.

5.3.3 Formation mechanism of nanoscale grains combining dislocation slip and twinning

Due to the microstructure characterization in Fig. 86 and Fig. 87, the initial grains of machined surface are refined significantly to nanoscale under HSM. The deformation mechanism of Ti-6Al-4V alloy under high strain rate is a combination of dislocation slip and twinning. The grain refinement of HSM surface is mainly derived from cDRX, and the typical dislocation cell structure is developed by generation, migration, annihilation and suppression of dislocation. Meanwhile, twinning is motivated to accommodate plastic deformation in addition to dislocation slip under high strain rate. According to Eq. (57) and (61), high density of dislocation and precipitation of β phase particles, which are easily obtained during deformation process in HSM surface, are dominant factor for nano-scale grain refinement.

During HSM process, high strain rate ($10^5 s^{-1}$) induces high dislocation density and dislocation cell structure are formed which leads to local misorientation in grains interior. At the same time, the probability of twin nucleation increases rapidly and twinning is promoted as a significant contribution to increase more plastic deformation. The complicated stress state is beneficial for the formation of secondary twins, leading to enhanced self-interaction of TBs. The short deformation time and self-interaction have great suppression effect on the extension of TBs and deformation twins remain at nanoscale finally. Besides that, dislocation slip can occur in twins and react with TB for further plastic deformation. With the continuous dislocation migration from cell interior to cell wall, the local misorientation between adjacent cells increases to form LAGB. And then LAGB gradually evolves into HAGB as a result from the continuous accumulation of dislocation. Generally, in high stacking fault energy materials, dynamic recovery takes place with ease, resulting in dislocation annihilation and grain growth. However, with the precipitation of β phase particles,

the pinning force of precipitation on GBs increases so that the migration of dislocation is limited during short deformation time. The precipitation is beneficial for dislocation accumulation, leading to the suppression of dynamic recovery. In this way, the precipitation has an opposite influence on cDRX and dislocation pile-up makes misorientation increasing until the grains are refined further. The formation of HAGB and precipitation of β phase continuously develop with increasing strain, resulting in nano-scale grains refinement.

5.4 Summary of the chapter

The gradient of microstructure in the machined surface and subsurface is investigated experimentally and by simulation. The strain, strain rate and temperature gradients along the distance beneath the surface are determined through a CEL cutting model, which provides the input parameters for the CA model. Then, the predicted microstructure evolution in the machined surface and subsurface is simulated by the CA model including the cDRX and dDRX mechanism. The CA model is validated by comparing the predicted microstructure with that obtained experimentally using PED and TEM techniques. Finally, grain refinement mechanisms in different regions of the machined surface and subsurface are analyzed based on the experimental and simulated results. General conclusions can be drawn as follows:

1) Two layers with different grain structures are found in machined surface and subsurface: (1) a “Nano grains” layer with cDRX grains characteristics (2) a “refined grains” layer with dDRX grains characteristics.
2) By considering the cDRX and dDRX mechanism, CA model is developed to simulate the microstructure. The gradient of strain, strain rate and temperature beneath the machined surface results in the formation of the above mentioned two layers. When the strain and temperature decrease to a critical value, the condition for cDRX grains nucleation cannot be met, then two layers are formed due to different grain refinement mechanisms.
3) Relatively higher temperature and strain near the machined surface region results in a significant grain refinement based on a combination mechanism of cDRX and dDRX, while the “refined grains” layer is formed mainly by cDRX.
4) As for the formation of “nano grains” layer, microstructure evolution undergoes the following steps: dislocation generation and accumulation, subgrains formation, cDRX grains generation, dDRX grains nucleation at cDRX grain boundary, dDRX grain growth and finally nano grains are formed. cDRX mechanism which provides a large number of grain boundaries for the grain nucleation promotes the activation of dDRX mechanism, which is the key to generate nano grains.

5) At the cutting speed of 250 m/min, the strain rate changes significantly as the distance beneath the surface increases. In the deformed layer with lower strain rate, dislocation slip is the main deformation mode. While in the highly perturbed layer with higher strain rate, severe grain refinement, precipitation of β phase and twinning are activated for nanoscale grains formation.

6) Twinning plays an important role in materials deformation under high strain rate. Large numbers of twins, accounting for about 14% of total GB, are observed at the machined surface, and under current boundary conditions $\{10\bar{1}1\}$ and $\{10\bar{1}2\}$ twins are the main mode of deformation twins. Due to the change of principal stress direction and stress state transformation, self-interaction of TBs is enhanced to form secondary twins. The short deformation time and self-interaction have great suppression effect on the extension of TBs and deformation twins remain at nanoscale.

7) Large amounts of β phase particles precipitation are observed in the machined surface due to the severe deformation and rapid heating process, which will finally influence cDRX negatively. Precipitation of β phase has significant pinning effects on dislocation and inhibition on grains recovery and growth, eventually leading to the further refinement of grains.

The accurate prediction of microstructure in machined surface and subsurface is of great significance to build the strong correlation between **process mechanics – surface integrity** (including the microstructure) – **functional performance and lifepan** of components (fatigue, corrosion, etc). Considering the shortage of the CA model used in this study which does not consider the effect of twinning and phase transformation existing in the real cutting process of Ti-6Al-4V under HSM, the CA model can only work well under certain assumptions to predict the microstructure evolution in machining process. Therefore, the twinning and phase transformation will be considered in a future work to develop a more accurate model to simulate microstructure evolution in machining.

6 Assessment of other surface integrity characteristics using both experimental and modelling approaches

6.1 Design and setup of orthogonal cutting experiments for surface integrity analysis

Orthogonal cutting tests of Ti-6Al-4V titanium alloy were conducted at CNC lathe machine using polycrystalline diamond (PCD) cutting tools under dry conditions, as shown in Fig. 96. The objective is to investigate the influence of the cutting conditions on other surface integrity characteristics than microstructure (already investigated in the previous chapter), including: surface roughness, microhardness and residual stress. Considering that the cutting tests are conducted in the range of HSM and the generation of surface integrity from machining needed a relatively stable temperature in the machined surface and subsurface, which mean a relatively long cutting time. Due to the rapid tool wear of cemented carbide cutting tools in HSM, PCD inserts are used instead of the uncoated cemented carbide cutting.

These tests were conducted on disks with a diameter of 80 mm and a thickness of 3 mm (equal to the width of cut). Tool geometry in the tool-in-hand system according to the ISO standard 3002-1:1982/AMD 1:1992 was carefully inspected using an Alicona InfiniteFocusSL microscope. The tool geometry is represented by PCD tools with a rake angle (γ) of 0°±0.26°, a clearance angle (α) of 7°±0.29°, and a cutting edge radius(r_n) of 5 μm±0.7μm. Cutting speed (V_c), uncut chip thickness (h), and tool flank wear (VB) are varied to investigate the effect of the these parameters on the residual stress distribution in the machined surface and subsurface. The cutting conditions are summarized in Table 23.

During the machining tests, the forces are measured by a Kistler dynamometer model 9121, and the machined surfaces are collected for further surface morphology, microhardness, and residual stress analysis.

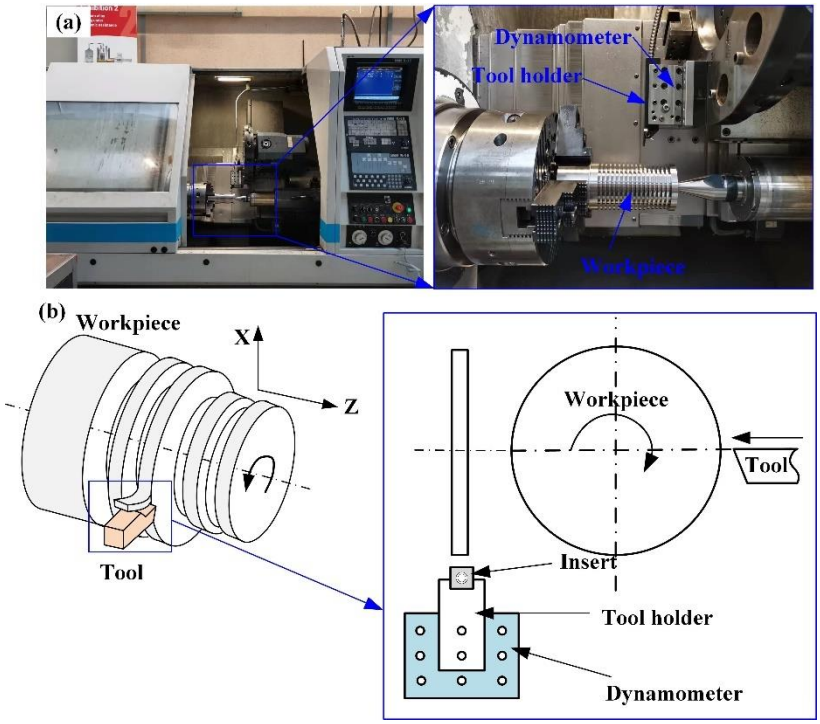

Fig. 96: Experimental tests using CNC lathe machine: (a) experimental setup, and (b) schematic representation of orthogonal cutting configuration.

Table 23: Cutting conditions for orthogonal cutting of Ti-6Al-4V alloy using CNC lathe machine.

Cutting condition (case number)	Cutting tool	Cutting speed (m/min)	Uncut chip thickness (mm)	Tool wear (VB) (mm)	Analysis
No.1	PCD	125	0.1	VB=0	Surface roughness, Microhardness, Residual stresses
No.2	PCD	250	0.1	VB=0	
No.3	PCD	375	0.1	VB=0	
No.4	PCD	500	0.1	VB=0	
No.5	PCD	250	0.15	VB=0	
No.6	PCD	250	0.1	VB=0.2	

6.2 Considerations about the cyclic nature of the cutting process

As mentioned by Astakhov [219], the cutting process has a cyclic nature, and the dynamics of the cycles are considered in terms of variation of the cutting force, cutting temperature, chip morphology, and other major machining outcomes. One first evidence of this cyclic nature of chip formation processes in machining Ti-6Al-4V alloy is the chip serration, as shown in Fig. 97 for different cutting speeds. Others evidences [98,220] are the cyclic variation of the forces and temperatures, and consequently of the surface integrity characteristics (surface topography, microstructure, microhardness, plastic strain, residual stress, etc.).

Therefore, in the following sections the surface topography, microhardness and residual stress will be analyzed by considering the cyclic nature of chip formation.

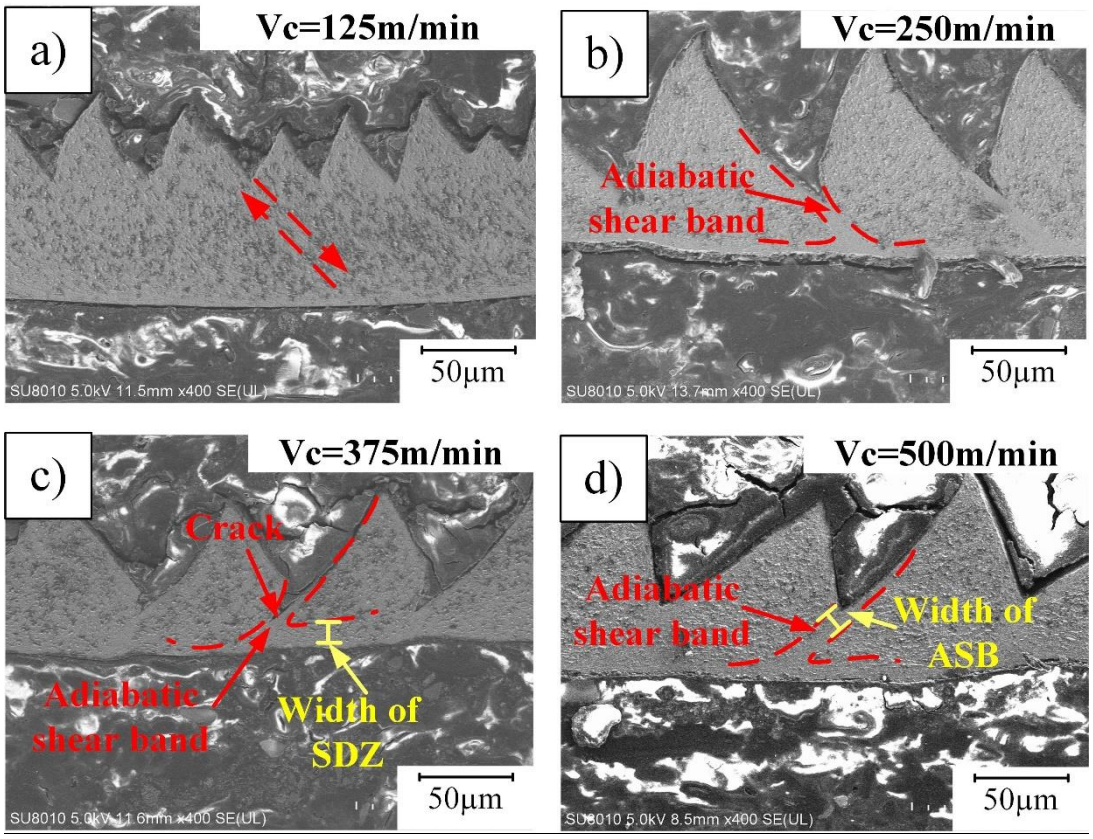

Fig. 97: Chip geometry for different cutting speeds (ASB - adiabatic shear band; SDZ - secondary deformation zone).

6.3 Plastic strain and surface topography at the machined surface

The cutting CEL model described in Chapter 3, designed by CEL2 model, is used to analyze the influence of the cyclic nature of the chip formation on the plastic strain at the machined surface and the surface topography along the cutting direction, although the same analysis could be done using the other cutting CEL model presented in the same Chapter (CEL1 model). Fig. 98 shows the plastic strain distribution in the machined surface for several cutting speeds. The same as for the cutting force (Fig. 29 and Fig. 35), a cyclic variation of the plastic strain in the cutting direction is obtained. This cyclic variation is due to the changes of the state of stress, and consequently localization of the strain in the shear bands.

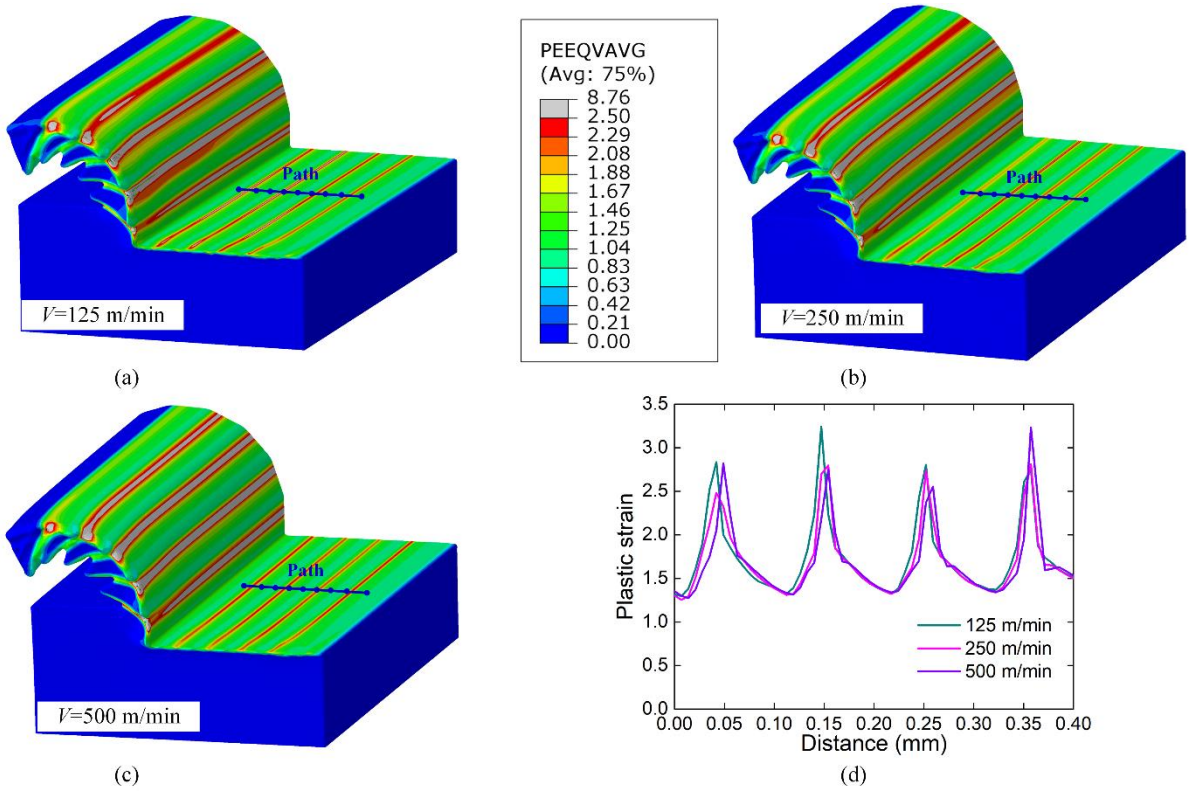

Fig. 98: Distribution of the plastic strain (PEEQVAVG) obtained by CEL simulation for a cutting speed of (a) 125 m/min, (b) 250 m/min, (c) 500 m/min; (d) plastic strain profiles at the machined surface along the cutting direction, for several cutting speeds.

As far as surface topography is concerned, observations to the machined surfaces have carried out and shows in Fig. 99 (a) ~ (d). These observations have revealed the presence of marks at the machined surface, which may be a consequence the cyclic nature of the cutting process. Therefore, the frequency of these marks or surface topography undulation should be correlated with the frequency of chip formation. The frequency of these marks can be calculated knowing the distance of two neighbor marks and the cutting speed. Similarly, the frequency of chip formation can be calculated using the distance between two segments of the serrated chips and the chip speed (equal to the cutting speed divided by the chip compression ratio). For the cutting conditions indicated in Fig. 99 (a) ~ (d), the frequency of surface undulation is equal to 22.6 KHz, 49.0 KHz, 88.0 KHz and 124.4 KHz, respectively. In other end, the frequency of serrated chip formation, calculate considering the distance between each 5 marks, is equal to 23.1 KHz, 47.2 KHz, 74.5 KHz and 105.4 KHz. This proves that these mark in the machined surface are a consequence of the cyclic nature of the cutting process. The frequency of surface undulation increases when the cutting speed increases from 125 m/min to

500 m/min, which shows a similar trend with the research work from Su et al. [221]. As the uncut chip thickness increases from 0.1 mm to 0.15 mm (Fig. 99 (b) and (e)), the frequency of surface undulation decreases, which is also validated by Melkote et al. [222]. When tool wear occurs (Fig. 99 (f)), these marks disappear but not the chip nature of chip formation (chips are still serrated), which is a consequence of the intense friction between the tool flank face and the machined surface.

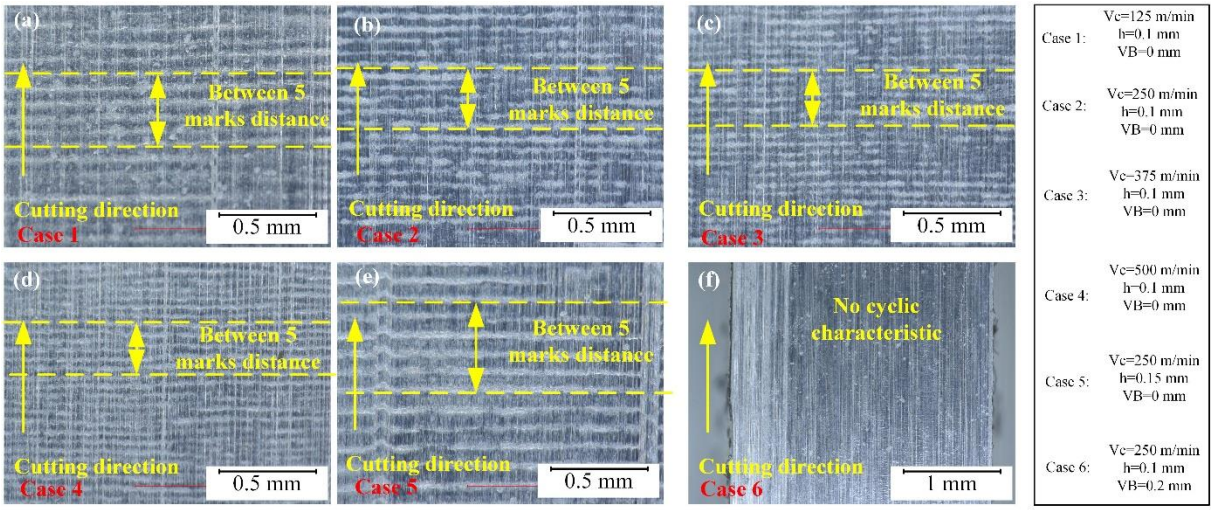

Fig. 99 Experimental observation of cyclic characteristics of surface profile in case 1~5 and no cyclic characterization in case 6.

Fig. 100 shows both simulated and experimental topography of the machined surface for several cutting speeds: 125, 250 and 500 m/min. As can be seen, the surface topography varies cyclically in the cutting direction. Moreover, the measured total height of the roughness profile (R_t) obtained by the white light interferometer and the simulated profile of the surface topography in the cutting direction are very similar in terms of amplitude and period for the highest cutting speed of 500 m/min, and slightly different for the other speeds of 125 and 250 m/min. These results show the influence of the cyclic nature of chip formation in machining Ti-6Al-4V on the plastic strain and surface roughness. However, other parameters of the surface integrity is also affected, including the microstructure and the residual stresses [223].

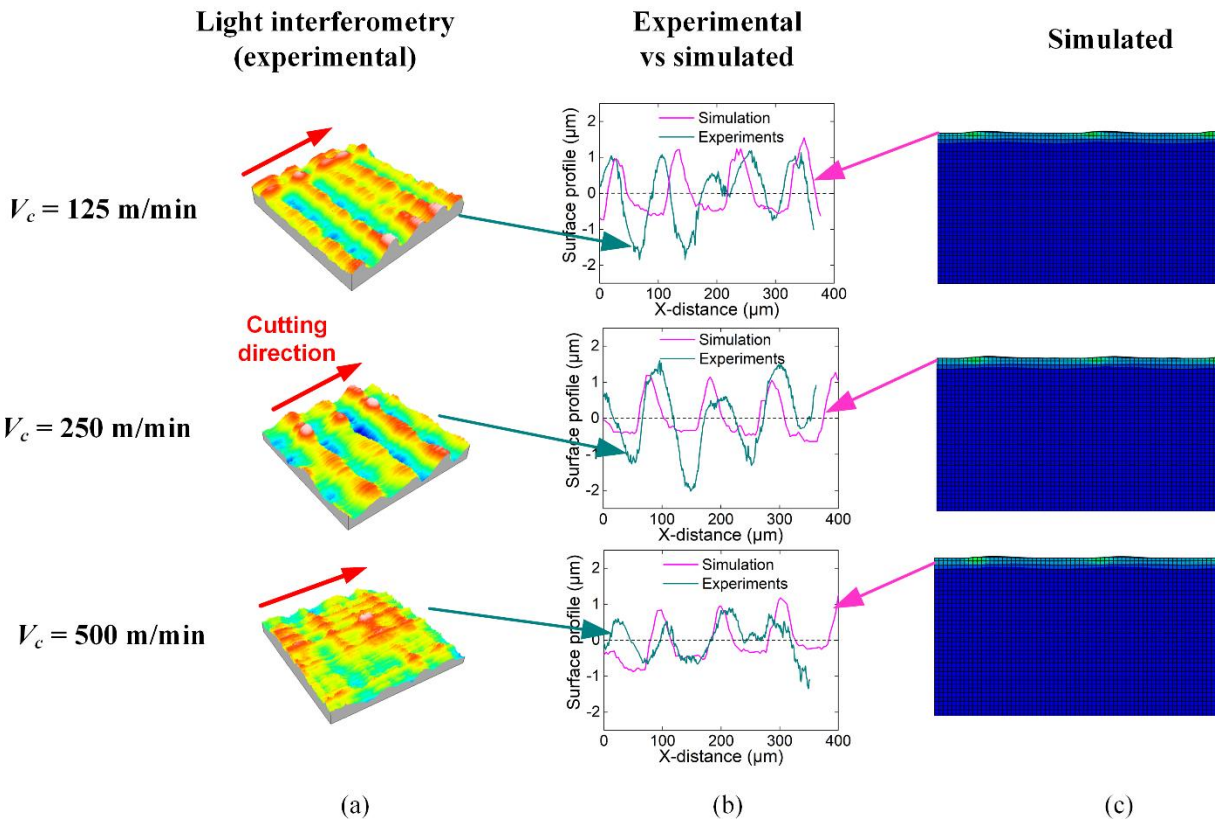

Fig. 100: (a) Measured surface topography obtained by white light interferometry (R_t parameter), (b) comparison between simulated and measured profiles, and (c) simulation surface topography obtained by CEL simulations (cutting speeds: 125, 250 and 500 m/min).

Some corresponding surface defects are formed with the periodical fluctuation of surface. As shown in Fig. 101, the surface defects are mainly composed of dimples which always appear at the valley of machined surface. The shape of dimples transforms from elongated to equiaxed and their size become smaller which reflects the fracture mechanism. As a result, we deduce that when the cutting force decreases to a relatively lower value the ploughing and friction force are not enough for removing the defect from materials fracture.

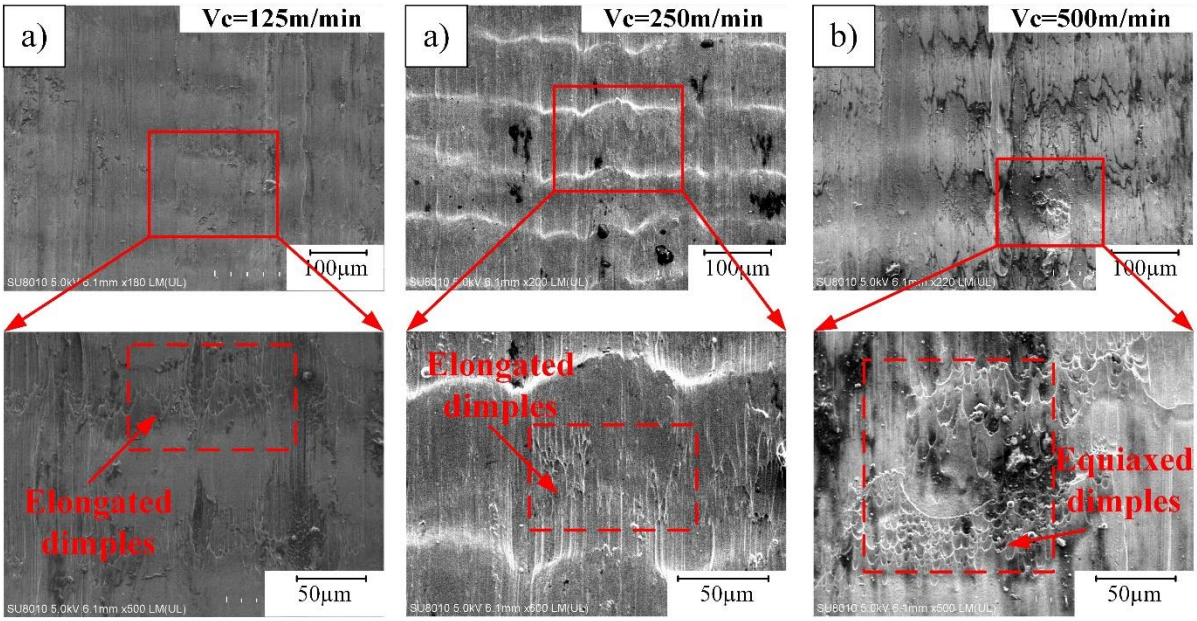

Fig. 101: Surface defect characteristics at different cutting speeds.

To better understand the effect of chip morphology on the forces, the process of chip formation is divided into two steps: the first stage is the early stage of the adiabatic shear band formation, which results in an increase of the cutting force. The second stage is the damage and fracture inside the shear band, resulting in a decrease of the cutting force. As shown in Fig. 102 a), the equivalent plastic deformation is inhomogeneous and periodical along the path shown in this figure connecting the point A to point B. The simulated cutting force for a cutting speed of 250 m/min also shows a periodical fluctuation with an average value around about 400 N (see Fig. 102 b). As mentioned above, the cutting force in the first stage is much higher than the one in the second stage, and the amplitude of fluctuation is correlated to the chip morphology. The machining surface would be compressed and rubbed by the tool flank face, thus the thrust force (force acting perpendicular to the machined surface) would fluctuate as well and generates an inhomogeneous plastic deformation of the machined surface.

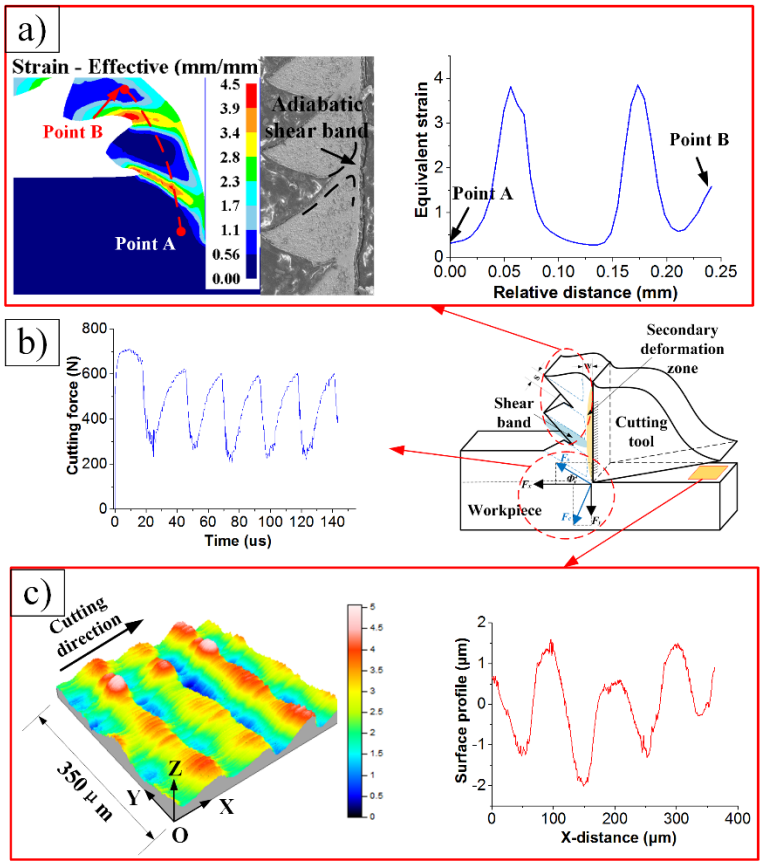

Fig. 102: The schematic of relationship of a) serrated chip, b) cutting force and c) surface profile.

6.4 Microhardness distribution at the machined surface and subsurface

Thermal and mechanical loadings generated by machining (plastic deformation, heating and cooling process) will introduce hardening or softening into the work material, which directly affect the microstructure (such as dislocation density evolution, grain size change, phase transformation, etc.) and the mechanical properties of the machined surface/subsurface and chips. Several studies [224–226] found in the literature have shown that the microhardness at the machined surface and subsurface of the part is higher than that of the bulk, which is caused by higher dislocation density, finer grain size and martensitic transformation. In order to identify the improvement of the proposed microhardness prediction, the most used microhardness prediction model (Hall-Petch model) only considering the effect of grain refinement is defined as traditional model in this thesis. The experimental determination and accurate prediction of the microhardness are of great significance to study the effect of machining process on surface integrity.

6.4.1 Microhardness model considering the microstructure effects

Cutting process cause temperature rise and plastic deformation of the machined surface and subsurface, leading to work hardening, material softening and other phenomena, which affects the material hardness. In

several studies found in the literature, the microhardness model considered the temperature and strain generated in the cutting process. However, temperature and strain are not the direct causes of the changes in microhardness of the work material, and the microstructure is the key point to build and a model of material microhardness. The main microstructure characteristics affecting the microhardness of materials are phase transition, dislocation density, grain size and twinning. The effect of phase transition on the microstructure of materials is determined by different crystal structures. The dislocation density directly determines the plastic deformation ability of the material. When the dislocation is difficult to prolificate in the material, its microhardness increases. When the grain size is smaller, the content of grain boundary will increase, and the grain boundary has a significant hindrance effect on the dislocation movement, which will cause the processing strengthening phenomenon of materials, and also cause the rise of microhardness. Twins and dislocations are the basic forms of plastic deformation. When the content of twins increases, the further occurrence of twins will be hindered, and the microhardness will eventually increase.

The prediction of microhardness caused by cutting mainly depends on the accurate prediction of microstructure. The microhardness of the machined surface and subsurface can be predicted by including the relationship between microstructure parameters and microhardness (theory of strengthening) [227] in the CEL model proposed in Chapter 3 (CEL 1 model). Theoretical models of dislocation density and grain size have already fully described in sections 5.3.1 and 4.1.4.

Due to the short deformation time of the material in cutting, the material in the deformation zone will undergo two stages of rapid temperature rise and cooling. During the rapid temperature rise stage, the transformation from α-Ti to β-Ti will occur, which is similar to the austenite transformation process [228]. The volume fraction of β-Ti can be calculated by the following equation:

$$f_\beta = 1 - \exp\left[A\left(\frac{T - T_s}{T_e - T_s} \right)^D \right] \tag{63}$$

where T is the local temperature, T_s is the initial temperature of the phase transformation (about 600℃), T_e is the temperature when the phase transformation from α-Ti to β-Ti is completed (about 980℃), A and D are the material constants.

In the rapid cooling stage, Ti-6Al-4V will undergo a transformation to α′ /α″ , and the cooling rate in the cutting process can reach 105℃/s, which is similar to the martensitic transformation [229]. The equation for calculating the phase volume fraction of α′ /α″ is as follows:

$$f_{\alpha'} = f_{\beta}\left\{1-\exp\left[-\chi\left(M_s - T\right)\right]\right\} \tag{64}$$

where, M_s is the initial temperature of martensitic transformation, χ is the material constant, f_β is the volume fraction of β phase at the rapid temperature rise stage in the cutting process.

During HSM, strong mechanical loading is applied to the workpiece, which also contributes to phase transition. Therefore, in the Avrami model, the influence of mechanical stress on Ti-6Al-4V phase transformation should be considered to modify the initial phase transformation temperature [76]. The transformation from α-Ti to β-Ti during rapid heating is confirmed to be a non-diffusive martensitic transformation process [230]. In the process of Ti-6Al-4V thermal processing, the material is submitted to large and rapid thermo-mechanical loadings, which promotes the transformation of α -Ti to β-Ti. By correcting the local stress with the initial phase transformation temperature, the critical condition for phase transformation can be described more accurately:

$$\frac{dP}{dT} = \frac{\Delta H_{tr}}{T\Delta V_{tr}} \tag{65}$$

where, dP is local stress, T is initial phase transition temperature, ΔH_{tr} is enthalpy of phase transition, and ΔV_{tr} is volume change caused by phase transition.

The activation of twins is more difficult than the generation of dislocation, and the activation of twins follows the Zener-Hollomon (ZH) relation. The generation of twins occurs only when the stress, strain rate, and temperature reach critical values [71]. To calculate the volume fraction and size of deformation twins, the critical fractional shear stress (CRSS) activated by twins needs to be calculated using the following equation:

$$\sigma_c = K\dot{\varepsilon}^{(-1/m+1)}e^{Q/(m+1)RT} + k_c d^{-0.5} \tag{66}$$

In this equation, k_c is the ZH strengthening factor. According to the study of Meyers et al. [231], the value of k_c corresponding to the Ti-6Al-4V alloy is 18MPa·mm$^{1/2}$. Twin systems start when the flow stress of materials is greater than the critical shear stress and the ZH factor is greater than the critical value.

According to relevant studies, the average distance between adjacent twins is correlated with the volume fraction of twins and their thicknesses [232], and its equation is shown as follows:

$$\frac{1}{l} = \frac{1}{2t} * \frac{f_t}{1-f_t} \tag{67}$$

The evolution of volume fraction f_t of deformation twins can be described by the following equation:

$$f_t = f_{t0}\left(1-e^{-\beta\left(\varepsilon-\varepsilon_{init}\right)}\right)^m \tag{68}$$

where, f_{t0} is the volume fraction of twin saturation, ε_{init} is the critical strain of twin excitation, and β and m are the material constants.

The microhardness of materials after plastic deformation is the superposition of the incremental microhardness caused by the evolution of initial microhardness and the microstructure characteristics, and its can be calculated using the following equation:

$$\begin{aligned} h_{total} &= h_0 + \Delta h_d + \Delta h_{HP} + \Delta h_{PT} + \Delta h_t \\ \Delta h_d &= k_h M_t \alpha_h G b \sqrt{\rho_{tot}} \\ \Delta h_{HP} &= k_{HP}\left(d / d_0\right)^{-1/2} \\ \Delta h_{PT} &= \sum f_i\left(h_i - h_0\right) \\ \Delta h_t &= k_t\left(l / d_0\right)^{-1/2} \times \left[1+\left(M-1\right) f_t\right] \end{aligned} \tag{69}$$

where, h_0 is the initial microhardness of material, Δh_d, Δh_{HP}, Δh_{PT} and Δh_t are the increments of microhardness caused by dislocation density change, HP effect of grain size change, phase transformation and twin strengthening. The values of the coefficients of the microhardness model for the Ti-6Al-4V alloy are shown in Table 24. They were extracted from the works of Rinaldi et al. [232] and Wang et al.[233].

Table 24: Values of the coefficients of the microhardness model for Ti-6Al-4V alloy ([232], [233]*).*

Parameters	Value	Parameters	Value
A	-1.86	ΔH_{tr} (kJ mol^{-1})	4.1
D	4.35	k_c(Mpa mm$^{1/2}$)	18
T_s (℃)	600	m	16.49
T_e (℃)	980	K	23
M_s (℃)	400	f_{t0}	0.417
χ	1.32	β	27.15

This microhardness model was implemented in ABAQUS/Explicit through a VUSDFLD subroutine, and applied to predict the microhardness in the chip and machined surface and subsurface. Fig. 103 shows the flowchart of the microhardness calculation using the above described microhardness model.

Fig. 103: Flowchart of microhardness calculation using the microhardness model implemented in Abaqus/Explicit through a user subroutine VUSDFLD.

6.4.2 Microhardness prediction and comparison with experimental values (model validation)

To compare the predicted microhardness using the proposed microhardness model with that obtained experimentally, samples were extracted from the machined workpieces and polished using different abrasive papers. Then, Vickers microhardness tests were carried out on the cross-section of the samples using the microhardness testing machine HXD-1000TMC. These tests were performed at different depths beneath the surface using a constant load of 25 gf (equivalent to 0.2452 N) applied during 15s. Fig. 104 shows the matrix of indentation used to measure the microhardness. In order to avoid the influence of one indentation into another, a distance of about 30 microns between adjacent indentations was used. Moreover, the matrix of indentation shown in Fig. 104 was repeated 6 times to calculate the an average microhardness and the corresponding standard deviation .

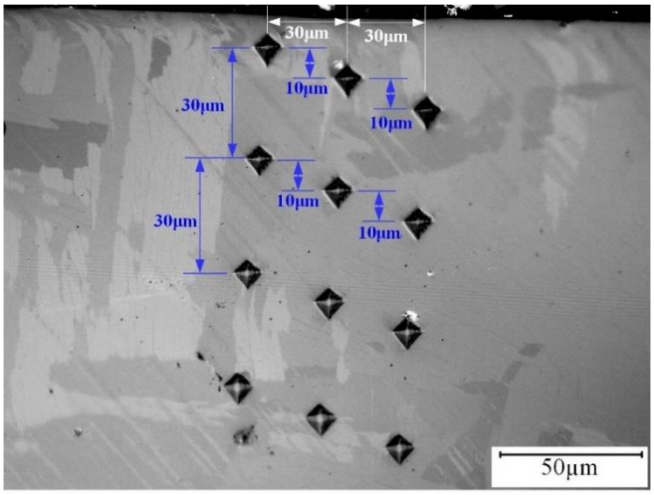

Fig. 104: Matrix of indentations used to determine the Vickers microhardness beneath the machined surface.

Fig. 105 shows both predicted and measured microhardness values for several cutting speeds. This figure shows that the microhardness model is able to capture the microhardness distribution in the machined surface and subsurface with an error between about 8%-15%. Therefore, this model can be applied to accurately predict the microhardness distribution in the machined surface and subsurface, induced by machining of Ti-6Al-4V alloy for the range of cutting conditions used in this work.

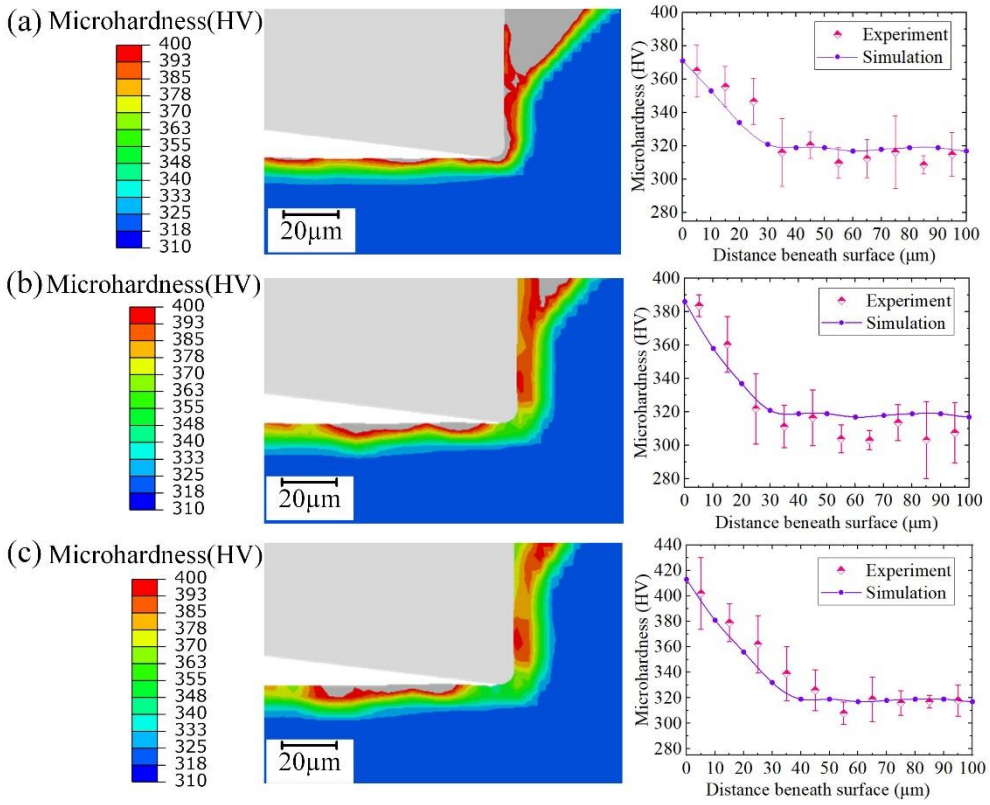

Fig. 105: Experimental and simulated Vickers microhardness in the machined subsurface for several cutting speeds: a) 125 m/min, b) 250 m/min and c) 500 m/min.

6.4.3 Influence of the cutting conditions on the predicted microhardness distribution in the machined surface and subsurface

Fig. 106 shows the predicted microhardness distributions along the distance beneath the surface for different machining conditions (uncut chip thickness, tool cutting edge, and tool wear VB). It shows that the uncut chip thickness can significantly affect the micro-hardness of the machined surface and subsurface when it increases from 0.1 mm to 0.2 mm. However, when tool cutting edge radius increases from 5 to 10 μm the microhardness of the machined surface slightly increases. According to Zhang et al. [234] increasing the cutting edge radius increases the mechanical loading on the machined surface, but has no significant effect on the temperature distribution of the machined surface. Mechanical loading can promote the dislocation accumulation and the increase of microhardness. Concerning to the tool wear VB, the microhardness and the depth of hardened layer induced by machining are increasing significantly when VB increases to 0.2 mm. Tool wear leads to a fast increase in the mechanical loading on the machined surfaces, which can lead to an increased hardening caused by dislocation and twinning [235]. The friction between the tool flank face

and the machined surface will generate higher temperature, which will promote the phase transition [236]. The gradient of mechanical and thermal loadings caused by tool wear will increase rapidly. Therefore, tool wear has a significant effect on the microhardness of the machined surface and subsurface.

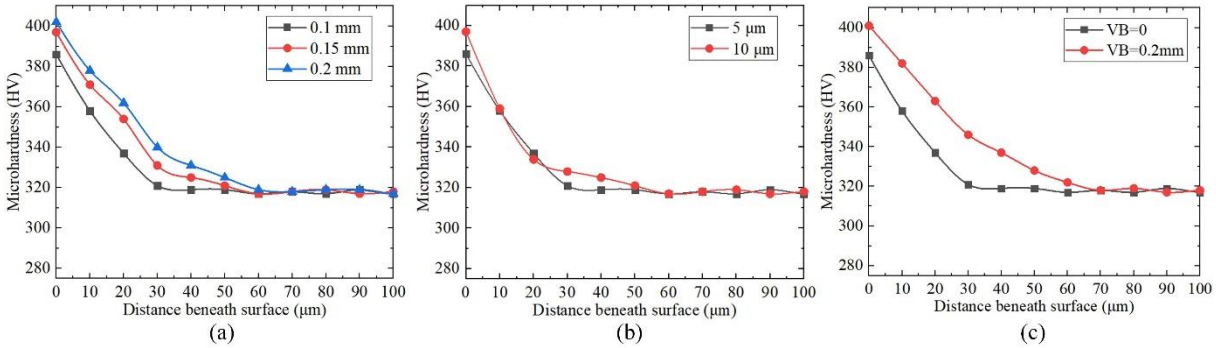

Fig. 106: Distribution of the microhardness in the machined surface and subsurface for different values of: (a) uncut chip thickness with same designed tools at cutting speed of 250 m/min, (b) cutting edge radius with 5 and 10 μm (other tool geometry from designed tools) at cutting speed of 250 m/min and uncut chip thickness of 0.1 mm, and (c) tool flank wear VB=0 and 0.2 mm (other tool geometry from designed tools) at cutting speed of 250 m/min and uncut chip thickness of 0.1 mm.

The microhardness distribution in the machined surface may results from the contribution of different microstructure characteristics. Fig. 107 shows the contribution of each microstructure characteristic used in the microhardness model on the microhardness distribution in the machined surface and subsurface. It can be found that the hardening effect caused by dislocation accumulation is high on the machined surface, and it decreases as the distance beneath the surface increases. The accumulation of dislocation is accompanied by grain refinement, so the impact of grain size here on microhardness is relatively low, accounting for about 20%. Moreover, the contribution of phase transformation and twinning to the microhardness is smaller than dislocation accumulation, accounting for about 15% of the total hardening. In addition, it is worth noting that for the cutting condition indicated in Fig. 107, the contribution of the microstructure characteristics to microhardness is not always applicable, which needs more strict microstructure characterization and mechanical testing to be validated.

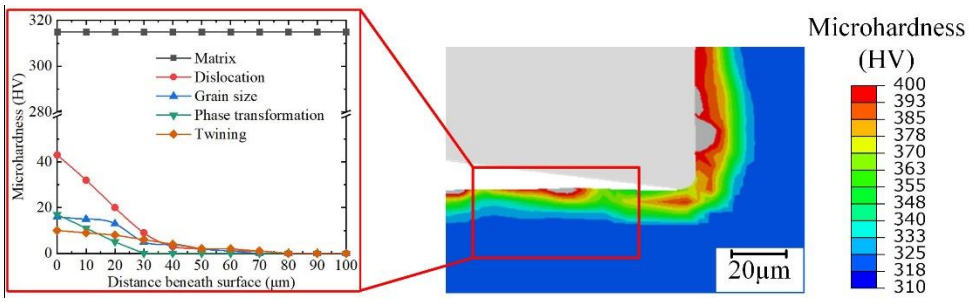

Fig. 107: Microhardness distribution at the machined surface and subsurface considering the contributions of different microstructure characteristics (cutting speed: 250 m/min, uncut chip thickness: 0.1 mm).

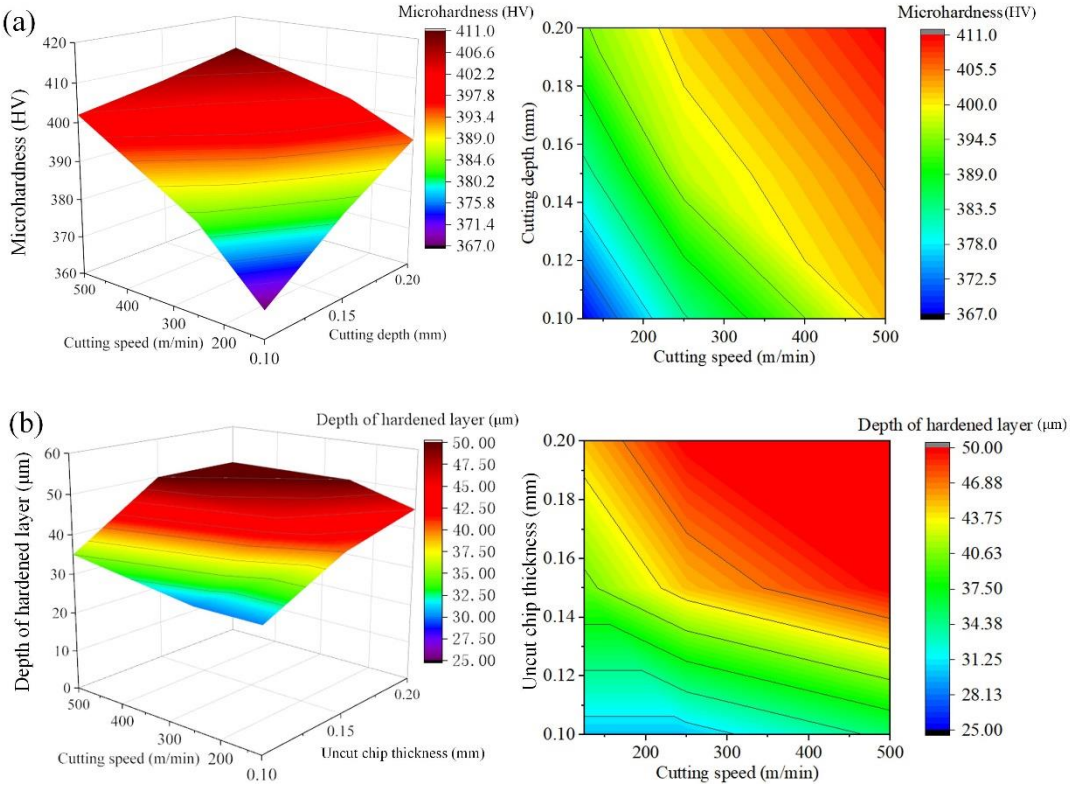

Fig. 108: Influence of the cutting speed and uncut chip thickness on the distribution of the: (a) microhardness, and (b) depth of hardened layer.

The influence of cutting speed and uncut chip thickness on the microhardness of the machined surface and subsurface are analyzed, and the results are shown in Fig. 108. This figure shows that the microhardness and the depth of hardened layer increase with both the cutting speed and uncut chip thickness. For example, when the uncut chip thickness is equal to 0.1 mm and the cutting speed increases from 125 m/min to 250 m/min, the microhardness increases from 367 HV to 383 HV, the hardeness increases from 15.4% to 20.4% in relation to the hardness of the bulk material, and the thickness of the hardened layer is 30 μm. It can also be seen

from this figure that both cutting speed and uncut chip thickness have significant effects on the microhardness. However, the cutting speed has a lower effect on the thickness of the hardened layer when compared to the uncut chip thickness.

Difference between the proposed microhardness model developed in this research work with the traditional Hall-Petch model (defined in section 6.4) [30, 69-71] are compared in terms of accuracy rate, computational time and complexity level, as shown in Table 25. Among these parameters, the accuracy rate is calculated by comparing the predicted microhardness with the experimental measured one, and the computation time is obtained from the total time to conduct the machining simulations (using the proposed CEL1 model described in section 3.3) by using different microhardness models. To sum up, it is of great significance to improve the prediction accuracy without significantly increase the computational time and the complexity level.

Table 25 Summary of the accuracy rate, computation time and complexity level between traditional [30, 69-71] and the proposed microhardness models

Model	Features	Accuracy rate	Computation time	Complexity level
Traditional model [30, 69-71]	Dislocation density Grain size	89.7%~92.5%	4.5 hours	Low
Proposed model	Dislocation density Grain size Twinning Phase transformation	93.5%~95.8%	4.8 hours	Average

6.5 Residual stress distribution in the machined surface and subsurface

Due to the main drawback of low computational efficiency, a numerical approach to calculate the residual stress in machining of Ti-6Al-4V titanium alloy is proposed. CEL approach and explicit solver is adopted to simulate the cutting process. To improve calculation efficiency and reduce the effects of cumulative error, the Lagrangian approach and implicit solver is applied to simulate the cooling process of workpiece. In contrast to the approach only using explicit solver (called traditional approach in this thesis), the improvement of the proposed approach using both explicit and implicit solver is identified.

6.5.1 Experimental determination of the residual stress

The distributions of the residual stresses along the depth beneath the machined surface were measured in the longitudinal (direction of primary motion) and in the transversal (normal to the direction of primary motion) directions, as shows in Fig. 109. They were determined by the X-Ray diffraction technique using the $\sin^2\phi$

method using Proto XRD 1200 equipment. To determine the residual stress beneath the surface, the layers were successively removed by the electrolytic polishing method to avoid reintroducing additional residual stresses. Measurements were made with the diffraction of copper Kα radiation from the {213} crystallographic plane of the Ti-6Al-4V alloy and performed in the center of the machined surface. The irradiation zone had a length of 3 mm and a width of 1 mm. Diffractions were recorded for 29 tilt angles ψ varying between ±45°. The changes of crystal lattice spacing can result in the retained elastic strain component, which can be calculated using the following equation:

$$\varepsilon_{\phi\psi}^{hkl} = S_1\left[\sigma_{11}^s + \sigma_{22}^s\right] + 1/2\, S_2 \sigma_\phi \sin^2\psi \tag{70}$$

The X-ray elasticity constants S_1 and $1/2S_2$ providing the proportionality between measured strains and calculated stresses have been calculated owing to an elastic self-consistent model: $S_1 = -2.83\times10^{-6}$ MPa^{-1}, $1/2S_2 = 11.68\times10^{-6}$ MPa^{-1}.

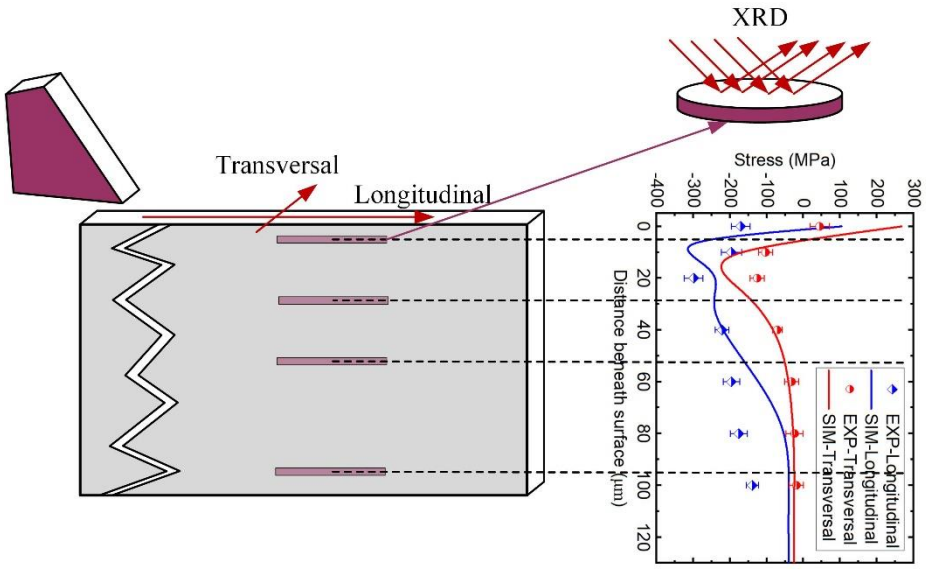

Fig. 109: Approach used for residual stress determination in longitudinal and transversal directions.

6.5.2 Modeling and simulation of the residual stresses

Due to the main drawback of low computational efficiency of the explicit solver and the lack of consideration of the whole process, which also includes workpiece unloading and cooling down to room temperature, an approach for modeling and simulating the residual stress in orthogonal cutting of Ti-6Al-4V titanium alloy is proposed. This approach includes the following three main steps as shown in Fig. 110: (1) cutting process

(workpiece loading) (Fig. 110a), (2) workpiece unloading (Fig. 110b), and (3) cooling down the workpiece to the room temperature (Fig. 110c). To simulate both cutting process (workpiece loading) and workpiece unloading steps a model including the CEL approach (Abaqus/Explicit solver) and a VUHARD subroutine of the constitutive model is used (called as Model I). To improve calculation efficiency and reduce the effects of cumulative error, a model including the Lagrangian approach (Abaqus/Standard solver) and a UHARD subroutine of the constitutive model is used to simulate the cooling step of the workpiece (called as Model II). A strategy of data transfer from Model I to Model II and mesh rebuilding is developed and described as follows. This strategy includes the following sequence:

1) Post-processing of cutting simulation results
2) Rebuilding the mesh part for RS simulation based on cutting simulation results
3) Extracting and applying of strain, stress, and temperature between different models

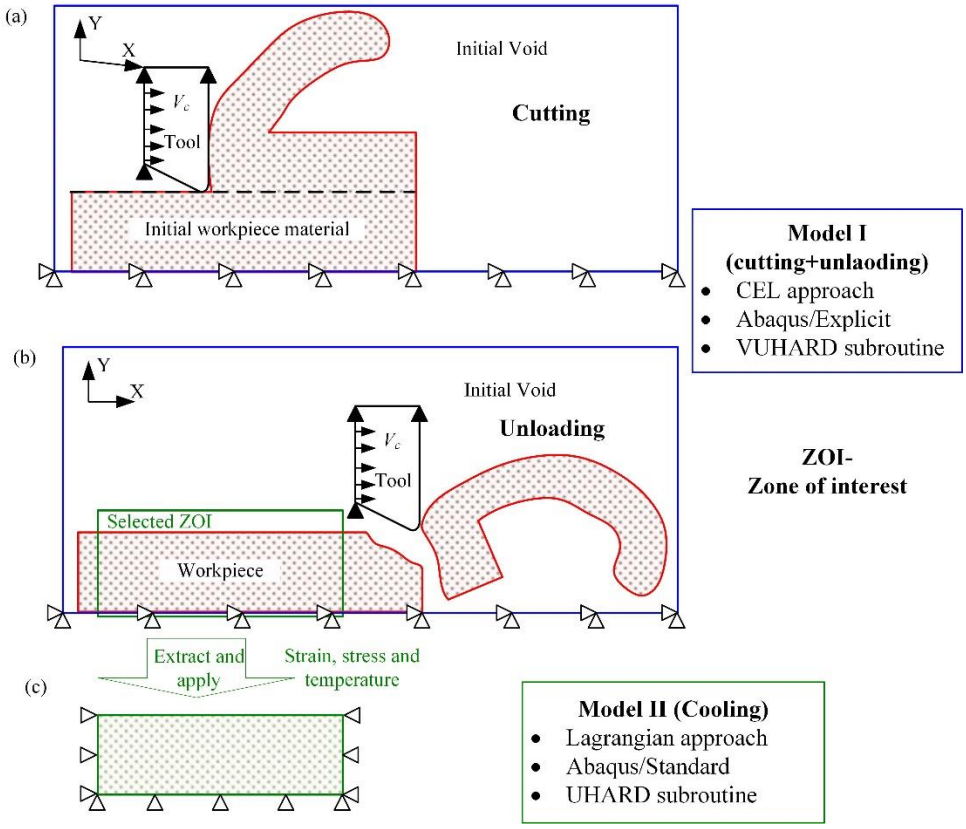

Fig. 110: Schematic representation of the simulation approach to obtain the residual stress in machining of Ti-6Al-4V titanium alloy: (a) cutting process (workpiece loading), (b) workpiece unloading; and (c) workpiece cooling.

1) Post-processing of cutting simulation results

The post-processing of simulation results is conducted to extract the data from the Abaqus output .ODB file based on the structure/contents of this file, which includes model data and the simulation results [237]. The procedure of post-processing of cutting simulation results is presented by the flowchart shown in Fig. 111, and it was implemented through a python script. This procedure is composed by several steps, described as follows. Step 1: After importing the required modules keywords, the corresponding action is executed. Step 2: Then, the name and path of the input and output files are specified in the configuration file and the name of the configuration file is passed to the script as a parameter. Step 3: Through opening the ODB file, the developed script can access the contents according to Abaqus data structure and hierarchy. Step 4: selection of a zone of interest (ZOI) in the workpiece without the chip, tool, and the transient cutting regions at the workpiece, and extraction of the results from Model I. In order to identify ZOI, model data is applied to address the node coordination and results data is used to record the element deformation, both of which make mesh rebuilding possible.

It is worth noting that the simulation results on the nodes can be directly extracted, while the results on the elements need to be decomposed to nodes before extraction. The selections of ZOI is very important for the post-processing of the simulation results. After the cutting process, the tool and the formed chip do not need to be transferred to Model II. Moreover, due to the transient conditions when the cutting tool enter and leave (formation of exit burr) the workpiece, the initial and end zones of the workpiece are not suitable for participation in the subsequent calculation of residual stress. Therefore, the zone of the workpiece containing the machined surface in the intermediate stable region is transferred to Model II.

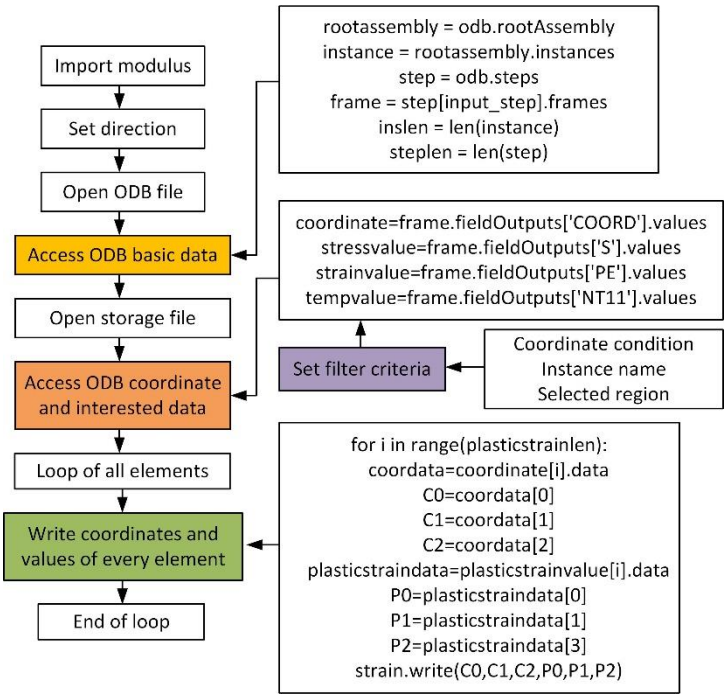

Fig. 111: Flowchart of post-processing of cutting simulation results by developing a python script.

2) Rebuilding the mesh part for RS simulation based on cutting simulation results

The mesh part rebuilding technique is the basis to achieve the accurate extraction and application of data on nodes between different models, when the whole process simulation involves different element types, solvers, analysis steps, and boundary conditions, especially for the workpiece with distorted element. The residual stress simulation approach proposed in this study uses two types of element types: 3D Eulerian elements (EC3D8RT) in Model I and 2D Lagrangian elements (CPE4RT) for Model II. As shown in Fig. 112, the flowchart for rebuilding the mesh part is divided into four steps: (1) access the node label and corresponding coordinates, (2) access the element label and node connectivity, and (3) select the ZOI shown in Fig. 110 and the four nodes in the same cutting plane (XY plane in Fig. 112) from 3D Eulerian elements with eight nodes, (4) generate new models by writing input INP file and changing the element type to the 2D Lagrangian element. Through decomposition and composition of the element and node information of mesh part, the selection of solver, element type even FE software can be independent. The boundary conditions used in Model II are shown at the bottom side of Fig. 112, where the workpiece is constrained in the Y-direction in the bottom side, and in the X-direction in both left and right sides.

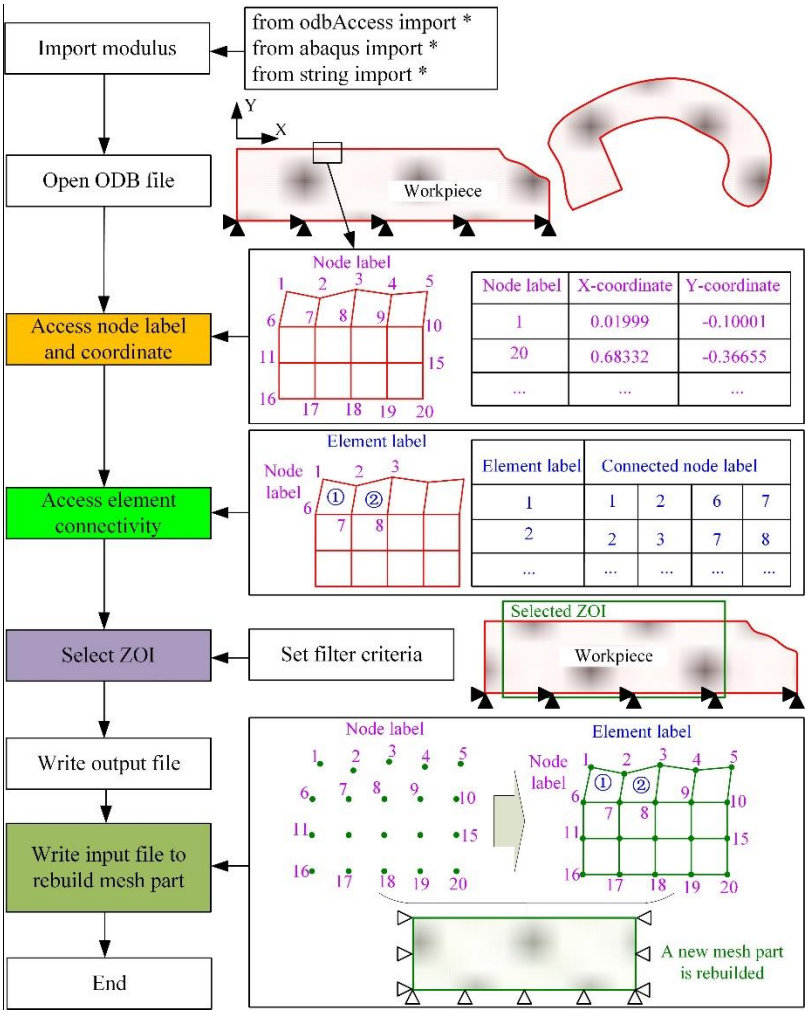

Fig. 112: Flowchart of rebuilding the mesh part.

3) Extracting and applying of strain, stress, and temperature between different models

Due to the node coordinates used to rebuild the mesh part and associate the results data are the same one, the error in extracting and applying process can be reduced significantly. The application of strain, stress, and temperature from Model I to Model II is conducted by reading the data file from the last step and assigning data to every node in the function of a predefined condition. The stress and strain are predefined using SIGINI and HARDINI subroutines of ABAQUS to match the coordinates and apply data on nodes. The assignment of temperature is applied using the pre-processing function of "AnalyticalField". After modeling stress relaxation from the cooling process, the heat convection (23 $W/m^2/°C$) is applied to the top surface of the workpiece and the set of boundary conditions is presented in (c), and then an Abaqus/Standard solver and UHARD subroutine is used to simulate the cooling process until room temperature.

6.5.3 Measured and simulated residual stresses results

Fig. 113 shows both simulated and measured in-depth residual stress in the longitudinal and transversal directions for the cutting conditions shown in Table 23. The typical in-depth residual stress profile is shown in Fig. 114. In general, the residual stress at the machined surface may be tensile or compressive. Residual stress beneath surface changes continuously until the maximum compressive residual stress (MRS) is achieved, and then decreases gradually close to the initial stress state of the bulk material. As shown in Fig. 114, the in-depth residual stress profile is characterized by the following four parameters: 1) residual stress at the machined surface (SRS), 2) maximum compressive residual stress beneath the surface (MRS), 3) depth of the maximum compressive residual stress (Depth_MRS), 4) depth of the layer affected by residual stress (Layer_RS).

Experimentally, when the new tool is used the residual stresses at the machined surface (SRS) are slightly tensile or almost zero in the transversal direction and compressive in the longitudinal direction. For the cutting conditions shown in Table 23, and considering whole the residual stress profile, the residual stress in the longitudinal direction is more compressive than the stress in the transversal direction. The increase of the cutting speed from 125 m/min to 500 m/min (from case 1 to case 4 in Fig. 113) has a minor effect the residual stresses, just an increase of the MRS. The increase of the uncut chip thickness from 0.1 mm to 0.15 mm (by comparing cutting condition number 2 with number 5 in Fig. 118) results in: 1) an increase of the thickness of the layer affected by the transversal residual stress induced by machining from about 60 μm to 100 μm; 2) an decrease of Layer_RS in the longitudinal direction induced by machining; 3) the MRS become more compressive in the transversal direction and less compressive in the longitudinal direction.

Experimentally, when the worn tool is used (Fig. 113 (f)), the longitudinal direction SRS becomes tensile reaching 200 MPa, the MRS become more compressive in both directions, and the location of the maximum compressive residual stress beneath the surface (Depth_MRS) shifts further from the surface in both directions.

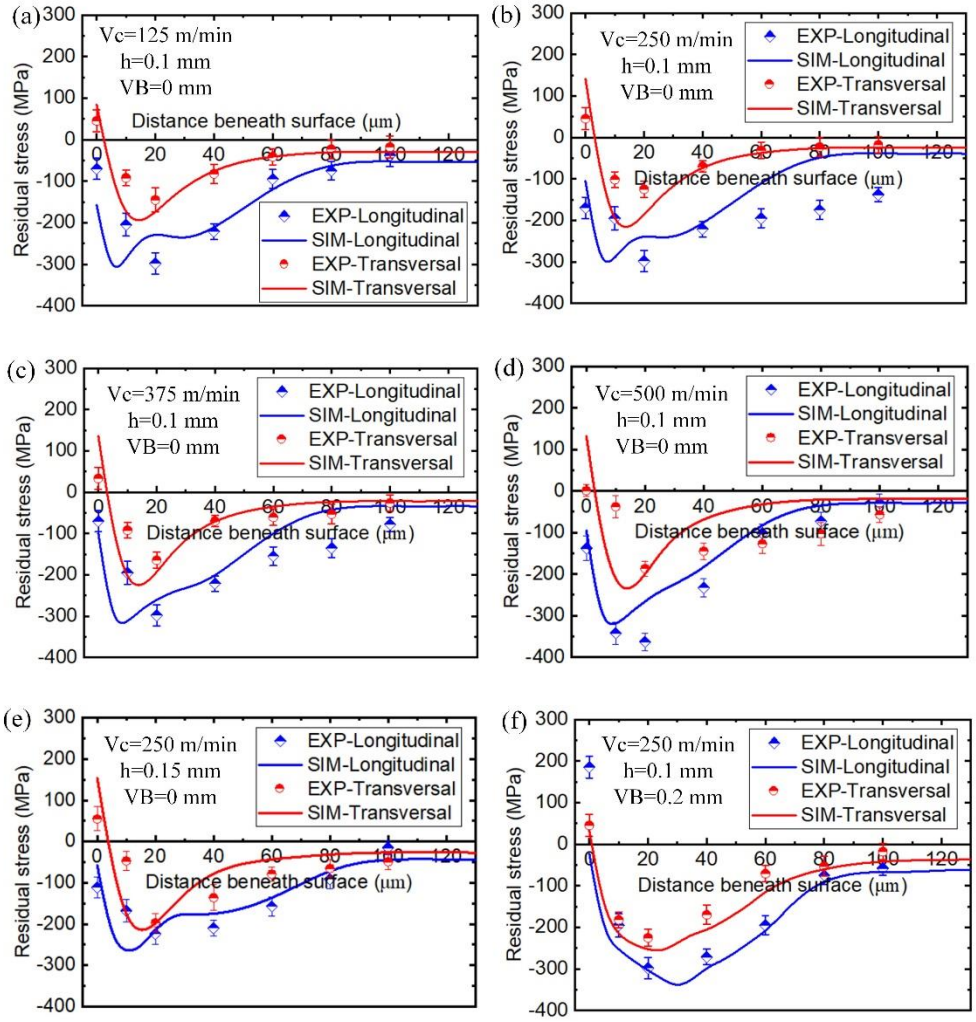

Fig. 113: Comparison between predicted and measured residual stress in the longitudinal and transversal directions for the cutting conditions number (case number): (a) 1, (b) 2, (c) 3, (d) 4, (e) 5, and (f) 6.

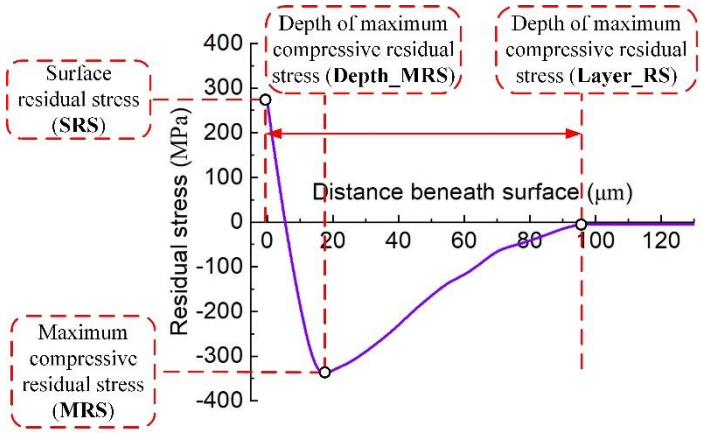

Fig. 114 Schematic representation of four parameters characterizing the typical in-depth residual stress profile in machining Ti-6Al-4V.

As far as the simulated residual stresses are concerned, they follow the general trend of the experimental

ones, thus the proposed residual stress simulation approach can predict well the residual stress in the longitudinal and transversal directions. However, to quantitatively evaluate the ability of the proposed simulation approach to predict the residual stresses, the simulated and experimental values of the four above-mentioned parameters characterizing in-depth residual stress are shown from Fig. 115 to Fig. 118. Fig. 115 shows both simulated and measured SRS. The absolute error of predicted SRS is within 150 MPa for both longitudinal and transversal directions, except that of tool wear condition (case 6) that reaches about 200 MPa. When compared with the results from traditional Lagrangian approach, the SRS predicted by the proposed residual stress simulation approach in longitudinal direction can be predicted more accurately than that in transversal direction, while traditional Lagrangian approach shows a contrary trend [8].

Fig. 116 shows the simulated and measured MRS. The difference between simulated and measured MRS in longitudinal direction reaches 18% in average and 24% in maximum. While in transversal direction, this difference is 24% in average and 31% in maximum. Therefore, the proposed residual stress simulation approach predicts relatively well the MRS.

Fig. 117 and Fig. 118 shows the simulated and measured Depth_MRS and Layer_RS), respectively. Due to the limitation of selection of experimental testing depth, the Depth_MRS and Layer_RS cannot be found very well, so an estimation of these two parameters is conducted. In general, these two thicknesses can be quite well predicted by the proposed residual stress simulation approach. Especially, the maximum difference between predicted and measured Layer_RS is less than 20%.

The above difference between simulations and experimental results can be attributed to the limitation of the CEL approach to reproduce the material springback, which has a significant influence on the residual stresses distribution in the machined surface and subsurface. Besides that, the tool-workpiece contact model used in the proposed cutting model is not accurate enough to describe the real contact between the tool flank face and the machined surface.

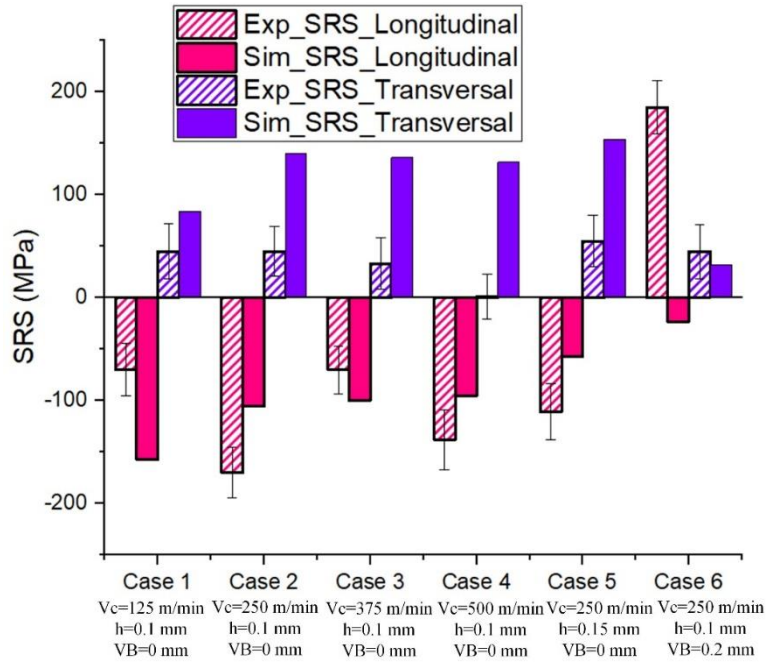

Fig. 115: Simulated and measured residual stress at machined surface (SRS).

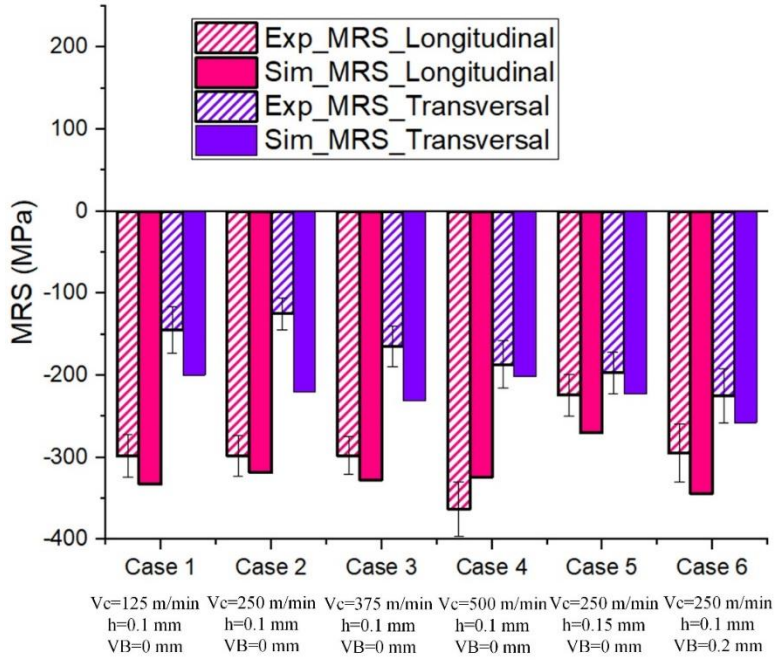

Fig. 116 Simulated and measured maximum compressive residual stress beneath the machined surface (MRS).

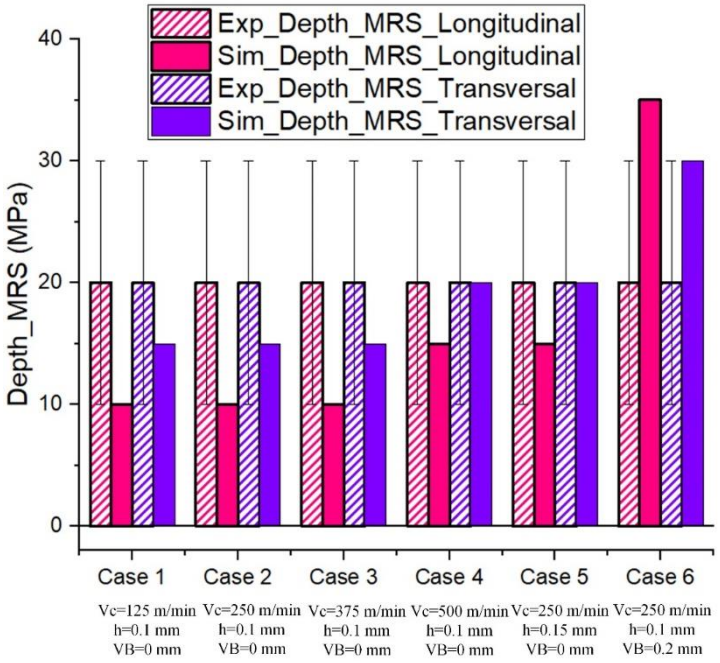

Fig. 117 Simulated and measured depth of maximum compressive residual stress beneath the machined surface (Depth_MRS).

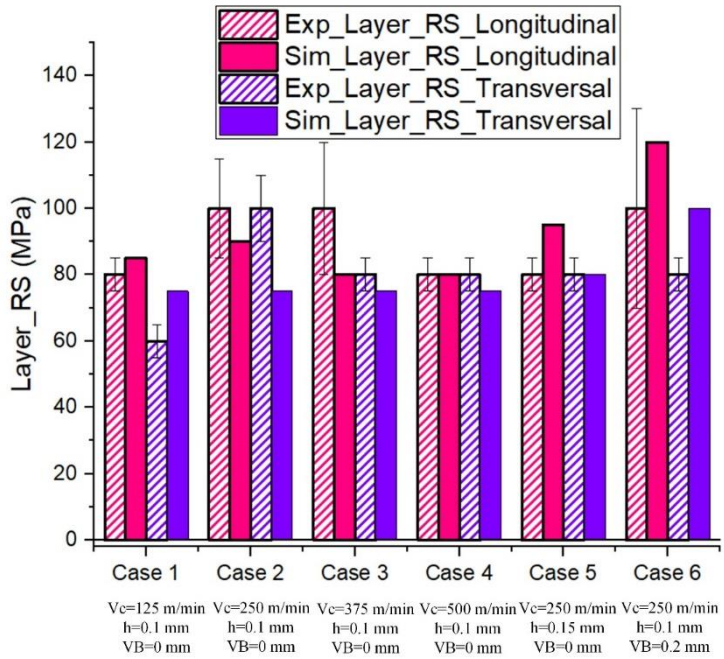

Fig. 118 Simulated and measured thickness of the layer affected by residual stress (Layer_RS).

As mentioned above, the residual stress will be also studied by considering the effect of the cyclic nature of chip formation in machining Ti-6Al-4V. Fig. 119 shows the simulated longitudinal and transversal residual

stress at the machined surface and along the cutting direction, for all the cutting conditions. As shown in this figure, due to the cyclic nature of the chip formation process these stresses vary cyclically. Mabrouki et al. [238] also found this kind of cyclic variation of the residual stresses along the cutting direction. In the cutting direction, the average surface residual stress and standard deviation for the cutting speed of 125 m/min, 250 m/min, 375 m/min, 500 m/min are 22.2±65.2 MPa, 94.7±73.5 MPa, 104.2±66.5 MPa, and 122.7±63.2 MPa, respectively. Therefore, increasing the cutting speed from 125 m/min to 500 m/min, the average longitudinal residual stress at the machined surface slightly increases, and its amplitude reaches a maximum of 250 MPa. It is worth noting that the longitudinal residual stress at the machined surface for a cutting speed of 125 m/min varies from predominant tensile stress to slightly compressive stress. Concerning to the uncut chip thickness, when this parameter changes from 0.1 mm to 0.15 mm (from condition number 2 to number 5 in Fig. 119), the average longitudinal residual stress at the machined surface and the standard deviation changes from 94.7±73.5 MPa to 89.7±82.5 MPa, respectively. Moreover, the periodic variation of the residual stress increases from 83 μm to 114 μm, which is similar to the surface topography shown in Fig. 100. Concerning tool wear, comparing cutting condition number 2 (new tool) with number 6 (worn tool with VB=0.2mm) in Fig. 120, the average surface residual stress and standard deviation in the cutting direction are 94.7±73.5 MPa and 113.4±12.1 MPa, respectively. It is worth to nothing, that the amplitude of the residual stresses decreases significantly when the worn tool was used. Even if the cyclic nature of chip formation is still present, its impact on the residual stresses in the machined surface and subsurface is less important that the tool flank wear. The influence of this cyclic nature of residual stress on component functional performance, especially the fatigue life and stress corrosion cracking, need to be further investigated.

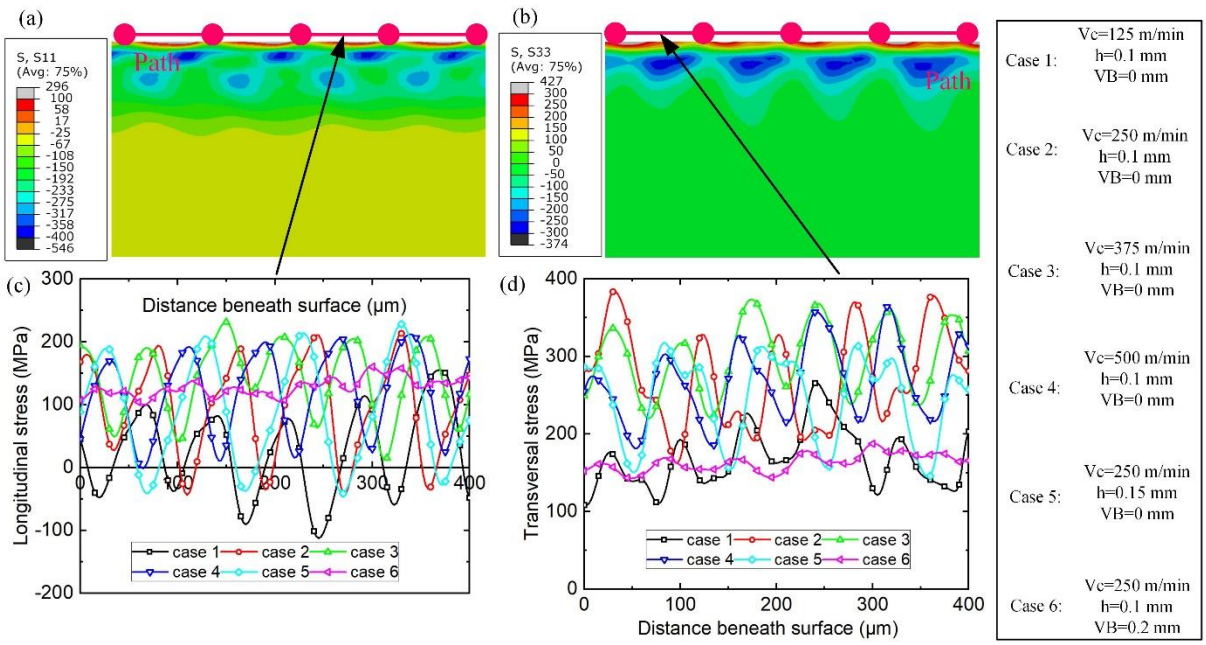

Fig. 119: Simulated cyclic distribution of residual stress in longitudinal and transversal directions from superficial surface of the workpiece.

The difference between the proposed approach for modelling the residual stress in metal cutting developed in this research work with the traditional one (defined in section 6.5) [239–241] are compared in terms of accuracy rate, computational time and complexity level, as shown in Table 26. To sum up, the proposed approach for modelling the residual stress shows a remarkable improvement in prediction accuracy. Besides that, the proposed approach can significantly reduce the computation time when compared with the traditional model [239–241]. It is worth noting that the proposed approach using both explicit and implicit solvers is based on the techniques of data transfer and mesh rebuilding, whose complexity level is much higher than traditional approach.

Table 26 Summary of accuracy rate, computation time and complexity level between traditional [239–241] and proposed approaches for modelling the residual stress in metal cutting.

Approach	Features	Accuracy rate	Computation time	Complexity level
Traditional approach [239–241]	1.Cutting model: explicit solver 2.Cooling model: explicit solver	74.1%~82.5%	81 hours	Low
Proposed approach	1.Cutting model: explicit solver 2.Cooling model: implicit solver	81.4%~93.9%	5.2 hours	High

6.6 Summary of the chapter

A CEL-based model using a constitutive model considering the effect of the state of stress in the mechanical behavior of the work material permitted to simulate the cyclic variation of the plastic strain and surface topography in the machined part along the cutting direction, which is validated by comparing the frequency of surface undulation and chip segmentation frequency, both obtained experimentally. Because of this, the other important parameters of the surface integrity (e.g. residual stress, microstructure, and microhardness) should also vary cyclically. This capability of the CEL-based model provides a completely new perspective for simulating the surface integrity, which is particular important for predicting the functional performance and life of the machined parts for critical applications [242]. This new ability with a great practical significance is achieved when a suitable constitutive model is used in the cutting simulations.

A model of material microhardness induced by machining was established, which includes the contribution of several microstructure characteristics. At the machined surface, the hardening phenomenon caused by dislocation accumulation is dominant, decreasing as the beneath the surface increases. Moreover, the accumulation of dislocation is accompanied by grain refinement, and the temperature and strain rate of the machined surface are not sufficient to significantly increase the microhardness by phase transformation and twinning. The microhardness model was validated by comparing the simulated microhardness with those obtained experimentally. This model was applied to investigate the influence of the uncut chip thickness, tool cutting edge radius and tool wear on the microhardness in the machined surface and subsurface.

A residual stress simulation approach composed by two models (Model I and Model II) is proposed to predict the residual stress in machining of Ti-6Al-4V titanium alloy by using different numerical approaches (CEL and Lagrangian), solvers and element types. This residual stress simulation approach permitted to simulate the cutting and unloading (Model I), and cooling (Model II) processes. The accuracy of this approach is verified by comparing the simulated residual stresses with those obtained experimentally using X-ray diffraction technique. Due to the cyclic nature of the cutting process the longitudinal and transversal residual stresses vary cyclically along the cutting direction.

7 General conclusions and recommendations for future work

7.1 General conclusions

This Ph.D dissertation aims to investigate the microstructure evolution and the surface integrity (surface topography, microstructure, microhardness and residual stresses) in High Speed Machining (HSM) of Ti-6Al-4V titanium alloy, using multiscale modelling and experimental approaches. The main conclusions are summarized as follows.

A model based on the Finite Element Method (FEM) using Coupled Eulerian- Lagrangian (CEL) approach is used to simulate the orthogonal cutting process. This cutting model includes the proposed constitutive model considering the influence of strain hardening, strain-rate, temperature, and state of stress (e.g., stress triaxiality and Lode parameter) in the material plasticity and damage. Compared with the traditional Lagrangian method, CEL approach can effectively avoid mesh distortion and has significant advantages in predicting the surface integrity. Moreover, simulated cutting force and chip geometry obtained using the proposed constitutive model are compared with those obtained using the Johnson-Cook (J-C) model, and experimental data. Both chip geometry and cutting force predicted by the proposed constitutive model is closer to the experimental one than the J-C constitutive model. The CEL approach combined with the proposed constitutive model can also simulate the material side flow, which results in a larger width of chip compared to the width of cut, and in the formation of lateral burr on the workpiece.

A multiscale model of grain refinement induced by dynamic recrystallization (DRX) occurring in HSM of Ti-6Al-4V is established, through finite element (FE) and cellular automata (CA) methods. At the macroscale, an orthogonal cutting model of HSM of Ti-6Al-4V is developed by utilizing Johnson-Mehl-Avrami-Kolmogorov (JMAK) DRX model. At the microscale, the CA model is proposed considering dislocation density evolution, grain nucleation and growth. The 2D mesoscopic microstructure evolution is simulated successfully by the CA model in which the input deformation parameters come from the FE simulations of the orthogonal cutting process. Identical microstructure predictions from both CA and FE methods show a reasonable agreement with the transmission electron microscope (TEM) results, without considering twinning and phase transformation in the simulations. It proves that the combination of FE and CA methods is an effective approach to achieve a more comprehensive understanding of the microstructure evolution and its effect on mechanical behavior during HSM. It shows that the rise of both DRX volume fraction and DRX

grain size finally results in the slightly decrease of the average grain size in the serrated chips with the increase of cutting speed, which leads to the strain softening phenomenon of flow stress.

The grain refinement mechanisms in the white and deformed layers (observed by OM or SEM) of the machined surface and subsurface are investigated, in which the thermal activation mechanism inducing a gradient of microstructure will be analyzed in detail. The gradient of strain, strain rate, and temperature beneath the machined surface is determined through the above proposed FE model. The microstructure characteristics in the machined surface and subsurface are obtained by precession electron diffraction (PED) and TEM techniques. Two layers with different grain structure (including cDRX and dDRX characteristics) are found in machined surface and subsurface. Relatively higher temperature and strain near the machined surface region results in a more significant grain refinement in the "nano grains" layer (characterized by TEM or PED) based on a combination of cDRX and dDRX mechanisms, while the "micro grains" layer (characterized by TEM or PED) is formed mainly by cDRX. Twins begin to play an important role in the plastic deformation of the work material because the strain rate in the white layer is higher than that in the deformed layer. The dynamic of the state of stress and the rapid heating of the machined surface produce large numbers of nanoscale β phase precipitations, which has critical pinning effects on dislocation and grain boundary movement, and will inhibit grains recovery and growth until nanoscale grains are formed.

The above mentioned CEL-based model is further improved for predicting other surface integrity characteristics in the machined surface and subsurface. This CEL-based model allows also to simulate the cyclic variation of the surface integrity characteristics (plastic strain, surface topography, and residual stresses) along the cutting direction. A predictive model of microhardness based on microstructure evolution was established to reveal the contribution of different microstructure characteristics on the microhardness generated by the cutting process. The hardening behavior caused by dislocation density and grain refinement is the principal contributor for the microhardness increases in the machined surface, while the contribution of phase transformation and twinning is minor. A residual stress simulation approach is proposed to predict the residual stress in machining of Ti-6Al-4V titanium alloy using numerical approaches (CEL and Lagrangian), solvers and element types. This residual stress simulation approach permitted to simulate the cutting and unloading, and cooling processes. The accuracy of this approach is verified by comparing the simulated residual stresses with those obtained experimentally using X-ray diffraction technique. Due to the cyclic nature of the cutting process the longitudinal and transversal residual stresses vary cyclically along the cutting direction.

7.2 Recommendations for future work

Based on the research work conducted in this thesis, subsequent research on the microstructure evolution and surface integrity in the cutting process should be carried out for the following reasons.

The 3D CEL model has shown obvious advantages in predicting lateral burr formation in metal cutting process, so how to extend this model to simulate various burr (exit burr, entrance burr, etc.) formation is of great significance for actual manufacturing production.

Considering the shortcomings of the CA model in this thesis, the model can only predict the microstructure evolution under certain assumptions because it does not consider the effects of twining and phase transformation. Therefore, the mechanisms of twinning and phase transformation should be considered in the subsequent research, to establish a more accurate model to simulate the microstructure evolution in machining. It is important to accurately predict the microstructure of the machined surface and subsurface for fully understanding the correlation between process mechanics – surface integrity – functional performance and lifespan of components.

In the current multiscale approach, JMAK model used in FE simulations is based on the critical strain, while the DRX model used in CA simulations is derived from dislocation density evolution. These two models are simulated individually in different scales. Proposing a unified and physics-based constitutive law for both FE and CA simulations is beneficial to further improve prediction accuracy and its application for other materials and manufacturing processes.

The influence of the surface integrity on the functional performance and life of the component is not yet fully understood. The functional performance of the component, such as fatigue, is closely related to the initiation of cracks and the microstructural characteristics such as the residence of slip band and inclusion particles, and the initial stage of its propagation is also significantly affected by grain boundaries. However, the effect of the microstructure on the initiation and propagation of fatigue cracks is often difficult to describe quantitatively. Therefore, a model that can quantitatively predict the fatigue crack initiation probability and propagation rate considering the microstructure characteristics (grain size, interfacial energy, slip band width, etc.) should be proposed.

The surface integrity of the final product also depends on the manufacturing processes applied before (casting, metal forming, etc.) and after machining (surface treatments, etc.). Moreover, the machining defects, residual stress, grain refinement, twin formation and phase transformation generated by the processes conducted before machining have significant influence on the material constitutive response, thus in the accuracy of the

machining models or other processes models conducted after machining. Therefore, a unified model for surface integrity prediction considering multiple processes needs to be developed, which is the foundation for the optimization of the manufacturing process chain found in the shop floor.

References

[1] M. Wan, X.Y. Ye, D.Y. Wen, W.H. Zhang, Modeling of machining-induced residual stresses, J. Mater. Sci. 54 (2019) 1–35. https://doi.org/10.1007/s10853-018-2808-0.

[2] R. M'Saoubi, J.C. Outeiro, H. Chandrasekaran, O.W. Dillon, I.S. Jawahir, A review of surface integrity in machining and its impact on functional performance and life of machined products, Int. J. Sustain. Manuf. 1 (2008) 203–236. https://doi.org/10.1504/IJSM.2008.019234.

[3] J.C. Outeiro, Residual stresses in machining, LTD, 2020. https://doi.org/10.1016/b978-0-12-818232-1.00011-4.

[4] T. Thepsonthi, T. Özel, Experimental and finite element simulation based investigations on micro-milling Ti-6Al-4V titanium alloy: Effects of cBN coating on tool wear, J. Mater. Process. Technol. 213 (2013) 532–542. https://doi.org/10.1016/j.jmatprotec.2012.11.003.

[5] B. Wang, Z. Liu, Q. Yang, Investigations of yield stress, fracture toughness, and energy distribution in high speed orthogonal cutting, Int. J. Mach. Tools Manuf. 73 (2013) 1–8. https://doi.org/10.1016/j.ijmachtools.2013.05.007.

[6] L.A. Denguir, J.C. Outeiro, G. Fromentin, V. Vignal, R. Besnard, A physical-based constitutive model for surface integrity prediction in machining of OFHC copper, J. Mater. Process. Technol. 248 (2017) 143–160. https://doi.org/10.1016/j.jmatprotec.2017.05.009.

[7] R. Liu, S. Melkote, R. Pucha, J. Morehouse, X. Man, T. Marusich, An enhanced constitutive material model for machining of Ti-6Al-4V alloy, J. Mater. Process. Technol. 213 (2013) 2238–2246. https://doi.org/10.1016/j.jmatprotec.2013.06.015.

[8] W. Cheng, J.C. Outeiro, Modelling orthogonal cutting of Ti-6Al-4 V titanium alloy using a constitutive model considering the state of stress, Int. J. Adv. Manuf. Technol. 119 (2022) 4329–4347. https://doi.org/10.1007/s00170-021-08446-9.

[9] P.J. Arrazola, T. Özel, Investigations on the effects of friction modeling in finite element simulation of machining, Int. J. Mech. Sci. 52 (2010) 31–42. https://doi.org/10.1016/j.ijmecsci.2009.10.001.

[10] X. Xu, J. Zhang, H. Liu, Y. He, W. Zhao, Grain refinement mechanism under high strain-rate deformation in machined surface during high speed machining Ti6Al4V, Mater. Sci. Eng. A. 752 (2019) 167–179. https://doi.org/10.1016/j.msea.2019.03.011.

[11] X. Xu, J. Outeiro, J. Zhang, B. Xu, W. Zhao, V. Astakhov, Machining simulation of Ti6Al4V using coupled Eulerian-Lagrangian approach and a constitutive model considering the state of stress, Simul. Model. Pract. Theory. 110 (2021) 102312. https://doi.org/10.1016/j.simpat.2021.102312.

[12] Y. Ayed, C. Robert, G. Germain, A. Ammar, Development of a numerical model for the understanding of the chip formation in high-pressure water-jet assisted machining, Finite Elem. Anal. Des. 108 (2016) 1–8. https://doi.org/10.1016/j.finel.2015.09.003.

[13] R. Quey, P.R. Dawson, F. Barbe, Large-scale 3D random polycrystals for the finite element method: Generation, meshing and remeshing, Comput. Methods Appl. Mech. Eng. 200 (2011) 1729–1745. https://doi.org/10.1016/j.cma.2011.01.002.

[14] Y. Avevor, J. Vincent, L. Faure, A. Moufki, S. Philippon, An ALE approach for the chip formation process in high speed machining with transient cutting conditions: Modeling and experimental validation, Int. J. Mech. Sci. 130 (2017) 546–557. https://doi.org/10.1016/j.ijmecsci.2017.06.021.

[15] K. Prakash Marimuthu, C.S.C. Kumar, H.P.T. Prasada, P. Marimuthu, C.S.C. Kumar, T. Prasada, K. Prakash Marimuthu, C.S.C. Kumar, H.P.T. Prasada, 2D Finite Element Thermo-Mechanical Model to Predict Machining Induced Residual Stresses Using ALE Approach, Mater. Today Proc. 5 (2018) 11780–11786. https://doi.org/10.1016/j.matpr.2018.02.147.

[16] F. Ducobu, E. Rivière-Lorphèvre, E. Filippi, Finite element modelling of 3D orthogonal cutting experimental tests with the Coupled Eulerian-Lagrangian (CEL) formulation, Finite Elem. Anal. Des. 134 (2017) 27–40. https://doi.org/10.1016/j.finel.2017.05.010.

[17] F. Ducobu, E. Rivière-Lorphèvre, E. Filippi, Application of the Coupled Eulerian-Lagrangian (CEL) method to the modeling of orthogonal cutting, Eur. J. Mech. A/Solids. 59 (2016) 58–66. https://doi.org/10.1016/j.euromechsol.2016.03.008.

[18] Y. Bai, T. Wierzbicki, A new model of metal plasticity and fracture with pressure and Lode dependence,

Int. J. Plast. 24 (2008) 1071–1096. https://doi.org/10.1016/j.ijplas.2007.09.004.

[19] M.N.A. Nasr, E.G. Ng, M.A. Elbestawi, Modelling the effects of tool-edge radius on residual stresses when orthogonal cutting AISI 316L, Int. J. Mach. Tools Manuf. 47 (2007) 401–411. https://doi.org/10.1016/j.ijmachtools.2006.03.004.

[20] Y. Zhang, D. Umbrello, T. Mabrouki, S. Rizzuti, D. Nelias, Y. Gong, On different FE-based models to simulate cutting operation of Titanium alloy (Ti-6Al-4V), Mechanika. 19 (2013) 349–357. https://doi.org/10.5755/j01.mech.19.3.4656.

[21] M. Sadeghifar, R. Sedaghati, W. Jomaa, V. Songmene, A comprehensive review of finite element modeling of orthogonal machining process: chip formation and surface integrity predictions, Int. J. Adv. Manuf. Technol. 96 (2018) 3747–3791. https://doi.org/10.1007/s00170-018-1759-6.

[22] G. Rotella, O.W. Dillon, D. Umbrello, L. Settineri, I.S. Jawahir, Finite element modeling of microstructural changes in turning of AA7075-T651 Alloy, J. Manuf. Process. 15 (2013) 87–95. https://doi.org/10.1016/j.jmapro.2012.09.005.

[23] T. Özel, A. Olleak, T. Thepsonthi, Micro milling of titanium alloy Ti-6Al-4V: 3-D finite element modeling for prediction of chip flow and burr formation, Prod. Eng. 11 (2017) 435–444. https://doi.org/10.1007/s11740-017-0761-4.

[24] F. Ducobu, E. Rivière-Lorphèvre, E. Filippi, Mesh influence in orthogonal cutting modelling with the Coupled Eulerian-Lagrangian (CEL) method, Eur. J. Mech. A/Solids. 65 (2017) 324–335. https://doi.org/10.1016/j.euromechsol.2017.05.007.

[25] F. Ducobu, P.J. Arrazola, E. Rivière-Lorphèvre, G.O. De Zarate, A. Madariaga, E. Filippi, The CEL Method as an Alternative to the Current Modelling Approaches for Ti6Al4V Orthogonal Cutting Simulation, Procedia CIRP. 58 (2017) 245–250. https://doi.org/10.1016/j.procir.2017.03.188.

[26] F. Shuang, X. Chen, W. Ma, Numerical analysis of chip formation mechanisms in orthogonal cutting of Ti6Al4V alloy based on a CEL model, Int. J. Mater. Form. 11 (2018) 185–198. https://doi.org/10.1007/s12289-017-1341-z.

[27] P.J. Arrazola, T. Özel, D. Umbrello, M. Davies, I.S. Jawahir, Recent advances in modelling of metal machining processes, CIRP Ann. - Manuf. Technol. 62 (2013) 695–718. https://doi.org/10.1016/j.cirp.2013.05.006.

[28] S. Buchkremer, F. Klocke, D. Veselovac, 3D FEM simulation of chip breakage in metal cutting, Int. J. Adv. Manuf. Technol. 82 (2016) 645–661. https://doi.org/10.1007/s00170-015-7383-9.

[29] Y.M. Arisoy, C. Guo, B. Kaftanoʇlu, T. Özel, Investigations on microstructural changes in machining of Inconel 100 alloy using face turning experiments and 3D finite element simulations, Int. J. Mech. Sci. 107 (2016) 80–92. https://doi.org/10.1016/j.ijmecsci.2016.01.009.

[30] D. Umbrello, A. Bordin, S. Imbrogno, S. Bruschi, 3D finite element modelling of surface modification in dry and cryogenic machining of EBM Ti6Al4V alloy, CIRP J. Manuf. Sci. Technol. 18 (2017) 92–100. https://doi.org/10.1016/j.cirpj.2016.10.004.

[31] A. Yıldız, A. Kurt, S. Yağmur, Finite element simulation of drilling operation and theoretical analysis of drill stresses with the deform-3D, Simul. Model. Pract. Theory. 104 (2020) 102153. https://doi.org/10.1016/j.simpat.2020.102153.

[32] A. Attanasio, E. Ceretti, J. Outeiro, G. Poulachon, Numerical simulation of tool wear in drilling Inconel 718 under flood and cryogenic cooling conditions, Wear. 458–459 (2020) 203403. https://doi.org/10.1016/j.wear.2020.203403.

[33] N. Ying, J. Feng, Z. Bo, A novel 3D finite element simulation method for longitudinal-torsional ultrasonic-assisted milling, Int. J. Adv. Manuf. Technol. 106 (2020) 385–400. https://doi.org/10.1007/s00170-019-04636-8.

[34] G. Liu, C. Huang, R. Su, T. Özel, Y. Liu, L. Xu, 3D FEM simulation of the turning process of stainless steel 17-4PH with differently texturized cutting tools, Int. J. Mech. Sci. 155 (2019) 417–429. https://doi.org/10.1016/j.ijmecsci.2019.03.016.

[35] J.C. Outeiro, J.C. Pina, R. M'Saoubi, F. Pusavec, I.S. Jawahir, Analysis of residual stresses induced by dry turning of difficult-to-machine materials, CIRP Ann. - Manuf. Technol. 57 (2008) 77–80. https://doi.org/10.1016/j.cirp.2008.03.076.

[36] X. Xu, J. Zhang, H. Liu, Y. Qi, Z. Liu, W. Zhao, Effect of morphological evolution of serrated chips on surface formation during high speed cutting Ti6Al4V, Procedia CIRP. 77 (2018) 147–150. https://doi.org/10.1016/j.procir.2018.08.262.

[37] M. Ostoja-Starzewski, P.Y. Sheng, I. Jasiuk, Damage patterns and constitutive response of random matrix-inclusion composites, Eng. Fract. Mech. 58 (1997) 581–606. https://doi.org/10.1016/s0013-

7944(97)00046-5.

[38] Y. He, J. Zhang, Y. Qi, H. Liu, A.R. Memon, W. Zhao, Numerical study of microstructural effects on chip formation in high speed cutting of ductile iron with discrete element method, J. Mater. Process. Technol. 249 (2017) 291–301. https://doi.org/10.1016/j.jmatprotec.2017.06.006.

[39] J. Zhang, Z. Liu, H. Liu, X. Xu, J. Outeiro, W. Zhao, Fragmented chip formation mechanism in high-speed cutting from the perspective of stress wave effect, CIRP Ann. 70 (2021) 53–56. https://doi.org/10.1016/j.cirp.2021.03.016.

[40] B.C. Burman, P.A. Cundall, O.D.L. Strack, A discrete numerical model for granular assemblies, Geotechnique. 30 (1980) 331–336. https://doi.org/10.1680/geot.1980.30.3.331.

[41] A. Hrennikoff, Solution of Problems of Elasticity by the Framework Method, J. Appl. Mech. 8 (1941) A169–A175. https://doi.org/10.1115/1.4009129.

[42] D. V. Griffiths, G.G.W. Mustoe, Modelling of elastic continua using a grillage of structuralelements based on discete element concepts, Int. J. Numer. Methods Eng. 50 (2001) 1759–1775. https://doi.org/10.1002/nme.99.

[43] Y. Wang, P. Mora, Macroscopic elastic properties of regular lattices, J. Mech. Phys. Solids. 56 (2008) 3459–3474. https://doi.org/10.1016/j.jmps.2008.08.011.

[44] Y. Jiang, J. Zhang, Y. He, H. Liu, W. Zhao, Nonlinear propagation of stress waves during high speed cutting, Appl. Phys. Lett. 109 (2016) 191904. https://doi.org/10.1063/1.4967514.

[45] Z. Liu, J. Zhang, Y. He, W. Zhao, A Godunov-type discrete element model for elastic-viscoplastic continuum impact problems, Int. J. Numer. Methods Eng. 122 (2021) 6384–6404. https://doi.org/10.1002/nme.6796.

[46] H. Chen, Y. Jiao, Y. Liu, Investigating the microstructural effect on elastic and fracture behavior of polycrystals using a nonlocal lattice particle model, Mater. Sci. Eng. A. 631 (2015) 173–180. https://doi.org/10.1016/j.msea.2015.02.046.

[47] Y. He, J. Zhang, T. Andriollo, J. Hattel, W. Zhao, Investigation of the elastoplastic and fracture behavior of solid materials considering microstructural anisotropy: A discrete element modeling study, Comput. Mater. Sci. 170 (2019) 109164. https://doi.org/10.1016/j.commatsci.2019.109164.

[48] Y. Horie, S. Case, Mesodynamics of shock waves in a polycrystalline metal, Shock Waves. 17 (2007) 135–141. https://doi.org/10.1007/s00193-007-0090-1.

[49] Z. Wang, Y. Cai, X. Luo, Modelling and simulation of cutting process by smoothed particle hydrodynamics (SPH): A review, in: ICAC 2019 - 2019 25th IEEE Int. Conf. Autom. Comput., IEEE, 2019: pp. 1–6. https://doi.org/10.23919/IConAC.2019.8895239.

[50] M. Madaj, M. Píška, On the SPH orthogonal cutting simulation of A2024-T351 alloy, Procedia CIRP. 8 (2013) 152–157. https://doi.org/10.1016/j.procir.2013.06.081.

[51] U. Heisel, W. Zaloga, D. Krivoruchko, M. Storchak, L. Goloborodko, Modelling of orthogonal cutting processes with the method of smoothed particle hydrodynamics, Prod. Eng. 7 (2013) 639–645. https://doi.org/10.1007/s11740-013-0484-0.

[52] S. Abolfazl Zahedi, M. Demiral, A. Roy, V. V. Silberschmidt, FE/SPH modelling of orthogonal micro-machining of f.c.c. single crystal, Comput. Mater. Sci. 78 (2013) 104–109. https://doi.org/10.1016/j.commatsci.2013.05.022.

[53] B. Takabi, M. Tajdari, B.L. Tai, Numerical study of smoothed particle hydrodynamics method in orthogonal cutting simulations – Effects of damage criteria and particle density, J. Manuf. Process. 30 (2017) 523–531. https://doi.org/10.1016/j.jmapro.2017.10.020.

[54] Q.X. Pei, C. Lu, F.Z. Fang, H. Wu, Nanometric cutting of copper: A molecular dynamics study, Comput. Mater. Sci. 37 (2006) 434–441. https://doi.org/10.1016/j.commatsci.2005.10.006.

[55] A. Sharma, D. Datta, R. Balasubramaniam, Molecular dynamics simulation to investigate the orientation effects on nanoscale cutting of single crystal copper, Comput. Mater. Sci. 153 (2018) 241–250. https://doi.org/10.1016/j.commatsci.2018.07.002.

[56] Z. Pan, Y. Feng, S.Y. Liang, Material microstructure affected machining: A review, Manuf. Rev. 4 (2017) 5. https://doi.org/10.1051/mfreview/2017004.

[57] S.N. Melkote, W. Grzesik, J. Outeiro, J. Rech, V. Schulze, H. Attia, P.J. Arrazola, R. M'Saoubi, C. Saldana, Advances in material and friction data for modelling of metal machining, CIRP Ann. - Manuf. Technol. 66 (2017) 731–754. https://doi.org/10.1016/j.cirp.2017.05.002.

[58] K. Huang, R.E. Logé, A review of dynamic recrystallization phenomena in metallic materials, Mater. Des. 111 (2016) 548–574. https://doi.org/10.1016/j.matdes.2016.09.012.

[59] M. Fanfoni, M. Tomellini, The Johnson-Mehl-Avrami-Kolmogorov model: A brief review, Nuovo Cim. Della Soc. Ital. Di Fis. D - Condens. Matter, At. Mol. Chem. Physics, Biophys. 20 (1998) 1171–1182. https://doi.org/10.1007/BF03185527.

[60] C. Zener, J.H. Hollomon, Effect of strain rate upon plastic flow of steel, J. Appl. Phys. 15 (1944) 22–32. https://doi.org/10.1063/1.1707363.

[61] S. Caruso, S. Di Renzo, D. Umbrello, A.D. Jayal, O.W. Dillon, I.S. Jawahir, Finite element modeling of microstructural changes in hard turning, Adv. Mater. Res. 223 (2011) 960–968. https://doi.org/10.4028/www.scientific.net/AMR.223.960.

[62] S. Caruso, S. Imbrogno, S. Rinaldi, D. Umbrello, Finite element modeling of microstructural changes in Waspaloy dry machining, Int. J. Adv. Manuf. Technol. 89 (2017) 227–240. https://doi.org/10.1007/s00170-016-9037-y.

[63] Q. Wang, Z. Liu, B. Wang, Q. Song, Y. Wan, Evolutions of grain size and micro-hardness during chip formation and machined surface generation for Ti-6Al-4V in high-speed machining, Int. J. Adv. Manuf. Technol. 82 (2016) 1725–1736. https://doi.org/10.1007/s00170-015-7508-1.

[64] G. Rotella, D. Umbrello, Finite element modeling of microstructural changes in dry and cryogenic cutting of Ti6Al4V alloy, CIRP Ann. - Manuf. Technol. 63 (2014) 69–72. https://doi.org/10.1016/j.cirp.2014.03.074.

[65] Y. Guo, C. Saldana, W. Dale Compton, S. Chandrasekar, Controlling deformation and microstructure on machined surfaces, Acta Mater. 59 (2011) 4538–4547. https://doi.org/10.1016/j.actamat.2011.03.076.

[66] Y. Estrin, H.S. Kim, Modelling microstructure evolution toward ultrafine crystallinity produced by severe plastic deformation, J. Mater. Sci. 42 (2007) 1512–1516. https://doi.org/10.1007/s10853-006-1282-2.

[67] H. Ding, N. Shen, Y.C. Shin, Modeling of grain refinement in aluminum and copper subjected to cutting, Comput. Mater. Sci. 50 (2011) 3016–3025. https://doi.org/10.1016/j.commatsci.2011.05.020.

[68] R. Liu, M. Salahshoor, S.N. Melkote, T. Marusich, A unified material model including dislocation drag and its application to simulation of orthogonal cutting of OFHC Copper, J. Mater. Process. Technol. 216 (2015) 328–338. https://doi.org/10.1016/j.jmatprotec.2014.09.021.

[69] E.O. Hall, The deformation and ageing of mild steel: II Characteristics of the Lüders deformation, Proc.

Phys. Soc. Sect. B. 64 (1951) 742–747. https://doi.org/10.1088/0370-1301/64/9/302.

[70] N.J. Petch, The cleavage strength of polycrystals, Journal of Iron and Steel Institute, J. Iron Steel Inst. 174 (1953) 25–28.

[71] Q. Wang, Z. Liu, Plastic deformation induced nano-scale twins in Ti-6Al-4V machined surface with high speed machining, Mater. Sci. Eng. A. 675 (2016) 271–279. https://doi.org/10.1016/j.msea.2016.08.076.

[72] Y.M. Arisoy, T. Özel, Prediction of machining induced microstructure in Ti-6Al-4V alloy using 3-D FE-based simulations: Effects of tool micro-geometry, coating and cutting conditions, J. Mater. Process. Technol. 220 (2015) 1–26. https://doi.org/10.1016/j.jmatprotec.2014.11.002.

[73] Y. Guo, C. Saldana, W. Dale Compton, S. Chandrasekar, Controlling deformation and microstructure on machined surfaces, Acta Mater. 59 (2011) 4538–4547. https://doi.org/10.1016/j.actamat.2011.03.076.

[74] J. Zhang, C.C. Tasan, M.J. Lai, A.C. Dippel, D. Raabe, Complexion-mediated martensitic phase transformation in Titanium, Nat. Commun. 8 (2017) 14210. https://doi.org/10.1038/ncomms14210.

[75] S. Han, S.N. Melkote, M.S. Haluska, T.R. Watkins, White layer formation due to phase transformation in orthogonal machining of AISI 1045 annealed steel, Mater. Sci. Eng. A. 488 (2008) 195–204. https://doi.org/10.1016/j.msea.2007.11.081.

[76] A. Ramesh, S.N. Melkote, Modeling of white layer formation under thermally dominant conditions in orthogonal machining of hardened AISI 52100 steel, Int. J. Mach. Tools Manuf. 48 (2008) 402–414. https://doi.org/10.1016/j.ijmachtools.2007.09.007.

[77] R. Mahnken, M. Wolff, C. Cheng, A multi-mechanism model for cutting simulations combining visco-plastic asymmetry and phase transformation, Int. J. Solids Struct. 50 (2013) 3045–3066. https://doi.org/10.1016/j.ijsolstr.2013.05.008.

[78] C. Duan, W. Kong, Q. Hao, F. Zhou, Modeling of white layer thickness in high speed machining of hardened steel based on phase transformation mechanism, Int. J. Adv. Manuf. Technol. 69 (2013) 59–70. https://doi.org/10.1007/s00170-013-5005-y.

[79] Z. Pan, S.Y. Liang, H. Garmestani, D.S. Shih, Prediction of machining-induced phase transformation and grain growth of Ti-6Al-4 V alloy, Int. J. Adv. Manuf. Technol. 87 (2016) 859–866. https://doi.org/10.1007/s00170-016-8497-4.

[80] Q. Wang, Z. Liu, D. Yang, A.U.H. Mohsan, Metallurgical-based prediction of stress-temperature induced rapid heating and cooling phase transformations for high speed machining Ti-6Al-4V alloy, Mater. Des. 119 (2017) 208–218. https://doi.org/10.1016/j.matdes.2017.01.076.

[81] X.P. Zhang, R. Shivpuri, A.K. Srivastava, Role of phase transformation in chip segmentation during high speed machining of dual phase titanium alloys, J. Mater. Process. Technol. 214 (2014) 3048–3066. https://doi.org/10.1016/j.jmatprotec.2014.07.007.

[82] V. Schulze, E. Uhlmann, R. Mahnken, A. Menzel, D. Biermann, A. Zabel, P. Bollig, I.M. Ivanov, C. Cheng, R. Holtermann, T. Bartel, Evaluation of different approaches for modeling phase transformations in machining simulation, Prod. Eng. 9 (2015) 437–449. https://doi.org/10.1007/s11740-015-0618-7.

[83] R. Zaera, J.A. Rodr ́guez-Mart ́nez, A. Casado, J. Fern ́ndez-S ́ez, A. Rusinek, R. Pesci, A constitutive model for analyzing martensite formation in austenitic steels deforming at high strain rates, Int. J. Plast. 29 (2012) 77–101. https://doi.org/10.1016/j.ijplas.2011.08.003.

[84] W.S. Choi, E.L. Pang, W.S. Ko, H. Jun, H.J. Bong, C. Kirchlechner, D. Raabe, P.P. Choi, Orientation-dependent plastic deformation mechanisms and competition with stress-induced phase transformation in microscale NiTi, Acta Mater. 208 (2021) 116731. https://doi.org/10.1016/j.actamat.2021.116731.

[85] W. Zhang, X. Wang, Y. Hu, S. Wang, Predictive modelling of microstructure changes, micro-hardness and residual stress in machining of 304 austenitic stainless steel, Int. J. Mach. Tools Manuf. 130–131 (2018) 36–48. https://doi.org/10.1016/j.ijmachtools.2018.03.008.

[86] G.B. Olson, M. Cohen, Kinetics of strain-induced martensitic nucleation, Metall. Trans. A. 6 (1975) 791–795. https://doi.org/10.1007/BF02672301.

[87] Y. Kaynak, S. Manchiraju, I.S. Jawahir, D. Biermann, Chip formation and phase transformation in orthogonal machining of NiTi shape memory alloy: microstructure-based modelling and experimental validation, CIRP Ann. 69 (2020) 85–88. https://doi.org/10.1016/j.cirp.2020.04.025.

[88] N. Shen, H. Ding, Z. Pu, I.S. Jawahir, T. Jia, Enhanced Surface Integrity from Cryogenic Machining of AZ31B Mg Alloy: A Physics-Based Analysis with Microstructure Prediction, J. Manuf. Sci. Eng. Trans. ASME. 139 (2017) 1–13. https://doi.org/10.1115/1.4034279.

[89] N. Shen, H. Ding, J. Gao, Cryogenic cutting of AZ31B-O Mg alloy for improved surface integrity-part II: Physics-based process modeling of surface microstructural alteration, ASME 2015 Int. Manuf. Sci.

Eng. Conf. MSEC 2015. 1 (2015) 1–9. https://doi.org/10.1115/MSEC20159324.

[90] Q. Wang, Z. Liu, Microhardness Prediction Based on a Microstructure-Sensitive Flow Stress Model During High Speed Machining Ti-6Al-4V, J. Manuf. Sci. Eng. Trans. ASME. 140 (2018) 091003. https://doi.org/10.1115/1.4039889.

[91] S. Rinaldi, D. Umbrello, S.N. Melkote, Modelling the effects of twinning and dislocation induced strengthening in orthogonal micro and macro cutting of commercially pure titanium, Int. J. Mech. Sci. 190 (2021) 106045. https://doi.org/10.1016/j.ijmecsci.2020.106045.

[92] R.L. Goetz, V. Seetharaman, Modeling dynamic recrystallization using cellular automata, 1998. https://doi.org/10.1016/S1359-6462(97)00500-9.

[93] R. Ding, Z.X. Guo, Coupled quantitative simulation of microstructural evolution and plastic flow during dynamic recrystallization, Acta Mater. 49 (2001) 3163–3175. https://doi.org/10.1016/S1359-6454(01)00233-6.

[94] N. Shen, A. Samanta, H. Ding, Microstructure Simulations for Orthogonal Cutting via a Cellular Automaton Model, Procedia CIRP. 58 (2017) 543–548. https://doi.org/10.1016/j.procir.2017.03.264.

[95] C.Z. Duan, L.C. Zhang, Adiabatic shear banding in AISI 1045 steel during high speed machining: Mechanisms of microstructural evolution, Mater. Sci. Eng. A. 532 (2012) 111–119. https://doi.org/10.1016/j.msea.2011.10.071.

[96] R. M'Saoubi, D. Axinte, S.L. Soo, C. Nobel, H. Attia, G. Kappmeyer, S. Engin, W.M. Sim, High performance cutting of advanced aerospace alloys and composite materials, CIRP Ann. - Manuf. Technol. 64 (2015) 557–580. https://doi.org/10.1016/j.cirp.2015.05.002.

[97] A. Thakur, S. Gangopadhyay, State-of-the-art in surface integrity in machining of nickel-based super alloys, Int. J. Mach. Tools Manuf. 100 (2016) 25–54. https://doi.org/10.1016/j.ijmachtools.2015.10.001.

[98] T. Mabrouki, C. Courbon, Y. Zhang, J. Rech, D. Nélias, M. Asad, H. Hamdi, S. Belhadi, F. Salvatore, Some insights on the modelling of chip formation and its morphology during metal cutting operations, Comptes Rendus - Mec. 344 (2016) 335–354. https://doi.org/10.1016/j.crme.2016.02.003.

[99] H. Liu, J. Zhang, X. Xu, Y. Jiang, Y. He, W. Zhao, Effect of microstructure evolution on chip formation and fracture during high-speed cutting of single phase metals, Int. J. Adv. Manuf. Technol. 91 (2017) 823–833. https://doi.org/10.1007/s00170-016-9823-6.

[100] R. Bejjani, M. Balazinski, H. Attia, P. Plamondon, G. L'Espérance, Chip formation and microstructure evolution in the adiabatic shear band when machining titanium metal matrix composites, Int. J. Mach. Tools Manuf. 109 (2016) 137–146. https://doi.org/10.1016/j.ijmachtools.2016.08.001.

[101] S. Shekhar, S. Abolghasem, S. Basu, J. Cai, M.R. Shankar, Effect of severe plastic deformation in machining elucidated via rate-strain-microstructure mappings, J. Manuf. Sci. Eng. Trans. ASME. 134 (2012) 031008. https://doi.org/10.1115/1.4006549.

[102] Z.P. Wan, Y.E. Zhu, H.W. Liu, Y. Tang, Microstructure evolution of adiabatic shear bands and mechanisms of saw-tooth chip formation in machining Ti6Al4V, Mater. Sci. Eng. A. 531 (2012) 155–163. https://doi.org/10.1016/j.msea.2011.10.050.

[103] H. Liu, J. Zhang, X. Xu, W. Zhao, Experimental study on fracture mechanism transformation in chip segmentation of Ti-6Al-4V alloys during high-speed machining, J. Mater. Process. Technol. 257 (2018) 132–140. https://doi.org/10.1016/j.jmatprotec.2018.02.040.

[104] C. Herbert, D. Axinte, M. Hardy, P.D. Brown, Investigation into the characteristics of white layers produced in a nickel-based superalloy from drilling operations, Mach. Sci. Technol. 16 (2012) 40–52. https://doi.org/10.1080/10910344.2012.648520.

[105] J. Du, Z. Liu, S. Lv, Deformation-phase transformation coupling mechanism of white layer formation in high speed machining of FGH95 Ni-based superalloy, Appl. Surf. Sci. 292 (2014) 197–203. https://doi.org/10.1016/j.apsusc.2013.11.111.

[106] J.D.P. Velásquez, A. Tidu, B. Bolle, P. Chevrier, J.J. Fundenberger, Sub-surface and surface analysis of high speed machined Ti-6Al-4V alloy, Mater. Sci. Eng. A. 527 (2010) 2572–2578. https://doi.org/10.1016/j.msea.2009.12.018.

[107] A. Ramesh, S.N. Melkote, L.F. Allard, L. Riester, T.R. Watkins, Analysis of white layers formed in hard turning of AISI 52100 steel, Mater. Sci. Eng. A. 390 (2005) 88–97. https://doi.org/10.1016/j.msea.2004.08.052.

[108] J. Barry, G. Byrne, Chip formation, acoustic emission and surface white layers in hard machining, 2002. https://doi.org/10.1016/S0007-8506(07)61467-X.

[109] J.M. Zhou, V. Bushlya, R.L. Peng, S. Johansson, P. Avdovic, J.E. Stahl, Effects of tool wear on subsurface deformation of nickelbased superalloy, Procedia Eng. 19 (2011) 407–413.

https://doi.org/10.1016/j.proeng.2011.11.133.

[110] R. M'Saoubi, T. Larsson, J. Outeiro, Y. Guo, S. Suslov, C. Saldana, S. Chandrasekar, Surface integrity analysis of machined Inconel 718 over multiple length scales, CIRP Ann. - Manuf. Technol. 61 (2012) 99–102. https://doi.org/10.1016/j.cirp.2012.03.058.

[111] I. Ghamarian, Y. Liu, P. Samimi, P.C. Collins, Development and application of a novel precession electron diffraction technique to quantify and map deformation structures in highly deformed materials - As applied to ultrafine-grained titanium, Acta Mater. 79 (2014) 203–215. https://doi.org/10.1016/j.actamat.2014.06.063.

[112] P.A. Midgley, A.S. Eggeman, Precession electron diffraction - A topical review, IUCrJ. 2 (2015) 126–136. https://doi.org/10.1107/S2052252514022283.

[113] G.R. Johnson, W.H. Cook, A constitutive model and data from metals subjected to large strains, high strain rates and high temperatures, Proc. 7th Int. Symp. Ballist. Hague, Netherlands. (1983) 541–547.

[114] G.R. Johnson, W.H. Cook, A Constitutive modeling and data for metals subjected to large strain rates and high temperatures, Proc. 7th Int. Symp. Ballist. (1983) 541–547.

[115] F. Ducobu, P.J. Arrazola, E. Rivière-Lorphèvre, E. Filippi, On the selection of an empirical material constitutive model for the finite element modeling of Ti6Al4V orthogonal cutting, including the segmented chip formation, Int. J. Mater. Form. 14 (2021) 361–374. https://doi.org/10.1007/s12289-020-01535-2.

[116] B. Wang, Z. Liu, Shear localization sensitivity analysis for Johnson-Cook constitutive parameters on serrated chips in high speed machining of Ti6Al4V, Simul. Model. Pract. Theory. 55 (2015) 63–76. https://doi.org/10.1016/j.simpat.2015.03.011.

[117] M. Calamaz, D. Coupard, F. Girot, A new material model for 2D numerical simulation of serrated chip formation when machining titanium alloy Ti-6Al-4V, Int. J. Mach. Tools Manuf. 48 (2008) 275–288. https://doi.org/10.1016/j.ijmachtools.2007.10.014.

[118] M. Sima, T. Özel, Modified material constitutive models for serrated chip formation simulations and experimental validation in machining of titanium alloy Ti-6Al-4V, Int. J. Mach. Tools Manuf. 50 (2010) 943–960. https://doi.org/10.1016/j.ijmachtools.2010.08.004.

[119] D. Umbrello, S. Rizzuti, J.C. Outeiro, R. Shivpuri, Modeling of the flow stress for AISI H13 tool steel

during hard machining processes, in: AIP Conf. Proc., 2007.

[120] G. Rotella, D. Umbrello, Finite element modeling of microstructural changes in dry and cryogenic cutting of Ti6Al4V alloy, CIRP Ann. - Manuf. Technol. 63 (2014) 69–72. https://doi.org/10.1016/j.cirp.2014.03.074.

[121] L.A. Denguir, J.C. Outeiro, G. Fromentin, V. Vignal, R. Besnard, Orthogonal Cutting Simulation of OFHC Copper Using a New Constitutive Model Considering the State of Stress and the Microstructure Effects, in: Procedia CIRP, Elsevier B.V., 2016: pp. 238–241. https://doi.org/10.1016/j.procir.2016.03.208.

[122] W. Cheng, J. Outeiro, J.P. Costes, R. M'Saoubi, H. Karaouni, V. Astakhov, A constitutive model for Ti6Al4V considering the state of stress and strain rate effects, Mech. Mater. 137 (2019) 103103. https://doi.org/10.1016/j.mechmat.2019.103103.

[123] I. Time, Mémoire sur le Rabotage de Métaux, Expédition pour la confection des papiers de l'Etat, Petersbourg, Russia, 1877.

[124] J.T. Nicolson, Experiments with a Lathe-Tool Dynamometer, Proc. Inst. Mech. Eng. 67 (1904) 883–935. https://doi.org/10.1243/pime_proc_1904_067_018_02.

[125] F.W. Taylor, The Art of Cutting Metals, Sci. Am. 63 (1907) 25942–25944. https://doi.org/10.1038/scientificamerican01121907-25942supp.

[126] M. Okoshi, S. Fucui, Researches on the cutting action of planning tool by micokinematographic, photoelastic and piezoelectric methods, Sci. Pap. Inst. Phys. Chem. Res. 22 (1933) 97–166.

[127] X. Zhang, R. Shivpuri, A.K. Srivastava, Chip fracture behavior in the high speed machining of titanium alloys, J. Manuf. Sci. Eng. Trans. ASME. 138 (2016) 1–14. https://doi.org/10.1115/1.4032583.

[128] B. Wang, Z. Liu, Evaluation on fracture locus of serrated chip generation with stress triaxiality in high speed machining of Ti6Al4V, Mater. Des. 98 (2016) 68–78. https://doi.org/10.1016/j.matdes.2016.03.012.

[129] T.H.C. Childs, P.J. Arrazola, P. Aristimuno, A. Garay, I. Sacristan, Ti6Al4V metal cutting chip formation experiments and modelling over a wide range of cutting speeds, J. Mater. Process. Technol. 255 (2018) 898–913. https://doi.org/10.1016/j.jmatprotec.2018.01.026.

[130] Y. Bai, T. Wierzbicki, Application of extended Mohr-Coulomb criterion to ductile fracture, Int. J. Fract. 161 (2010) 1–20. https://doi.org/10.1007/s10704-009-9422-8.

[131] B. Wang, X. Xiao, V.P. Astakhov, Z. Liu, The effects of stress triaxiality and strain rate on the fracture strain of Ti6Al4V, Eng. Fract. Mech. 219 (2019) 106627. https://doi.org/10.1016/j.engfracmech.2019.106627.

[132] F.J. Zerilli, R.W. Armstrong, Dislocation-mechanics-based constitutive relations for material dynamics calculations, J. Appl. Phys. 61 (1987) 1816–1825. https://doi.org/10.1063/1.338024.

[133] F.J. Zerilli, Dislocation mechanics-based constitutive equations, Metall. Mater. Trans. A Phys. Metall. Mater. Sci. 35 A (2004) 2547–2555. https://doi.org/10.1007/s11661-004-0201-x.

[134] H. Mecking, U.F. Kocks, Kinetics of flow and strain-hardening, 1981. https://doi.org/10.1016/0001-6160(81)90112-7.

[135] Y. Estrin, H.S. Kim, Modelling microstructure evolution toward ultrafine crystallinity produced by severe plastic deformation (Journal of Materials Science (2007) 42 (9092-9096) DOI:10.1007/s10853-006-1260-8), J. Mater. Sci. 43 (2008) 1174. https://doi.org/10.1007/s10853-007-2269-3.

[136] S. Imbrogno, S. Rinaldi, D. Umbrello, L. Filice, R. Franchi, A. Del Prete, A physically based constitutive model for predicting the surface integrity in machining of Waspaloy, Mater. Des. 152 (2018) 140–155. https://doi.org/10.1016/j.matdes.2018.04.069.

[137] P.S. Follansbee, U.F. Kocks, A constitutive description of the deformation of copper based on the use of the mechanical threshold stress as an internal state variable, Acta Metall. 36 (1988) 81–93. https://doi.org/10.1016/0001-6160(88)90030-2.

[138] M. Field, J.F. Kahles, J.T. Cammett, Review of Measuring Methods for Surface Integrity., 1972. https://www.shotpeener.com/library/pdf/1972000.pdf%0Ahttp://scholar.google.com/scholar?hl=en&btnG=Search&q=intitle:Review+of+measuring+methods+for+surface+integrity#0.

[139] Z. Liao, A. la Monaca, J. Murray, A. Speidel, D. Ushmaev, A. Clare, D. Axinte, R. M'Saoubi, Surface integrity in metal machining - Part I: Fundamentals of surface characteristics and formation mechanisms, Int. J. Mach. Tools Manuf. 162 (2021) 103687. https://doi.org/10.1016/j.ijmachtools.2020.103687.

[140] W. Grzesik, W. Grzeski, W. Grzesik, A revised model for predicting surface roughness in turning, 1996. https://doi.org/10.1016/0043-1648(95)06825-2.

[141] I. Korkut, M.A. Donertas, The influence of feed rate and cutting speed on the cutting forces, surface roughness and tool-chip contact length during face milling, Mater. Des. 28 (2007) 308–312. https://doi.org/10.1016/j.matdes.2005.06.002.

[142] G.C. Nie, K. Zhang, J. Outeiro, S. Caruso, D. Umbrello, H. Ding, X.M. Zhang, Plastic strain threshold determination for white layer formation in hard turning of AISI 52100 steel using micro-grid technique and finite element simulations, J. Manuf. Sci. Eng. Trans. ASME. 142 (2020) 1–7. https://doi.org/10.1115/1.4045798.

[143] T. Obikawa, Y. Takemura, Y. Akiyama, J. Shinozuka, H. Sasahara, Microscopic phase-dependent residual stresses in the machined surface layer of two-phase alloy, J. Mater. Process. Technol. 209 (2009) 4496–4501. https://doi.org/10.1016/j.jmatprotec.2008.10.039.

[144] Z. Pu, J.C. Outeiro, A.C. Batista, O.W. Dillon, D.A. Puleo, I.S. Jawahir, Enhanced surface integrity of AZ31B Mg alloy by cryogenic machining towards improved functional performance of machined components, Int. J. Mach. Tools Manuf. 56 (2012) 17–27. https://doi.org/10.1016/j.ijmachtools.2011.12.006.

[145] L.A. Denguir, J.C. Outeiro, G. Fromentin, Multi-physical analysis of the electrochemical behaviour of OFHC copper surfaces obtained by orthogonal cutting, Corros. Eng. Sci. Technol. 56 (2021) 189–198. https://doi.org/10.1080/1478422X.2020.1836879.

[146] D. Yang, Z. Liu, Surface plastic deformation and surface topography prediction in peripheral milling with variable pitch end mill, Int. J. Mach. Tools Manuf. 91 (2015) 43–53. https://doi.org/10.1016/j.ijmachtools.2014.11.009.

[147] G. Liu, C. Huang, H. Zhu, Z. Liu, Y. Liu, C. Li, The modified surface properties and fatigue life of Incoloy A286 face-milled at different cutting parameters, Mater. Sci. Eng. A. 704 (2017) 1–9. https://doi.org/10.1016/j.msea.2017.07.072.

[148] E. Brinksmeier, D. Meyer, C. Heinzel, T. Lübben, J. Sölter, L. Langenhorst, F. Frerichs, J. Kämmler, E. Kohls, S. Kuschel, Process Signatures-The Missing Link to Predict Surface Integrity in Machining, Procedia CIRP. 71 (2018) 3–10. https://doi.org/10.1016/j.procir.2018.05.006.

[149] T. Dos Santos, J.C. Outeiro, R. Rossi, P. Rosa, A New Methodology for Evaluation of Mechanical Properties of Materials at Very High Rates of Loading, Procedia CIRP. 58 (2017) 481–486.

https://doi.org/10.1016/j.procir.2017.03.258.

[150] D. Yameogo, B. Haddag, H. Makich, M. Nouari, A physical behavior model including dynamic recrystallization and damage mechanisms for cutting process simulation of the titanium alloy Ti-6Al-4V, Int. J. Adv. Manuf. Technol. 100 (2019) 333–347. https://doi.org/10.1007/s00170-018-2663-9.

[151] G.R. Johnson, W.H. Cook, Fracture characteristics of three metals subjected to various strains, strain rates, temperatures and pressures, Eng. Fract. Mech. 21 (1985) 31–48. https://doi.org/10.1016/0013-7944(85)90052-9.

[152] Y.M. Abushawashi, Modeling of metal cutting as purposeful fracture of work material, ProQuest Diss. Theses; Thesis. (2013) 264. https://dl.dropboxusercontent.com/u/12349645/SIM/DISSERTATION_YALLA.pdf%0Ahttps://ui.adsabs.harvard.edu/abs/2013PhDT.....367A/exportcitation.

[153] T.J. Holmquist, G.R. Johnson, A computational constitutive model for glass subjected to large strains, high strain rates and high pressures, J. Appl. Mech. Trans. ASME. 78 (2011) 541–547. https://doi.org/10.1115/1.4004326.

[154] D.S.C. Simulia, Abaqus Analysis User's Manual, 2016.

[155] L.C. da Silva, P.R. da Mota, M.B. da Silva, E.O. Ezugwu, Á.R. Machado, Study of burr behavior in face milling of PH 13-8 Mo stainless steel, CIRP J. Manuf. Sci. Technol. 8 (2015) 34–42. https://doi.org/10.1016/j.cirpj.2014.10.003.

[156] T. Régnier, G. Fromentin, B. Marcon, J. Outeiro, A. D'Acunto, A. Crolet, T. Grunder, Fundamental study of exit burr formation mechanisms during orthogonal cutting of AlSi aluminium alloy, J. Mater. Process. Technol. 257 (2018) 112–122. https://doi.org/10.1016/j.jmatprotec.2018.02.037.

[157] R. Liu, E. Eaton, M. Yu, J. Kuang, An Investigation of Side Flow during Chip Formation in Orthogonal Cutting, Procedia Manuf. 10 (2017) 568–577. https://doi.org/10.1016/j.promfg.2017.07.053.

[158] V. Pednekar, V. Madhavan, A.H. Adibi-Sedeh, Investigation of the transition from plane strain to plane stress in orthogonal metal cutting, Am. Soc. Mech. Eng. Appl. Mech. Div. AMD. 255 (2004) 513–528. https://doi.org/10.1115/IMECE2004-62167.

[159] X. Xu, J. Zhang, J. Outeiro, B. Xu, W. Zhao, Multiscale simulation of grain refinement induced by dynamic recrystallization of Ti6Al4V alloy during high speed machining, J. Mater. Process. Technol.

286 (2020) 116834. https://doi.org/10.1016/j.jmatprotec.2020.116834.

[160] M. Calamaz, D. Coupard, F. Girot, A new material model for 2D numerical simulation of serrated chip formation when machining titanium alloy Ti-6Al-4V, Int. J. Mach. Tools Manuf. 48 (2008) 275–288. https://doi.org/10.1016/j.ijmachtools.2007.10.014.

[161] T. Özel, M. Sima, A.K. Srivastava, B. Kaftanoglu, Investigations on the effects of multi-layered coated inserts in machining Ti-6Al-4V alloy with experiments and finite element simulations, CIRP Ann. - Manuf. Technol. 59 (2010) 77–82. https://doi.org/10.1016/j.cirp.2010.03.055.

[162] G. Chen, C. Ren, X. Yang, X. Jin, T. Guo, Finite element simulation of high-speed machining of titanium alloy (Ti-6Al-4V) based on ductile failure model, Int. J. Adv. Manuf. Technol. 56 (2011) 1027–1038. https://doi.org/10.1007/s00170-011-3233-6.

[163] Y. Zhang, T. Mabrouki, D. Nelias, Y. Gong, FE-model for Titanium alloy (Ti-6Al-4V) cutting based on the identification of limiting shear stress at tool-chip interface, Int. J. Mater. Form. 4 (2011) 11–23. https://doi.org/10.1007/s12289-010-0986-7.

[164] N.N. Zorev, Interrelationship between shear processes occurring along tool face and on shear plane in metal cutting., Roceedings Int. Res. Prod. Eng. Conf. (1963) 42–49.

[165] C. Courbon, F. Pusavec, F. Dumont, J. Rech, J. Kopac, Influence of cryogenic lubrication on the tribological properties of Ti6Al4V and Inconel 718 alloys under extreme contact conditions, in: Lubr. Sci., John Wiley and Sons Ltd, 2014: pp. 315–326. https://doi.org/10.1002/ls.1254.

[166] V.P. Astakhov, Metal Cutting Mechanics, CRC press, 1998. https://doi.org/10.1201/9781466571778.

[167] B. Wang, Z. Liu, Investigations on the chip formation mechanism and shear localization sensitivity of high-speed machining Ti6Al4V, Int. J. Adv. Manuf. Technol. 75 (2014) 1065–1076. https://doi.org/10.1007/s00170-014-6191-y.

[168] M.F. Poletica, Contact Loads on Cutting Tool Interface Surfaces, Mashinostroenie, Moscow, 1969.

[169] V.P. Astakhov, J. Outeiro, Importance of Temperature in Metal Cutting and Its Proper Measurement/Modeling, in: J.P. Davim (Ed.), Meas. Mach. Tribol., Springer International Publishing, 2019: pp. 1–47. https://doi.org/10.1007/978-3-030-03822-9_1.

[170] V.P. Astakhov, S. Shvets, The assessment of plastic deformation in metal cutting, J. Mater. Process.

Technol. 146 (2004) 193–202. https://doi.org/10.1016/j.jmatprotec.2003.10.015.

[171] B. Pan, K. Qian, H. Xie, A. Asundi, Two-dimensional digital image correlation for in-plane displacement and strain measurement: A review, Meas. Sci. Technol. 20 (2009). https://doi.org/10.1088/0957-0233/20/6/062001.

[172] J.C. Outeiro, S. Campocasso, L.A. Denguir, G. Fromentin, V. Vignal, G. Poulachon, Experimental and numerical assessment of subsurface plastic deformation induced by OFHC copper machining, CIRP Ann. - Manuf. Technol. 64 (2015) 53–56. https://doi.org/10.1016/j.cirp.2015.04.080.

[173] D. Zhang, X.M. Zhang, H. Ding, Hybrid digital image correlation-finite element modeling approach for modeling of orthogonal cutting process, J. Manuf. Sci. Eng. Trans. ASME. 140 (2018). https://doi.org/10.1115/1.4038998.

[174] D. Zhang, X.M. Zhang, W.J. Xu, H. Ding, Stress Field Analysis in Orthogonal Cutting Process Using Digital Image Correlation Technique, J. Manuf. Sci. Eng. Trans. ASME. 139 (2017). https://doi.org/10.1115/1.4033928.

[175] X. Pang, Y. Zeng, J. Zhang, W. Deng, Analytical model and experimental verification of Poisson burr formation in ductile metal machining, J. Mater. Process. Technol. 290 (2021) 116966. https://doi.org/10.1016/j.jmatprotec.2020.116966.

[176] P.D. Littlewood, T.B. Britton, A.J. Wilkinson, Geometrically necessary dislocation density distributions in Ti-6Al-4V deformed in tension, Acta Mater. 59 (2011) 6489–6500. https://doi.org/10.1016/j.actamat.2011.07.016.

[177] G. Kugler, R. Turk, Modeling the dynamic recrystallization under multi-stage hot deformation, Acta Mater. 52 (2004) 4659–4668. https://doi.org/10.1016/j.actamat.2004.06.022.

[178] R. Ding, Z.X. Guo, Coupled quantitative simulation of microstructural evolution and plastic flow during dynamic recrystallization, 2001. https://doi.org/10.1016/S1359-6454(01)00233-6.

[179] W. Roberts, B. Ahlblom, A nucleation criterion for dynamic recrystallization during hot working, Acta Metall. 26 (1978) 801–813. https://doi.org/10.1016/0001-6160(78)90030-5.

[180] R. Ding, Z.X. Guo, Microstructural modelling of dynamic recrystallisation using an extended cellular automaton approach, 2002. https://doi.org/10.1016/S0927-0256(01)00211-7.

[181] M. Qian, Z.X. Guo, Cellular automata simulation of microstructural evolution during dynamic recrystallization of an HY-100 steel, Mater. Sci. Eng. A. 365 (2004) 180–185. https://doi.org/10.1016/j.msea.2003.09.025.

[182] H.P. Stüwe, B.B. Ortner, Recrystallization in Hot Working and Creep, Met. Sci. 8 (1974) 161–167. https://doi.org/10.1179/msc.1974.8.1.161.

[183] R. Ding, Z.X. Guo, Microstructural evolution of a Ti-6Al-4V alloy during β-phase processing: Experimental and simulative investigations, Mater. Sci. Eng. A. 365 (2004) 172–179. https://doi.org/10.1016/j.msea.2003.09.024.

[184] K.J. Song, Z.B. Dong, K. Fang, X.H. Zhan, Y.H. Wei, Cellular automaton modelling of dynamic recrystallisation microstructure evolution during friction stir welding of titanium alloy, Mater. Sci. Technol. (United Kingdom). 30 (2014) 700–711. https://doi.org/10.1179/1743284713Y.0000000389.

[185] Y. Estrin, A. Vinogradov, Extreme grain refinement by severe plastic deformation: A wealth of challenging science, Acta Mater. 61 (2013) 782–817. https://doi.org/10.1016/j.actamat.2012.10.038.

[186] L.S. Tóth, Y. Estrin, R. Lapovok, C. Gu, A model of grain fragmentation based on lattice curvature, Acta Mater. 58 (2010) 1782–1794. https://doi.org/10.1016/j.actamat.2009.11.020.

[187] L.S. Toth, C. Gu, Ultrafine-grain metals by severe plastic deformation, Mater. Charact. 92 (2014) 1–14. https://doi.org/10.1016/j.matchar.2014.02.003.

[188] M. Avrami, Kinetics of phase change. II Transformation-time relations for random distribution of nuclei, J. Chem. Phys. 8 (1940) 212–224. https://doi.org/10.1063/1.1750631.

[189] Q. Wang, Z. Liu, B. Wang, Q. Song, Y. Wan, Evolutions of grain size and micro-hardness during chip formation and machined surface generation for Ti-6Al-4V in high-speed machining, Int. J. Adv. Manuf. Technol. 82 (2016) 1725–1736. https://doi.org/10.1007/s00170-015-7508-1.

[190] Y. He, H. Ding, L. Liu, K. Shin, Computer simulation of 2D grain growth using a cellular automata model based on the lowest energy principle, Mater. Sci. Eng. A. 429 (2006) 236–246. https://doi.org/10.1016/j.msea.2006.05.070.

[191] Z. Liao, M. Polyakov, O.G. Diaz, D. Axinte, G. Mohanty, X. Maeder, J. Michler, M. Hardy, Grain refinement mechanism of nickel-based superalloy by severe plastic deformation - Mechanical machining case, Acta Mater. 180 (2019) 2–14. https://doi.org/10.1016/j.actamat.2019.08.059.

[192] G. Sutter, G. List, Very high speed cutting of Ti-6Al-4V titanium alloy - Change in morphology and mechanism of chip formation, Int. J. Mach. Tools Manuf. 66 (2013) 37–43. https://doi.org/10.1016/j.ijmachtools.2012.11.004.

[193] A. Molinari, C. Musquar, G. Sutter, Adiabatic shear banding in high speed machining of Ti-6Al-4V: Experiments and modeling, 2002. https://doi.org/10.1016/S0749-6419(01)00003-1.

[194] M.S. Dargusch, S. Sun, J.W. Kim, T. Li, P. Trimby, J. Cairney, Effect of tool wear evolution on chip formation during dry machining of Ti-6Al-4V alloy, Int. J. Mach. Tools Manuf. 126 (2018) 13–17. https://doi.org/10.1016/j.ijmachtools.2017.12.003.

[195] K. Huang, R.E. Logé, A review of dynamic recrystallization phenomena in metallic materials, Mater. Des. 111 (2016) 548–574. https://doi.org/10.1016/j.matdes.2016.09.012.

[196] B. Beausir, J.J. Fundenberger, Analysis Tools for Electron and X-ray diffraction, ATEX-Software, Www. Atex-Software. Eu, Univ. Lorraine-Metz. (2017).

[197] T. Sakai, A. Belyakov, R. Kaibyshev, H. Miura, J.J. Jonas, Dynamic and post-dynamic recrystallization under hot, cold and severe plastic deformation conditions, Prog. Mater. Sci. 60 (2014) 130–207. https://doi.org/10.1016/j.pmatsci.2013.09.002.

[198] W. Pantleon, Resolving the geometrically necessary dislocation content by conventional electron backscattering diffraction, Scr. Mater. 58 (2008) 994–997. https://doi.org/10.1016/j.scriptamat.2008.01.050.

[199] J.F. Nye, Some geometrical relations in dislocated crystals, Acta Metall. 1 (1953) 153–162. https://doi.org/10.1016/0001-6160(53)90054-6.

[200] J.W. Kysar, Y. Saito, M.S. Oztop, D. Lee, W.T. Huh, Experimental lower bounds on geometrically necessary dislocation density, Int. J. Plast. 26 (2010) 1097–1123. https://doi.org/10.1016/j.ijplas.2010.03.009.

[201] T. Benjamin Britton, A.J. Wilkinson, Stress fields and geometrically necessary dislocation density distributions near the head of a blocked slip band, Acta Mater. 60 (2012) 5773–5782. https://doi.org/10.1016/j.actamat.2012.07.004.

[202] J. Jiang, T.B. Britton, A.J. Wilkinson, Measurement of geometrically necessary dislocation density with high resolution electron backscatter diffraction: Effects of detector binning and step size,

Ultramicroscopy. 125 (2013) 1–9. https://doi.org/10.1016/j.ultramic.2012.11.003.

[203] H. Matsumoto, V. Velay, A. Chiba, Flow behavior and microstructure in Ti-6Al-4V alloy with an ultrafine-grained α-single phase microstructure during low-temperature-high-strain-rate superplasticity, Mater. Des. 66 (2015) 611–617. https://doi.org/10.1016/j.matdes.2014.05.045.

[204] Q. Wang, Z. Liu, B. Wang, A.U. Hassan Mohsan, Stress-induced orientation relationship variation for phase transformation of α-Ti to β-Ti during high speed machining Ti-6Al-4V, Mater. Sci. Eng. A. 690 (2017) 32–36. https://doi.org/10.1016/j.msea.2017.02.098.

[205] M. Cabibbo, S. Zherebtsov, S. Mironov, G. Salishchev, Loss of coherency and interphase α/β angular deviation from the Burgers orientation relationship in a Ti-6Al-4V alloy compressed at 800 ℃, J. Mater. Sci. 48 (2013) 1100–1110. https://doi.org/10.1007/s10853-012-6842-z.

[206] H. Qin, J.J. Jonas, Variant selection during secondary and tertiary twinning in pure titanium, Acta Mater. 75 (2014) 198–211. https://doi.org/10.1016/j.actamat.2014.04.065.

[207] L. Bao, Y. Zhang, C. Schuman, J.S. Lecomte, M.J. Philippe, X. Zhao, C. Esling, Multiple twinning in pure hexagonal close-packed titanium, J. Appl. Crystallogr. 46 (2013) 1397–1406. https://doi.org/10.1107/S002188981302253X.

[208] T. Gladman, On the theory of the effect of precipitate particles on grain growth in metals, Proc. R. Soc. London. Ser. A. Math. Phys. Sci. 294 (1966) 298–309. https://doi.org/10.1098/rspa.1966.0208.

[209] C.H. Wörner, A. Cabo, On the grain growth inhibition by second phases particles, Acta Metall. 35 (1987) 2801–2804. https://doi.org/10.1016/0001-6160(87)90278-1.

[210] D.G. Lee, S. Lee, Y. Lee, Effect of precipitates on damping capacity and mechanical properties of Ti-6Al-4V alloy, Mater. Sci. Eng. A. 486 (2008) 19–26. https://doi.org/10.1016/j.msea.2007.08.053.

[211] N. Moelans, B. Blanpain, P. Wollants, Pinning effect of second-phase particles on grain growth in polycrystalline films studied by 3-D phase field simulations, Acta Mater. 55 (2007) 2173–2182. https://doi.org/10.1016/j.actamat.2006.11.018.

[212] Y.T. Zhu, X.Z. Liao, X.L. Wu, Deformation twinning in nanocrystalline materials, Prog. Mater. Sci. 57 (2012) 1–62. https://doi.org/10.1016/j.pmatsci.2011.05.001.

[213] N.P. Gurao, R. Kapoor, S. Suwas, Deformation behaviour of commercially pure titanium at extreme

strain rates, Acta Mater. 59 (2011) 3431–3446. https://doi.org/10.1016/j.actamat.2011.02.018.

[214] F. Xu, X. Zhang, H. Ni, Q. Liu, {1 1 $\bar{2}$ 4} deformation twinning in pure Ti during dynamic plastic deformation, Mater. Sci. Eng. A. 541 (2012) 190–195. https://doi.org/10.1016/j.msea.2012.02.021.

[215] N. Tao, K. Lu, Dynamic plastic deformation (DPD): A novel technique for synthesizing bulk nanostructured metals, J. Mater. Sci. Technol. 23 (2007) 771–774.

[216] P. Vo, M. Jahazi, S. Yue, P. Bocher, Flow stress prediction during hot working of near-α titanium alloys, Mater. Sci. Eng. A. 447 (2007) 99–110. https://doi.org/10.1016/j.msea.2006.10.032.

[217] L. Bao, C. Schuman, J.S. Lecomte, M.J. Philippe, X. Zhao, C. Esling, A study of twin variant selection and twin growth in titanium, Adv. Eng. Mater. 13 (2011) 928–932. https://doi.org/10.1002/adem.201100055.

[218] M. Lentz, M. Risse, N. Schaefer, W. Reimers, I.J. Beyerlein, Strength and ductility with {10 11}-{1012} double twinning in a magnesium alloy, Nat. Commun. 7 (2016) 1–7. https://doi.org/10.1038/ncomms11068.

[219] V.P. Astakhov, Metal Cutting Mechanics, 1998. https://doi.org/10.1201/9781466571778.

[220] Y. Liu, M. Agmell, D. Xu, A. Ahadi, J.E. Stahl, J. Zhou, Numerical contribution to segmented chip effect on residual stress distribution in orthogonal cutting of Inconel718, Int. J. Adv. Manuf. Technol. 109 (2020) 993–1005. https://doi.org/10.1007/s00170-020-05702-2.

[221] G. Su, Z. Liu, L. Li, B. Wang, Influences of chip serration on micro-topography of machined surface in high-speed cutting, Int. J. Mach. Tools Manuf. 89 (2015) 202–207. https://doi.org/10.1016/j.ijmachtools.2014.10.012.

[222] S.N. Melkote, R. Liu, P. Fernandez-Zelaia, T. Marusich, A physically based constitutive model for simulation of segmented chip formation in orthogonal cutting of commercially pure titanium, CIRP Ann. - Manuf. Technol. 64 (2015) 65–68. https://doi.org/10.1016/j.cirp.2015.04.060.

[223] J.C. Outeiro, F. Rossi, G. Fromentin, G. Poulachon, G. Germain, A.C. Batista, Process mechanics and surface integrity induced by dry and cryogenic machining of AZ31B-O magnesium alloy, in: Procedia CIRP, Post-print, Elsevier, Italy, 2013: pp. 487–492. https://doi.org/10.1016/j.procir.2013.06.138.

[224] K. Moussaoui, M. Mousseigne, J. Senatore, R. Chieragatti, F. Monies, Influence of milling on surface

integrity of Ti6Al4V-study of the metallurgical characteristics: Microstructure and microhardness, Int. J. Adv. Manuf. Technol. 67 (2013) 1477–1489. https://doi.org/10.1007/s00170-012-4582-5.

[225] Y.M. Arisoy, T. Özel, Machine learning based predictive modeling of machining induced microhardness and grain size in Ti-6Al-4V alloy, Mater. Manuf. Process. 30 (2015) 425–433. https://doi.org/10.1080/10426914.2014.961476.

[226] Q. Wang, Z. Liu, Microhardness Prediction Based on a Microstructure-Sensitive Flow Stress Model During High Speed Machining Ti-6Al-4V, J. Manuf. Sci. Eng. Trans. ASME. 140 (2018) 1–15. https://doi.org/10.1115/1.4039889.

[227] P.N. Kalu, D.R. Waryoba, A JMAK-microhardness model for quantifying the kinetics of restoration mechanisms in inhomogeneous microstructure, Mater. Sci. Eng. A. 464 (2007) 68–75. https://doi.org/10.1016/j.msea.2007.01.124.

[228] Z. Pan, D.S. Shih, A. Tabei, H. Garmestani, S.Y. Liang, Modeling of Ti-6Al-4V machining force considering material microstructure evolution, Int. J. Adv. Manuf. Technol. 91 (2017) 2673–2680. https://doi.org/10.1007/s00170-016-9964-7.

[229] W. Zhang, X. Wang, Y. Hu, S. Wang, Quantitative Studies of Machining-Induced Microstructure Alteration and Plastic Deformation in AISI 316 Stainless Steel Using EBSD, J. Mater. Eng. Perform. 27 (2018) 434–446. https://doi.org/10.1007/s11665-018-3129-9.

[230] V. Schulze, E. Uhlmann, R. Mahnken, A. Menzel, D. Biermann, A. Zabel, P. Bollig, I.M. Ivanov, C. Cheng, R. Holtermann, T. Bartel, Evaluation of different approaches for modeling phase transformations in machining simulation, Prod. Eng. 9 (2015) 437–449. https://doi.org/10.1007/s11740-015-0618-7.

[231] M.A. Meyers, A. Mishra, D.J. Benson, Mechanical properties of nanocrystalline materials, Prog. Mater. Sci. 51 (2006) 427–556. https://doi.org/10.1016/j.pmatsci.2005.08.003.

[232] S. Rinaldi, D. Umbrello, S.N. Melkote, Modelling the effects of twinning and dislocation induced strengthening in orthogonal micro and macro cutting of commercially pure titanium, Int. J. Mech. Sci. 190 (2021) 106045. https://doi.org/10.1016/j.ijmecsci.2020.106045.

[233] Q. Wang, Z. Liu, Microhardness Prediction Based on a Microstructure-Sensitive Flow Stress Model During High Speed Machining Ti-6Al-4V, J. Manuf. Sci. Eng. Trans. ASME. 140 (2018) 091003. https://doi.org/10.1115/1.4039889.

[234] D. Yang, X. Xiao, X. Liang, Analytical modeling of residual stress in orthogonal cutting considering tool edge radius effect, Int. J. Adv. Manuf. Technol. 103 (2019) 2965–2976. https://doi.org/10.1007/s00170-019-03744-9.

[235] X. Liang, Z. Liu, Q. Wang, B. Wang, X. Ren, Tool wear-induced microstructure evolution in localized deformation layer of machined Ti–6Al–4V, J. Mater. Sci. 55 (2020) 3636–3651. https://doi.org/10.1007/s10853-019-04214-z.

[236] X. Zhang, R. Shivpuri, A.K. Srivastava, Role of tool flank wear and machining speed in developing of residual stress in machined surface during high speed machining of titanium alloys, ASME 2015 Int. Manuf. Sci. Eng. Conf. MSEC 2015. 1 (2015) 1–9. https://doi.org/10.1115/MSEC20159401.

[237] Q. Liu, J. Li, J. Liu, ParaView visualization of Abaqus output on the mechanical deformation of complex microstructures, Comput. Geosci. 99 (2017) 135–144. https://doi.org/10.1016/j.cageo.2016.11.008.

[238] T. Mabrouki, F. Girardin, M. Asad, J.F. Rigal, Numerical and experimental study of dry cutting for an aeronautic aluminium alloy (A2024-T351), Int. J. Mach. Tools Manuf. 48 (2008) 1187–1197. https://doi.org/10.1016/j.ijmachtools.2008.03.013.

[239] T. Özel, D. Ulutan, Prediction of machining induced residual stresses in turning of titanium and nickel based alloys with experiments and finite element simulations, CIRP Ann. - Manuf. Technol. 61 (2012) 547–550. https://doi.org/10.1016/j.cirp.2012.03.100.

[240] P. Dahlman, The influence of rake angle, cutting feed and cutting depth on residual stresses in hard turning, J. Mater. Process. Technol. 147 (2004) 181–184. https://doi.org/10.1016/j.matprotec.2003.12.014.

[241] M.N.A. Nasr, E.G. Ng, M.A. Elbestawi, A modified time-efficient FE approach for predicting machining-induced residual stresses, Finite Elem. Anal. Des. 44 (2008) 149–161. https://doi.org/10.1016/j.finel.2007.11.005.

[242] I.S. Jawahir, E. Brinksmeier, R. M'Saoubi, D.K. Aspinwall, J.C. Outeiro, D. Meyer, D. Umbrello, A.D. Jayal, Surface integrity in material removal processes: Recent advances, CIRP Ann. - Manuf. Technol. 60 (2011) 603–626. https://doi.org/10.1016/j.cirp.2011.05.002.

List of publications

[1]. **X. Xu**, J. Outeiro, J. Zhang, B. Xu, W. Zhao, V. Astakhov, **Machining simulation of Ti-6Al-4V using coupled Eulerian-Lagrangian approach and a constitutive model considering the state of stress**, Simulation Modeling Practice and Theory. 110 (2021) 102312.

[2]. **X. Xu**, J. Zhang, J. Outeiro, B. Xu, W. Zhao, **Multiscale simulation of grain refinement induced by dynamic recrystallization of Ti-6Al-4V alloy during high speed machining**, Journal of Materials Processing Technology. 286 (2020) 116834.

[3]. **X. Xu**, J. Zhang, H. Liu, Y. He, W. Zhao, **Grain refinement mechanism under high strain-rate deformation in machined surface during high speed machining Ti-6Al-4V**, Materials Science and Engineering A. 752 (2019) 167–179.

[4]. **X. Xu**, J. Outeiro, J. Zhang, B. Li, W. Zhao, **Simulation of material side flow using a 3D coupled Eulerian-Lagrangian approach and a constitutive model considering the stress state**, Procedia CIRP. 102 (2021) 441–446.

[5]. **X. Xu**, J. Zhang, H. Liu, Y. Qi, Z. Liu, W. Zhao, **Effect of morphological evolution of serrated chips on surface formation during high speed cutting Ti-6Al-4V**, Procedia CIRP. 77 (2018) 147–150.

[6]. J. Zhang, **X. Xu**, J. Outeiro, H. Liu, W. Zhao, **Simulation of Grain Refinement Induced by High-Speed Machining of OFHC Copper Using Cellular Automata Method**, Journal of Manufacturing Science and Engineering, Transaction of ASME. 142 (2020).

[7]. H. Liu, **X. Xu**, J. Zhang, Z. Liu, Y. He, W. Zhao, **The state of the art for numerical simulations of the effect of the microstructure and its evolution in the metal-cutting processes**, International Journal of Machine Tools and Manufacture. 177 (2022) 103890.

HESAM UNIVERSITÉ

Arts et Métiers Sciences et Technologies

Xiang XU

Modelling of microstructure evolution and surface integrity in high speed machining of Ti-6Al-4V alloy

Résumé

Le développement rapide de l'industrie aérospatiale est la motivation pour augmenter la productivité de la fabrication en gardant la même qualité de pièce ou même en l'améliorant. L'usinage à grande vitesse (UGV) des matériaux difficiles à usiner comme les alliages à base de titane est un moyen d'atteindre une productivité élevée. Dorénavant, la plupart des travaux de recherche sur l'intégrité de surface en usinage sont basés sur l'analyse phénoménologique et impliquent rarement une analyse théorique des phénomènes physiques responsables de la modification des propriétés de la couche proche de la surface. Dans ces travaux de recherche, l'évolution de la microstructure et l'intégrité de surface induites par l'UGV de l'alliage Ti-6Al-4V sont étudiées à l'aide d'approches de modélisation et expérimentales. Une approche de modélisation multi-échelles combinant des simulations par éléments finis utilisant l'approche CEL et la méthode des automates cellulaires a permis de simuler l'évolution de la microstructure lors de l'usinage, y compris dans la surface et la sous-couche usinées. La topographie de la surface, la déformation plastique, la microdureté et les contraintes résiduelles dans la surface et la sous-couche usinées ont également été simulées, révélant l'influence de la nature cyclique du procédé de coupe sur ces caractéristiques d'intégrité de surface.

Mots clés : Modélisation multi-échelle, Usinage à Grande Vitesse, Ti-6Al-4V, Microstructure, Recristallisation Dynamique, Intégrité de Surface.

Abstract

The rapid development of aerospace industry is the motivation for increasing the manufacturing productivity keeping the same part quality or even improving it. High-speed machining (HSM) of difficult-to-cut materials like Titanium-based alloys is a way to achieve a high productivity. So far, most of research works on surface integrity in machining are based on the phenomenological analysis and rarely involve a theoretical analysis of the physical phenomena responsible for the modification of the near surface layer properties. In this research work, the microstructure evolution, and the surface integrity in HSM of Ti-6Al-4V alloy are investigated using modelling and experimental approaches. A multiscale modelling approach combining finite element simulations using CEL approach and cellular automata method permitted to simulate the microstructure evolution in machining, including in the machined surface and subsurface. Surface topography, plastic strain, microhardness, and residual stresses of the machined surface and subsurface were also simulated, revealing the influence of the cyclic nature of the cutting process in these surface integrity characteristics.

Keywords: Multiscale-modelling, High Speed Machining, Ti-6Al-4V, Microstructure, Dynamic Recrystallization, Surface Integrity.